



**University of
Nottingham**

UK | CHINA | MALAYSIA

Rational Synthesis of Activated Carbons for Enhanced CO₂ Uptake and Methane Storage

Thesis submitted to the University of Nottingham for the degree of
Doctor of Philosophy, January 2024

Nawaf Albeladi

20205375

Supervised by

Professor Robert Mokaya

**School of Chemistry
University of Nottingham**

Abstract

The atmospheric concentration of CO₂ has reached alarming levels, primarily due to the combustion of fossil fuels. This surge in CO₂ concentrations has led to rising global temperatures, increased frequency of extreme weather events, and threats to all forms of life on Earth. This scenario necessitates the urgent need to develop CO₂ capture and removal technologies to ensure a more sustainable future. Moreover, the use of fossil fuels not only contributes significantly to CO₂ emissions but reserves and supply are also limited. This Thesis covers themes on the rational preparation of porous carbons that are targeted at the capture of CO₂ or the storage of gases (e.g. methane) that may be used as transitional energy sources towards a fossil-free economy. In this regard, **Chapter 1** explores the state-of-the art on potential solutions, including CO₂ capture and storage via physisorption on porous materials, with a focus on readily synthesised activated carbons. Additionally, the chapter highlights the potential of methane-based natural gas as an alternative to conventional fossil fuels for vehicular transport, given its abundant reserves and lower carbon emissions. The storage of methane for vehicular use may be achieved using porous materials. However, the preparation of porous materials that meet set targets, such as those outlined by the US Department of Energy (DOE), remains a challenge. The considerations that must be carefully considered in seeking suitable materials for such gas storage applications include precise control over porosity parameters such as surface area, pore volume, pore size, and packing density. Therefore, both the ability to accurately modulate the textural properties and a comprehensive understanding of the relationship between gas (CO₂ or CH₄) uptake capacity and pore size are essential. This thesis is aimed to address these issues.

Chapter 2 concentrates on material characterisation to gain a comprehensive understanding of the targeted porous carbon nanostructures. To fully assess these

materials, a combination of chemical, structural, and surface characterisation techniques have been employed. This chapter provides a concise overview of the equipment and techniques used for the characterisation of the materials prepared during this research programme.

Regarding preparation routes to activated carbons, this work investigates two primary synthesis methods. Firstly, **Chapter 3** delves into the effect of the air-carbonisation treatment. This study aimed to investigate the impact of air-carbonisation temperature followed by potassium hydroxide (KOH) activation on the structure and gas adsorption performance of activated carbons. It primarily focused on the effect of air-carbonisation treatment on the O/C ratio (a measure of a precursor's susceptibility to activation) in carbonaceous matter. The study found a role of air-carbonisation temperature in tailoring the porosity, surface area, and packing density of the activated carbons. It revealed a very notable trend in the O/C ratio of the carbonaceous matter, which decreases as the temperature increases. This knowledge enables the optimal design of the pore structure of the activated carbons, resulting in porous carbons with high CO₂ uptake, at 25 °C, of 2.0 and 5.2 mmol g⁻¹ at 0.15 and 1 bar, respectively. As a result of the ability to adjust the O/C ratio of the precursor, activated carbons with a high packing density of up to 0.79 g cm⁻³ were obtained, resulting in high CH₄ uptake, wherein the gravimetric and volumetric uptake reach of 0.38 g g⁻¹ and 278 cm³ (STP) cm⁻³, respectively, at 25 °C and 100 bar.

The second approach centres on the effect of the activation technique when utilising N-rich precursors generated via varying pathways. Thus in **Chapter 4**, a N source was introduced to biomass-derived carbonaceous matter through the use of additives, resulting in a incorporation of N in the precursor. This process involves adding melamine or urea as a nitrogen source to an activation mixture containing biomass-derived carbonaceous matter of low O/C ratio (air-carbonised date seed, *Phoenix dactylifera*, ACDS), and KOH as an activating agent. These carbons exhibit a broad range of surface areas and porosity characteristics, controlled by varying the amount of melamine or urea, the KOH/ACDS ratio, and the activation temperature. The N added to the activation mix serves as both an N-dopant and porogen, with the later effect enabling the formation of larger pores, extending the pore size distribution into the mesopore region, and increasing the surface area. This results in carbons with tunable porosity and variable packing density, suitable for enhanced CO₂ and

methane uptake. The carbons exhibited excellent low-pressure CO₂ capture at 25 °C, of 1.7 mmol g⁻¹ at 0.15 bar and 4.7 mmol g⁻¹ at 1 bar. The porosity and packing density of the carbons also were directed and modulated towards methane storage, showing a gravimetric uptake of up to 0.42 g g⁻¹ at 25 °C and 100 bar, and volumetric storage capacity of up to 266 cm³ (STP) cm⁻³ at 25 °C and 100 bar.

Expanding on the knowledge gained in **Chapter 4** from KOH activation of precursors with nonhomogeneous incorporation of N additives and low O/C ratio precursors, **Chapter 5** explores activated carbons derived from precursors with homogeneous incorporation of N. **Chapter 5** explores the potential of N-rich crosslinkable imidazolium-based ionic liquids as a new class of carbon precursors for activated carbons. Upon carbonisation, the ionic liquids yield carbonaceous matter (designated as IL-C) with the unusual combination of a high N content and low O/C atomic ratio. During activation, the resulting ionic liquid-derived carbonaceous matter (IL-C) generates activated carbons with a mix of micro- and mesoporosity, having ultra-high surface area of up to ~4000 m² g⁻¹ and a pore volume of up to 3.3 cm³ g⁻¹. These carbons, due to their porosity and packing density, exhibit outstanding gravimetric and volumetric methane uptake of up to 0.53 g g⁻¹ and 289 cm³ (STP) cm⁻³, respectively, at 25 °C and 100 bar. This surpasses both gravimetric and volumetric methane storage targets, making these ionic liquid-derived activated carbons the first porous materials (carbon or MOF) to meet both gravimetric and volumetric storage targets as set by the US DoE.

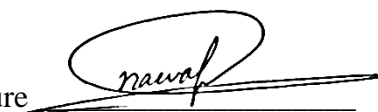
To further enhance understanding of the role of N in shaping the porosity of activated carbons, **Chapter 6** goes beyond KOH activation to explore non-hydroxide activation of IL-C. Activated carbons were generated via chemical activation of IL-C using a non-hydroxide activating agent, potassium oxalate (PO). Due to the very low atomic ratio O/C of 0.116 of IL-C, and gentler activating nature of PO, the generated activated carbons display moderate to high surface area of 447 to 2202 m² g⁻¹, depending on the activation temperature. The porosity of the activated carbon could be tailored to exhibit a highly microporous structure with porosity suitable for post-combustion CO₂ uptake, having CO₂ capacities of 1.6 and 4.2 mmol g⁻¹ At 25 °C and pressures of 0.15 and 1 bar, respectively. As a benefit of PO being a milder and greener activating agent, the activated carbons have excellent properties in terms of high packing density (0.98 cm³ g⁻¹) combined with a high surface area density (2039 m² cm⁻³), which

translates to excellent volumetric methane gas uptake. At 100 bar and 25 °C, the carbons achieve total volumetric uptake of 282 cm³ (STP) cm⁻³ along with excellent deliverable capacity of 200 cm³ (STP) cm⁻³ (for a pressure swing of 100 bar → 5 bar).

Chapter 7 provides a summary and conclusions of this thesis, along with a future look at specific aspects. As an overview, this thesis delves into the rational and intentional synthesis of activated carbons for which various precursors and activation techniques are explored. The outcome has yielded exceptional activated carbons distinguished by the possibility of deliberately tailoring the porosity towards high surface area and pore volume. The motivation of the thesis is achieving porosity in the activated carbons that is suitable for addressing challenges associated with CO₂ uptake and optimising methane storage. This research also opens up new possibilities in terms of applications for the synthesised activated carbons. A particularly promising application for future exploration lies in the utilisation of these activated carbons for hydrogen storage, presenting an exciting prospect for further investigation.

Declaration

I hereby declare that this thesis with the title "*Rational Synthesis of Activated Carbons for Enhanced CO₂ Uptake and Methane Storage*," represents my original work and has been written by myself has not been previously submitted for any other academic qualification or degree. All sources, materials, and contributions from others, which are referenced in this thesis, have been duly acknowledged and cited. I affirm that all data, figures, and findings presented in this thesis are accurate, complete, and authentic to the best of my knowledge.

Signature 

Date 7 May 2024

Acknowledgments

From the initial steps of my PhD journey to the moment of submitting my thesis, this journey has been a challenge, pushing the boundaries of my knowledge, resilience, and passion for academic exploration, serving as a constant reminder that the pursuit of knowledge is an exhilarating adventure. Such a journey would not be possible without the advice and support of many people.

First and foremost, I would like to thank the government of the Kingdom of Saudi Arabia for funding my PhD studentship together with Taibah University.

I am profoundly grateful to my thesis supervisor, Professor Robert Mokaya, whose expertise, patience, and unwavering support have been instrumental in shaping this work. Your guidance and mentorship have been a source of inspiration.

I would also like to extend my particular thanks to the technical staff in the School of Chemistry, Neil Barnes and Mark Guyler, for their invaluable assistance with various techniques, and to Dr Tang in elemental analysis. Additionally, I am grateful to the Nanoscale and Microscale Research Centre (NMRC), and especially to Michael Fay, for their exceptional assistance with the scanning electron microscopy, transmission electron microscopy images, and X-Ray Photo Spectroscopy, which were pivotal in this study.

My heartfelt appreciation also goes to my family, who have been my unwavering pillars of support throughout this journey. Especially my mother and my father and my siblings, have been a constant source of encouragement and belief in my abilities. I am grateful to my beloved wife, Zainab, and our two beautiful daughters, Savanna and Eva. Your unwavering support, patience, and understanding during the most demanding moments of this journey have kept me motivated and reminded me of the importance of family. As my daughter Savanna aptly expressed, 'My children always

want to play with me, and they are so funny and full of joy. However, their Dad hardly ever has the time to join in because he works incredibly hard on his computer to provide for us, ensuring we can one day embark on an airplane journey to Saudi Arabia.' Your love and understanding of my commitment to this journey have been a constant source of motivation.

Finally, this thesis would not have been possible without the help and support of the members of our research group in the School of Chemistry.

Contents

Abstract	ii
Declaration	vi
Acknowledgments	vii
Contents	ix
List of Publications	xiv
My Contribution to these Papers	xv
Presentations	xvi
Poster Sessions	xvii
Abbreviations	xviii
Chapter 1	1
Introduction	1
1.1 Climate Change and Global Warming	1
1.2 Net Zero Emissions (NZE)	2
1.3 Chemisorption and physisorption	3
1.3.1 Influence of surface characteristics on adsorption process	5
1.3.2 Differences in gas adsorption behaviour	7
1.4 Porosity	8
1.5 Porous Materials	9
1.5.1 Metal-Organic Framework (MOFs)	9
1.5.2 Zeolites	10

1.5.3 Activated Carbons (ACs)	11
1.5.3.1 Mode of Carbonisation.....	14
1.5.3.2 Modulating Porosity.....	15
1.6 Carbon Capture and Storage (CCS)	19
1.7 Methane storage	21
1.7.1 Fundamental Concept of Methane Storage	25
1.8 Motivations & Objectives	28
References	30
Chapter 2	44
Experimental Methodology	44
2.1 Characterisation method	44
2.1.1 Elemental CHN Analysis ¹	44
2.1.2 Thermogravimetric Analysis (TGA).....	46
2.1.3 Powder X-ray Diffraction (PXRD)	47
2.1.4 Electron Microscopy	49
2.2 Porosity and Physisorption.....	51
2.2.1 Pore characteristics and filling mechanisms	51
2.2.2 Principles of Physisorption	55
2.2.3 Types of physisorption isotherms	56
2.2.4 Brunauer-Emmett-Teller (BET) adsorption theory.....	60
2.2.5 Pore size distribution (PSD).....	65
2.3 Gas uptake measurement	67
References	69
Chapter 3	72
Effect of Air-Carbonisation Temperature on the Porosity and Gas Adsorption Performance of Biomass-Derived Activated Carbons	72
Abstract	72

3.1 Introduction	74
3.2 Experimental section	76
3.2.1 Material synthesis	76
3.2.2 Material characterisation	77
3.2.3 Gas uptake measurements of (CO ₂ and CH ₄)	78
3.3 Results and discussion	78
3.3.1 Yield and elemental analysis	78
3.3.2 Structural and morphological characterisation	82
3.3.3 Porosity and textural properties	90
3.3.4 Gas uptake measurements	99
3.3.4.1 CO ₂ uptake	99
3.3.4.2 Methane storage	106
3.4 Conclusion	113
References	114
Chapter 4	120
Modulating The Porosity of N-doped Carbon Materials for Enhanced CO₂ Capture and Methane Uptake	120
Abstract	120
4.1 Introduction	121
4.2 Experimental Section	123
4.2.1 Synthesis of N-doped carbons	123
4.2.2 Materials Characterisation	125
4.2.3 Gas (CO ₂ & CH ₄) Uptake Measurements	126
4.3 Results and Discussion	126
4.3.1 Yield and elemental compositions of N-doped carbons	126
4.3.2 TGA analysis and the morphology of N-doped carbons	130
4.3.3 Porosity and textural properties	136

4.3.4 Gas uptake	144
4.3.4.1 CO ₂ uptake	144
4.3.4.2 Methane storage	149
4.4 Conclusion	158
References	159
Chapter 5	164
Ultra-high surface area ionic-liquid-derived carbons that meet both gravimetric and volumetric methane storage targets	164
Abstract	164
5.1 Introduction	165
5.1.1 Ionic liquids as carbon precursors	165
5.1.2 Previous studies of ionic liquids as carbon precursors	166
5.2 Ionic liquid-derived activated carbon for methane storage	167
5.3 Experimental section	171
5.3.1 Materials	171
5.3.2 Materials Characterisation	171
5.3.3 Methane uptake measurements	173
5.4 Results and discussion	173
5.4.1 Nature of ionic and composition of liquid-derived carbons	173
5.4.2 Porosity of ionic-liquid derived activated carbons	188
5.4.3 Methane storage of ionic-liquid derived activated carbons	202
5.4.3.1 Comparison with benchmark materials	211
5.4.3.2 Link between nature of precursor porosity and enhanced methane uptake	220
5.5 Conclusions	224
References	225

Chapter 6	231
Non-Hydroxide Activated Carbons Derived from Ionic Liquid Precursor for Enhanced CO₂ and Methane Storage	231
Abstract	231
6.1 Introduction	232
6.2 Experimental and Methodology	233
6.2.1 Materials preparation	233
6.2.2 Materials characterisation	234
6.2.3 Gas uptake measurements	235
6.3 Results and discussion	235
6.3.1 Nature of ionic liquid-derived carbons and elemental composition	235
6.3.2 Textural properties and porosity	242
6.4 Gas uptake	248
6.4.1 CO ₂ uptake	248
6.4.2 CH ₄ uptake	252
6.5 Conclusion	257
References	258
Chapter 7	262
Summary and Future Outlook	262

List of Publications

- I. Nawaf Albeladi, L. Scott Blankenship and Robert Mokaya, **Ultra-high surface area ionic-liquid-derived carbons that meet both gravimetric and volumetric methane storage targets**, *Energy & Environmental Science*, 2024, <https://doi.org/10.1039/D3EE03957A>.
- II. L. Scott Blankenship, Nawaf Albeladi, Thria Alkhaldi, Asma Madkhali and Robert Mokaya, **Brute force determination of the optimum pore sizes for CO₂ uptake**, *Energy Advances*, 2022 (1), 1009-1020, doi: [10.1039/d2ya00149g](https://doi.org/10.1039/d2ya00149g).
- III. Nawaf Albeladi, Anti Kur, Robert Mokaya, Jo Darkwa, Sarah Roger-Lund, Mark Worall, John Calautit, Rabah Boukhanouf, **Synthesis and Characterisation of Doped Magnesium Hydroxide for Medium Heat Storage Application**, *Materials*, 2023 (18), 6296, <https://doi.org/10.3390/ma16186296>.

My Contribution to these Papers

Publication I, the author conducted all experimental work, the methodology and formal analysis, investigation, and writing.

Publication II, the author contributed to the synthesis of some samples and the measurement of some isotherms.

Publication III, the author participated in synthesising all the materials, methodology, conducting formal analysis, investigation, and writing.

Note: The work described in publication III has not been included in this thesis, as it was a collaborative effort with another research group.

Presentations

- I. Nawaf Albeladi and Robert Mokaya, '*Ultra-high surface area and high methane storage capacity of activated carbons derived from crosslinkable Imidazolium-based Ionic Liquid*' Talk at Internal MBS & Material Seminars, 9th February 2022.

- II. Nawaf Albeladi and Robert Mokaya, '*Low carbonisation temperature for conversion of biomass to porous carbon with enhanced CO₂ uptake*', Talk at School of Chemistry PhD Symposium 13th July 2022.

Poster Sessions

- I. Nawaf Albeladi and Robert Mokaya, poster session entitled '***Direct Carbonisation of Crosslinkable Imidazolium-Based Ionic Liquid Precursor for Porous Carbon Material***' at the 15th International conference on materials chemistry (MC15), online event, 12th – 15th July 2021.

- II. Nawaf Albeladi and Robert Mokaya '***Ultra-High Surface Area and Exceptional Methane Storage Capacity of Activated Carbons Derived from Crosslinkable Imidazolium-Based Ionic Liquids***' at 5th Annual UK Porous Materials Conference (UKPorMat 2022), University of Strathclyde, Glasgow 13th – 14th June 2022.

- III. Nawaf Albeladi and Robert Mokaya '***Modulating the porosity of N-doped carbon materials for enhanced CO₂ capture and methane uptake***' at the 6th Annual UK Porous Materials Conference (UKPorMat 2023), University of Sheffield, 19th – 20th June 2023.

Abbreviations

AC: Activated Carbon

ACDS: Air-Carbonised Date Seed

ANG: Adsorbed Natural Gas

BET: Brunauer, Emmet, and Teller Theory

BMI: 1-butyl-3-methylimidazolium

CCS: Carbon Capture and Storage

CNG: Compressed Natural Gas

DFT: Density Functional Theory

DOE: Department of Energy

GHGs: Green House Gasses

HTb: Hookah Tobacco

HTC: Hydrothermal Carbonisation

IL: Ionic Liquid

IL-C: Carbonised Ionic Liquid

IL-AC: Ionic Liquid Derived Activated Carbons (Activated via KOH)

IL-AC-PO: Ionic Liquid Derived Activated Carbons (Activated via PO)

IUPAC: International Union of Pure and Applied Chemistry

KOH: Potassium Hydroxide

LNG: Liquefied Natural Gas

MOF: Metal Organic Framework

NG: Natural Gas

NZE: Net Zero Emissions

NLDFT: Non-Local Density Functional Theory

O/C: Oxygen-to-Carbon Atomic Ratio

PO: Potassium Oxalate

P-XRD: Powder X-ray Diffraction

PSD: Pore Size Distribution

SEM: Scanning Electron Microscopy

SAD: Surface Area Density

STP: Standard Temperature and Pressure

TGA: Thermogravimetric Analysis

TEM: Transmission Electron Microscopy

XPS: X-ray Photoelectron Spectroscopy

Chapter 1

Introduction

1.1 Climate Change and Global Warming

The world is currently facing a climate and ecological crisis that poses a severe threat to all life on Earth.^{1, 2} Within the context of 21st-century challenges, the depletion of fossil fuels and the associated pollution have emerged as highly significant concerns. This is closely tied to the consistent increase in global energy consumption, primarily driven by industrialisation and human desire to enhance both living standards and sustainability.³ This rapid economic expansion has given rise to an insatiable demand for energy, which is predominantly met by fossil fuels. However, this heavy reliance on fossil fuels has resulted in both environmental and economic issues, due to fossil fuels being both finite and non-renewable, while their use releases environmentally harmful by-products, including greenhouse gases (GHGs), such as carbon dioxide (CO₂), methane (CH₄) and nitrous oxide (N₂O).³ These gases contribute to the phenomenon of global warming by creating a greenhouse effect, trapping heat from the sun, and gradually raising the planet's temperature.¹

According to the Intergovernmental Panel on Climate Change (IPCC), human activities, including burning fossil fuels, deforestation, and industrial processes, have led to a significant increase in greenhouse gas concentrations in the atmosphere.¹ As a result, the earth's average temperature has already risen more than 1.2 °C above pre-industrial levels.¹ Without effective climate change mitigation policies, global warming will reach 1.5 °C by 2030.^{1, 4}

Considerable efforts are now being made to reduce emissions of CO₂, widely recognised as the primary greenhouse gas responsible for global warming, as a result of the burning of fossil fuels.⁵⁻⁷ A focus has also been placed on transitioning to renewable energy sources, such as solar, wind, hydro, and biomass-based processes. However, stabilising atmospheric CO₂ levels is a long-term endeavour, necessitating

a multifaceted approach.⁸ This approach encompasses improvements in energy efficiency, a transfer to low-carbon fuels, the use of CO₂ capture technologies, and the adoption of sustainable and clean energy sources.^{1, 4, 9-11}

1.2 Net Zero Emissions (NZE)

Mitigating climate change is no longer a choice but an existential imperative. According to the Paris Agreement,⁸ the objective is to keep global warming well below 2 °C above pre-industrial levels, which demands a major reduction in greenhouse gas emissions, as well as considerable transitions in the energy sector, alongside initiatives to capture CO₂.^{8, 12-14} Although bioremediation of carbon-capturing ecosystems plays a significant role in offsetting GHG emissions, it may not fulfil either the Paris Climate Agreement or the UK's goal of achieving Net Zero Emissions (NZE) by 2050.^{8, 14, 15}

To meet these ambitious emissions reduction targets set by international agreements, it is clear that the development of novel, low-cost CO₂ capture technologies is essential.^{16, 17} These technologies will have a crucial role in achieving NZE as part of the short-term solution. Additionally, it is also important for the global economy to rapidly transition from the use of fossil fuels for vehicles, towards cleaner and renewable resources, i.e. CH₄, as a transitional energy source, and H₂ as a long term solution.¹⁸⁻²⁰

NZE represents a transformative goal against climate change, signifying that the total GHG emissions released into the atmosphere are balanced by actions that remove or offset an equivalent amount of emissions.⁷ Thus, NZE necessitates a comprehensive approach including emissions reduction strategies, the widespread adoption of renewable energy, afforestation efforts, and the implementation of carbon capture and storage (CCS) technologies.^{7, 11} This indicates the need for effective CO₂ capture methods and a transition to cleaner energy sources to fulfil the ambitious emissions reduction targets set by international agreements and national goals.

However, there are a number of economic and practical challenges related to the effective capture, storage and transportation of CO₂, CH₄, and H₂, particularly as they exist in the gas phase under ambient conditions.^{16, 18, 21-26} For example, currently, industrial CO₂ capture primarily relies on reactions with liquid amines, a method that faces challenges due to its relatively low CO₂ adsorption capacity combined with an

energy-intensive amine regeneration process.^{27, 28} Similarly, the storage of CH₄ and H₂ traditionally involves compression or liquefaction, leading to high energy costs associated with maintaining the required pressures and temperatures, which limits their practical use in mobile or vehicular applications.^{16, 18, 21, 24, 26, 29-31}

To address these challenges, promising alternative solutions have emerged in the form of chemical (chemisorption) or physical (physisorption) adsorption of the gases onto suitable solid materials.¹⁶ In particular, physisorption has the advantage of facile adsorbate regeneration through pressure reduction (pressure swing processes) or temperature increase (temperature swing processes). The sorption technology, if properly applied, can offer promising solutions to the capture and storage challenges associated with CO₂, CH₄, and H₂. Porous materials, such as metal organic frameworks (MOFs),³²⁻³⁴ porous polymers,³⁵ porous inorganic membranes,³⁶ and zeolites³⁷⁻³⁹ present potential gas storage solutions. However, the use of these materials faces limitations such as high production costs and finite lifecycles due to thermal instability or reactivity with contaminants such as water.¹⁶ In contrast, porous carbons have emerged as a promising candidate for gas storage due to being relatively inexpensive to produce and their high thermal and chemical stability.^{16, 24, 40} Furthermore, the porosity of carbon can be tailored to target selective adsorption of specific gases under a variety of set uptake and release conditions with respect to pressure and temperature.^{16, 41, 42}

1.3 Chemisorption and physisorption

Adsorption can be defined as a surface phenomenon where molecules of a gas or liquid phase (adsorbate) are attached to the surface of a solid or liquid (adsorbent).⁴³ Adsorption could be classified into two main types according to the interaction that occurs between the adsorbate molecules and the surface of the adsorbent: chemisorption and physisorption.⁴³

Chemisorption (chemical adsorption) occurs when the adsorbate molecules form a chemical bond with the surface of the adsorbent. This type of adsorption is usually characterised by the formation of strong bonds (including covalent, ionic, and hydrogen bonding) that can significantly alter the electronic structures of the adsorbate and the adsorbent.⁴³ Due to these strong interactions, chemisorption typically involves higher activation energies and is often irreversible. Chemisorption is usually limited

to the formation of a monolayer because once the surface sites are occupied, no additional adsorption can occur without removing the first layer.⁴³ This implies that chemisorption efficiency increases with the surface area of the adsorbent. Chemisorption is highly selective and occurs only when a chemical connection between the adsorbent and the adsorbate is possible.⁴³ For example, H₂ can be stored via chemisorption particularly through the use of compounds containing H₂ such as chemical hydrides and nitrides, which can then be released under specific conditions.⁴⁴ For instance, magnesium hydride, a material noted for its high H₂ storage capacity and cost-effectiveness, has a high H₂ storage capacity of up to 7.6 wt%. However, releasing this stored hydrogen requires heating the material to ~ 300 °C, which consumes about 2.4 wt% of the stored hydrogen, and only about 5.2 wt% of the originally stored hydrogen is available for practical use.⁴⁴ This illustrates the fundamental challenges associated with storing H₂ and other gases like CO₂ or CH₄ using chemisorption.⁴⁴

Physisorption (physical adsorption), on the other hand, involves targeted species being adhered to and accumulated via weaker interactions, typically van der Waals forces, which do not involve significant exchange or sharing of electrons between the adsorbate and the adsorbent.⁴³ Unlike chemisorption, physisorption is characterised by a lower heat of adsorption and is generally reversible. It can also facilitate the formation of multilayers of the adsorbate, where the first layer serves as the substrate for subsequent layers. The physisorption of H₂, for example, allows it to be stored in its molecular form, with the adsorption enthalpy being sufficiently low.⁴⁵ This offers added advantages for the regeneration of the stored H₂, whether by increasing the temperature (temperature swing processes) or decreasing the pressure (pressure swing processes).¹⁶ This results in fast kinetics, thereby increasing the energy efficiency of storing H₂ or other gases such as CO₂ or CH₄ on porous materials via physisorption. This type of sorption is discussed in detail in **Chapter 2 section 2.2**

Table 1.1. Comparison between chemisorption and physisorption.^{43, 46}

Parameter	Chemisorption	Physisorption
Nature of bond	Strong chemical bonds	Weak van der Waals forces
Surface layer	Monolayer phenomenon	Multilayers phenomenon
Reversibility (desorption)	Inherently irreversible	Reversible
Enthalpy of adsorption	High (typically 80–240 kJ/mol)	Low (typically less than 40 kJ/mol)
Temperatures dependence	Increase with temperature	Decrease with temperature
Adsorption speed	Slow at low temperature and fast at high temperature	Rapid
Specificity	High specific and selective	Less specific, and dependent on several factors such as pore width and nature of the adsorbate

1.3.1 Influence of surface characteristics on adsorption process

The adsorption mechanisms of these gases on solid adsorbents are influenced by several factors such as textural properties (surface area, pore volume, and pore size), and the nature of the surface, including defect sites and functional groups.⁴⁷⁻⁵⁰ For instance, increasing the surface area of the adsorbent allows more adsorbate to be adsorbed by increasing the number of adsorption sites. This factor is crucial for both types of adsorption (chemisorption and physisorption), especially in chemisorption, which is limited to a monolayer phenomenon.^{43, 46} At lower pressures, smaller pores contribute significantly to the measured amount of adsorbed gas. Smaller pores may preferentially adsorb smaller molecules due to strong adsorbate–adsorbent interactions, thereby enhancing selectivity.^{16, 29, 51} Studies have shown that CO₂ uptake at low pressures (0.15 and 1 bar) is primarily influenced by pore size rather than the total surface area.^{16, 29, 52} Narrow micropores are more effective at creating strong interactions between CO₂ molecules and the adsorbents, resulting in higher uptake compared to larger micropores and mesopores. Additionally, the presence of a mix of

porosities can also play a role in enhancing the diffusion of molecules into the adsorbent, improving adsorption efficiency and capacity.^{16, 29, 52}

While surface area and pore volume are foundational characteristics that determine the potential capacity of an adsorbent, the nature of the surface (including defect sites and functional groups) plays a crucial role in the specificity, selectivity, and overall effectiveness of adsorption.^{47, 48, 53-56} In general, the gas adsorption on a solid surface can be enhanced via functionalisation of the pore surfaces with heteroatoms (e.g., nitrogen, oxygen, etc.).^{29, 47, 48} The presence of nitrogen functional groups on the surface of porous carbon, for example, serves two main purposes in enhancing gas adsorption properties: (i) Active sites for adsorption by attracting gas molecules to the carbon surface and providing specific sites where they can interact and adhere through various interactions such as van der Waals forces, hydrogen bonding, and dipole-dipole interactions. This increases the overall adsorption capacity of the material by providing more binding sites for gas molecules.⁵³ (ii) Increasing the polarity of the carbon framework. The presence of polar functional groups alters the surface properties of the carbon material and makes it more attractive to gas molecules such as CO₂, which can interact with these groups. Although CO₂ is not a polar molecule, it can form polar adducts upon interaction, thus enhancing the selectivity.⁵³ For example, Yao Li *et al.* prepared porous carbon spheres with high nitrogen doping and demonstrated the impact of nitrogen functionalisation on the adsorption properties.⁵³ The presence of nitrogen groups on the carbon surface was found to enhance the adsorption capacity and selectivity for CO₂, CH₄, and N₂ gases, exhibited a high CO₂ and CH₄ capacity, as well as a low N₂ uptake, under ambient conditions.⁵³ This indicates that the nature of the surface, particularly the presence of nitrogen functional groups, plays a significant role in influencing the adsorption behaviour of the porous carbon.

Oxygen-containing functional groups on carbon adsorbents influence their hydrophobicity/hydrophilicity and acidity/basicity.⁴⁷ The presence of polar oxygen groups increases hydrophilicity, which is generally unfavourable for CO₂ adsorption because it intensifies competition between CO₂ and moisture for adsorption sites.^{47, 48} Oxidation of porous carbon materials introduces various oxygen functionalities, classified as acidic, basic, or neutral, endowing the surface with electron-acceptor properties.^{47, 57} Specific groups such as –COOH, lactone, and phenol increase surface

acidity, while groups like pyrone and carbonyl contribute to surface basicity.^{48, 58-60} Research findings on the role of oxygen-containing groups in CO₂ adsorption include those by Babu *et al.* reported that both –COOH and –OH groups significantly improved the CO₂ adsorption capacity of VACNTs at ambient pressures when comparing the adsorption capacities before and after functionalisation.^{48, 61} Tiwari *et al.* observed that carbons derived from epoxy resin with a high content of basic oxygen-containing groups showed a high CO₂ adsorption capacity of 0.65 mmol g⁻¹ at 30 °C and attributed this to the high oxygen content and surface basicity, which result in higher selectivity towards CO₂ compared to N₂.⁶²

1.3.2 Differences in gas adsorption behaviour

Understanding the specific interactions between different gases and adsorbent materials is essential for designing selective adsorbent materials. These interactions are influenced by molecular characteristics such as kinetic diameter and quadrupole moment, which affect how gases are adsorbed onto surfaces, particularly in physisorption processes.^{51, 63, 64} The gases of interest in this thesis, such as CO₂, CH₄, and N₂, have distinct behaviours based on their molecular characteristics, influencing their interaction with adsorbent materials.

Table 1.2. Physical properties of relevant molecules and their implications.^{64, 65}

Species	Kinetic Diameter (Å)	Boiling Point (°C)	Quadrupole Moment (μ)
H ₂	2.89	–252	0.260
CO ₂	3.30	–78	2.139
CH ₄	3.80	–161	0.000
N ₂	3.64	–196	0.697
O ₂	3.46	–183	0.155

For instance, kinetic diameter affects the ability of a gas molecule to penetrate pore spaces in adsorbents. This parameter is important in assessing the diffusion behaviours of gases within microporous structures, where pore size acts as a fundamental limiting factor. Although gases such as O₂ (3.46 Å) and N₂ (3.64 Å) have similar kinetic diameters, suggesting comparable diffusion behaviours, their adsorption performance can still differ significantly due to other molecular properties.^{51, 63} like the quadrupole

moment. For instance, despite their similar kinetic diameters, O₂ can probe porosity that N₂ cannot. This difference is attributed to the poor diffusion of N₂ in very small pores, which arises from the influence of N₂'s large quadrupole moment.⁵¹ Additionally, the polar groups on the surface of many carbons may interact with N₂'s large quadrupole moment, further hindering its diffusion compared to O₂, which lacks such a moment.⁵¹

A high quadrupole moment, as seen in CO₂ (2.139 Debye), indicates a strong interaction with the electric field gradients around the surface of the adsorbent.^{51, 63} This can enhance selective adsorption on polar sites within the adsorbent. On the other hand, gases like CH₄, with a quadrupole moment of zero, have weaker interactions with these sites, making their adsorption less selective and more dependent on physical characteristics such as pore size and surface area. For instance, the high quadrupole moment of CO₂ compared to N₂ and CH₄ explains the enhanced selectivity of certain adsorbents towards CO₂ under similar conditions.

Although the surface chemistry of a porous carbon can influence its capacity to capture CO₂, and the general ability of a porous material to adsorb gases,^{47, 48, 53-56} for activated carbons, the primary determinant of CO₂ capture efficiency is porosity.^{29, 66-68} Enhancing the overall surface area and pore volume can indeed enhance gas adsorption;^{49, 69} however, the extent of these enhancements is limited by the pore size.^{29, 66, 70-72} This ideal pore width varies depending on the surface chemistry^{55, 56} and pore geometry^{73, 74} of the adsorbent. Controlling these variables may enhance adsorbent performance for a specific gas. The optimal pore size is also found to vary significantly with pressure at a constant temperature.^{75, 76} For CO₂ capture, carbons with pore widths of < 5 Å are found to be optimal at 0.1 bar, whereas at 1.0 bar, the optimal width increases to < 8 Å.⁷⁶ At higher pressure, the presence of wider pores (i.e., larger micropores and mesopores) have shown to be of greater significance.^{70, 77, 78} Understanding these relationships is crucial for the tailored design of carbon adsorbents, potentially leading to more effective technologies for industrial CO₂ capture and storage.

1.4 Porosity

The concept of porosity involves the presence of empty spaces, voids, or pores within a material, and has been observed for millennia in various natural structures, i.e. rocks,

biological tissues, and charcoal. The term ‘porous’ is used to describe a material or substance possessing interconnected spaces, voids, or pores within its structure, allowing it to absorb, store, or transmit, fluids, gases, or other substances.⁷⁹ Porous materials now play an increasingly significant role in various scientific and technological domains, due to their versatile applications across diverse fields, including environmental remediation and energy storage. The International Union of Pure and Applied Chemistry (IUPAC) has categorised porous materials into three groups, depending on the size of their pore diameters (d), namely, microporous materials (pore diameters < 2 nm), mesoporous materials (pore diameters ranging from 2 nm to 50 nm), and macroporous materials (pore diameters > 50 nm).⁸⁰ See **Chapter 2 Section 2.2** for further details.

1.5 Porous Materials

There is currently considerable research being undertaken into energy storage, CO₂ capture, and the removal of pollutants from water due to its significant role in advancing solutions for various environmental issues. Over the past few decades, porous materials have exhibited excellent performance in these applications, driving developments in this field and establishing it as a crucial area of research. This has led to the development of a wide array of porous materials for various applications, including, metal-organic frameworks (MOFs),^{33, 81} zeolites,⁸² and porous carbon, in particular activated carbons (ACs).^{16, 29} These materials have gained extensive attention owing to their unique properties, including their framework structure, high surface area, and tunable pore sizes. In addition, there is now a focus on exploring novel synthesis methods and designing porous materials with enhanced properties to further expand their applications in crucial energy storage and environmental remediation applications.

1.5.1 Metal-Organic Framework (MOFs)

MOFs are crystalline materials constructed from metal ions or clusters coordinated with organic ligands, and are known for their potential to achieve high surface areas (>7,000 m²/g) and tunable pore sizes, making them highly versatile for gas adsorption. MOF properties can be customised by selecting specific metal ions and ligands, and can be engineered to selectively adsorb specific guest species and thus find use in various applications, i.e. gas storage, separation, and catalysis.^{83, 84} MOFs have been

extensively investigated as adsorbents for energy carrier gas storage for H₂ and CH₄ storage, CO₂ capture.^{26, 33, 34, 81, 85-89} For example, the best MOFs for CH₄ storage are HKUST-1,⁹⁰ which can store 281 cm³ (STP) cm⁻³ at 25 °C and 100 bar, and monolithic MOFs (monoHKUST-1 and monoUiO-66_D)^{86, 91} with capacities of 275 and 296 cm³ (STP) cm⁻³, respectively, at 25 °C and 100 bar. However, MOFs also exhibit certain drawbacks, such as susceptibility to structural instability and degradation in the presence of moisture or harsh chemical environments, high synthesis costs due to the use of rare or costly metal ions and organic linkers, and limitations in high-temperature applications due to decomposition at moderate temperatures.^{92, 93}

1.5.2 Zeolites

Zeolites are crystalline aluminosilicate minerals with a well-defined porous structure and a network of interconnected channels and cages. They have microporous structures with uniform pore sizes, which is advantageous for selective size-based adsorption. They can be found in nature or synthesised from various raw materials with tailored properties. Zeolites have been widely used in several applications especially in the petrochemical industry as catalysts, in gas separations, and demonstrate a slight advantage over MOFs in terms of suitability for post-combustion CO₂ adsorption.^{38, 82, 94-96} However, their performance in CH₄ storage is limited due to their relatively low surface area, which can only store up to 10 mmol g⁻¹ of methane at 100 bar and 25 °C.⁹⁷ It should, however, be noted that zeolites have some limitations, including being highly hydrophilic and susceptible to degrade in acidic or alkaline environments, which can alter their structure and limit their performance. In addition, they demonstrate an inefficient uptake capacity and selectivity at higher pressure, while their synthesis often necessitates high-temperature and high-pressure conditions, resulting in energy-intensive and costly processes.⁹⁸⁻¹⁰⁴ Furthermore, despite their fixed and uniform pore sizes, they exhibit relatively low surface area, which limits their applications for gas storage especially at high pressure (> 5 bar). Moreover, zeolites exhibit low heat resistance, rendering them susceptible to losing crystallinity and structural integrity at elevated temperatures.¹⁰⁵

1.5.3 Activated Carbons (ACs)

Activated carbons (ACs) are a class of porous amorphous materials made from carbonaceous matter (the precursor) treated with an activating agent, in an activation process, to create a network of nanoporous structure (pores).¹⁰⁶ Activated carbons are capable of achieving a high internal pore volume of $> 1 \text{ cm}^3 \text{ g}^{-1}$ and high surface area of $> 2500 \text{ m}^2 \text{ g}^{-1}$.^{16, 29, 106} Thus, their porosity is an important factor in predicting and understanding their performance for a given application. Activated carbons exhibit remarkable versatility across various applications, including water purification,¹⁰⁷ gas mixture separation,^{108, 109} CO_2 capture for post-combustion applications,^{69, 110} storage of gases such as CO_2 ,¹¹¹⁻¹¹³ H_2 ,^{49, 50, 72, 114} and CH_4 ,^{41, 111, 115}, and electrochemical double-layer systems for energy storage.¹¹⁶⁻¹¹⁹ A wide range of materials have been employed as precursors for the synthesis of ACs.^{50, 69, 75, 110-113, 120-129} In general, activated carbons can be synthesised and prepared through a variety of methods, some of which allow for the prediction and control of the internal structure of the resulting materials. Broadly, the synthesis of the activated carbons can be divided into two methods: physical activation and chemical activation. In both methods, the use of carbon-rich starting materials (precursors) is essential to allow the materials to undergo the activation process.^{16, 29}

Physical activation can be achieved in two steps. First, the precursor is pyrolysed in an inert gas (e.g., N_2) at temperatures between 400 and 900 °C to remove volatile matter and increase the carbon content. Second, the pyrolysed precursor is then subjected to a high-temperature treatment, typically above 800 °C, in the presence of an activating agent (oxidising gas) such as steam, CO_2 , or air. During the gasification ensuing process, pores are created and the structure is developed, increasing the surface area of the resulting carbons and their adsorption properties. The type and size of porosity is dependent on the nature of the precursor, the type of gas used during the gasification process, and the activation temperature. For example, activating with CO_2 and steam can result in higher activating carbon yields than using air. This is due to the exothermic reaction between carbon and oxygen in the air activation, causing a faster combustion process that consumes more of the carbon.²⁹ Additionally, higher activating temperatures generally lead to widening of pores and changes in surface area of the resulting carbons.^{16, 29, 106}

Chemical activation, on the other hand, is a single-step process involving the treatment of the precursor material with a chemical agent (also known as the activating agent or porogen), which is thoroughly mixed with the precursor followed by thermal treatment.^{16, 29, 106} Commonly employed activating agents include alkali metal hydroxides, phosphoric acid, or zinc chloride. Chemical activation typically yields carbons with better control of porosity compared to physical activation methods. The choice of activating agent along with the amount used (with respect to the precursor) can significantly influence the size and distribution of pores in the final carbon material and thus the surface area. Hence, control over the type and amount of activating agent offer the ability to tailor the porosity and fine-tune the desired properties of the final activated carbon product.^{16, 29, 106}

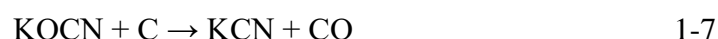
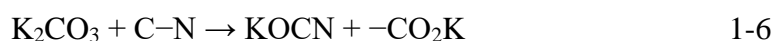
Among various activating agents, potassium hydroxide (KOH) is the most commonly used for chemical activation, and is known for producing high surface area and well-developed porosity in carbon materials. Its strong alkaline properties enable efficient activation of the carbon precursor, resulting in a highly porous structure with enhanced adsorption properties. The activation mechanism of KOH depends on several variables, including experimental preparation parameters, and the nature, type and reactivity of the precursor. A number of studies have sought to understand the reaction mechanism of KOH activation.^{29, 130-135} Firstly, the activation mechanism of N-free precursors, assumed that KOH dehydrates to form potassium oxide (K₂O) and steam (H₂O) (Eq.1-1). The steam then gasifies and exfoliates the C-precursor framework via a physical reaction to produce carbon monoxide (CO) and hydrogen (H₂), which subsequently form CO₂ and H₂ leading to some pore formation, at approximately 600 °C (Eq. 1-2 & 1-3).^{133, 134} Finally, K₂O reacts with CO₂ to form K₂CO₃, (Eq.1-4). The formation of K₂CO₃ occurs through the removal of carbon atoms from the precursor material by K intercalation at elevated temperatures, leading to the creation of pores within the precursor framework.



During this phase, K_2CO_3 can undergo a redox reaction with carbon at temperatures $> 700\text{ }^\circ\text{C}$, resulting in the creation of metallic potassium (K) and the release of CO (Eq.1-5).^{29, 135, 136} As carbon is used up in this process, pores are generated. Furthermore, the formation of metallic potassium enables chemical exfoliation through the insertion of potassium between the layers of carbon sheets.^{137, 138}



However, the presence of N heteroatoms in the precursor can alter the activation mechanism and lead to different chemical reactions during activation.^{78, 132, 133, 139-143} Mochizuki Tsubouchi, *et al.* proposed a mechanism involving the removal of N-containing species and the formation of inorganic salts (KOCN or KCN) through the following reaction:¹³⁹



This means, the formation of K_2CO_3 as described in equations (1-1 to 1-4) undergoes a reaction with C-N on the surface of the precursor, leading to the evolution of potassium cyanate (KOCN) and $(-CO_2K)$ on the carbon lattice, (Eq.1-6).^{133, 139, 144} KOCN is a reactive form which, upon further heating, acts as an oxidising agent and reacts with the carbons creating significant porosity, as well as releasing potassium cyanide (KCN) and CO, (Eq.1-7). Larger pores are created as more of the N atoms become involved in the reaction, and the strong interaction between N and K^+ depends on how much of each is present in the precursor.^{132, 133} The mechanism and the effect of N in the pore formation are discussed in details in **Chapter 4**.

The preparation of ACs usually involves an initial step, known as carbonisation treatment, which induces the materials into a carbon-rich precursor. This pre-activation treatment is important as it has a significant impact on the nature of the precursor and its elemental composition, both of which play a key role in porosity development in the final ACs.^{16, 29, 49, 145}

1.5.3.1 Mode of Carbonisation

Prior to the activation process, the starting materials are usually subjected to thermal treatment in order to enrich the carbon content of the precursor. These treatment processes include Hydrothermal Carbonisation (HTC),^{129, 146-148} Pyrolysis,¹⁴⁹⁻¹⁵² or Flash Air-Carbonisation.^{41, 145, 153}

Hydrothermal Carbonisation (HTC). This involves thermally treating biomass or other types of organic matter at relatively low temperatures (250–350 °C) under autogenous pressure in the presence of water, resulting in the production of a carbon-rich material known as hydrochar.^{146, 154-156}

Pyrolysis. In this carbonisation process, carbon content enrichment is typically achieved through thermal treatment of the starting materials at elevated temperatures (600–900 °C) in the absence of oxygen, usually in a nitrogen or argon atmosphere.^{129, 146-148}

Flash Air-Carbonisation. The idea that inspired this carbonisation process originated as the result of a fire at the University of Nottingham on September 12th, 2014, which engulfed a partially constructed all-wood Carbon Neutral Laboratory (CNL).¹⁵⁷ The University's Materials Chemistry Laboratory (Mokaya group) subsequently obtained a charred wooden beam in order to explore the unique properties of this uniquely formed carbon material.¹⁵³ It was found that the intense heat had converted the wood into carbon in the presence of air, resulting in a carbon-rich material, designated as air-carbonised wood, drawing its significance from both the CNL wood construction and the air-carbonisation process. This carbon, designated as CNL carbon, was then directly activated by Haffner-Staton, *et al.* resulting in high carbon yield and high packing density in the generated activated carbons.¹⁵³ It was demonstrated that the manner in which the CNL carbon was generated had an impact on its susceptibility to activation, showing resistance to activation and therefore serving as an excellent precursor for high microporous carbon materials.¹⁵³ later, in a subsequent study, Hirst, *et al.* attempted to prepare CNL carbon type carbonaceous matter in the laboratory by means of a similar process to that which generated the CNL carbon, but using lab controlled and reproducible conditions. This enabled the successful preparation of ACs with properties similar to those produced from the activation of the CNL carbon.¹⁴⁵ To achieve this, sawdust was used as starting material, and thermally treated in a furnace

at controlled temperature under N₂ gas. Once at 400 °C, the sawdust was subjected to a flash of air for between five to ten minutes. The resulting carbonaceous matter exhibited properties similar to those of the CNL carbon, thus paving the way for a new and simple carbonisation process.¹⁴⁵ This, flash-air-carbonisation method, offers several advantages over conventional methods, HTC or pyrolysis, as it is greener, requires less energy, and offers a rapid conversion of biomass into carbon-rich materials with high carbon content and low levels of impurities.^{111, 115, 145, 153}

1.5.3.2 Modulating Porosity

The control and modulation of the porosity of an adsorbent for small gas molecule adsorption is highly desirable in the field of porous materials. Various techniques have been developed to tailor the porosity of ACs, in attempts to allow precise control over the pore size distribution and surface area with the aim of enabling enhanced gas adsorption properties for specific applications. There has, in particular, recently been considerable interest in porosity modulation methods aimed at enhancing volumetric gas storage capacity especially for on-board applications where storage space is limited.¹⁶

Choice of Precursor Material: The type of precursor material used plays a significant role in determining the porosity of ACs. Various precursors, such as sawdust,^{112, 113, 128} date seeds,^{41, 115, 158} coconut shells,^{159, 160} polymers,^{161, 162} or ionic liquids,^{163, 164} can lead to activated carbons with varying pore structures. It has been demonstrated that the elemental composition of the precursor, particularly the relative amounts of O and C (i.e., as signified by the atomic O/C ratio) has a direct impact on the resulting porosity (for example the micropore/mesopore mix) in a manner that can enable the prediction of activation behaviour (i.e. susceptibility or resistance to activation).¹⁶ Easily activateable precursors tend to more readily form mesopores while those that are resistant to activation are dominated by micropores. Thus, precursors with lower O content (low O/C ratio) show some resistance to activation and tend to produce ACs with higher microporosity, while those with higher O content (higher O/C ratio) are more susceptible to activation, resulting in mesoporous structures.^{16, 106, 115, 165} This phenomenon is attributed to the so-called susceptibility of a precursor to activation. Altwala and Mokaya have achieved one of the lowest O/C ratios for any biomass-derived carbonaceous matter (designated as ACDS – air-carbonised date seed) by

using date seeds (*Phoenix dactylifera*) as starting materials along with the air-carbonisation method.¹¹⁵ More importantly, the O/C ratio has a significant influence on the surface area density (SAD), i.e. ratio of surface area to pore volume, of resulting activated carbons. This is important because the SAD is a crucial measure/indicator of volumetric gas uptake for activated carbons. For example, the O/C ratio of the ACDS carbon is as low as 0.156, meaning it generates highly microporous carbons with a high packing density and surface area density. This combination of properties translate to enhanced volumetric gas storage and thus suitability of ACDS-derived ACs as adsorbent in the confined space of a tank for portable storage applications.¹¹⁵ Therefore, careful selection of the precursor material is crucial in achieving the desired porosity for optimal storage capacity in on-board applications.

Activation Process: The choice of the activation process and the activation conditions, including the type and quantity of the activating agent and the activation temperature, also play a significant role. The physical and chemical activation processes are described in detail on **Page 11**. KOH is a popular choice in the production of ACs, due to its ability to fine-tune the textural properties (surface area and pore volume) of activated carbon materials.^{16, 29, 50, 120, 166-169} The use of KOH enables the creation of highly porous carbon materials with exceptional adsorption properties, resulting in enhanced adsorption capacity. Nevertheless, a range of chemical reagents have also been considered, including ZnCl_2 , H_3PO_4 , and NaOH .^{167, 170-175} ZnCl_2 and H_3PO_4 serve as dehydrating agents, while KOH and NaOH function as oxidants.^{16, 29, 106} In general, as the quantity of the activating agent increases, porosity development (measured in terms of surface area and pore volume) tends to increase. However, this increase is often accompanied by a broadening of the pore size distribution, a phenomenon dependent on the specific activating agent employed.^{29, 106, 176} Molina-Sabio and Rodriguez-Reinoso observed that activating peach stones with KOH primarily widens microporosity, while ZnCl_2 facilitates the development of both broad micropores and small mesopores, and H_3PO_4 develops the formation of larger mesopores and even macropores.¹⁷⁷ Furthermore, many researchers have noted an optimal temperature for porosity development, a value that varies depending on both the activating agent and the carbon precursor. Thus, an elevation in activating temperatures leads to increases in the surface area, combined with maximum broadening of porosity, which then

decreases in response to any further rises in the activating temperatures due to porosity collapse or shrinkage.^{16, 29, 106}

Gentler Activation Agents. Hydroxide-based activating agents are corrosive in nature and usually lead to low yields. Potassium Oxalate (PO, $K_2C_2O_4$), is known for its gentle nature as an activating agent, and has been found to offer higher product yields.^{128, 178, 179} When PO is subjected to pyrolysis, it undergoes decomposition within the temperature range of 500–600 °C, as indicated by the following reaction:¹⁰⁶



Subsequently, K_2CO_3 reacts with the carbonaceous material at temperatures higher than 700 °C, initiating a redox reaction with carbon as shown below:¹⁰⁶



This reaction leads to the formation of partial etching of carbon atoms, contributing to the development of microporosity. Further reactions occur at higher temperatures, creating additional porosity and enhancing the carbons' pore volume, usually within the micropore region.^{16, 106} The textural properties of materials derived from PO activation primarily consist of highly microporous carbons, accompanied by some small mesopores in some cases. Typically, these materials exhibit moderate surface areas of up to 2000 m² g⁻¹. Moreover, the yield of the activation process, particularly from biomass-derived carbonaceous matter, can be as high as 30–70%, thus representing an increase of 30–50% compared to activation with KOH.¹⁷⁹

Altwala and Mokaya have demonstrated that PO can be used to produce ACs with a high degree of microporosity by carefully selecting specific activation conditions. In contrast to KOH activation, variations in the amount of PO used had a minimal impact on the porosity of the resulting carbons, while the activation temperature was found to be the key factor in controlling the porosity of the PO-derived activated carbons. In addition, the pore size of the PO-derived activated carbons falls in the size range of 6–8 Å (approaching 100% microporosity), which is particularly well-suited for efficient CO₂ storage, especially under low-pressure conditions relevant to post-combustion capture. At 25 °C, PO-derived activated carbons can store up to 1.8 mmol g⁻¹ of CO₂ at 0.15 bar and 5.0 mmol g⁻¹ of CO₂ at 1 bar.¹⁷⁹

Compaction. The compaction approach, first reported in 2015 by the Mokaya group,¹¹⁴ is a mechanical compression, in which a mix of a precursor and activating agent (solid–solid) is compacted into a pellet, using a hydraulic compaction machine, prior to activation. The purpose of this pre-activation step is to bring the precursor-activating agent mixture closer together so as to maximise the activation process. This method has shown some success in modulating AC's porosity. A variety of precursors have been compactivated using either KOH or PO as activating agent. KOH-compactivated samples exhibit superior CO₂ and H₂ performance compared to their conventionally activated counterparts.^{69, 113, 114, 179}

Balahmar, *et al.* reported that mechanochemically activated (i.e. compactivated) ACs derived from biomass exhibited a 25% increase in surface area and a 75% increase in pore volume compared to conventional carbons. These were primarily attributed to the formation of small micropores (5.8–6.5 Å), resulting in a significant increase in CO₂ storage capacity at low pressure. The CO₂ uptake for compactivated carbons exceeded that of analogous conventionally ACs, increasing from 1.3 to 2.0 mmol g⁻¹ at 0.15 bar and from 4.3 to 5.8 mmol g⁻¹ at 1 bar.¹¹³ However, when Altwala and Mokaya compared the compaction process using PO as an activating agent to conventional activation, they observed that both methods resulted in carbons with similar textural properties.¹⁷⁹ Despite compactivated samples generally exhibiting higher porosity compared to powder samples, a pattern consistent with studies using KOH as an activating agent, it is noteworthy that compaction did not significantly alter pore size distribution to the same extent as KOH activation.^{113, 114} This finding aligns with the established understanding that the amount of PO does not play a crucial role in determining the porosity. Therefore, it could be concluded that the PO exists in excess amount, indicating that the close interaction with sawdust particles resulting from compaction does not significantly impact the overall effectiveness of the activator. This suggests that the compaction process using PO may not follow the same approach as when using KOH.

Pre-mixed Precursors. A simple way of changing the precursor composition is to mix two precursors with significantly different elemental composition. The Mokaya group determined that a greater degree of control over porosity could be achieved by activating a mixture of precursor than activating any one of them alone.^{41, 165} For example, this can be demonstrated by mixing polypyrrole (PPY) with air-carbonised

date seed (ACDS/PPY mixture) or with CNL carbon (CNL/PPY mixture), each having different O/C ratios of 0.672 (PPY), 0.156 (ACDS), and 0.185 (CNL carbon).⁴¹ These precursors are known for their contrasting responses to activation with KOH under any given activation conditions. For KOH activation at KOH/precursor ratio of 4 and 800 °C, PPY is highly susceptible to activation and achieves high surface area of up to 3200 m² g⁻¹ and a pore volume of 2.0 cm³ g⁻¹. In contrast, ACDS and CNL are known for their high resistance to activation, only achieving surface area of ca. 2000 m² g⁻¹ when activated singly. Interestingly, highly controlled properties of activated carbons derived from the pre-mixtures were obtained in a manner unachievable using any of the three precursors singly. Increasing amounts of ACDS or CNL in a PPY/(ACDS or CNL) mixture led to a reduction in mesoporosity. This reduction is attributed to the decrease in the O/C ratio of the overall mixture. More specifically, mesoporosity is influenced by the amount of PPY in the mixture, with the mesopore size increasing in line with the amount of PPY. It was possible to prepare activated carbon with an ultra-high surface area (up to 3890 m² g⁻¹) and pore volume (up to 2.40 cm³ g⁻¹) from premixtures thus achieving porosity unreachable with any of the precursors singly. This rational synthesis provided carbons with balanced properties suitable for CH₄ uptake, having excellent gravimetric methane uptake, reaching up to 28.4 mmol g⁻¹ (equivalent to 0.46 g g⁻¹) at 25 °C and 100 bar, with a total volumetric CH₄ uptake of up to 260 cm³ (STP) cm⁻³. The influence of PPY on the textural properties was primarily attributed to the presence of N.¹⁶ Similar observations were made when using N-containing additives. For example, Sevilla, *et al.* reported that KOH activation of glucose in the absence of N resulted in highly microporous carbons with moderate surface area of 1300–1700 m² g⁻¹. In contrast, when melamine (as N source) was added, hierarchical micro-/mesoporous carbons with a surface area as high as 3500 m² g⁻¹ and a pore volume of up to 2.7 cm³ g⁻¹ were produced.⁷⁸ This emphasizes the role of N in enhancing the surface area and porosity in the resulting carbons.

1.6 Carbon Capture and Storage (CCS)

While numerous strategies have been proposed to reduce atmospheric CO₂ levels, Carbon Capture and Storage (CCS) techniques have emerged as one of the most effective approaches.^{4, 22} The CCS technology represents a strategy aimed at both capturing CO₂ emissions and secure storage underground. This prevents their release into the atmosphere, so mitigating global warming and addressing the issue of climate

change. The CCS technology involves capturing and mitigating CO₂ emissions in industrial processes and can be classified into three main categories: pre-combustion capture, oxy-combustion capture and post-combustion capture.¹⁸⁰ As discussed in the following sections, these methods differ in terms of the stage at which CO₂ is captured, the type of technology used for capture, and associated energy.

Firstly, pre-combustion capture aims to convert the fossil fuel into a gas mixture of H₂ and CO₂ prior to combustion, by reacting the fuel with steam and O₂ in a gasifier, which produces syngas consisting of H₂, CO, and CO₂. This is then treated with a shift reaction to convert CO to CO₂ and H₂. The CO₂ is then separated from the H₂ using a physical or chemical solvent, before being stored. However, this method demands complex processes and adds to the cost of energy production.¹⁸¹

Secondly, oxy-fuel combustion employs oxygen-enriched air during the combustion process, which produces a flue gas consisting mainly of CO₂ and water vapour, with the former then being separated using a physical or chemical solvent. It should be noted that, while oxy-fuel combustion shows promise, its widespread adoption faces various challenges, particularly in terms of energy requirements and cost-effectiveness.^{182, 183}

Finally, Post-combustion capture involves removing CO₂ from flue gas after combustion.^{184, 185} Typically, this is achieved through chemical adsorption (with liquid amines), membrane separation technologies, or solid porous sorbents. Chemical adsorption, specifically the method known as chemical capture via liquid amines, involves reactions between the flue gas and amines to form a soluble chemical complex. The solvent is then regenerated by heating, releasing the captured CO₂, which can be compressed and stored. However, this process has been found to demonstrate various drawbacks, including high energy consumption during solvent regeneration, the high cost of maintaining equipment due to the corrosive nature of amines, and environmental concerns related to amine production and disposal.¹⁸⁶⁻¹⁸⁸

Membrane-based CO₂ capture and separation uses a membrane, typically made from a polymer, to selectively permeate CO₂ from the flue gas, to allow it to pass through while excluding other molecules due to size differences.^{189, 190} While this process offers a potential advantage over chemical adsorption, particularly by avoiding

chemical regeneration, it can also face challenges, i.e. membrane degradation under high-pressure conditions.¹⁹¹

Unlike chemical adsorption or membrane separation technologies, solid porous adsorbents such as MOFs,^{34, 192} Zeolites,^{37, 39} and activated carbons^{128, 143, 179, 193} are a promising technology for CO₂ capture and storage and hold the potential to be more energy-efficient and cost-effective.

Activated carbon offers several advantages for selective CO₂ capture and storage, owing to its availability, cost-effectiveness, exceptional thermal and chemical stability, high surface area, tunable porosity, straightforward preparation and generation processes, as well as structural versatility.^{16, 29} For post-combustion CO₂ capture measurements, uptake at 1 bar is a common benchmark, depending on the CO₂ partial pressure in the flue gases. Therefore, achieving uptake at pressures ≤ 1 bar is important for targeting materials. At 25 °C, CO₂ uptake of up to 2.0 mmol g⁻¹ at 0.15 bar, and 5.8 mmol g⁻¹ at 1 bar has been recorded for activated carbons.¹¹³

However, it should be recognised that CCS technologies are viewed as simply short-term strategies for mitigating greenhouse gas emissions, and that it is therefore also crucial to explore alternative energy sources capable of reducing global warming and GHG emissions. These include a consideration of natural gas (NG), which offers a cleaner and more sustainable energy future, as well as reducing CO₂ in the atmosphere through less-polluting renewable energies. While H₂ technology is the ideal solution to replace the fossil fuels, it has not yet reached a practical stage of development and delivery, indicating the benefits of NG as a clean transitional fuel to facilitate a lowering of CO₂ emissions.

1.7 Methane storage

As noted above, the associated environmental concerns relating to fossil fuels have prompted the search for cleaner and renewable energy sources. One solution is natural gas (NG), which is primarily composed of CH₄ (CH₄, ~70%), and can be produced sustainably from the breakdown of biomass, and which burns far more cleanly (with respect to CO₂ emissions) compared to fossil fuels.^{87, 194} The Joint Research Centre of the European Commission therefore considers NG a promising alternative to traditional fossil fuels, including for use in vehicles.²⁰ Firstly, NG is readily available,

with approximately 368 billion m³ capable of being extracted, with just 1% of this source providing sufficient clean-burning fuel for global consumption.¹⁹⁵⁻¹⁹⁷ Secondly, NG emits the lowest amount of greenhouse gases of any available fossil fuel.²⁰ However, as shown in **Figure 1.1**, natural gas has a drawback regarding its volumetric energy density. For instance, one litre of NG burned under Standard Temperature and Pressure (STP) conditions produces 0.033 MJ of energy, i.e. 0.11% of the energy generated by the combustion of the same amount of gasoline under the same conditions, ie. 34.2 MJ.²⁰ Therefore, to improve energy efficiency and enable the widespread use of natural gas in vehicles with extended driving ranges, it is crucial to focus on enhancing storage efficiency towards better volumetric energy density.

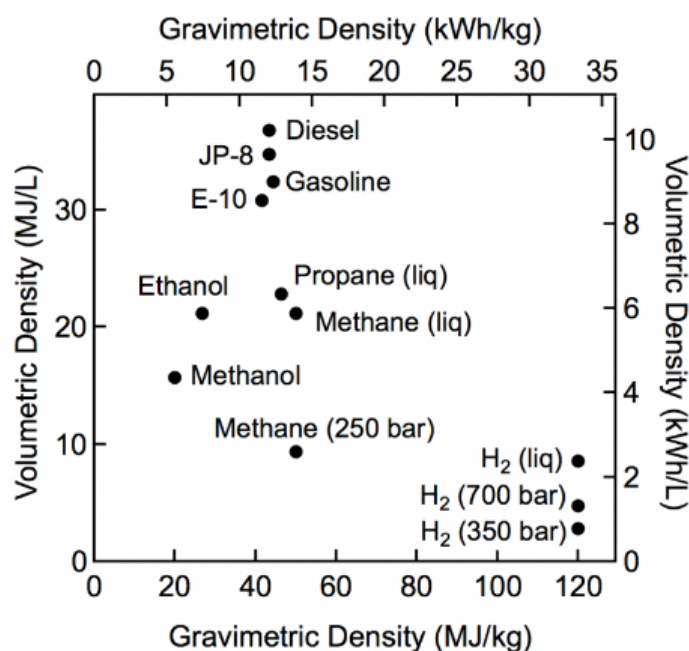


Figure 1.1. Comparison of specific energy (energy per mass or gravimetric density) and energy density (energy per volume or volumetric density) for several fuels.¹⁹⁸

Conventional Methods for the Storage of Natural Gas. The use of NG poses challenges due to its low volumetric energy density compared to fossil fuel-based petroleum.⁸⁷ This particularly relates to storage and transportation. In particular, there remain difficulties in using CH₄ as fuel for automobiles associated with its cost-effectiveness and safe storage and delivery at ambient conditions. NG is conventionally stored in two forms: compressed natural gas (CNG) and liquefied natural gas (LNG).^{20, 199} For CNG, the gas is stored at high pressure in stainless steel

vessels and filled to approximately 180–250 bar at room temperature. However, it would require over four gallons of CNG to provide the same energy equivalent as one gallon of diesel fuel, which is impractical for conventional vehicles. Alternatively, to increase the energy density of NG, it can be stored as liquefied natural gas (LNG) by cooling to temperatures below its boiling point, typically around 110 K. This process can increase the energy density, reaching up to 22.2 MJ/L at moderate pressures (2–6 bar), so increasing what can be achieved with CNG by 2.4 times.²⁰ However, despite the higher energy density of LNG, the technology requires the use of bulky and well-insulated storage tanks to maintain the fuel at low temperatures, adding both significant cost and complexity, particularly when it comes to vehicles.²⁰

Adsorbed Natural Gas (ANG). To address the challenges posed by CNG and LNG, storing CH₄ at relatively low pressures and room temperature through adsorption has emerged as a promising solution. As an alternative to CNG and LNG, Adsorbed Natural Gas (ANG) has therefore been extensively researched since the early 1970s to store natural gas at higher densities at ambient temperature and moderate pressure of up to 35 bar.^{87, 90} Adsorption in porous materials offers the potential to achieve energy densities similar to CNG but at much lower pressure ~ 100 bar, and being almost one-third the density of LNG at significantly higher temperature.^{20, 200} ANG operates at lower pressures than CNG, so eliminating the need for thick and costly vessels to hold high storage pressures, along with the use of multistage compressors for filling CNG tanks. As illustrated in the **Figure 1.2**, there is much reduction in the pressure, when using ANG comparing to CNG.²⁰¹ Additionally, ANG technology is a promising solution for energy storage, especially in the natural-gas-fuelled vehicle sector, as it is compatible with flat tanks, thus enabling the installation of multiple storage tanks in vehicles without any loss of passenger or cargo space. This efficiency therefore acts to extend the driving range, which makes ANG an attractive option for vehicular use.

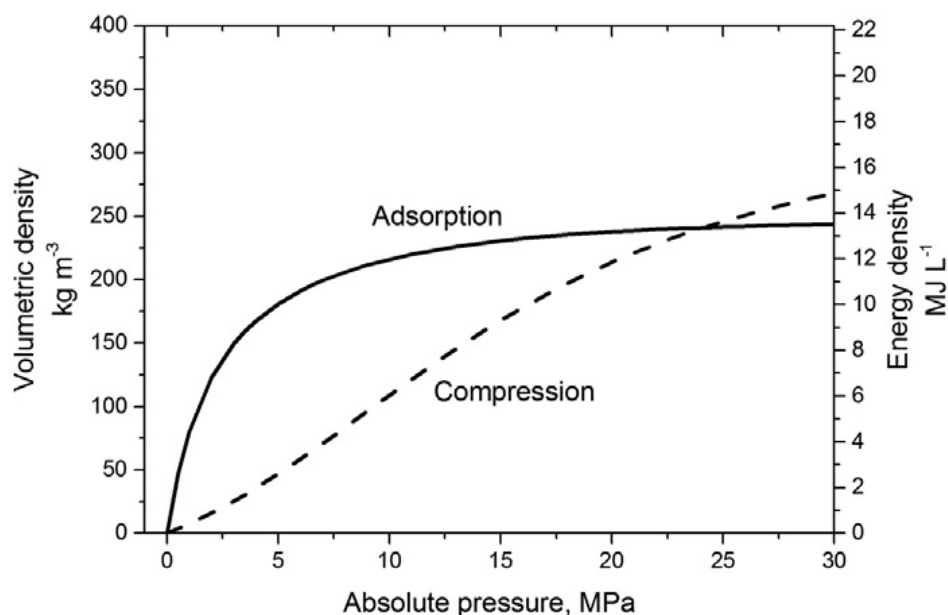


Figure 1.2. Comparing ANG (Adsorbed Natural Gas) technology to CNG (Compressed Natural Gas) technology in terms of the pressure needed to achieve the required energy.²⁰¹

ANG has therefore emerged as the most promising method for ensuring safety and achieving the desired volumetric storage capacity within a reasonable driving range. The success of this technology lies in the development of efficient adsorbent materials. Porous sorbents have already proven successful in commercial applications, particularly in capturing and storing small molecules such as CH_4 .²⁰²⁻²⁰⁵ ANG has become a viable competitor to CNG and LNG due to its significantly higher energy density, cost-effectiveness, and enhanced safety.^{206, 207} In particular, the lower-pressure requirements of adsorption offer increased safety in comparison to the use of compression, as well as enhancing overall efficiency at the point of use. For this reason, the U.S. Department of Energy (DOE) has established storage capacity targets for CH_4 as part of its efforts to advance storage technologies for vehicles and transportation. These target capacities are set for moderate pressures of 35-100 bar and 25 °C at $263 \text{ cm}^3 \text{ (STP) cm}^{-3}$ (for volumetric measurements) and 0.5 g g^{-1} (for gravimetric capacity).²⁰⁸

In addition, various porous materials, including zeolites,²⁰⁹ Metal-Organic Frameworks (MOFs),^{20, 85, 86, 88, 91, 200, 210, 211} and activated carbons,^{41, 87, 111, 115, 212-214} have been investigated and evaluated in the search for materials with high CH_4 storage capacity. Activated carbons, with their advantages of being low cost, having a high surface area and tunable porosity, offer a very attractive combination of properties.²⁰⁶

1.7.1 Fundamental Concept of Methane Storage

The fundamental concept of methane storage is to adsorb methane gas onto a solid material, such as a metal-organic framework (MOF), zeolite or activated carbon, at pressure of 35 – 100 bar and temperature of 25 °C. The stored methane can then be released by either reducing the pressure or increasing the temperature, allowing it to be used as a fuel source for various applications, such as transportation. The goal is to achieve high storage capacities, both volumetrically and gravimetrically, while maintaining safe and efficient storage and release of the methane. As basic step to evaluate methane storage of porous materials requires using an appropriate instrument (see **Chapter 2 section 2.3**) equipped with a high purity methane source. The instrument allows for an evaluation of CH₄ uptake at a very low pressure (i.e. near to zero) up to the targeted pressure (generally 100 bar) at 25 °C, and accurately measuring the weight changes using a microbalance upon the gradual increase in the methane pressure. The amount of methane adsorbed by the materials is represented by isotherms of methane adsorbed versus the pressures applied. The instrument usually allow for collecting results as excess uptake in unit of mmol g⁻¹.³²

Excess, Absolute and Total Methane Adsorption. These three concepts are frequently used to describe the CH₄ adsorption into a solid material. Excess adsorption (n_{ex}) refers to the amount of adsorbed gas molecules that have interactions with the pore surface of the material. This means that the gas molecules are held onto the surface of the material by weak van der Waals forces.¹⁷³ Absolute adsorption, on the other hand, takes into account the sum of the gas molecules that interact with the pore surface of the materials, in addition to those gas molecules that remain in the adsorb region without interaction (gas–solid interaction) with the materials pore surface.^{200, 215} Total adsorption (n_{tot}) is the total amount of gas molecules inside the pores of a material,^{200, 216} taking into account the bulk density, P_{bulk} , of the gas, the temperature and pressure conditions under which the adsorption is taking place, according to the following equation:

$$n_{tot} = n_{ex} + P_{bulk}(P, T) \times V_p \quad 1-10$$

Where P_{bulk} is obtained from the National Institute of Standards and Technology (NIST) Refprop database at <https://webbook.nist.gov/chemistry/fluid/> and V_p is the

total pore volume of the adsorbing solid material, usually determined from N₂ sorption analysis at 77 K.

Gravimetric and Volumetric Methane Uptake are measurements used to describe the amount of CH₄ capable of being stored in a given mass or volume of a solid material. The gravimetric uptake represents the mass of CH₄ adsorbed per unit mass of adsorbent, i.e. the amount of CH₄ stored is expressed in grams of CH₄ per gram of AC. The volumetric uptake, on the other hand, is expressed as the volume of CH₄ adsorbed under standard temperature and pressure (STP) divided by the volume of the adsorbent. This means that the amount of CH₄ stored is expressed in litres of methane per litre of AC. It should be recognised that the volumetric uptake is more important for practical applications, including storage for use in vehicles, for which the amount of CH₄ capable of being delivered is crucial.²⁰⁰

Deliverable Capacity, (also known as working capacity), is the amount of methane that can be delivered from the adsorbent to the engine when the adsorption pressure is reduced to the minimum inlet pressure.²⁰⁰ It is more important than the methane storage capacity in practical applications because it determines the driving range of natural gas vehicles (NGVs). Basically, the total storage capacity is the maximum amount of methane that can be stored in the adsorbent, while the working capacity is the amount of methane that can be delivered from the adsorbent to the engine when the adsorption pressure is reduced to the minimum inlet pressure. The working capacity is calculated as the difference in the amount of methane adsorbed between uptake pressure (35, 65 or 100 bar) and 5 bar.²⁰⁰ To achieve a high working capacity, a material should adsorb a low amount of methane at low pressures (below 5 bar), while at the same time adsorbing a significant amount at higher pressures. This requires well-balanced textural properties, such as a high surface area density (SAD), a high packing density, and a mix of porosity (micro-meso structure), which are essential to maximise the deliverable methane of adsorbent materials.^{41, 111, 115, 193, 217-221}

Porous Materials for Methane Storage. Interest in NG as a vehicular fuel has rapidly increased since the 1980s,²⁰⁰ leading to extensive research into CH₄ storage technology using porous materials, including MOFs,^{200, 211} Covalent Organic Frameworks (COFs),²²² zeolites,^{223, 224} Porous Organic Polymers (POPs),^{225, 226} and porous carbons,

as particularly activated carbons.^{41, 221} Methane storage capacity in zeolites is often limited by their low to moderate surface area, (typically $< 1000 \text{ m}^2 \text{ g}^{-1}$); at 100 bar and 25 °C, zeolites may store up to ca. 10 mmol g^{-1} of methane.⁹⁷ On the other hand, MOFs can achieve superior gravimetric CH_4 uptake due to their higher surface area and pore volume. For instance, at 23 °C, MOFs have been reported to achieve methane storage capacities of 25 mmol g^{-1} at 65 bar and 33 mmol g^{-1} at 100 bar.²²⁷ The current records for MOFs in terms of volumetric methane uptake at 25 °C include HKUST-1,⁹⁰ which can store $281 \text{ cm}^3 (\text{STP}) \text{ cm}^{-3}$ at 25 °C and 100 bar, and monolithic MOFs (monoHKUST-1 and monoUiO-66_D)^{86, 91} with volumetric methane capacities of 275 and $296 \text{ cm}^3 (\text{STP}) \text{ cm}^{-3}$, respectively. However, it is important to note that the ideal crystallographic density of the MOF is often used to calculate volumetric uptake of powder forms of MOFs. Thus the values reported only represent the maximum possible capacity. Moreover, the actual packing density of MOFs is typically much lower than the crystallographic density, resulting in actual volumetric uptake values being lower than those calculated via crystallographic density by $\sim 25\%$.^{200, 228} On the other hand, porous carbons and in particular activated carbons, have recently revealed a promising performance for methane uptake, owing to their high surface area and pore volume, mix porosity and high packing density.^{41, 111, 115, 193} Furthermore, due to their high mechanical stability, activated carbons can also be compacted without loss of porosity or diminution of gravimetric uptake capacity for methane.^{16, 29, 41, 42}

1.8 Motivations & Objectives

The work described in this thesis aims to address the pressing need for efficient gas capture and storage by investigating the potential of activated carbons as promising materials for energy-related applications, such as carbon capture and storage (CCS) and adsorbed natural gas (ANG). The specific objectives of the thesis are outlined below, corresponding to each of the four results chapters:

First, the objective of **Chapter 3**, “Enhancing Biomass-Derived Activated Carbons for Gas Adsorption” is to investigate the impact of air-carbonisation temperature on the porosity and gas adsorption performance of activated carbons derived from biomass sources. It primarily focuses on the effect of air-carbonisation treatment on the O/C ratio, which serves as a measure of a precursor’s susceptibility to activation. By varying the O/C ratio of the precursor, it can be used then as a tool to modulate the textural properties, such as surface area, pore volume, pore size, and packing density, of the resulting activated carbons, towards enhanced CO₂ and/or CH₄ adsorption.

Second, the objective of **Chapter 4**, “Modulating Porosity in N-doped Carbon Materials” focuses on synthesising activated carbons with carefully controlled porosity suitable for methane storage. Modulation is achieved by introducing a N-containing additive as a mediator for activation of the precursor. To create activated carbons with the ideal porosity and high packing density necessary for efficient methane storage, a precursor with a low O/C ratio (air-carbonised date seeds, *Phoenix dactylifera*, ACDS), known for its high resistance to activation, is selected. The flash air-carbonisation method, in combination with KOH as the activating agent and judicious use of N-containing additives, are controlled in order to allow control over the resulting activated carbons' textural properties. Simply, the low O/C ratio of ACDS enhances its resistance to activation, leading to higher packing density and high surface area density (SAD). Simultaneously, the presence N in the activation mix increases surface area and provides flexibility in tailoring porosity and creating a balance between microporosity and mesoporosity. These deliberate modifications are expected to yield activated carbons with desired properties to enhance both gravimetric and volumetric methane uptake.

Third, the objective of **Chapter 5**, on exploring Ionic Liquid-Derived activated carbons is rooted in the growing understanding of the relationship between the

elemental composition of a carbon precursor (O/C ratio) and its susceptibility to activation. This understanding is essential as it enables the prediction of the textural parameters of the resulting activated carbon, such as the proportion and level of microporosity and mesoporosity. Additionally, the presence of N within the framework of a carbonaceous precursor also plays a role in determining the textural properties of activated carbons. In a sense, the presence of N can have the opposite effect to that of low O/C ratio. While N promotes the development of high mesoporosity and a high surface area, a low O/C ratio operates in the opposite direction, favouring the creation of microporous carbons with moderate surface area but high packing. A combination of these two factors is used in the hope to optimise both gravimetric and volumetric methane uptake. For this, investigating crosslinkable imidazolium-based ionic liquids as new class for carbon precursors presents a promising approach, which allows for porosity control towards high surface area but without excessive diminution of microporosity and packing density.

Fourth, the objective of **Chapter 6**, “Utilising Non-Hydroxide Activated Carbons” was to utilise a greener and non-hydroxide activating agent in the synthesis of activated carbons from ionic liquid precursor. By fine-tuning the activation conditions, the aim was to generate carbons with high microporosity, ideal for CO₂ uptake. Additionally, these materials would ideally be optimised towards high packing density thus potentially enhancing their volumetric methane storage capacity.

References

1. V. Masson-Delmotte, P. Zhai, S. Pirani, C. Connors, S. Péan, N. Berger, Y. Caud, L. Chen, M. Goldfarb and P. M. Scheel Monteiro, in *Climate Change 2021: The Physical Science Basis. Contribution of Working Group I to the Sixth Assessment Report of the Intergovernmental Panel on Climate Change (IPCC)*, 2021, DOI: 10.1017/9781009157896.001, ch. Summary for Policymakers, p. 3–32.
2. V. Ramanathan and Y. Xu, *Proceedings of the National Academy of Sciences*, 2010, **107**, 8055-8062.
3. J. L. Holechek, H. M. Geli, M. N. Sawalhah and R. Valdez, *Sustainability*, 2022, **14**, 4792.
4. D. Y. Leung, G. Caramanna and M. M. Maroto-Valer, *Renewable and Sustainable Energy Reviews*, 2014, **39**, 426-443.
5. D. Archer, *Journal of Geophysical Research Oceans*, 2005, **110**, C09.
6. S. Solomon, G.-K. Plattner, R. Knutti and P. Friedlingstein, *Proceedings of the National Academy of Sciences*, 2009, **106**, 1704-1709.
7. S. Fankhauser, S. M. Smith, M. Allen, K. Axelsson, T. Hale, C. Hepburn, J. M. Kendall, R. Khosla, J. Lezaun and E. Mitchell-Larson, *Nature Climate Change*, 2022, **12**, 15-21.
8. C. F. Schleussner, J. Rogelj, M. Schaeffer, T. Lissner, R. Licker, E. M. Fischer, R. Knutti, A. Levermann, K. Frieler and W. Hare, *Nature Climate Change*, 2016, **6**, 827-835.
9. S. J. Davis, N. S. Lewis, M. Shaner, S. Aggarwal, D. Arent, I. L. Azevedo, S. M. Benson, T. Bradley, J. Brouwer and Y.-M. Chiang, *Science*, 2018, **360**, eaas9793.
10. A. J. Friedemann, *Life after fossil fuels: A Reality Check on Alternative Energy*, Springer, Cham (Suiza), 2021.
11. S. Bouckaert, A. F. Pales, C. McGlade, U. Remme, B. Wanner, L. Varro, D. D'Ambrosio and T. Spencer, *Net zero by 2050: A roadmap for the global energy sector*, 2021.
12. T. Kuramochi, A. Ramirez, W. Turkenburg and A. Faaij, *Progress in Energy and Combustion Science*, 2012, **38**, 87-112.
13. C. C. Lin, R. X. He and W. Y. Liu, *Energies*, 2018, **11**, 3432.

-
14. G. P. Peters, R. M. Andrew, J. G. Canadell, S. Fuss, R. B. Jackson, J. I. Korsbakken, C. Le Quere and N. Nakicenovic, *Nature Climate Change*, 2017, **7**, 118-122.
 15. GOV.UK, *UK becomes first major economy to pass net zero emissions law*, <https://www.gov.uk/government/news/uk-becomes-first-major-economy-to-pass-net-zero-emissions-law>, (accessed 21st August, 2023).
 16. L. S. Blankenship and R. Mokaya, *Materials Advances*, 2022, **3**, 1905-1930.
 17. S. Choi, J. H. Drese and C. W. Jones, *ChemSusChem*, 2009, **2**, 796-854.
 18. U. Eberle, B. Muller and R. von Helmolt, *Energy & Environmental Science*, 2012, **5**, 8780-8798.
 19. M. S. Dresselhaus and I. L. Thomas, *Nature*, 2001, **414**, 332-337.
 20. K. V. Kumar, K. Preuss, M. M. Titirici and F. Rodriguez-Reinoso, *Chemical Reviews*, 2017, **117**, 1796-1825.
 21. T. A. Makal, J. R. Li, W. Lu and H. C. Zhou, *Chemical Society Reviews*, 2012, **41**, 7761-7779.
 22. D. M. D'Alessandro, B. Smit and J. R. Long, *Angewandte Chemie International Edition*, 2010, **49**, 6058-6082.
 23. Q. Wang, J. Luo, Z. Zhong and A. Borgna, *Energy & Environmental Science*, 2011, **4**, 42-55.
 24. D. Lozano-Castello, J. Alcaniz-Monge, M. A. de la Casa-Lillo, D. Cazorla-Amoros and A. Linares-Solano, *Fuel*, 2002, **81**, 1777-1803.
 25. J. Romanos, S. Sweany, T. Rash, L. Firlej, B. Kuchta, J. C. Idrobo and P. Pfeifer, *Adsorption Science & Technology*, 2014, **32**, 681-691.
 26. R. E. Morris and P. S. Wheatley, *Angewandte Chemie International Edition*, 2008, **47**, 4966-4981.
 27. Z. Liang, K. Fu, R. Idem and P. Tontiwachwuthikul, *Chinese Journal of Chemical Engineering*, 2016, **24**, 278-288.
 28. K. S. Fisher, K. Searcy, G. T. Rochelle, S. Ziaii and C. Schubert, *Advanced amine solvent formulations and process integration for near-term CO₂ capture success*, Trimeric Corporation, 2007.
 29. M. Sevilla and R. Mokaya, *Energy & Environmental Science*, 2014, **7**, 1250-1280.
 30. L. Schlapbach and A. Züttel, *Nature*, 2001, **414**, 353-358.

-
31. P. Pfeifer, L. Aston, M. Banks, S. Barker, J. Burrell, S. Carter, J. Coleman, S. Crockett, C. Faulhaber, J. Flavin, M. Gordon, L. Hardcastle, Z. Kallenborn, M. Kemiki, C. Lapilli, J. Pobst, R. Schott, P. Shah, S. Spellerberg, G. Suppes, D. Taylor, A. Tekeci, C. Wexler, M. Wood, P. Buckley, T. Breier, J. Downing, S. Eastman, P. Freeze, S. Graham, S. Grinter, A. Howard, J. Martinez, D. Radke, T. Vassalli and J. Ilavsky, *Chaos: An Interdisciplinary Journal of Nonlinear Science*, 2007, **17**, 041108.
32. Y. He, W. Zhou, G. Qian and B. Chen, *Chemical Society Reviews*, 2014, **43**, 5657-5678.
33. D. Farrusseng, *Metal-organic frameworks: applications from catalysis to gas storage*, John Wiley & Sons, 2011.
34. M. Ding, R. W. Flaig, H.-L. Jiang and O. M. Yaghi, *Chemical Society Reviews*, 2019, **48**, 2783-2828.
35. J.-Y. Lee, C. D. Wood, D. Bradshaw, M. J. Rosseinsky and A. I. Cooper, *Chemical Communications*, 2006, 2670-2672.
36. M. Pera-Titus, *Chemical Reviews*, 2014, **114**, 1413-1492.
37. R. V. Siriwardane, M.-S. Shen, E. P. Fisher and J. Losch, *Energy & Fuels*, 2005, **19**, 1153-1159.
38. J. Weitkamp, M. Fritz and S. Ernst, *Zeolites as media for hydrogen storage*, Elsevier, 1993, pp. 11-19.
39. R. Krishna and J. M. van Baten, *Journal of Membrane Science*, 2010, **360**, 323-333.
40. H. Nishihara and T. Kyotani, *Chemical Communications*, 2018, **54**, 5648-5673.
41. A. Altwala and R. Mokaya, *Journal of Materials Chemistry A*, 2022, **10**, 13744-13757.
42. I. Toda, H. Toda, H. Akasaka, S. Ohshio, S. Himeno and H. Saitoh, *Journal of the Ceramic Society of Japan*, 2013, **121**, 464-466.
43. P. Pourhakkak, A. Taghizadeh, M. Taghizadeh, M. Ghaedi and S. Haghdoust, in *Interface science and technology*, Elsevier, 2021, vol. 33, pp. 1-70.
44. R. Pedicini, B. Schiavo, P. Rispoli, A. Saccà, A. Carbone, I. Gatto and E. Passalacqua, *Energy*, 2014, **64**, 607-614.
45. L.-J. Ma, T. Han, J. Jia and H.-S. Wu, *RSC Advances*, 2020, **10**, 37770-37778.
46. M. Králík, *Chemical Papers*, 2014, **68**, 1625-1638.

-
47. B. Petrovic, M. Gorbounov and S. M. Soltani, *Carbon Capture Science & Technology*, 2022, **3**, 100045.
 48. D. Saha and M. J. Kienbaum, *Microporous and Mesoporous Materials*, 2019, **287**, 29-55.
 49. T. S. Blankenship and R. Mokaya, *Energy & Environmental Science*, 2017, **10**, 2552-2562.
 50. L. S. Blankenship, N. Balahmar and R. Mokaya, *Nature Communications*, 2017, **8**, 1545.
 51. L. S. Blankenship, J. Jagiello and R. Mokaya, *Materials Advances*, 2022, **3**, 3961-3971.
 52. A. M. Aljumialy and R. Mokaya, *Materials Advances*, 2020, **1**, 3267-3280.
 53. Y. Li, S. Wang, B. Wang, Y. Wang and J. Wei, *Nanomaterials*, 2020, **10**, 174.
 54. M. L. Botomé, P. Poletto, J. Junges, D. Perondi, A. Dettmer and M. Godinho, *Chemical Engineering Journal*, 2017, **321**, 614-621.
 55. L. Wang and R. T. Yang, *The Journal of Physical Chemistry C*, 2012, **116**, 1099-1106.
 56. S. Kayal and A. Chakraborty, *Chemical Engineering Journal*, 2018, **334**, 780-788.
 57. C. Vagner, G. Finqueneisel, T. Zimny, P. Burg, B. Grzyb, J. Machnikowski and J. Weber, *Carbon*, 2003, **41**, 2847-2853.
 58. C. Goel, H. Bhunia and P. K. Bajpai, *RSC Advances*, 2015, **5**, 93563-93578.
 59. M. Montes-Morán, D. Suárez, J. Menéndez and E. Fuente, *Carbon*, 2004, **42**, 1219-1225.
 60. M. V. Lopez-Ramon, F. Stoeckli, C. Moreno-Castilla and F. Carrasco-Marin, *Carbon*, 1999, **37**, 1215-1221.
 61. D. J. Babu, M. Bruns, R. Schneider, D. Gerthsen and J. r. J. Schneider, *Journal of Physical Chemistry C*, 2017, **121**, 616-626.
 62. D. Tiwari, C. Goel, H. Bhunia and P. K. Bajpai, *RSC Advances*, 2016, **6**, 97728-97738.
 63. J. Jagiello, J. Kenvin, C. O. Ania, J. B. Parra, A. Celzard and V. Fierro, *Carbon*, 2020, **160**, 164-175.
 64. C. G. D. I. R. RAAB, *Molecular Physics*, 1998, **93**, 49-56.
 65. B. E. Poling, J. M. Prausnitz and J. P. O'connell, *The properties of gases and liquids*, McGraw-hill New York, 2001.

-
66. B. Adeniran and R. Mokaya, *Chemistry of Materials*, 2016, **28**, 994-1001.
 67. S.-Y. Lee and S.-J. Park, *Journal of Colloid and Interface Science*, 2013, **389**, 230-235.
 68. N. P. Wickramaratne and M. Jaroniec, *Journal of Materials Chemistry A*, 2013, **1**, 112-116.
 69. M. Cox and R. Mokaya, *Sustainable Energy & Fuels*, 2017, **1**, 1414-1424.
 70. M. Sevilla, J. B. Parra and A. B. Fuertes, *ACS Applied Materials & Interfaces*, 2013, **5**, 6360-6368.
 71. S. Choi, M. A. Alkhabbaz, Y. G. Wang, R. M. Othman and M. Choi, *Carbon*, 2019, **141**, 143-153.
 72. E. Masika and R. Mokaya, *Journal of Physical Chemistry C*, 2012, **116**, 25734-25740.
 73. M. Rzepka, P. Lamp and M. De la Casa-Lillo, *The Journal of Physical Chemistry B*, 1998, **102**, 10894-10898.
 74. S. Hlushak, *Physical Chemistry Chemical Physics*, 2018, **20**, 872-888.
 75. M. De la Casa-Lillo, F. Lamari-Darkrim, D. Cazorla-Amoros and A. Linares-Solano, *Journal of Physical Chemistry B*, 2002, **106**, 10930-10934.
 76. V. Presser, J. McDonough, S.-H. Yeon and Y. Gogotsi, *Energy & Environmental Science*, 2011, **4**, 3059-3066.
 77. M. E. Casco, M. Martinez-Escandell, J. Silvestre-Albero and F. Rodriguez-Reinoso, *Carbon*, 2014, **67**, 230-235.
 78. M. Sevilla, A. S. M. Al-Jumialy, A. B. Fuertes and R. Mokaya, *ACS Applied Materials & Interfaces*, 2018, **10**, 1623-1633.
 79. P. A. Webb and C. Orr, *Analytical methods in fine particle technology*, Micromeritics Instrument Corporation, 1997.
 80. M. Thommes, K. Kaneko, A. V. Neimark, J. P. Olivier, F. Rodriguez-Reinoso, J. Rouquerol and K. S. W. Sing, *Pure and Applied Chemistry*, 2015, **87**, 1051-1069.
 81. M. Schröder, *Functional Metal-Organic Frameworks: Gas Storage, Separation and Catalysis*, Springer, 2010, 35-76.
 82. J. Miao, Z. Lang, T. Xue, Y. Li, Y. Li, J. Cheng, H. Zhang and Z. Tang, *Advanced Science*, 2020, **7**, 2001335.
 83. H.-C. Zhou, J. R. Long and O. M. Yaghi, *Chemical Reviews*, 2012, **112**, 673-674.

-
84. H. Furukawa, K. E. Cordova, M. O’Keeffe and O. M. Yaghi, *Science*, 2013, **341**, 1230444.
85. B. M. Connolly, D. G. Madden, A. E. H. Wheatley and D. Fairen-Jimenez, *Journal of the American Chemical Society*, 2020, **142**, 8541-8549.
86. B. M. Connolly, M. Aragonés-Anglada, J. Gandara-Loe, N. A. Danaf, D. C. Lamb, J. P. Mehta, D. Vulpe, S. Wuttke, J. Silvestre-Albero, P. Z. Moghadam, A. E. H. Wheatley and D. Fairen-Jimenez, *Nature Communications*, 2019, **10**, 2345.
87. A. Policicchio, R. Filosa, S. Abate, G. Desiderio and E. Colavita, *Journal of Porous Materials*, 2017, **24**, 905-922.
88. D. Alezi, Y. Belmabkhout, M. Suyetin, P. M. Bhatt, L. J. Weselinski, V. Solovyeva, K. Adil, I. Spanopoulos, P. N. Trikalitis, A. H. Emwas and M. Eddaoudi, *Journal of the American Chemical Society*, 2015, **137**, 13308-13318.
89. L. J. Murray, M. Dincă and J. R. Long, *Chemical Society Reviews*, 2009, **38**, 1294-1314.
90. J. A. Mason, M. Veenstra and J. R. Long, *Chemical Science*, 2014, **5**, 32-51.
91. T. Tian, Z. Zeng, D. Vulpe, M. E. Casco, G. Divitini, P. A. Midgley, J. Silvestre-Albero, J. C. Tan, P. Z. Moghadam and D. Fairen-Jimenez, *Nature Materials*, 2018, **17**, 174-179.
92. L. Bellarosa, S. Calero and N. López, *Physical Chemistry Chemical Physics*, 2012, **14**, 7240-7245.
93. J. R. Long and O. M. Yaghi, *Chemical Society Reviews*, 2009, **38**, 1213-1214.
94. E. Masika and R. Mokaya, *Energy & Environmental Science*, 2014, **7**, 427-434.
95. Y. D. Xia, R. Mokaya, G. S. Walker and Y. Q. Zhu, *Advanced Energy Materials*, 2011, **1**, 678-683.
96. M. Sevilla, N. Alam and R. Mokaya, *Journal of Physical Chemistry C*, 2010, **114**, 11314-11319.
97. A. Alonso, J. Moral-Vico, A. A. Markeb, M. Busquets-Fité, D. Komilis, V. Puentes, A. Sánchez and X. Font, *Science of the Total Environment* 2017, **595**, 51-62.
98. L. Nie, Y. Mu, J. Jin, J. Chen and J. Mi, *Chinese Journal of Chemical Engineering*, 2018, **26**, 2303-2317.

-
99. M. Moshoeshoe, M. S. Nadiye-Tabbiruka and V. Obuseng, *American Journal of Materials Science*, 2017, **7**, 196-221.
100. Y. Li, L. Li and J. Yu, *Chem*, 2017, **3**, 928-949.
101. M. Abu Ghalia and Y. Dahman, *Energy Technology*, 2017, **5**, 356-372.
102. N. Hedin, L. Chen and A. Laaksonen, *Nanoscale*, 2010, **2**, 1819-1841.
103. S. Cavenati, C. A. Grande and A. E. Rodrigues, *Journal of Chemical & Engineering Data*, 2004, **49**, 1095-1101.
104. G. Aguilar-Armenta, G. Hernandez-Ramirez, E. Flores-Loyola, A. Ugarte-Castaneda, R. Silva-Gonzalez, C. Tabares-Munoz, A. Jimenez-Lopez and E. Rodriguez-Castellon, *Journal of Physical Chemistry B*, 2001, **105**, 1313-1319.
105. G. Perot and M. Guisnet, *Journal of Molecular Catalysis*, 1990, **61**, 173-196.
106. M. Sevilla, N. Diez and A. B. Fuertes, *ChemSusChem*, 2021, **14**, 94-117.
107. P. Hadi, M. Xu, C. Ning, C. S. K. Lin and G. McKay, *Chemical Engineering Journal*, 2015, **260**, 895-906.
108. H.-J. Schröter, *Gas Separation & Purification* 1993, **7**, 247-251.
109. U. Morali, H. Demiral and S. Sensoz, *Powder Technology*, 2019, **355**, 716-726.
110. H. M. Coromina, D. A. Walsh and R. Mokaya, *Journal of Materials Chemistry A*, 2016, **4**, 280-289.
111. I. Alali and R. Mokaya, *Energy & Environmental Science*, 2022, **15**, 4710-4724.
112. N. Balahmar, A. S. Al-Jumialy and R. Mokaya, *Journal of Materials Chemistry A*, 2017, **5**, 12330-12339.
113. N. Balahmar, A. C. Mitchell and R. Mokaya, *Advanced Energy Materials*, 2015, **5**, 1500867.
114. B. Adeniran and R. Mokaya, *Nano Energy*, 2015, **16**, 173-185.
115. A. Altwala and R. Mokaya, *Energy & Environmental Science*, 2020, **13**, 2967-2978.
116. F. Béguin and E. Frackowiak, *Carbons for electrochemical energy storage and conversion systems*, CRC Press, 2009.
117. Y. Zhu, S. Murali, M. D. Stoller, K. J. Ganesh, W. Cai, P. J. Ferreira, A. Pirkle, R. M. Wallace, K. A. Cychosz, M. Thommes, D. Su, E. A. Stach and R. S. Ruoff, *Science*, 2011, **332**, 1537-1541.

-
118. S. Bhoyate, C. K. Ranaweera, C. Zhang, T. Morey, M. Hyatt, P. K. Kahol, M. Ghimire, S. R. Mishra and R. K. Gupta, *Global Challenges*, 2017, **1**, 1700063.
119. N. Albeladi, Master of Science in Chemistry (MSChem) Electronic Theses & Dissertations, Pittsburg State University, 2018.
120. M. Sevilla, A. B. Fuertes and R. Mokaya, *Energy & Environmental Science*, 2011, **4**, 1400-1410.
121. J. Marco-Lozar, M. Kunowsky, F. Suarez-Garcia, J. Carruthers and A. Linares-Solano, *Energy & Environmental Science*, 2012, **5**, 9833-9842.
122. M. Sevilla, R. Foulston and R. Mokaya, *Energy & Environmental Science*, 2010, **3**, 223-227.
123. C. Robertson and R. Mokaya, *Microporous and Mesoporous Materials*, 2013, **179**, 151-156.
124. M. Sevilla, A. B. Fuertes and R. Mokaya, *International Journal of Hydrogen Energy*, 2011, **36**, 15658-15663.
125. L. Wei and G. Yushin, *Nano Energy*, 2012, **1**, 552-565.
126. M. Sevilla, R. Mokaya and A. B. Fuertes, *Energy & Environmental Science*, 2011, **4**, 2930-2936.
127. H. Chen, Y. C. Guo, F. Wang, G. Wang, P. R. Qi, X. H. Guo, B. Dai and F. Yu, *New Carbon Materials*, 2017, **32**, 592-599.
128. A. Altwala and R. Mokaya, *Energy Advances*, 2022, **1**, 216-224.
129. M. Sevilla, J. A. Maciá-Agulló and A. B. Fuertes, *Biomass and Bioenergy*, 2011, **35**, 3152-3159.
130. A. R. Mohamed, M. Mohammadi and G. N. Darzi, *Renewable and Sustainable Energy Reviews*, 2010, **14**, 1591-1599.
131. B. Sakintuna and Y. Yürüm, *Industrial & Engineering Chemistry Research*, 2005, **44**, 2893-2902.
132. J. E. Eichler, J. N. Burrow, Y. Wang, D. C. Calabro and C. B. Mullins, *Carbon*, 2022, **186**, 711-723.
133. J. V. Guerrero, J. N. Burrow, J. E. Eichler, M. Z. Rahman, M. V. Namireddy, K. A. Friedman, S. S. Coffman, D. C. Calabro and C. B. Mullins, *Energy & Fuels*, 2020, **34**, 6101-6112.
134. J. C. Wang and S. Kaskel, *Journal of Materials Chemistry*, 2012, **22**, 23710-23725.

-
135. D. Lozano-Castelló, J. Calo, D. Cazorla-Amorós and A. Linares-Solano, *Carbon*, 2007, **45**, 2529-2536.
136. D. W. McKee, *Fuel*, 1983, **62**, 170-175.
137. S. Kelemen and C. Mims, *Surface Science* 1983, **133**, 71-88.
138. R. Xue and Z. Shen, *Carbon*, 2003, **41**, 1862-1864.
139. N. Tsubouchi, M. Nishio and Y. Mochizuki, *Applied Surface Science*, 2016, **371**, 301-306.
140. A. B. Fuertes and M. Sevilla, *Carbon*, 2015, **94**, 41-52.
141. C. Schneidermann, N. Jäckel, S. Oswald, L. Giebeler, V. Presser and L. Borchardt, *ChemSusChem*, 2017, **10**, 2416-2424.
142. C. Schneidermann, C. Kensy, P. Otto, S. Oswald, L. Giebeler, D. Leistenschneider, S. Grätz, S. Dörfler, S. Kaskel and L. Borchardt, *ChemSusChem*, 2019, **12**, 310-319.
143. M. Sevilla, W. Sangchoom, N. Balahmar, A. B. Fuertes and R. Mokaya, *ACS Sustainable Chemistry & Engineering*, 2016, **4**, 4710-4716.
144. E. Fuente, R. R. Gil, R. P. Giron, M. A. Lillo-Rodenas, M. A. Montes-Moran, M. J. Martin and A. Linares-Solano, *Carbon*, 2010, **48**, 1032-1037.
145. E. A. Hirst, A. Taylor and R. Mokaya, *Journal of Materials Chemistry A*, 2018, **6**, 12393-12403.
146. M.-M. Titirici and M. Antonietti, *Chemical Society Reviews*, 2010, **39**, 103-116.
147. M. Sevilla and A. B. Fuertes, *Chemistry—A European Journal*, 2009, **15**, 4195-4203.
148. L.-P. Xiao, Z.-J. Shi, F. Xu and R.-C. Sun, *Bioresource Technology* 2012, **118**, 619-623.
149. A. Demirbas and G. Arin, *Energy Sources* 2002, **24**, 471-482.
150. F. Shafizadeh, *Journal of Analytical and Applied Pyrolysis* 1982, **3**, 283-305.
151. A. V. Bridgwater, D. Meier and D. Radlein, *Organic Geochemistry* 1999, **30**, 1479-1493.
152. M. Fang, D. Shen, Y. Li, C. Yu, Z. Luo and K. Cen, *Journal of Analytical and Applied Pyrolysis* 2006, **77**, 22-27.
153. E. Haffner-Staton, N. Balahmar and R. Mokaya, *Journal of Materials Chemistry A*, 2016, **4**, 13324-13335.

-
154. J. A. Libra, K. S. Ro, C. Kammann, A. Funke, N. D. Berge, Y. Neubauer, M.-M. Titirici, C. Fühner, O. Bens and J. Kern, *Biofuels*, 2011, **2**, 71-106.
155. B. Hu, K. Wang, L. Wu, S. H. Yu, M. Antonietti and M. M. Titirici, *Advanced Materials*, 2010, **22**, 813-828.
156. M. Sevilla and A. B. Fuertes, *Carbon*, 2009, **47**, 2281-2289.
157. BBC, *University of Nottingham labs destroyed in fire*, <https://www.bbc.co.uk/news/av/uk-29186503>, (accessed 5th October, 2023).
158. A. E. Ogungbenro, D. V. Quang, K. A. Al-Ali, L. F. Vega and M. R. M. Abu-Zahra, *Journal of Environmental Chemical Engineering*, 2018, **6**, 4245-4252.
159. W. Li, K. B. Yang, J. H. Peng, L. B. Zhang, S. H. Guo and H. Y. Xia, *Industrial Crops and Products*, 2008, **28**, 190-198.
160. Z. H. Hu, M. P. Srinivasan and Y. M. Ni, *Carbon*, 2001, **39**, 877-886.
161. S. Dutta, A. Bhaumik and K. C. W. Wu, *Energy & Environmental Science*, 2014, **7**, 3574-3592.
162. V. Rozyyev, D. Thirion, R. Ullah, J. Lee, M. Jung, H. Oh, M. Atilhan and C. T. Yavuz, *Nature Energy*, 2019, **4**, 604-611.
163. S. G. Zhang, K. Dokko and M. Watanabe, *Materials Horizons*, 2015, **2**, 168-197.
164. Z. L. Xie and D. S. Su, *European Journal of Inorganic Chemistry*, 2015, 1137-1147.
165. N. Balahmar and R. Mokaya, *Journal of Materials Chemistry A*, 2019, **7**, 17466-17479.
166. D. Lozano-Castello, D. Cazorla-Amoros, A. Linares-Solano and D. Quinn, *Carbon*, 2002, **40**, 989-1002.
167. C. Ge, D. D. Lian, S. P. Cui, J. Gao and J. J. Lu, *Processes*, 2019, **7**, 592.
168. K. Xia, R. Xiong, Y. Chen, D. Liu, Q. Tian, Q. Gao, B. Han and C. Zhou, *Colloids and Surfaces A: Physicochemical and Engineering Aspects*, 2021, **622**, 126640.
169. J. Ludwinowicz and M. Jaroniec, *Carbon*, 2015, **94**, 673-679.
170. O. Boujibar, A. Souikny, F. Ghamouss, O. Achak, M. Dahbi and T. Chafik, *Journal of Environmental Chemical Engineering*, 2018, **6**, 1995-2002.
171. P. Wang, G. Zhang, W. Chen, Q. Chen, H. Jiao, L. Liu, X. Wang and X. Deng, *ACS Omega*, 2020, **5**, 23460-23467.

-
172. E. Mehrvarz, A. A. Ghoreyshi and M. Jahanshahi, *Frontiers of Chemical Science and Engineering*, 2017, **11**, 252-265.
173. Y. Song, X. Zhou and J. A. Wang, *Energy Sources, Part A*, 2021, **43**, 1337-1347.
174. J. Singh, S. Basu and H. Bhunia, *Journal of the Taiwan Institute of Chemical Engineers*, 2019, **102**, 438-447.
175. L. Li, F. Sun, J. Gao, L. Wang, X. Pi and G. Zhao, *RSC Advances*, 2018, **8**, 14488-14499.
176. M. Sevilla, P. Valle-Vigon and A. B. Fuertes, *Advanced Functional Materials*, 2011, **21**, 2781-2787.
177. M. Molina-Sabio and F. Rodriguez-Reinoso, *Colloids and Surfaces A: Physicochemical and Engineering Aspects*, 2004, **241**, 15-25.
178. M. Sevilla, G. A. Ferrero and A. B. Fuertes, *Carbon*, 2017, **114**, 50-58.
179. A. Altwala and R. Mokaya, *RSC Advances*, 2022, **12**, 20080-20087.
180. M. Kanniche, R. Gros-Bonnivard, P. Jaud, J. Valle-Marcos, J. M. Amann and C. Bouallou, *Applied Thermal Engineering*, 2010, **30**, 53-62.
181. D. Jansen, M. Gazzani, G. Manzolini, E. van Dijk and M. Carbo, *International Journal of Greenhouse Gas Control* 2015, **40**, 167-187.
182. R. Stanger, T. Wall, R. Spörl, M. Paneru, S. Grathwohl, M. Weidmann, G. Scheffknecht, D. McDonald, K. Myöhänen, J. Ritvanen, S. Rahiala, T. Hyppänen, J. Mletzko, A. Kather and S. Santos, *International Journal of Greenhouse Gas Control* 2015, **40**, 55-125.
183. T. Wall, Y. H. Liu, C. Spero, L. Elliott, S. Khare, R. Rathnam, F. Zeenathal, B. Moghtaderi, B. Buhre, C. D. Sheng, R. Gupta, T. Yamada, K. Makino and J. L. Yu, *Chemical Engineering Research & Design*, 2009, **87**, 1003-1016.
184. Y. Wang, L. Zhao, A. Otto, M. Robinius and D. Stolten, *Energy Procedia*, 2017, **114**, 650-665.
185. A. Samanta, A. Zhao, G. K. H. Shimizu, P. Sarkar and R. Gupta, *Industrial & Engineering Chemistry Research*, 2012, **51**, 1438-1463.
186. S. Delgado, B. Valentin, D. Bontemps and O. Authier, *Industrial & Engineering Chemistry Research*, 2018, **57**, 6057-6067.
187. B. Dutcher, M. H. Fan and A. G. Russell, *ACS Applied Materials & Interfaces*, 2015, **7**, 2137-2148.

188. U. E. Aronu, H. F. Svendsen, K. A. Hoff and O. Juliussen, *Energy Procedia*, 2009, **1**, 1051-1057.
189. J. K. Adewole, A. L. Ahmad, S. Ismail and C. P. Leo, *International Journal of Greenhouse Gas Control* 2013, **17**, 46-65.
190. K. Ramasubramanian and W. S. W. Ho, *Current Opinion in Chemical Engineering*, 2011, **1**, 47-54.
191. C. E. Powell and G. G. Qiao, *Journal of Membrane Science*, 2006, **279**, 1-49.
192. Q. H. Qian, P. A. Asinger, M. J. Lee, G. Han, K. M. Rodriguez, S. Lin, F. M. Benedetti, A. X. Wu, W. S. Chi and Z. P. Smith, *Chemical Reviews*, 2020, **120**, 8161-8266.
193. I. Alali and R. Mokaya, *Journal of Materials Chemistry A*, 2023, **11**, 6952-6965.
194. I. Angelidaki, L. Treu, P. Tsapekos, G. Luo, S. Campanaro, H. Wenzel and P. G. Kougias, *Biotechnology Advances* 2018, **36**, 452-466.
195. J. Sun, T. A. Brady and M. J. Rood, *Preprints of Papers, American Chemical Society, Division of Fuel Chemistry*, 1996, **41**, CONF-960376-.
196. B. U. Haq, *Science*, 1999, **285**, 543-544.
197. R. A. Kerr, *Science*, 2004, **303**, 946-947.
198. Department of Energy (DOE), *Hydrogen Storage*, <https://www.energy.gov/ee/fuelcells/hydrogen-storage>, (accessed 1st October, 2023).
199. X. Wang, J. French, S. Kandadai and H. T. Chua, *Journal of Chemical & Engineering Data*, 2010, **55**, 2700-2706.
200. B. Li, H. M. Wen, W. Zhou, J. Q. Xu and B. L. Chen, *Chem*, 2016, **1**, 557-580.
201. N. Bimbo, A. J. Physick, A. Noguera-Díaz, A. Pugsley, L. T. Holyfield, V. P. Ting and T. J. Mays, *Chemical Engineering Journal*, 2015, **272**, 38-47.
202. S. Alhasan, R. Cariveau and D.-K. Ting, *International Journal of Environmental Studies*, 2016, **73**, 343-356.
203. iNatGas, *The Natural Gas Industry Solutions*, <https://inatgas.com/>, (accessed 19th October, 2023).
204. *Natural Gas Fueling Infrastructure Development*, [https://afdc.energy.gov/fuels/natural_gas_infrastructure.html#:~:text=Compressed%20natural%20gas%20\(CNG\)%20and,more%20safety%20precautions%20during%20fueling](https://afdc.energy.gov/fuels/natural_gas_infrastructure.html#:~:text=Compressed%20natural%20gas%20(CNG)%20and,more%20safety%20precautions%20during%20fueling), (accessed 19th October, 2023).

-
205. G. Basich and T. Dao, *CNG Use Expands Among Government Agencies*, <https://www.government-fleet.com/152834/cng-use-expands-among-government-agencies>, (accessed 19th October, 2023).
206. Ingevity, *Adsorbed Natural Gas*, https://www.ingevity.com/news/market_category/adsorbed-natural-gas/, (accessed 19th October, 2023).
207. Daigas G&P Solution, *Biogas purification and adsorption storage system*, https://www.daigasgps.co.jp/en/service/engineering/energy/biogas_stocksystem/, (accessed 19th October, 2023).
208. The DOE MOVE Program, *Methane Opportunities for Vehicular Energy*, <https://arpa-e.energy.gov/technologies/programs/move>, (accessed 19th October, 2023).
209. H. Nishihara and T. Kyotani, *Chemical Communications*, 2018, **54**, 5648-5673.
210. Y. C. Lin, C. L. Kong, Q. J. Zhang and L. Chen, *Advanced Energy Materials*, 2017, **7**, 1601296.
211. Y. Peng, V. Krungleviciute, I. Eryazici, J. T. Hupp, O. K. Farha and T. Yildirim, *Journal of the American Chemical Society*, 2013, **135**, 11887-11894.
212. P. N. Quirant, C. Cuadrado-Collados, A. J. Romero-Anaya, J. S. Albero and M. M. Escandell, *Industrial & Engineering Chemistry Research*, 2020, **59**, 5775-5785.
213. M. Feroldi, A. C. Neves, C. E. Borba and H. J. Alves, *Journal of Cleaner Production*, 2018, **172**, 921-926.
214. O. F. Cruz Jr, J. Silvestre-Albero, M. E. Casco, D. Hotza and C. R. Rambo, *Materials Chemistry and Physics*, 2018, **216**, 42-46.
215. W. Zhou, H. Wu, M. R. Hartman and T. Yildirim, *Journal of Physical Chemistry C*, 2007, **111**, 16131-16137.
216. E. Poirier and A. Dailly, *Journal of Physical Chemistry C*, 2008, **112**, 13047-13052.
217. A. Kumar, H. P. Veluswamy, R. Kumar and P. Linga, *Applied Energy*, 2019, **235**, 21-30.
218. T. A. Rash, A. Gillespie, B. P. Holbrook, L. H. Hiltzik, J. Romanos, Y. C. Soo, S. Sweany and P. Pfeifer, *Fuel*, 2017, **200**, 371-379.

-
219. M. E. Casco, F. Rey, J. L. Jorda, S. Rudic, F. Fauth, M. Martinez-Escandell, F. Rodriguez-Reinoso, E. V. Ramos-Fernandez and J. Silvestre-Albero, *Chemical Science*, 2016, **7**, 3658-3666.
220. M. E. Casco, M. Martinez-Escandell, K. Kaneko, J. Silvestre-Albero and F. Rodriguez-Reinoso, *Carbon*, 2015, **93**, 11-21.
221. M. E. Casco, M. Martínez-Escandell, E. Gadea-Ramos, K. Kaneko, J. Silvestre-Albero and F. Rodríguez-Reinoso, *Chemistry of Materials*, 2015, **27**, 959-964.
222. H. Furukawa and O. M. Yaghi, *Journal of the American Chemical Society*, 2009, **131**, 8875-8883.
223. V. Menon and S. Komarneni, *Journal of Porous Materials*, 1998, **5**, 43-58.
224. O. Talu, S. Y. Zhang and D. T. Hayhurst, *The Journal of Physical Chemistry* 1993, **97**, 12894-12898.
225. S. Bracco, D. Piga, I. Bassanetti, J. Perego, A. Comotti and P. Sozzani, *Journal of Materials Chemistry A*, 2017, **5**, 10328-10337.
226. W. Lu, D. Yuan, D. Zhao, C. I. Schilling, O. Plietzsch, T. Muller, S. Brase, J. Guenther, J. Blumel and R. Krishna, *Chemistry of Materials*, 2010, **22**, 5964-5972.
227. D.-z. Li, L. Chen, G. Liu, Z.-y. Yuan, B.-f. Li, X. Zhang and J.-q. Wei, *New Carbon Materials*, 2021, **36**, 468-496.
228. I. Senkovska and S. Kaskel, *Microporous and Mesoporous Materials*, 2008, **112**, 108-115.

Chapter 2

Experimental Methodology

2.1 Characterisation method

Considerable attention has been devoted to the synthesis of nanostructured porous materials in recent years. Research has focused on their characterisation in order to obtain a comprehensive understanding of these nanostructures. To fully assess these materials, a combination of chemical, structural, and surface characterisation techniques have been employed. This chapter provides a concise overview of the equipment and techniques used for the characterisation of the materials prepared during this research programme.

The samples were characterised and analysed using a variety of techniques (CHN analysis, TGA, XRD, SEM, TEM, BET analysis, and gas uptake using an IGA or XEMIS instrument).

2.1.1 Elemental CHN Analysis¹

Elemental (CHN) analysis is a combustion-based technique used to determine the content of C, H, and N in a sample. The technique involves high-temperature combustion of the sample. Initially, a small amount of the sample (typically 2 mg) is placed in a combustion boat and combusted in a high temperature furnace (975 °C) under pure oxygen gas. When the sample combusts, the C and H in the sample are converted CO₂ and H₂O, respectively, while the N is converted to N₂. The combustion products are carried through the system by a flow of helium gas (see **Figure 2.1**.) The generated gases are then passed over suitable reagents in the combustion tube to ensure complete oxidation and the removal of undesirable by-products such as sulphur, phosphorus, and halogen gases. Subsequently, the separated gases are quantified using specific detection methods that are tailored to each element (C, H or N). CO₂ and H₂O are typically measured using infrared detection, while N₂ is often detected using

thermal conductivity. By accurately measuring the volumes of these gases, the instrument calculates the C, H and N content in the sample.

All the samples used in this study were submitted to the Analytical Services Unit of the School of Chemistry for analysis using a CE-440 Elemental Analyser to determine the C, H and N content.

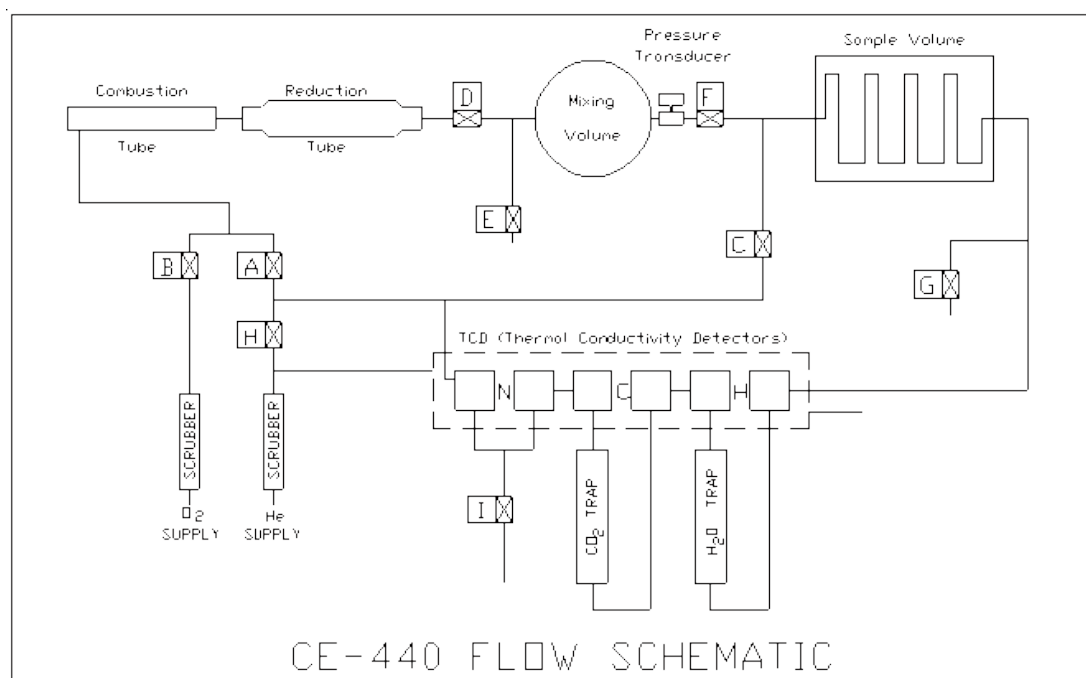


Figure 2.1. Schematic diagram of the CHN microanalyser.¹

2.1.2 Thermogravimetric Analysis (TGA)

TGA is a thermal analysis technique used to analyse the thermal stability of materials upon heating. The materials are characterised by measuring changes in weight as a function of temperature. The TGA technique is also used to measure other properties including composition, purity, decomposition reaction, decomposition temperatures, and absorbed moisture content of materials.

During the heating process, the mass of samples is monitored and every thermal change of the samples, such degradation or vaporisation of bound species, is recorded with accurate temperatures as illustrated in **Figure 2.2**.

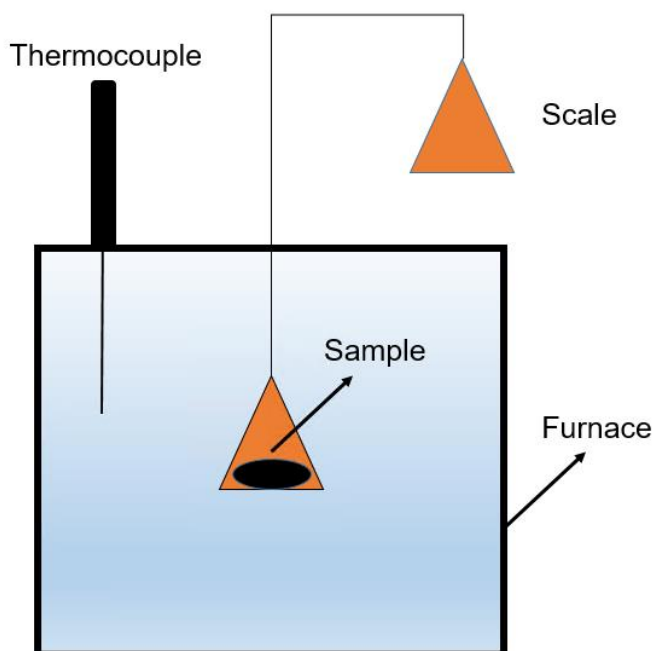


Figure 2.2. Schematic diagram of the TGA instrument.

The decomposition of samples may be defined by two characteristic temperatures; T_i and T_f , as depicted in **Figure 2.3**. T_i indicates the onset temperature which is when the mass change starts; T_f is the temperature at which the mass change is accomplished.

In this study, thermal analysis was conducted using a TA Instrument SDT Q600 analyser, applying the appropriate temperature, ramp rate, and atmospheric conditions.

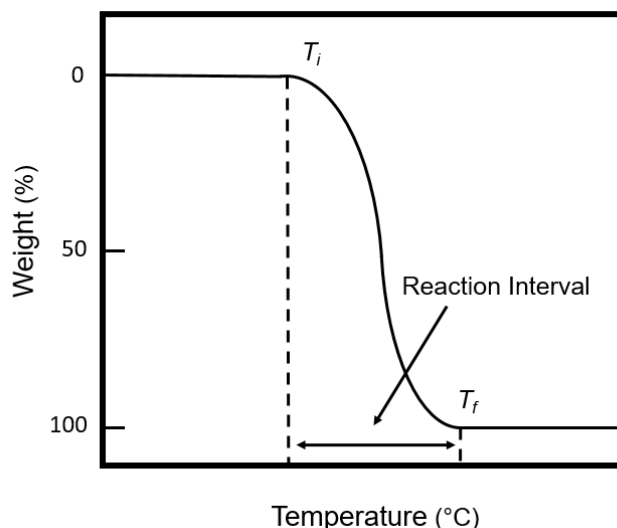


Figure 2.3. TGA curve showing decomposition temperature T_i and the final temperature T_f .

2.1.3 Powder X-ray Diffraction (PXRD)

Powder XRD is a structural analysis technique that makes it possible to determine the crystallographic density and crystal structure of solid materials. The basic principle of an X-ray instrument is illustrated in **Figure 2.4**. The sample is placed at the centre of the instrument and is illuminated with a beam of X-rays. The X-ray tube and the detector move in a synchronised motion. The signals coming from the samples are recorded and are plotted where the observed peaks are related to the atomic structure of the sample.

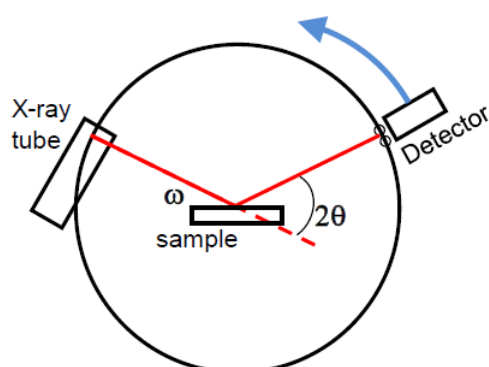


Figure 2.4. Schematic representation of powder X-ray diffraction (PXRD) experiment.

An X-ray is an electromagnetic radiation beam with a very short wavelength of approximately 1 angstrom (\AA).² In Powder XRD (PXRD), X-rays that are used for analysis are generated by bombarding a metal target, typically copper (Cu), with electrons from a filament. The high-energy electrons produced from the filament collide with the Cu atoms, ionizing some of the Cu 1s electrons. Subsequently, an electron from an outer shell fills the vacant 1s level and the energy released during this transition appears as X-radiation. The specific X-ray radiation generated from the 2p to 1s transition in copper atoms is known as $\text{CuK}\alpha$ radiation, with a characteristic wavelength of 1.5418 \AA and 8.04 kiloelectron volts (keV) of energy. This $\text{CuK}\alpha$ radiation is commonly used in PXRD experiments, including those conducted at The University of Nottingham.

Bragg provides a simplified explanation of the X-ray diffraction principle.² Materials are made of many small crystals, each of which is composed of a regular arrangement of atoms. Each atom is composed of a nucleus surrounded by a cloud of electrons. As an X-ray is a high-energy beam with a repeating wavelength that is similar to the distance between atoms in the crystal (i.e. interplanar spacing, d), a special interference effect, called diffraction, can be used to measure the distance between the atoms. When X-rays interact with atoms in a crystal, they are scattered and produce a diffraction pattern, containing information about the atomic arrangement within the crystal. The diffracted radiation may be in phase (constructive interference) or out of phase (destructive interference), depending on the angle of incidence (θ) and interplanar spacing (see **Figure 2.5**). The diffraction pattern allows for the measurement of distances between atoms. The regular arrangement of lattice points within the crystal structure enables conditions for constructive interference, as described by Bragg's equation²:

$$n\lambda = 2d\sin\theta$$

Where n is the order of diffraction ($n = 1, 2, 3, \dots$), λ is the wavelength of the X rays, d is the interplanar spacing and the θ is the incident angle of X-rays (see **Figure 2.5**).

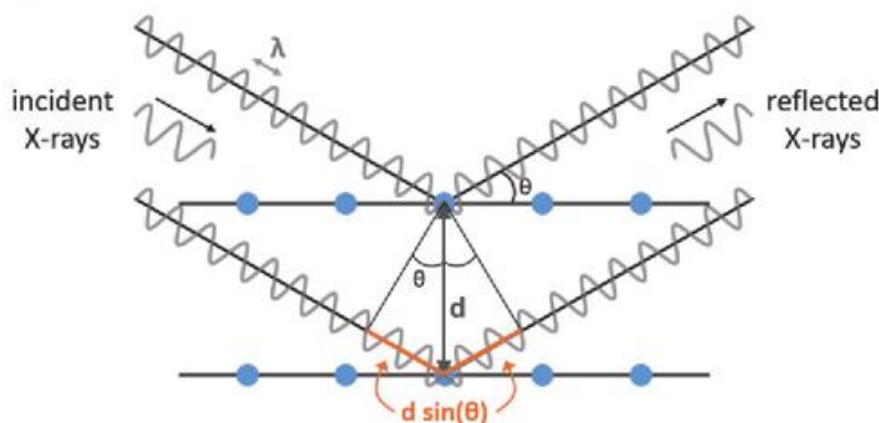


Figure 2.5. Schematic representation of Bragg's law for X-ray diffraction.²

Amorphous materials, such as activated carbons, do not have a periodic array with long range order, so they do not produce a diffraction pattern. Their X-ray scattering features broad, poorly defined amorphous 'humps'.

In this thesis, XRD analysis was conducted using a PANalytical X'PERT PRO MPD diffractometer equipped with a sealed tube Cu source and CuK α radiation ($\lambda = 1.5418 \text{ \AA}$). The instrument operated at 40 kV and 40 mA. XRD patterns were recorded over the 2° to 80° range using a 20 mm aperture with a step size of 0.02° and a step time of 2 seconds.

2.1.4 Electron Microscopy

Scanning Electron Microscopy (SEM) is a powerful imaging technique that provides detailed information about the surface morphology, topography, and elemental composition of materials. SEM analysis consists of an electron source, electromagnetic lenses, and an electron detector. The electron beam, produced by an electron gun at the top of the microscope, is used instead of light, based on wave-particle duality. The electron beam is accelerated and focused on the surface of a sample through electromagnetic lenses. When the high-energy electron beam interacts with the sample, some electrons pass through the sample. These are called unscattered electrons. Other electrons are reflected. The emission of secondary electrons, backscattered electrons, and X-rays are used in SEM technology and can be collected by the detectors to produce SEM images across the sample.³

Secondary electrons, resulting from inelastic scattering, are low-energy electrons that facilitate the creation of topographical images and 3D structural information. Backscattered electrons, meanwhile, are high-energy electrons that are scattered back from the sample surface due to elastic interactions, providing additional information of the sample composition. In addition to imaging, SEM can also be coupled with energy-dispersive X-ray spectroscopy (EDS) to perform elemental analysis and elemental mapping within a sample. When the incident beam interacts with the surface of the sample, some inner shell electrons in the atoms are displaced, causing electrons from outer shells to drop down and fill the gaps, thus releasing energy in the form of X-rays. EDS presents semi-quantitative elemental analysis that provides information on the chemical composition and distribution of elements that are present in the sample in the targeted area.⁴

The SEM images of the samples used in this thesis were analysed using a JEOL 7000F FEG-SEM microscope with an accelerating voltage of 5 kV. The samples were loaded onto carbon conductive sticky tape for analysis.

Transmission Electron Microscopy (TEM) is an advanced imaging technique used to visualise the internal structure, morphology, and composition of materials at the nanoscale. In TEM, a high-energy electron beam is transmitted through an ultra-thin specimen (typically < 100 nm thick) loaded on a lacy carbon that allows for detailed imaging of internal features of the sample. The key components of a TEM include an electron source, electromagnetic lenses, and various detectors. The electron beam is generated by an electron gun and is accelerated towards the sample using electromagnetic lenses which also focus the beam onto the specimen. When the high-energy electron beam passes through the sample, it interacts with the atoms, resulting in the scattering and absorption of electrons. The transmitted electrons are then collected by a detector, such as a fluorescent screen or a camera, producing an image that reveals the sample's internal structure and composition.^{3, 5}

For the purposes of this thesis, TEM images were obtained using a JEOL 2100F instrument operating at 200 kV and equipped with a Gatan Orius CCD for imaging. Before analysis, carbon samples were suspended in distilled water and dispersed onto lacy carbon support films.

2.2 Porosity and Physisorption

Porous materials are defined as solids that have interconnected voids, holes, or spaces (the pores) within their structure.^{6, 7} These voids can be of various sizes and shapes, allowing for the adsorption or release of fluids or gases.⁷ This phenomenon is called physisorption, which refers to the physical adsorption of gas molecules onto solid surfaces. It is primarily driven by van der Waals forces between the adsorbent (porous materials) and the adsorptive (gas).⁷ Physisorption occurs because of the weak intermolecular forces between the gas molecules and the solid surface, allowing for easy attachment and detachment. This process is reversible and can be influenced by factors such as temperature and pressure.⁷

The size and width of the pores of the adsorbent material, as well as the nature of the gas molecules being adsorbed, play essential roles. The size and width of the pores determine the surface area available for adsorption, while the nature of the gas molecules affects their affinity to adsorb onto the solid surface. Understanding these factors is crucial to optimise physisorption processes for various applications, such as gas separation and storage.⁷

2.2.1 Pore characteristics and filling mechanisms

The accessibility of the pores of adsorbent materials depends on the size and diameter of the adsorptive molecules.⁷ This means that for the smallest adsorptive molecules (He), which exhibit a kinetic diameter of 2.6 Å, the minimum pores of any materials that the gas can probe should be $> 2.6 \text{ Å}$.^{7, 8}

According to the International Union of Pure and Applied Chemistry (IUPAC) (1985), pores can be divided into three categories based on their width: micropores (less than 20 Å), mesopores (20–500 Å), and macropores (greater than 500 Å).⁷ The main mechanism that explains the pore filling process (see **Figure 2.6**) is:

(i) micropore filling: The initial stage of adsorption always occurs at low relative pressures.^{6, 7} The low pressure required for adsorption is dependent on the size and shape of these micropores. In the case of narrow microporous (ultramicroporous, pores $< 7 \text{ Å}$),⁶ they are usually filled first with two or three molecules if N_2 gas is used as the adsorptive; this is called "primary microporous filling".⁷ The heat of adsorption at this stage is very high. This is attributed to the strong adsorbent-adsorbate interaction.^{7, 9}

For wider microporosity (supermicropores, pores $> 7 \text{ \AA}$)⁶ the filling process occurs at a higher relative pressure (0.01–0.15 bar) accompanied by reduction in the adsorbent-adsorbate interaction.⁷

(ii) Monolayer adsorption occurs as the pressure increases once all the accessible micropores are filled. Mesoporous (20 to 500 \AA)⁶ adsorption allows for monolayer adsorption, which involves the formation of a monolayer of gas molecules on the solid surface. This occurs when gas molecules are adsorbed individually and do not significantly interact with one another and are not significantly influenced by pore wall.^{10, 11}

(iii) Multilayer adsorption: As gas pressure increases, additional layers of gas molecules can accumulate atop the monolayer and are characterised by indirect contact with the adsorbent surface.⁷

(iv) Capillary condensation: In some cases, after the multilayer filling, the gas molecules may condense within smaller pores, leading to capillary condensation. This phenomenon occurs in mesoporous materials at relative pressures that are less than the saturation point. It is attributed to the vapour-liquid-like phase, which involves the pore being filled with liquid-like phase, sometimes leading to the phenomenon known as hysteresis^{7, 12} (see **Section 2.2.3**).

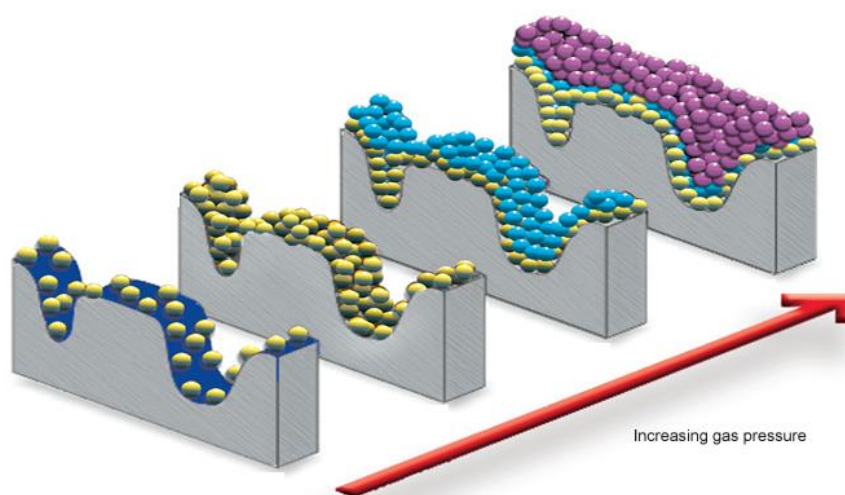


Figure 2.6. Representation of pore filling mechanism.¹³

Pores are classified on the basis of their accessibility to external fluids. There are two groups of pores (**Figure 2.7**):

(i) Closed pores: Closed pores are entirely isolated from neighbouring pores, making them inaccessible to external fluids. While these closed pores do not directly contribute to the adsorption or permeability of molecules, they do play a crucial role in influencing the mechanical properties of materials.¹⁴

(ii) Open pores: Open pores have a continuous channel of communication with the external surface of the material like (b), (c), (d), (e) and (f). Some open pores, like (b) and (f), are open only at one end. These are referred to as 'blind' or 'dead-end' pores. They are relevant in various applications, including those involving controlled fluid ingress. Pores that are open at both ends, such as (e), are known as 'through pores.' They provide a continuous pathway for fluid or gas penetration from one side of the material to the other.¹⁴

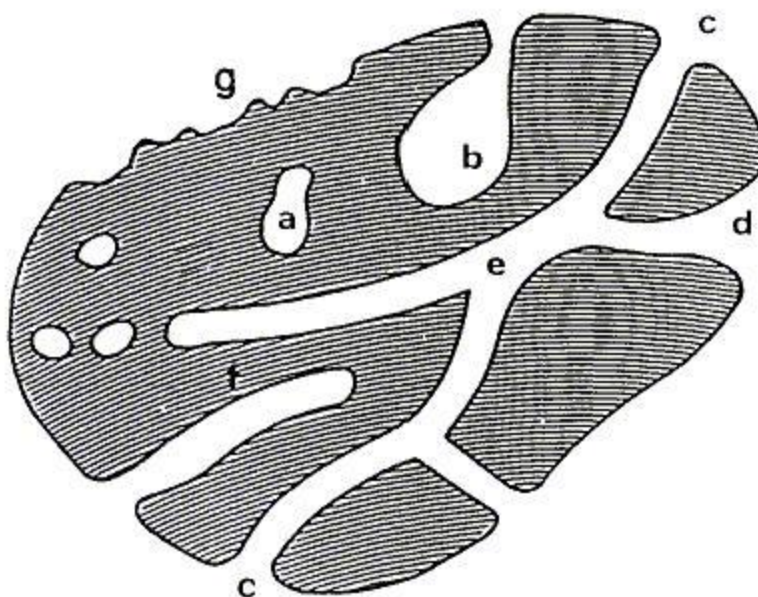


Figure 2.7. Schematic pore classification based on their accessibility (Copied from IUPAC)¹⁵: a - Closed pores, b, f - Pores open only at one end, c, d, g - Open pores, e - Pores open at two ends (Through pores).

In addition to the classifications discussed earlier, there is another possible classification for categorising pores based on their geometry. Kaneko's comprehensive review, along with the International Union of Pure and Applied Chemistry (IUPAC) guidelines, introduces a geometrical approach to pore classification.¹⁵ According to Kaneko's classification, pores are divided into distinct shapes as follows: cylinder, slit-shape, cone-shape, and ink-bottle. This classification closely aligns with that proposed by IUPAC, with the only difference being the replacement of cone-shape pores in Kaneko's categorization with funnel-shaped pores in IUPAC's scheme. These idealised shapes include cylinders, slit-shaped pores, cone-shaped or funnel-shaped pores and ink-bottle pores¹⁴⁻¹⁷, are illustrated in **Figure 2.8**.

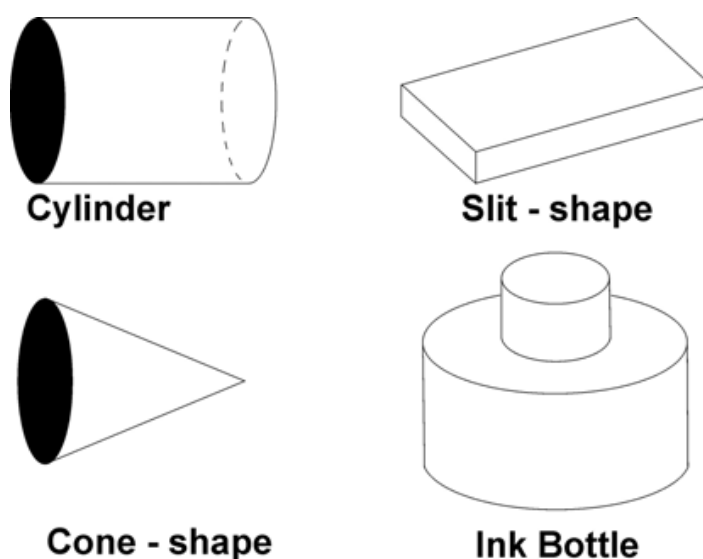


Figure 2.8. Pore geometry classification.¹⁴

2.2.2 Principles of Physisorption

Gas adsorption is a critical technique used for characterising the textural properties of porous materials, such as their surface area, pore volume, and pore size distribution (PSD). Understanding these properties is essential for a wide range of applications, including gas storage, catalysis, and separation.

The phenomenon of gas adsorption on solid surfaces and within pore spaces is a complex process that involves the interaction of mass and energy, as well as phase changes. When gases are physically adsorbed by solid materials, the amount adsorbed can be enhanced by increasing the pressure and decreasing the temperature in an exothermic process where energy is released.¹⁸ There are a number of theories that have provided the basic concepts for understanding gas adsorption on solid surfaces. The gas adsorption isotherm is a measurement of the amount of gas (expressed as the standard volume V_a , molar quantity n , or quantity q) that is adsorbed or desorbed on a clean solid surface (adsorbent) at a constant temperature (usually liquid nitrogen, LN_2 , temperature of -196°C) as a function of the applied pressure P .¹⁸ The quantity of gas adsorbed is conventionally expressed as its volume equivalent under standard conditions of temperature and pressure, STP, (0°C and 1 atm). The relative pressure, calculated by dividing the actual gas pressure (P) by the vapour pressure (P_o) of the gas adsorbed (adsorptive), is used to determine the applied pressure at a given temperature T at which the test is conducted.¹⁸ Prior to adsorption, the gas is referred to as the adsorptive; after adsorption, it is known as the adsorbate. Nitrogen gas is the gas that is generally used for these measurements, although other gases such as H_2 , O_2 , or CO_2 can also be employed.¹⁹ Irrespective of the method employed, all analyses must initially provide information in the form of quantity adsorbed or desorbed vs. pressure. Adsorption, or physisorption in specific instances, is measured as the relative pressure gradually increases from near zero to the saturation pressure (up to a relative pressure $P/P_o = 1$) and then desorption takes place, generating an isotherm. The shape of the isotherm, which represents the relationship between the adsorbed volume (V_a) and the relative pressure (P/P_o), depends on the structure of the adsorbent, specifically, the type of porosity.^{7, 15, 18, 20}

2.2.3 Types of physisorption isotherms

There are several types of physisorption isotherms that are commonly observed. The adsorption isotherms are highly dependent on the adsorbent structure and can vary in type and shape based on the porosity. The shape of the isotherms are classified into six types identified by The International Union of Pure and Applied Chemistry IUPAC (1985).²⁰ Over the last 30 years, gas adsorption analysis has improved significantly and more types of isotherms have been identified, bringing the number up to 8 isotherm types in total as shown in

Figure 2.9.⁷

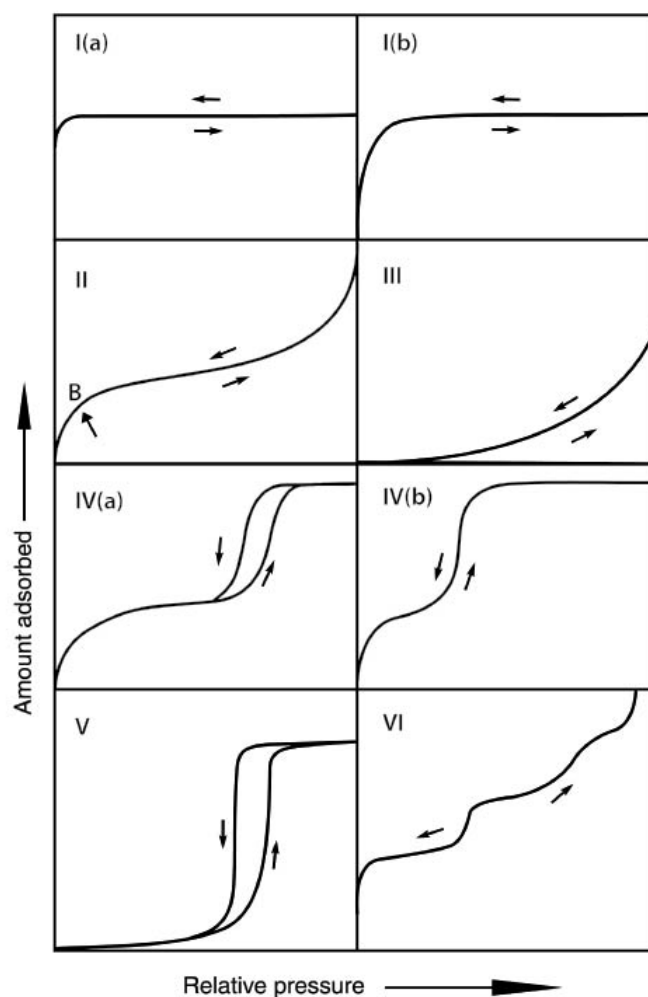


Figure 2.9. IUPAC (2015) classification of physisorption isotherms.⁷

As a common guideline, when analysing gas uptakes, adsorption at very low pressures ($P/P_o < 0.1$) indicates micropores, intermediate pressures ($0.1 < P/P_o < 0.5$) suggest mesopores, and high pressures imply macropores within the material structure.

Type I isotherms are typically observed for materials with micropores and a relatively small external surface area, such as some activated carbons and zeolites. The isotherm exhibits a steep initial uptake at very low pressures due to enhanced adsorbent-adsorptive interactions in narrow micropores. As the pressure increases, the adsorption gradually levels off, indicating pore filling. Usually, this type reveals two different shapes of isotherms:

- **Type 1(a)** is a characteristic of a microporous materials possessing mainly small microporous with pore width $< 10 \text{ \AA}$.
- **Type 1(b)** is a characteristic of microporous materials that have widening in the micro pore width and some level of narrow mesoporous (width $< \sim 25 \text{ \AA}$).

Type II isotherms are commonly observed in non-porous or macroporous materials. The shape is characterised by a broad knee, “point B”, which indicates the completion of filling of the first layer followed by a gradual curvature that corresponds to multilayer adsorption at higher pressure. The thickness of the multilayer adsorption increases with no limit at higher pressures.

Type III isotherms are similar to Type II but there is no “point B” so there is no indication of monolayer adsorption, meaning that the interaction between adsorbent and adsorbate is relatively weak with finite adsorption happening at high pressure $P/P_o = 1$.

Type IV isotherms are usually observed in mesoporous materials such as oxide gels, mesoporous silica and some metal-organic frameworks (MOFs).⁷ The behaviour of adsorption in mesopores is influenced by both adsorbent-adsorptive interactions and the interactions between the molecules in the condensed state. In this type of isotherm, initial adsorption follows a similar path as a Type II isotherm, with the formation of a monolayer–multilayer adsorption on the mesopore walls. However, unlike with Type II isotherms, following the monolayer formation there is a subsequent increase in adsorption at higher pressures. This increase is due to pore condensation,^{7, 12} where the

adsorbate molecules start to fill the mesopores beyond the monolayer coverage. The presence of pore condensation indicates the presence of mesopores with a wider size distribution and causes hysteresis loop in **Type IV(a)**,⁷ while the **Type IV(b)** isotherm can be seen in narrow mesoporous structures that have conical or cylindrical shapes and feature tapered ends. The adsorption behaviour in these mesopores is not influenced solely by the adsorbent-adsorptive interactions but also by the interactions between the adsorbed molecules themselves.

Type V: isotherms are rarely observed and show weak adsorbent-adsorbate interactions. At low pressures the isotherm shape is similar to the shape of Type III isotherms, with the pore filling starting at higher pressures.

Type VI: This isotherm is representative of layer-by-layer adsorption on a highly uniform non-porous material. The isotherms show reversible stepwise increase in adsorption with increasing pressure.

The physisorption isotherms can also show hysteresis loops that reveal more information about the adsorbent structure. The phenomenon of hysteresis loops is generally associated with capillary (or pore) condensation in mesoporous materials. Pore condensation occurs when the adsorbed gas condenses to a liquid-like phase within a pore at pressures (P) lower than the saturation pressure (P_o) of the corresponding bulk liquid.⁷

This form of hysteresis can be attributed to the difference in the adsorption and desorption pathways. During adsorption, the adsorbate molecules enter the pores of the adsorbent material and condense into a liquid-like phase as the pressure increases. However, during desorption, the adsorbate molecules remain in the liquid-like phase until the pressure decreases to a certain point, at which point they start to evaporate from the pores. This difference in the adsorption and desorption pathways leads to a difference in the amount of adsorbate present in the pores at a given pressure, resulting in the hysteresis loop. The shape and size of the hysteresis loop can provide information about the structure of a pore network of the adsorbent material. For example, a Type H1 hysteresis loop is typically observed in materials with slit-shaped pores, while a Type H2 loop is observed in materials with cylindrical pores. The size of the hysteresis loop can also be used to estimate the pore size distribution of the material.^{7, 12, 21, 22}

Although many different shapes of hysteresis loops have been recorded, the IUPAC classification specifies six main types as shown in **Figure 2.10**.⁷

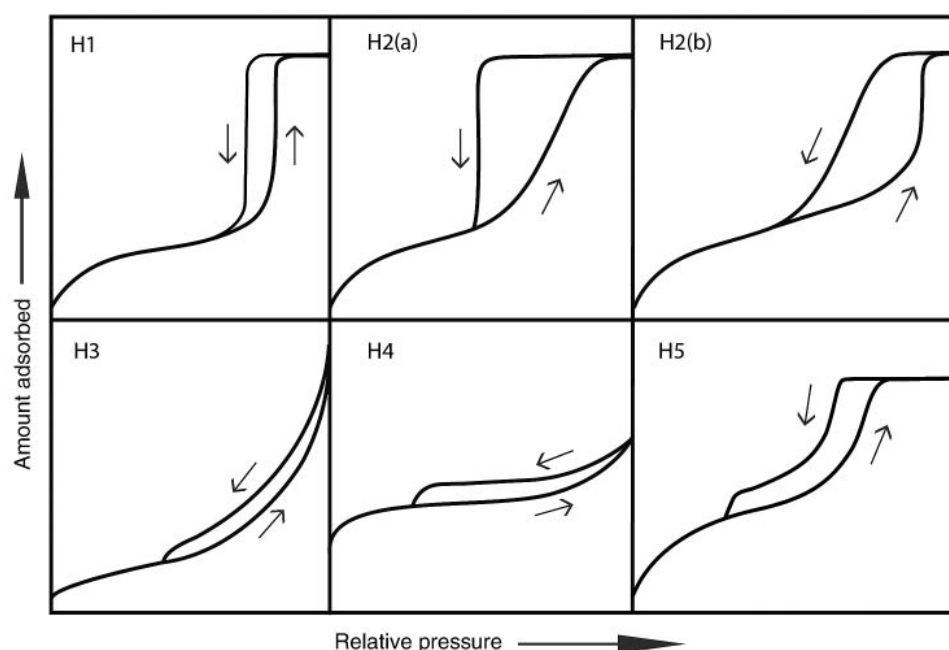


Figure 2.10. IUPAC (2015) classification of hysteresis loops.⁷

These six types of hysteresis loops are closely related to the particular features of the pore structure and underlying adsorption mechanism. They are:

Type H1 loop: This loop is characterised by sharp adsorption and desorption steps and is associated with mesoporous structure containing slit-shaped pores.

Type H2 loop: Type H2 is characterised by intricate pore structures where network effects play a significant role, revealing two types, namely:

- the **Type H2(a)** loop features a gradual adsorption step and a sharp desorption step indicating materials with cylindrical pores. The sharp desorption branch is caused by the blocking of the pore necks of narrow size distribution. Examples include silica gels, porous glasses (e.g., vycor), and some ordered mesoporous materials (e.g., SBA-16 and KIT-5 silicas).
- the **Type H2(b)** loop which is similar to the Type H2(a) in that it suggests pore blocking but with a wider distribution of pore neck widths. It has been observed in materials such as mesocellular silica foams and certain hydrothermally treated mesoporous ordered silicas.

Type H3 loop: The adsorption branch resembles a Type II isotherm, while the desorption branch is limited to cavitation-induced pressures. This loop occurs in materials with non-rigid aggregates of plate-like particles, such as certain clays.

Type H4 loop: The adsorption branch combines features of Types I and II isotherms, indicating a mix of micropores and mesopores structure. It is commonly found in aggregated crystals of zeolites, some mesoporous zeolites, and micro-mesoporous carbons.

Type H5 loop: This is an uncommon loop that is rarely observed. It is related to pore structures that contain a combination of open and partially blocked mesopores, such as plugged hexagonal templated silica.

2.2.4 Brunauer-Emmett-Teller (BET) adsorption theory

The Brunauer-Emmett-Teller (BET) theory,²³ proposed by Stephen Brunauer, P.H. Emmet, and Edward Teller in 1938, is an extension of the Langmuir theory.²⁴ Langmuir was the first to establish the connection between gas adsorption isotherms and surface areas. The Langmuir theory, proposed by Irving Langmuir in 1932, is based on the assumption that the entire surface is covered with a monomolecular layer of the adsorptive gas.²⁴ These adsorbed gas molecules collide with the solid surface for a period of time and assume no interactions between the adsorbed gas molecules themselves. The delay in the time is assumed to be responsible for the adsorption to occur. The BET theory, building upon the Langmuir model, introduces the concept of multimolecular layer adsorption.²³ Although the BET theory was not specifically formulated to characterise the adsorption of microporous materials, the BET surface area has become the widely accepted standard for the characterisation of porous materials in general.²⁵ It has received recognition from the International Union of Pure and Applied Chemistry (IUPAC) as “the most commonly employed method for evaluating the surface area of various porous and finely divided materials.”^{7, 20} Moreover, since 1995, it has been an established standard of the International Organization for Standardization (ISO) for surface area determination.²⁶ As a result, the BET surface area holds significant importance as a primary measure for assessing porous materials, including those with microporosity. This model relies on several fundamental assumptions,²⁰ namely, that (i) the surface of the adsorbent is flat and

homogeneous; (ii) the principle of the multimolecular layer adsorption, which is that, where the adsorbed gas molecules on the first layer act as a substrate for the second adsorption, this layer acts as a substrate for the third layer and so on for an infinite number of layers, (iii) the heat of adsorption for all layers, except the first one, are equivalent to the heat of condensation (evaporation); and (iv) the BET theory still assumes no interaction between neighbouring molecules. Based on all these assumptions, the BET equation is expressed as follows:^{18, 20}

$$\frac{P}{V_a(P_o - P)} = \frac{1}{V_m C} + \frac{C - 1}{V_m C} \left(\frac{P}{P_o} \right) \quad (2-1)$$

Where P the pressure of the gas, P_o is the saturation pressure of the gas, V_a is the total quantity of gas adsorbed at STP at pressure P , V_m is quantity of gas adsorbed of the monolayer, and C is a constant related to the enthalpy of adsorption.

According to the BET equation, a plot of $P/[V_a(P_o - P)]$ vs. P/P_o should generate a straight line at a specific relative pressure, with a slope equal to the $(C-1)/V_m C$, and an intercept value of $1/V_m C$. For most solid adsorbents when nitrogen is used as the adsorptive gas, the isotherm data plot, according to the aforementioned equation, gives a straight line at a relative pressure range, 0.05 – 0.30 (see **Figure 2.11**). The C value obtained by this linear regression should be positive, otherwise it is not going to have a physical meaning because the interaction energy with the solids would be higher than the gas-gas molecule. **Figure 2.12** illustrates a typical plot:

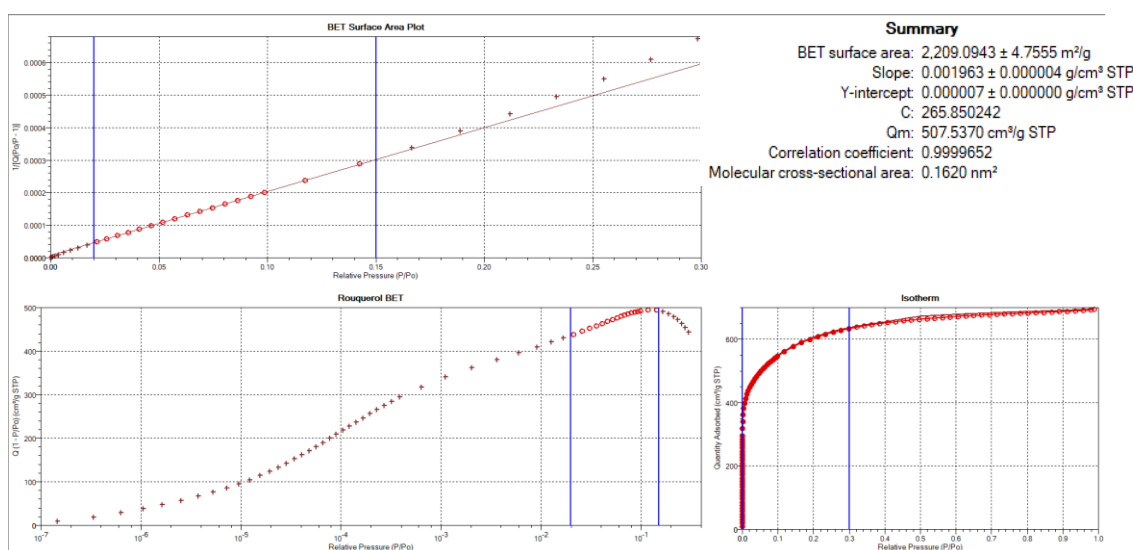


Figure 2.11. Screenshot of the BET surface area determination performed for the samples in this thesis.

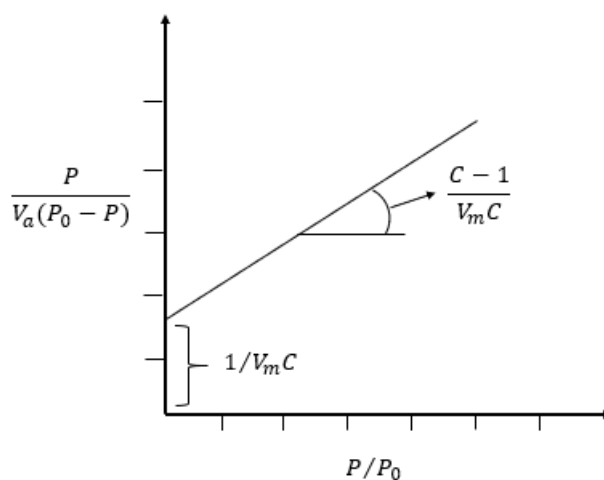


Figure 2.12. Relationship between $P / V_a(P_0 - P)$ and P/P_0 across the linear region.

Within this range the BET surface area can be calculated using the following equation:^{18, 20}

$$S_{BET} = \frac{V_m N_A \sigma_x}{V} \quad (2-2)$$

Where, S_{BET} is the BET surface area, V_m the quantity adsorbed on the monolayer, N_A corresponds to Avogadro's number (6.022×10^{23}), σ_x is the molecular cross-sectional area (nitrogen molecule = 0.162 nm^2), and V is the molar volume of the gas at STP (22414 mL).^{7, 18, 20}

The isotherm data can also reveal additional information, such as pore volume and pore size distribution (PSD). The pore volume is determined by measuring the quantity of gas adsorbed ($\text{cm}^3 \text{ g}^{-1}$) at a relative pressure near to the saturation vapour pressure ($P/P_o = 0.99$), where the pores are fully filled. This involves converting the quantity of gas adsorbed to the equivalent volume of liquid at the adsorption temperature. Specifically, for nitrogen at a temperature of -196°C , the conversion factor from the adsorbed amount to the volume of liquid adsorbate is $0.0015468 \text{ cm}^3 \text{ g}^{-1}$ at standard temperature and pressure (STP).

Using the data related to the sample given above as an example:

Quantity of gas adsorbed: $695 \text{ cm}^3 \text{ g}^{-1}$ at a relative pressure of ($P/P_o = 0.99$). So, by applying the conversion factor, the total pore volume will be calculated as follows:

$$\text{Total pore volume} = 695 \times 0.0015468 = 1.08 \text{ cm}^3 \text{ g}^{-1} \quad (2-3)$$

The thickness-plot (t-plot) method is commonly used to estimate the microstructure of the adsorbent (micropore volume and area). This is achieved when plotting the volume of the gas adsorbed vs. the adsorbate molecular film thickness, which yields a straight line. This line gives a positive intercept equivalent to the micropore volume. The most widely used and commonly employed methods to calculate the thickness are the Harkins and Jura,²⁷ Halsey,²⁸ and Broekhoff-de Boer equations,²⁹ which are recognised for their broad applicability.

The micropore surface area and micropore volume of the samples in this thesis were obtained from the t-plot analysis, using the Harkins and Jura thickness curve as illustrated in equation below:

$$t = \left[\frac{13.99}{0.034 - \log\left(\frac{P}{P_0}\right)} \right]^{1/2} \quad \text{Harkins and Jura Equation} \quad (2-4)$$

The values 13.99 and 0.034 are empirical and have been determined through experimental measurements and observations by Harkins and Jura.¹⁸ The t-plot data is used to calculate the value of y-intercept, which is then in turn used to calculate the micropore volume by converting it from a gas volume to liquid volume results. Additionally, the gradient of the linear region, as illustrated in the **Figure 2.13**, is used to calculate the micropore volume and surface area according to the following equations:

$$V_{micropore} = (0.0015468) \times (t - \text{plot intercept}) \quad (2-5)$$

$$S_{mesopore} = 1.5468 \times (t - \text{plot slope}) \quad (2-6)$$

$$S_{micropore} = S_{BET} - S_{mesopore} \quad (2-7)$$

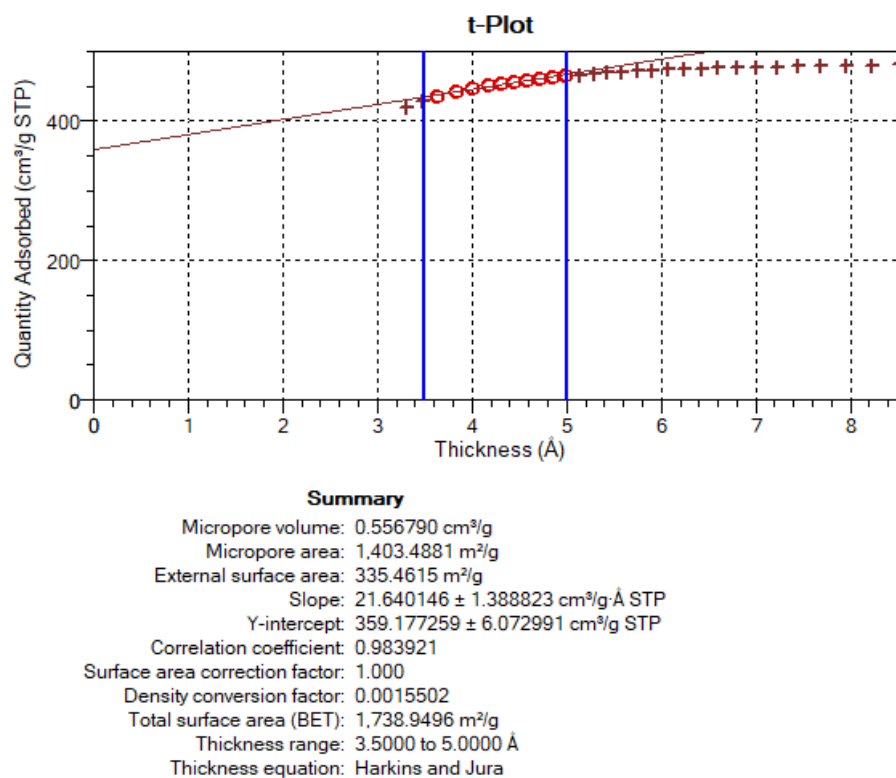


Figure 2.13. t-Plot illustration of a sample in the thesis.

2.2.5 Pore size distribution (PSD)

Pore size distribution information is very important for a number of applications and knowing all the size ranges is beneficial for understanding the capability of a material toward specific applications. A number of methods are employed to extract information about the pore structure, including pore size and pore size distribution, from adsorption/desorption isotherms of adsorbents. Some methods are applicable only to specific types of isotherms, depending on the shape and structure of the pores. The PSD of a material can be determined using the Kelvin equation taking into consideration the capillary condensation that occurs in narrow pores at pressures below the saturated vapour pressure of the adsorptive.¹⁸ The Kelvin equation describes the relationship between the changes in vapour pressure above the interface of a liquid cylindrical capillary with its radius.³⁰ However, the Kelvin equation is primarily based on monolayer adsorption and cannot be directly used to calculate pore size as it does not consider the occurrence of multilayer adsorption followed by capillary condensation in mesoporous materials.¹⁸ Various methods, such as the Barrett, Joyner,

and Halenda (BJH)³¹ model make use of modified versions of the Kelvin equation with a correction term for the thickness of the multilayer adsorbed film.¹⁸ However, studies have shown that Kelvin equation-based procedures, including the BJH method, that account for the wall thickness due to multilayer adsorption tend to significantly underestimate the pore size for narrow mesopores (pore size $< \sim 100$ Å), leading to an underestimation of approximately 20-30%.^{21, 22, 32, 33}

In recent decades, the use of Density Functional Theory (DFT), particularly Non-local Density Functional Theory (NL-DFT), is considered to be superior and a more reliable method for the analysis of PSD over the complete nanopore range.^{21, 34, 35} This theory presents a description of confined fluid behaviour in non-homogeneous systems which is based on the fundamental principles of statistical mechanics. The theory is based on classical and statistical thermodynamic principles, assuming the equilibrium thermodynamic state of the adsorbate-adsorptive in the gas phase under specific controlled conditions. Seaton and Walton were the first to propose a Density Functional Theory (DFT) model to calculate the pore size distribution from nitrogen adsorption isotherms of activated carbon.³⁶ A significantly improved model based on the non-local density functional theory (NL-DFT) evolved a few years later.²¹ The NL-DFT method enables the determination of pore size and pore size distribution from gas adsorption isotherms measured across a pressure range that extends from low relative pressure up to the saturation pressure of the fluid.^{33, 37} The NL-DFT method is capable of describing materials with a wide range of porosity, including micro-, meso-, and macroporous structures, including activated carbons. It provides a comprehensive model that can extract a continuous pore size distribution, allowing for an accurate quantification of the complete porosity profile of the material. For instance, in porous carbons, the one-dimensional infinite slit model assumes that pores are formed between infinite walls and generate a series of theoretical isotherms (kernels) that indicate the amount of gas adsorbed as a function of pore size and pressure at a specific temperature. By comparing these theoretical isotherms with experimentally measured isotherms, the PSD of the sample can be determined accurately.^{21, 33}

For the purposes of this study, nitrogen sorption (at -196 °C) isotherms and textural properties of the activated carbons were determined using a Micromeritics 3FLEX sorptometer. Prior to analysis, the carbons were degassed at 300 °C for 16 h under vacuum. The surface areas were calculated using the Brunauer–Emmett–Teller (BET)

method using the nitrogen adsorption data in the relative pressure (P/P_0) range between 0.05–0.30. The relative pressure (P/P_0) range used to determine the surface areas follows the Rouquerol Criterion, which makes use of the adsorption data up to the P/P_0 pressure where $V(1 - P/P_0)$ exhibits a maximum.^{7, 38, 39} Total pore volume was determined from the amount of nitrogen adsorbed at a relative pressure of 0.99. The micropore surface area and micropore volume were estimated using t-plot analysis. The pore size distribution (PSD) was determined using a Non-Local Density Functional Theory (NLDFT) model applied to nitrogen adsorption data.

2.3 Gas uptake measurement

The physical adsorption of a gas on a solid material can be defined as the process by which gas molecules (adsorbate) adhere to the surface of the solid material (adsorbent). These forces are caused by van der Waals interactions between the adsorbent surface and the adsorbate.⁷ This adsorption phenomenon is influenced by factors such as temperature, pressure, and the surface area and porosity of the solid material.

Gas uptake was determined using advanced gas sorption analysers, namely, the Hiden Intelligent Gravimetric Analyser (IGA-003) and the Hiden Isochema XEMIS Analyser. The gravimetric technique allows for the precise measurement of methane and CO₂ uptake on solid materials through highly accurate gravimetric sorption analysers. To quantify the amount of a specific gas adsorbed onto a porous material, a gravimetric uptake analysis is conducted using a microbalance to monitor changes in sample weight at various pressures. Pressure is systematically adjusted during adsorption and subsequently held constant at a predefined pressure point until equilibrium is reached. The recorded changes in weight versus pressure are used to determine the sorption uptake, which leads to the creation of the gas sorption isotherm.^{40, 41}

CO₂ Uptake Measurements. The CO₂ uptake isotherms of the carbons were measured at room temperature (ca. 25 °C) and at a pressure range of 0 to 20 bar using a Hiden intelligent gravimetric analyser (IGA-003). Prior to analysis, the carbon samples were outgassed under vacuum at 240 °C for several hours.

Methane Uptake Measurements. Methane uptake was determined using a Hiden Isochema XEMIS Analyser. Before the uptake measurements, the carbons were

degassed at 240 °C under vacuum for several hours. Adsorption–desorption isotherms were obtained at 25 °C over a methane (CH₄) pressure range of 0–100 bar.

References

1. CHN Microanalysis, <https://workspace.nottingham.ac.uk/x/vRHvDQ>, (accessed 18th July, 2023).
2. M. M. Woolfson, *An introduction to X-ray crystallography*, Cambridge University Press, 1997.
3. P. J. Goodhew and J. Humphreys, *Electron microscopy and analysis*, CRC Press, 2000.
4. P. Atkins, *Shriver and Atkins' inorganic chemistry*, Oxford University Press, USA, 2010.
5. Y. Leng, *Materials characterization: introduction to microscopic and spectroscopic methods*, John Wiley & Sons, 2009.
6. A. D. McNaught and A. Wilkinson, *Compendium of chemical terminology*, Blackwell Science Oxford, 1997.
7. M. Thommes, K. Kaneko, A. V. Neimark, J. P. Olivier, F. Rodriguez-Reinoso, J. Rouquerol and K. S. W. Sing, *Pure and Applied Chemistry*, 2015, **87**, 1051-1069.
8. D. Lide, *Handbook of Chemistry and Physics*, volume 88th edition, CRC Press, 88th edn., 2007, p. 154.
9. M. Dubinin, *Carbon*, 1989, **27**, 457-467.
10. S. J. Gregg, K. S. W. Sing and H. Salzberg, *Journal of the Electrochemical Society* 1967, **114**, 279Ca.
11. R. T. Yang, *Gas separation by adsorption processes*, World Scientific, 1997, vol. 1.
12. P. A. Monson, *Microporous and Mesoporous Materials*, 2012, **160**, 47-66.
13. Micromeritics Instrument Corporation, *Gas Adsorption Theory*, <https://www.micromeritics.com/resources/scientific-posters/>, (accessed 26th September, 2023).
14. B. Zdravkov, J. Čermák, M. Šefara and J. Janků, *Open Chemistry*, 2007, **5**, 385-395.
15. J. Rouquerol, D. Avnir, C. W. Fairbridge, D. H. Everett, J. Haynes, N. Pernicone, J. D. Ramsay, K. S. W. Sing and K. K. Unger, *Pure and Applied Chemistry*, 1994, **66**, 1739-1758.
16. K. Kaneko, *Journal of Membrane Science*, 1994, **96**, 59-89.

-
17. C. Lastoskie, K. E. Gubbins and N. Quirke, *The Journal of Physical Chemistry* 1993, **97**, 4786-4796.
 18. P. A. Webb and C. Orr, *Analytical methods in fine particle technology*, Micromeritics Instrument Corporation, 1997.
 19. L. S. Blankenship, J. Jagiello and R. Mokaya, *Materials Advances*, 2022, **3**, 3961-3971.
 20. K. S. W. Sing, D. H. Everett, R. A. W. Haul, L. Moscou, R. A. Pierotti, J. Rouquerol and T. Siemieniewska, *Pure and Applied Chemistry*, 1985, **57**, 603-619.
 21. J. Landers, G. Y. Gor and A. V. Neimark, *Colloids and Surfaces A: Physicochemical and Engineering Aspects*, 2013, **437**, 3-32.
 22. M. Thommes and K. A. Cychosz, *Adsorption*, 2014, **20**, 233-250.
 23. S. Brunauer, P. H. Emmett and E. Teller, *Journal of the American Chemical Society*, 1938, **60**, 309-319.
 24. I. Langmuir, *Journal of the American Chemical Society*, 1918, **40**, 1361-1403.
 25. J. Osterrieth, J. Rampersad, D. G. Madden, N. Rampal, L. Skoric, B. Connolly, M. Allendorf, V. Stavila, J. Snider and R. Ameloot, *Advanced Materials*, 2021, **34**, 2201502.
 26. International Organization for Standardization (ISO), *Determination of the specific surface area of solids by gas adsorption—BET method. Standard ISO 9277:2022(E)*, 3rd edn., <https://www.iso.org/obp/ui/en/#iso:std:iso:9277:ed-3:v1:en>).
 27. W. D. Harkins and G. Jura, *Journal of the American Chemical Society*, 1944, **66**, 1366-1373.
 28. G. Halsey, *The Journal of Chemical Physics* 1948, **16**, 931-937.
 29. D. H. Everett and R. H. Ottewill, *Surface Area Determination: Proceedings of the International Symposium on Surface Area Determination Held at the School of Chemistry, University of Bristol, UK, 16—18 July, 1969*, Elsevier, 2013.
 30. W. Thomson, *Proceedings of the Royal Society of Edinburgh*, 1872, **7**, 63-68.
 31. E. P. Barrett, L. G. Joyner and P. P. Halenda, *Journal of the American Chemical Society*, 1951, **73**, 373-380.

-
32. S. Lowell, J. E. Shields, M. A. Thomas and M. Thommes, *Characterization of porous solids and powders: surface area, pore size and density*, Springer Science & Business Media, 2006.
 33. M. Thommes and C. Schlumberger, *Annual Review of Chemical and Biomolecular Engineering*, 2021, **12**, 137-162.
 34. P. Tarazona, U. M. B. Marconi and R. Evans, *Molecular Physics*, 1987, **60**, 573-595.
 35. C. Lastoskie, K. E. Gubbins and N. Quirke, *Langmuir*, 1993, **9**, 2693-2702.
 36. N. Seaton and J. Walton, *Carbon*, 1989, **27**, 853-861.
 37. F. Porcheron, P. Monson and M. Thommes, *Langmuir*, 2004, **20**, 6482-6489.
 38. J. Rouquerol, P. Llewellyn and F. Rouquerol, *Studies in Surface Science and Catalysis*, 2006, **160**, 49-56.
 39. A. Galarneau, D. Mehlhorn, F. Guenneau, B. Coasne, F. Villemot, D. Minoux, C. Aquino and J. P. Dath, *Langmuir*, 2018, **34**, 14134-14142.
 40. B. Li, H. M. Wen, W. Zhou, J. Q. Xu and B. L. Chen, *Chem*, 2016, **1**, 557-580.
 41. C. Chilev, F. D. Lamari, E. Kirilova and I. Pentchev, *Chemical Engineering Research and Design*, 2012, **90**, 2002-2012.

Chapter 3

Effect of Air-Carbonisation Temperature on the Porosity and Gas Adsorption Performance of Biomass-Derived Activated Carbons

Abstract

The use of porous carbons derived from biomass sources as gas stores, particularly activated carbons, has attracted significant attention as a promising solution for energy-related applications such as carbon capture and storage (CCS) and storage of natural gas in the form of adsorbed natural gas (ANG). This study aimed to investigate the effect of air-carbonisation temperature on the structure and gas adsorption performance of activated carbons prepared from Hookah Tobacco (HTb). The findings of this study demonstrated the significance of air-carbonisation temperature, in the range of 300 to 550 °C, in determining the elemental composition and therefore O/C ratio of the resulting carbonaceous matter. This then enabled the modifying and tailoring of the porosity, surface area, O/C ratio and packing density of the resulting activated carbons. The O/C ratio of the carbonaceous matter could be varied in the range of 0.245 to 0.379, and generally decreased with carbonisation temperature. The surface area of the activated carbons was in the range of 402 to 3413 m² g⁻¹ with pore volume of 0.18–1.65 cm³ g⁻¹, depending on the air-carbonisation temperature (and thus O/C ratio of the carbonaceous matter), amount of activating agent used and activation temperature. High air-carbonisation temperature (450 or 550 °C) generated carbonaceous matter with lower O/C ratio and led to activated carbons with greater surface area and pore volume. On the other hand, lower air-carbonisation temperature generated carbonaceous matter with O/C ratio that resulted in microporous activated carbons. In this way, the pore structure of the activated carbons could be designed towards optimal CO₂ capture at 25 °C and low pressures; 2.0 and 5.2 mmol g⁻¹ at 0.15 and 1 bar, respectively. Furthermore, the ability to adjust O/C ratio of the precursor allowed porosity modulation towards activated carbons with a high packing density of up to 0.79 g cm⁻³, which are suited for enhanced gravimetric and volumetric

methane storage of up to 0.38 g g^{-1} and $278 \text{ cm}^3 \text{ (STP) cm}^{-3}$, respectively, at $25 \text{ }^{\circ}\text{C}$ and 100 bar. The findings emphasise the significance of air-carbonisation temperature in tailoring and optimising the properties of biomass-derived activated carbons for suitability in energy applications.

3.1 Introduction

Recently, among the most commonly used materials in the preparation of activated carbon, biomass-based materials have attracted significant attention due to their abundant availability, low cost, and sustainability.¹⁻⁸ The use of biomass (or biomass waste) as a starting material offers a sustainable approach for the production of activated carbons, and with careful synthesis, the properties of the carbons can be optimised to fulfil specific applications. The textural properties of activated carbons, such as pore volume, surface area, and packing density, can be influenced by several factors, including the nature and type of a precursor, mode of carbonisation, and activation parameters (type and amount of activating agent, as well as temperature).^{6, 9-14} Understanding and precisely controlling these factors can play a key role in tailoring the textural properties of the resulting activated carbons, which can significantly enhance their performance in targeted applications. Chemical activation with KOH is amongst the most widely used processes for the preparation and modulation of the porosity of activated carbons and can offer a higher degree of control over pore size distribution and surface area.^{1, 8, 15}

The textural properties (i.e., porosity, surface area and packing density) of the activated carbons are dependent on the activation conditions (amount and type of activating agents and activation temperature) and the nature and type of carbonaceous matter used as starting material (i.e. precursor).^{1, 6, 9, 12, 14, 16} For instance, the atomic O/C ratio of any carbonaceous matter has been shown to be a key factor in predicting susceptibility to activation and the type of the porosity generated with respect to the relative mix of microporosity and mesoporosity.^{1, 9, 11, 16} When the O/C ratio of a carbonaceous matter is low, the resulting activated carbons tend to be highly microporous with low to moderate surface area due to the resistance of such precursors to activation. On the other hand, carbonaceous matter with higher O/C ratio are more susceptible to activation, which results in activated carbons with higher surface area and a mix of micro- and mesoporous character.^{1, 9, 12} Furthermore, the O/C ratio of carbonaceous matter from any one biomass source can be varied via choice of carbonisation process. Alali and Mokaya prepared activated carbons from cloves (*Syzygium aromaticum*) via either hydrothermal carbonisation (HTC) or flash air-carbonisation (fA-C) followed by chemical activation with KOH. Both carbonisation routes (HTC and fA-C) yielded relatively similar carbonaceous matter, namely HCC

(from HTC) or ACC (from fA-C), with low O/C ratio of 0.36 and 0.31, respectively.³ They observed that the effect of the O/C ratio was reflected on the resulting activated carbons in that they generally had relatively similar levels of overall porosity and mix of microporosity and mesoporosity.¹⁶ However, although the yield of HCC and ACC were similar at 35%, the ACC-derived activated carbons offered higher yield, which hinted at slightly greater resistance to activation.¹⁶ However, there are hardly any studies that systematically probe the impact of carbonisation temperature on the O/C ratio. Zhang, *et al.* prepared a series of carbons via HTC of glucose at 190 °C followed by calcination of the resulting hydrochar (with an O/C ratio of 0.33) at temperatures ranging from 200 to 300 °C, and observed that the O/C ratio of the resulting low surface area (300 – 900 m² g⁻¹) carbons varied from 0.40 to 0.45.¹⁷ This compared with O/C ratio of 0.37 for glucose directly pyrolysed at 300 °C.¹⁷ The proportion of ultramicropores in the carbons was found to vary somewhat according to the mode of preparation and the final pyrolysis temperature.¹⁷ However, to date, we are not aware of any studies that systematically probe the impact of carbonisation temperature of biomass-derived precursors on the porosity of high surface area activated carbons. Any effect of carbonisation temperature would provide an effective extra tool for modulating the porosity of activated carbons.

Recent research on activated carbon preparation has mostly focused on the impact of activation factors such as activating agent type, activation temperature, and activating agent amount. Although the carbonisation step prior to activation is a crucial step in the production of activated carbon, it has been the subject of very few investigations.¹⁸⁻²⁰ Conventionally, the preparation of porous carbon materials from biomass often involves hydrothermal carbonisation (HTC)^{1, 21-23} or pyrolysis²⁴⁻²⁷ as an initial step to convert biomass into carbon-rich carbonaceous matter prior to activation. In HTC, biomass is converted into hydrochar through thermochemical degradation by heating in water and endogenous pressure at relatively low temperatures (250–350 °C), while in pyrolysis, the biomass is converted into carbon-rich matter via thermal treatment under an inert gas such as N₂ at elevated temperatures (typically 600–900 °C). Both HTC and pyrolysis can be time-consuming processes that require either high temperatures or specialised high-pressure equipment and typically take several hours. In this regard, the simpler flash air-carbonisation route that can be realised at low

temperatures, with less energy consumption for conversion of biomass to carbonaceous matter is an attractive alternative.^{3, 4, 7, 11}

The flash air-carbonisation of biomass materials has been presented as a green and simple process for producing activated carbons and is now known to generate carbonaceous matter with low O/C ratio. On activation, such O-poor precursors generate activated carbons with very interesting textural properties, which may be tuned to offer enhanced gas (CO₂ or methane) uptake.^{3, 4, 7, 11} However, although the effect of the nature and type of biomass on the O/C ratio of flash air-carbonised carbonaceous matter has been demonstrated,^{3, 4, 7, 11} the effect of the air-carbonisation temperature has not been systematically probed. It is desirable to establish the effect of the carbonisation temperature as it could potentially enable further fine tuning of the O/C ratio of carbonaceous matter and, in turn, the properties of the final activated carbons. Therefore, the work presented in this chapter examined the impact of air-carbonisation temperature on the structure and gas (CO₂ and methane) uptake performance of activated carbons generated from Hookah Tobacco waste via flash air-carbonisation followed by KOH activation. Hookah Tobacco has been selected as biomass source due to the fact that, although there are large amounts of tobacco waste, it has seldom been explored as a precursor for activated carbons especially for storage for energy related gases, CO₂ and methane.²⁸ Use of Hookah Tobacco can therefore offer insights on how waste tobacco may be generally used for the preparation of activated carbons, and additionally offers the opportunity to explore valorisation of waste into useful sustainable energy materials.

3.2 Experimental section

3.2.1 Material synthesis

The biomass used, Hookah Tobacco waste (designated as HTb), was flash air-carbonised as follows. A known amount of HTb was placed in an alumina boat and heated in a horizontal tube furnace, at heating ramp rate of 10 °C min⁻¹, up to 300, 350, 450 or 550 °C) under a flow of nitrogen gas. Once at the targeted temperature, the HTb was exposed to a flow of air only for 5 min, after which the furnace was allowed to cool down under a flow of nitrogen gas only. The resulting carbonaceous matter was designated as HTbx carbon where x is the carbonisation temperature. Thus HTb carbonised at 300 °C is denoted as HTb300.

For activation, the HTbx carbon and KOH were ground together into a fine powder, at a KOH/HTbx carbon weight ratio of 2 or 4, to give a homogeneous dark grey powder. The powder was placed in an alumina boat and heated in a horizontal tube furnace to 600, 700 or 800 °C at a heating ramp rate of 3 °C min⁻¹ under an atmosphere of nitrogen gas and held at the final temperature for 1 h, after which the furnace was allowed to cool under a flow of nitrogen to room temperature. The resulting activated samples were then collected and washed with stirring in 10% HCl at room temperature, and then repeatedly washed with deionized water until neutral pH was achieved for the filtrate and then dried in an oven at 100 °C. The resulting activated carbons were designated as HTbx-yT, where x is the flash air-carbonisation temperature, y is the KOH/HTbx carbon ratio and T is the activation temperature (in °C). Thus, an activated carbon derived from HTb300 at KOH/HTb300 ratio of 2 and at 800 °C is designated as HTb300-2800.

3.2.2 Material characterisation

Thermogravimetric analysis (TGA) was performed using a TA Instruments SDT Q600 analyser under flowing of air conditions (100 ml min⁻¹) and a heating ramp rate of 10 °C min⁻¹. Powder XRD analysis was performed using a PANalytical X'Pert PRO diffractometer with Cu-K α light source operating at (40 kV, 40 mA), with step size of 0.021 and 50 s time step between 2° and 80°. Elemental analysis, for C, H and N, was carried out using an Exeter Analytical CE-440 Elemental Analyser. Nitrogen sorption isotherms and textural characteristics of activated carbons were obtained using a Micromeritics 3FLEX sorptometer via nitrogen sorption analysis at -196 °C. Before analysis, the carbons were degassed at 240 °C for 16 h. The surface area was calculated using the Brunauer–Emmett–Teller (BET) method applied to adsorption data at the appropriate relative pressure (P/Po) range. The relative pressure (P/Po) range used to calculate the surface areas was according to the Rouquerol Criterion, which suggests use of adsorption data up to the P/Po pressure, where $V(1 - P/Po)$ exhibits a maximum, and that there should be a positive intercept and no negative value of C.²⁹⁻³¹ Adsorption beyond this value represents the point where the adsorbed amount increases less rapidly with pressure compared to the first adsorbed layer.³⁰ The pore volume was estimated from the total nitrogen adsorbed at pressure near saturation (P/Po \approx 0.99). T-plot analysis was used to calculate the micropore surface area and micropore volume. The pore size distribution (PSD) was determined using the non-local density

functional theory (NLDFT) model, applied to the nitrogen adsorption data. Scanning electron microscopy (SEM) images were obtained using a JEOL 7000F FEG-SEM microscope operating at accelerating voltage of 5 kV. Transmission electron microscopy (TEM) images were obtained using a JEOL 2100F instrument operating at 200 kV, and equipped with a Gatan Orius CCD for imaging. Prior to analysis, the carbon samples were suspended in distilled water and dispersed onto lacey carbon support films.

The packing density of the carbons was determined by pressing a known mass of carbon at a compaction pressure of 370 MPa in a 1.3 cm diameter die for 5 minutes at ambient temperature. The packing density could then be worked out from the mass and volume of the resulting carbon pellet.

3.2.3 Gas uptake measurements of (CO₂ and CH₄)

Gas uptake measurements were obtained using a Hiden Isochema Intelligent Gravimetric Analyser (IGA-003) for CO₂ uptake over the pressure range of 0–20 bar at room temperature. Prior the CO₂ uptake measurements, the carbons were outgassed at 240 °C for several hours. Methane uptake at 25 °C and pressure of 0–100 bar was determined using a Hiden Isochema XEMIS Analyser.

3.3 Results and discussion

3.3.1 Yield and elemental analysis

The elemental composition of the biomass source (Hookah Tobacco waste, HTb), and yields and elemental composition of air-carbonised Hookah Tobacco (HTbx), and the resulting activated carbons (HTbx-yT) are given in

Table 3.1. In the preparation of carbon-based materials, the yield of the resulting carbons after each process (carbonisation or activation) is an essential factor that is taken into consideration. Therefore, in this study, the yield of the resulting carbons produced after air-carbonisation (carbonaceous matter) and activation (activated carbon) was monitored in order to evaluate the effect of air-carbonisation temperature. The data shows that increasing the air-carbonisation temperature led to a decrease in yield of the HTbx carbonaceous matter. The yield of HTbx for carbonisation at 300 °C or 350 °C is similar at 34 wt% and 33 wt% for HTb300 and HTb350, respectively. The yield decreased to 25 wt% and 24 wt% for carbonisation at 450 °C (HTb450) and 550 °C (HTb550), respectively, as depicted in **Figure 3.1**. Thus, the yield decreases slightly when increasing the carbonisation temperature from 300 to 350 °C, followed by a significant drop for carbonisation at 450 °C, and then a slight further decrease at 550 °C. This could be attributed to the retention of some volatile matter in HTbx at low temperature, which then decreases or is eliminated at higher temperature. The trend suggest that the removal of any such volatile matter may be near complete at 450 °C, which is consistent with previous reports on thermal treatment of biomass in air.^{4,7}

The yield of activated carbons (HTbx-yT), on the other hand, increased in direct proportion to the air-carbonisation temperature. Activated carbons derived from HTb300 have yield ranging from 19 to 47 wt%, while the yield is 22 to 49 wt% for those derived from HTb350, 41 to 53 wt% from HTb450, and 31 to 72 wt% for carbons derived from HTb550. A possible explanation for this trend is that carbonaceous matter produced at lower carbonisation temperatures contains more volatiles, which are lost during activation. A similar trend was observed by Li, *et al.* who carbonised coconut shell, and found that carbonisation at higher temperatures resulted in a more organised structure of the coconut shell char compare to that obtained at lower carbonisation temperatures.²⁰

Regarding elemental composition, the HTb contains 43.6 wt% C, which, on carbonisation, generally increases with the carbonisation temperature to 62.9 wt% for HTb300, 66.8 wt% for HTb350, 70.6 wt% for HTb450, and 69.4 wt% for HTb550. As a consequence, the O content decreases from 48.6 wt% for HTb to 31.8 wt% (HTb300), 27.0 wt% (HTb350), 23.1 wt% (HTb450), and 26.6 wt% for HTb550. This results in lower O/C ratios of 0.379 (HTb300), 0.303 (HTb350), 0.245 (HTb450),

followed by an apparent slight increase to 0.287 for HTb550. The O/C atomic ratio of the raw HTb is 0.836, which is consistent with values typically observed for many other biomass sources, which are within the range of 0.75 to 1.0.^{4, 11} It is clear that increasing the air-carbonisation temperature has the effect of varying the elemental composition of the resulting HTbx carbonaceous matter, and in particular the O/C ratio. The impact of this variation is seen in the elemental compositions of the resulting activated carbons whose C content is in line with the O/C ratio of the HTbx carbons from which they are derived. The C content of activated carbons derived from HTb300 is in the range of 62–70 wt%, which range rises to 75–89 wt% (HTb350), 77–91 wt% (HTb450), and 75–89 wt% (HTb550). Consequently, the content of H and N gradually decreases at higher carbonisation temperatures and/or higher activation levels. Activation of HTbx at any given temperature increases the C content, with a more significant increase observed at higher levels of activation (higher activation temperature or amount of KOH). In this way, the varying O/C ratio of the HTbx carbons provides an opportunity to tailor the porosity and packing density of the resulting carbons, as described in the following sections.

Table 3.1. Elemental composition of the raw Hookah Tobacco biomass (HTb), and yield and elemental composition of air-carbonised Hookah Tobacco (HTbx), and corresponding activated carbons (HTbx-yT).

Sample	Yield [wt%]	C [%]	H [%]	N [%]	O [%]	(O/C) ^a
HTb-biomass	-	43.6	7.5	0.3	48.6	0.836
HTb300	34	62.9	4.6	0.7	31.8	0.379
HTb300-2600	47	65.5	2.3	0.5	31.7	0.363
HTb300-2700	41	66.6	1.1	0.0	32.3	0.364
HTb300-2800	19	69.8	0.4	0.0	29.8	0.320
HTb300-4600	40	66.7	1.5	0.4	31.4	0.353
HTb300-4700	23	61.6	1.3	0.3	36.8	0.448
HTb300-4800	21	62.5	0.5	0.0	37.0	0.444
HTb350	33	66.8	4.7	1.5	27.0	0.303
HTb350-2600	49	74.7	0.4	0.3	24.6	0.247
HTb350-2700	43	83.4	0.6	0.3	15.7	0.141
HTb350-2800	42	82.5	0.8	0.1	16.6	0.151
HTb350-4600	31	76.5	0.4	0.4	22.7	0.223
HTb350-4700	26	84.2	0.3	0.1	15.4	0.137
HTb350-4800	22	89.6	0.2	0.1	10.1	0.085
HTb450	25	70.6	3.8	2.5	23.1	0.245
HTb450-2600	44	81.4	0.5	0.1	18.0	0.166
HTb450-2700	42	86.1	0.4	1.1	12.4	0.108
HTb450-2800	41	91.4	0.0	0.0	8.6	0.071
HTb450-4600	53	76.9	0.3	0.2	22.6	0.220
HTb450-4700	48	88.4	0.1	0.1	11.4	0.097
HTb450-4800	40	89.3	0.0	0.0	10.7	0.090
HTb550	24	69.4	2.6	1.4	26.6	0.287
HTb550-2600	72	74.9	0.8	0.1	24.2	0.242
HTb550-2700	45	84.5	0.1	0.1	15.3	0.136
HTb550-2800	50	88.9	0.1	0.2	10.8	0.091
HTb550-4600	61	80.4	0.5	0.1	19.0	0.177
HTb550-4700	52	84.8	0.0	0.1	15.1	0.133
HTb550-4800	31	81.5	0.0	0.1	18.4	0.169

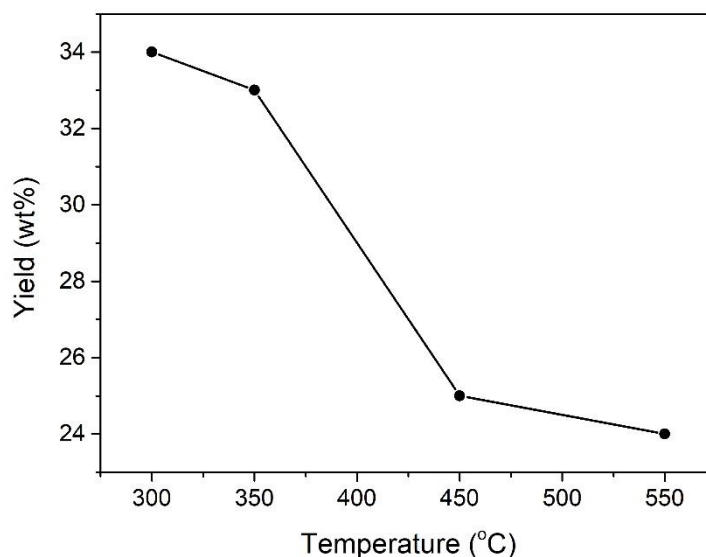


Figure 3.1. Effect of the air-carbonisation temperature of Hookah Tobacco on the yield of the resulting carbonaceous matter.

3.3.2 Structural and morphological characterisation

To evaluate the purity and thermal stability of both the air-carbonised carbonaceous matter and the resulting activated carbons, thermogravimetric analysis (TGA) was conducted under flowing air conditions. The TGA curves for the raw HTb and HTbx carbonaceous matter are shown in **Figure 3.2**. The raw HTb loses ca. 70% of its mass continuously up to 450 °C due to loss of moisture and degradation of the tobacco, followed by a sharp mass loss from carbon combustion that is complete at 500 °C. The observed trend is consistent with previous results on the combustion of tobacco.³² The residual mass from combustion of the raw HTb is 3 - 4 wt%, which is ascribed to ash. The curves of the HTbx carbons indicate thermal stability up to ~ 350 °C, followed by a significant mass loss between 350 °C and 600 °C due to carbon burn off. The residual mass of the HTbx carbons at 800 – 1000 °C varies between 4 and 10 wt% depending on the air-carbonisation temperature with higher values at higher temperature. This suggests that some of the inorganic matter (ash content) in tobacco is retained following the air-carbonisation process, and that the proportion rises especially for carbonisation at 350 to 550 °C. The TGA curves for representative activated carbons shown in **Figure 3.3** indicate a significant mass loss between 450°C and 650 °C due to carbon combustion, along with a minor loss below 120 °C due to moisture removal. The residual mass after heating the samples in air at 1000 °C is typically less than 5%

by weight, indicating the absence of significant amounts of inorganic residues but that the ash in HTbx may be retained during the activation process. Thermal stability of the activated carbons was found to be influenced by the activation temperature, with samples activated at 700 °C having a maximum burn-off temperature of 600 °C compared to up to 650 °C for carbons activated at 800 °C. This demonstrates the impact of activation temperature on thermal stability, with higher activation temperatures resulting in greater thermal stability, in line with previous research.^{10, 11, 33} Interestingly, the TGA curves of activated carbons obtained under the same activation conditions (activation temperature and KOH/HTbx ratio) are nearly identical with similar thermal stability regardless of the differences in the carbonisation temperature of the carbonaceous matter.

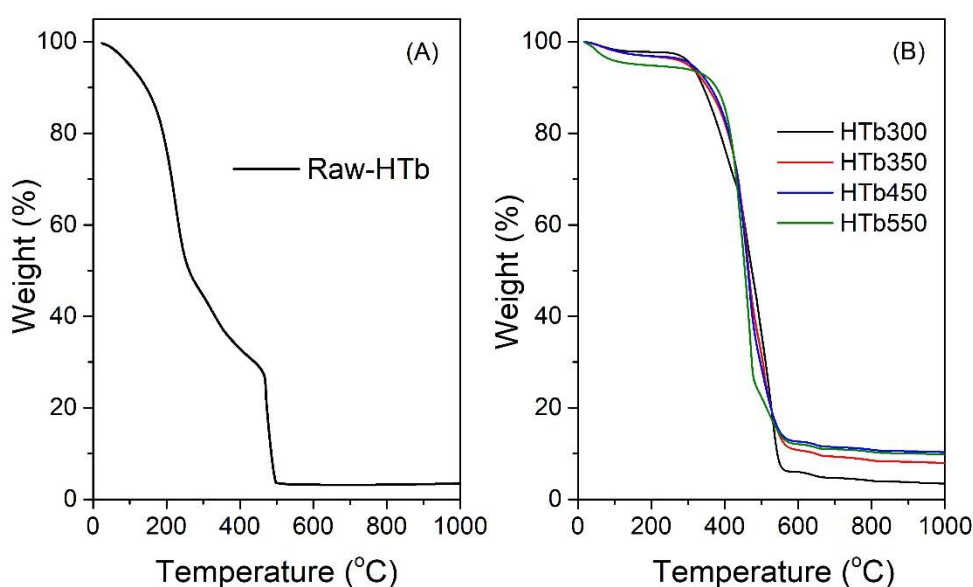


Figure 3.2. Thermogravimetric analysis (TGA) curves of (A) raw-HTb, (B) biomass-derived carbonaceous matter air-carbonised at various temperatures (300, 350, 450 and 550 °C).

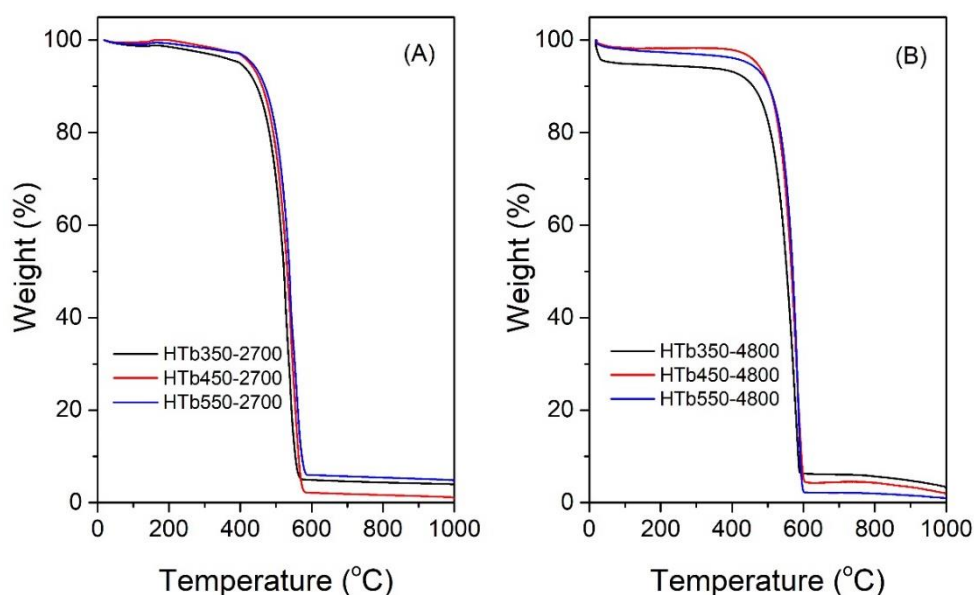


Figure 3.3. Thermogravimetric analysis (TGA) curves of activated carbons derived from Hookah Tobacco-derived carbonaceous matter air-carbonised at various temperatures.

The XRD patterns of HTbx carbons are presented in **Figure 3.4**. The patterns revealed a broad peak at 2-theta of 22° and 44°, corresponding to the positions at which the (002) and (100) diffractions arising from graphene stacks are expected. This suggests that the HTbx carbons have some degree of graphene-like stacking, which is greatly reduced or lost for the activated carbons due to the disruptive nature of the activation process. Interestingly, the carbonisation temperature did not seem to have any significant or consistent effect on the level of graphene stacking observed in the XRD patterns. The XRD analysis of the activated carbons (**Figure 3.5**, **Figure 3.6**, **Figure 3.7** and **Figure 3.8**) revealed a lack of prominent peaks associated with graphene stacking, which is in line with the anticipated effect of activation in disrupting graphitic domains.^{4, 16} However, it is worth noting that the carbon generated from the HTb300 precursor (lower carbonisation temperature) showed some degree of graphene-like stacking, as evidenced by the presence of a prominent peak at a 2-theta of 26.5°. Overall, the XRD patterns of the activated carbons are primarily amorphous, which is typical of KOH activated carbons.^{9, 12, 34}

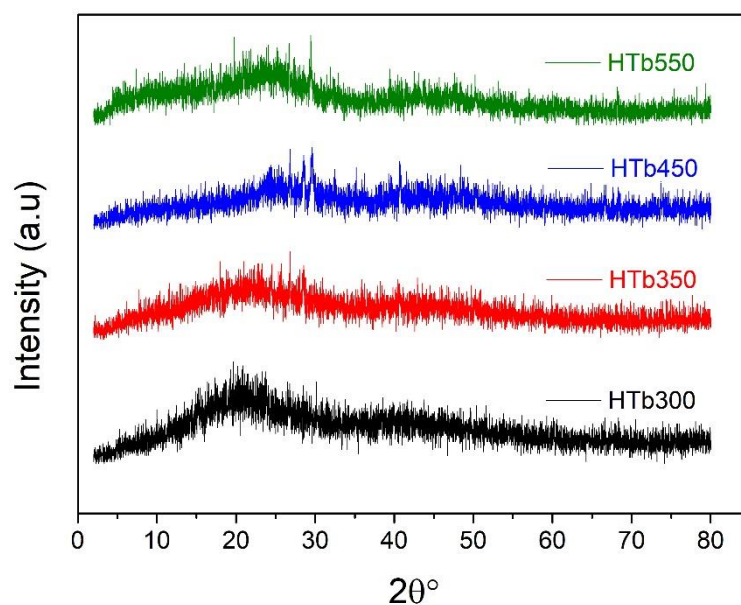


Figure 3.4. XRD pattern of biomass-derived HTBx carbonaceous matter air-carbonised at various temperatures (x = 300, 350, 450 or 550 °C).

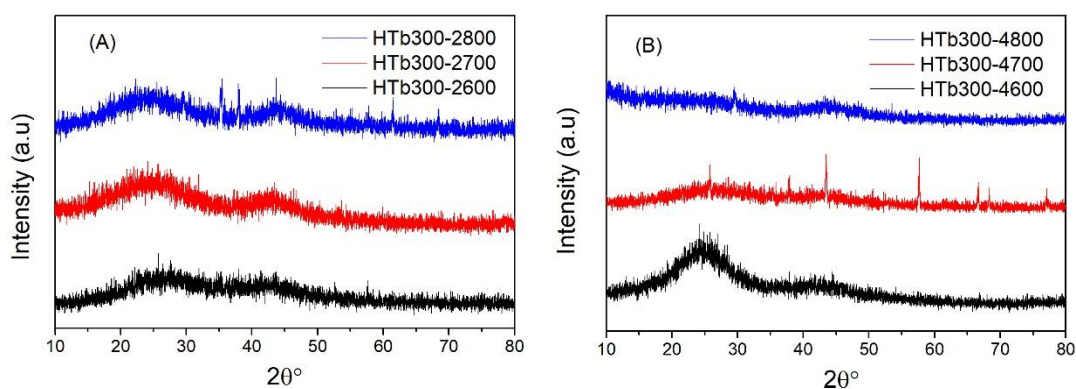


Figure 3.5. XRD patterns of HTb300-derived activated carbons.

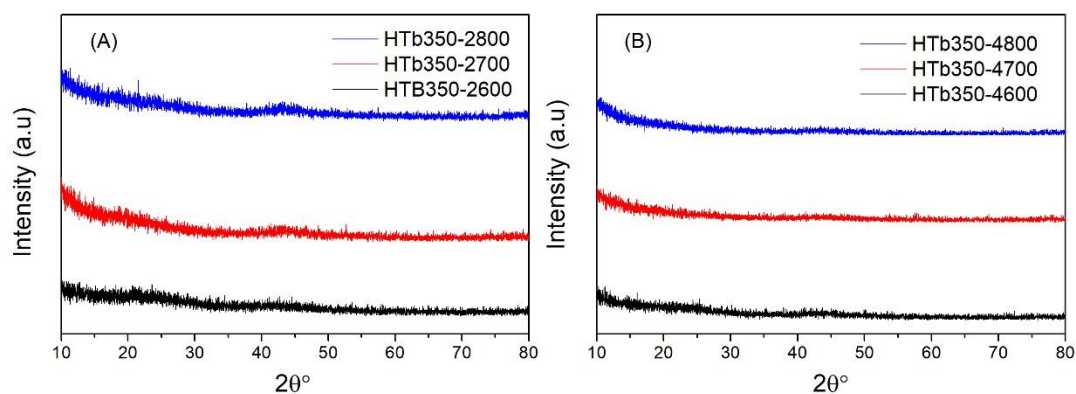


Figure 3.6. XRD patterns of HTb350-derived activated carbons.

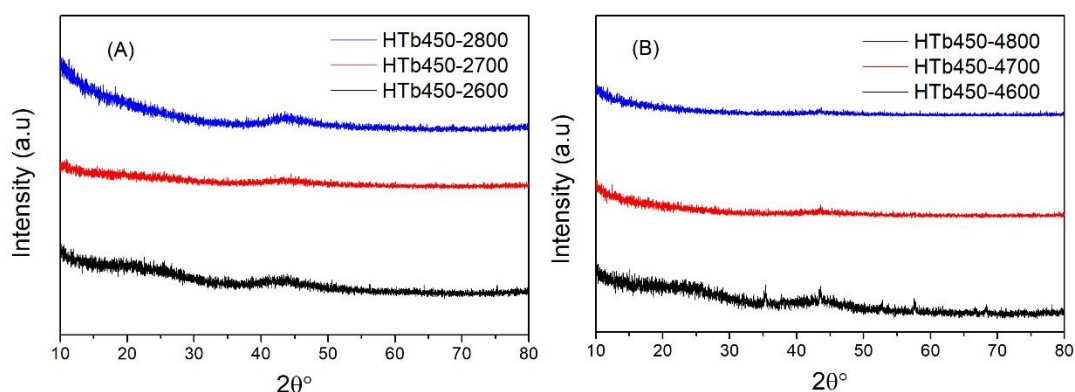


Figure 3.7. XRD patterns of HTb450-derived activated carbons.

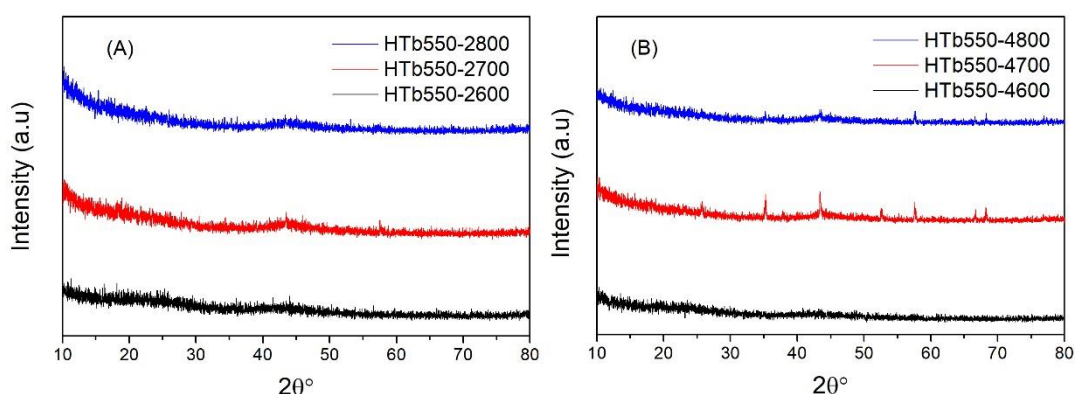
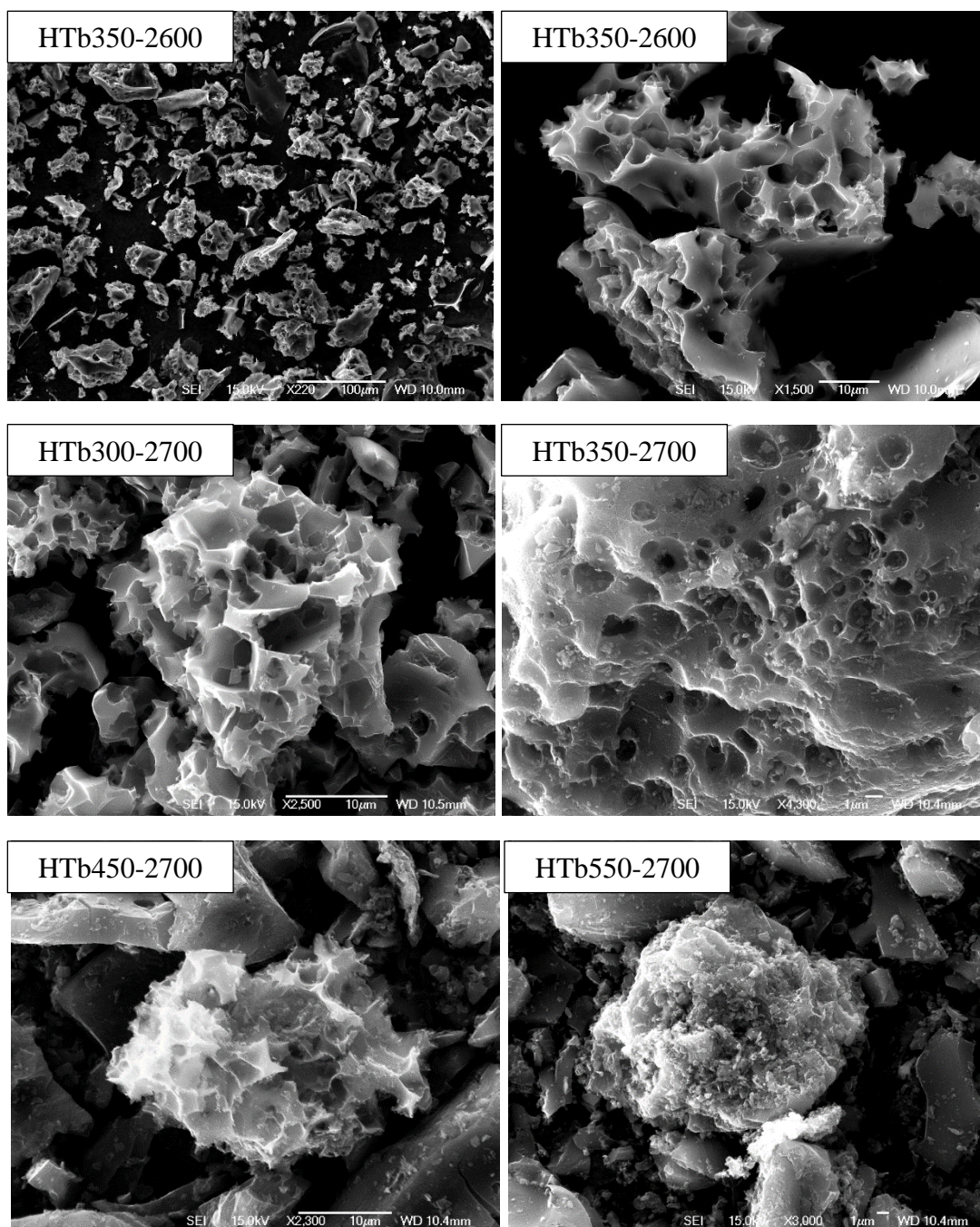


Figure 3.8. XRD patterns of HTb550-derived activated carbons.

To monitor morphology changes and the effect of carbonisation temperatures on activated carbons, scanning electron microscopy (SEM) and transmission electron microscopy (TEM) analysis were performed. The resulting SEM and TEM images of representative activated carbons are presented in **Figure 3.9** and **Figure 3.10**. According to the SEM images, the morphology of the activated carbons is characterised by irregularly shaped particles with sharp corners, which is typical of activated carbons.^{4, 6, 15, 35} The carbonisation temperatures and KOH/HTbx ratio appear to have an impact on the morphology of the activated carbons. Activated carbons generated from carbonaceous matter carbonised at low temperatures and/or activated at a low KOH/HTbx ratio of 2 (**Figure 3.9**) exhibit a greater degree of surface roughness, indicating a microporous structure. **Figure 3.10** displays representative TEM images of HTbx-4800 samples. The pore channel geometry and connectivity are

similar for all four samples, indicating a highly porous material. The TEM images reveal that sample HTb450-4800 has larger pores than HTb300-4800, which is consistent with the fact that the former was prepared at a higher carbonisation temperature and achieved a higher level of activation, which should generate larger pores.



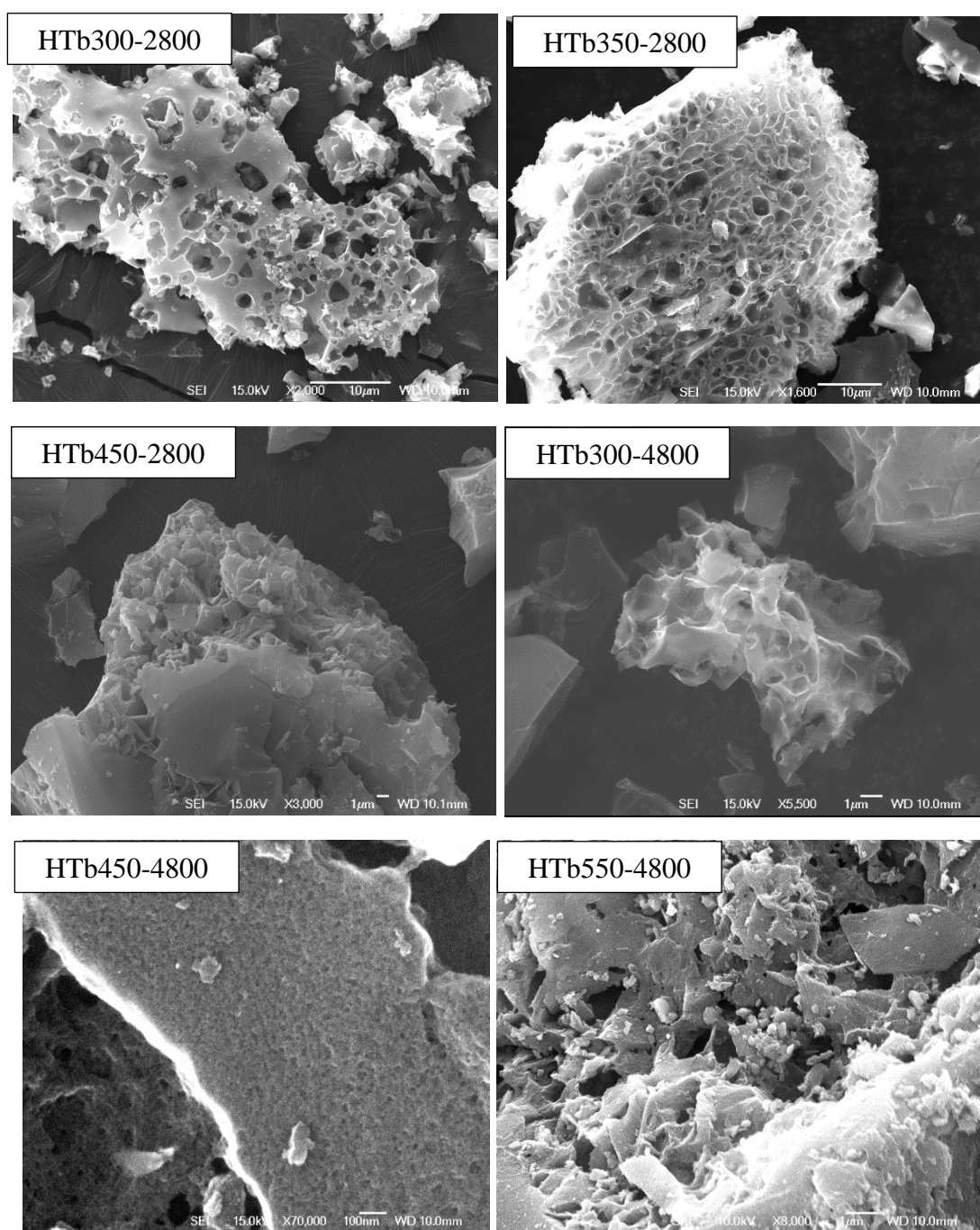


Figure 3.9. SEM images of HTbx-yT activated carbons derived from Hookah Tobacco following flash air-carbonisation and activation with KOH; x = air carbonisation temperature, y = KOH/HTbx carbon ratio, and T is activation temperature.

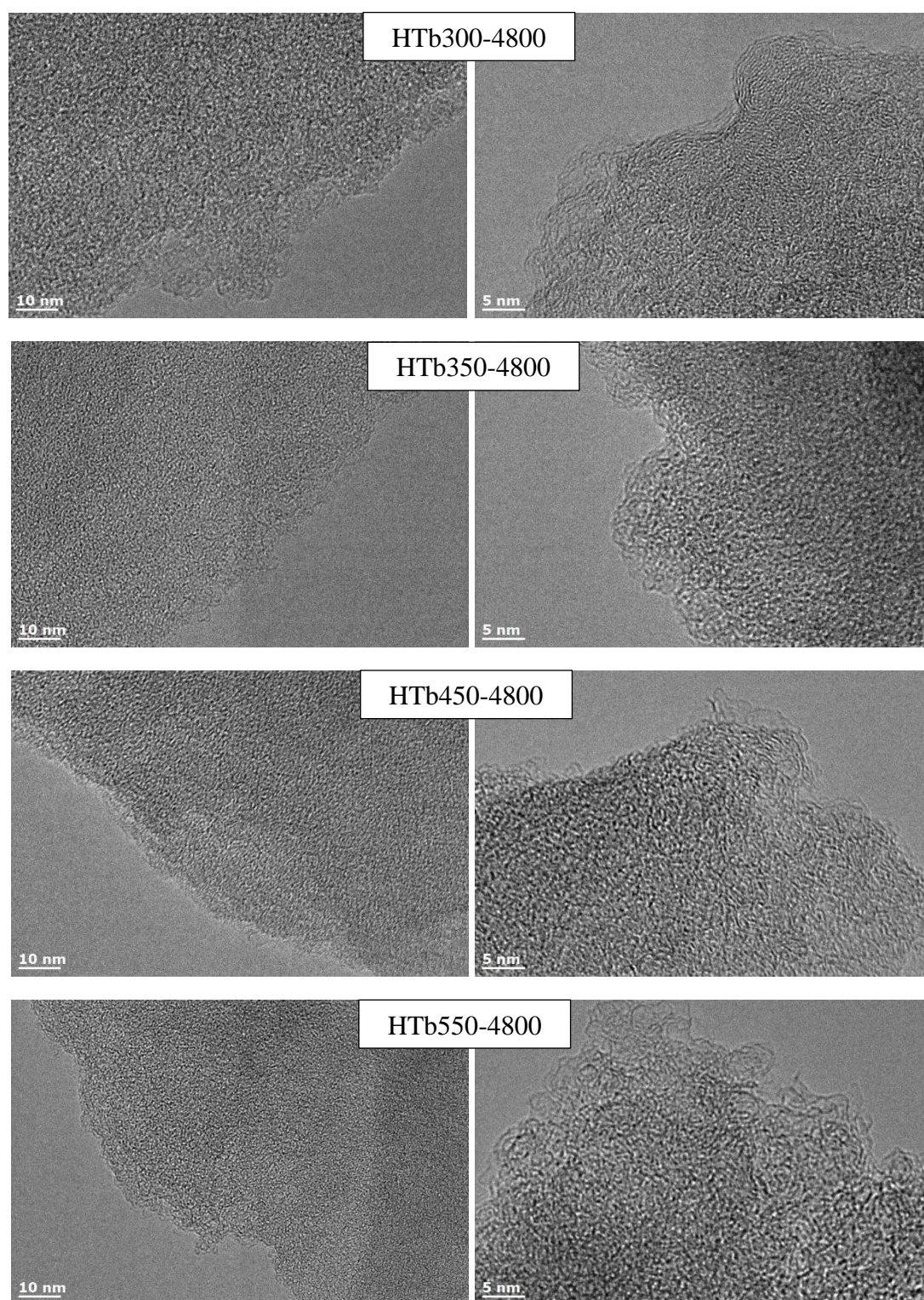


Figure 3.10. TEM images of HTbx-derived activated carbons activated at KOH/HTbx ratio of 4 and at 800 °C.

3.3.3 Porosity and textural properties

The nitrogen sorption isotherms and the pore size distribution (PSD) curves of the activated carbons are displayed in **Figure 3.11**, **Figure 3.12**, **Figure 3.13** and **Figure 3.14**. The isotherms are fully or predominantly type 1, which implies that most of the carbons are primarily microporous; the activated carbons have a high amount of nitrogen adsorbed at $P/P_0 < 0.1$, suggesting significant levels of microporosity. However, as the air-carbonisation temperature increases, the slope of the adsorption knee region (at relative pressure, P/P_0 , between 0.1 – 0.3) increases very slightly in some cases and becomes broader indicating the formation of somewhat larger pores.³⁶

³⁷ The quantity of nitrogen adsorbed, which is an indicator of the level of porosity generated, varies based on the (i) air-carbonisation temperature of the HTbx precursor (ii) amount of KOH used, i.e., KOH/HTbx ratio (2 or 4), and (iii) activation temperature. For any given activation conditions (KOH/HTbx ratio and temperature), the nitrogen sorption isotherms in most cases indicate a greater level of porosity for activated carbons derived from HTbx carbons air-carbonised at higher temperature. As the carbonisation temperature and/or activation severity increased (i.e., higher amounts of KOH and activation temperature), the quantity of nitrogen adsorbed by the activated carbons always increased. It is noteworthy, however, that HTb300-derived activated carbons (**Figure 3.11**), with the exception of HTb300-4800, exhibit little variation in the shape of their isotherms, which are characterised by a sharp adsorption knee at a very low relative pressure ($P/P_0 \sim 0.01$). This indicates the presence of a significant proportion of microporosity and the absence of pores larger than the micropore range (up to 20 Å). The exception, sample HTb300-4800, was obtained under more severe activation conditions, and exhibited much higher nitrogen adsorption with a broadening in the knee, indicating the presence of some larger micropores and some degree of mesoporosity. Upon increasing the carbonisation temperature to 350 °C, the HTb350-derived activated carbons, show an increase in the amount of nitrogen adsorbed with relatively sharp adsorption knee maintained at all activation conditions. A similar trend is observed for the isotherms of activated carbons derived from HTb450 and HTb550 (**Figure 3.13** and **Figure 3.14**) but with higher amounts of nitrogen adsorbed. At KOH/HTbx ratio of 2, HTb450 and HTb550 derived carbons still retain high microporosity but the pores are wider compared to those of HTb300 or HTb350 derived samples. At KOH/HTbx ratio of 4, HTb450 and

HTb550 derived carbons display significant mesoporous development, which is evident from the broadening of the knee in the isotherms and the high amount of nitrogen adsorption.

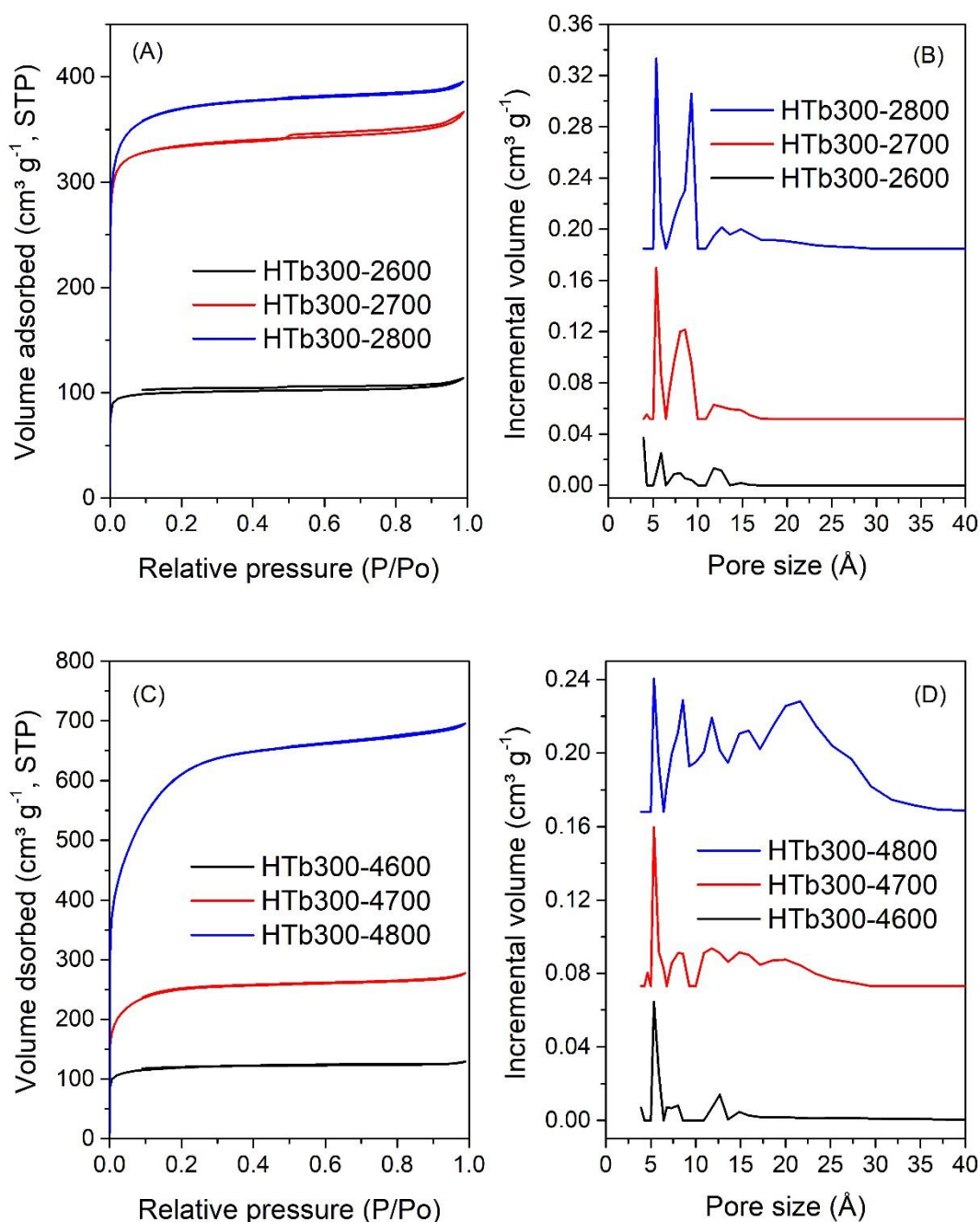


Figure 3.11. Nitrogen sorption isotherms (A, C) and corresponding pore size distribution curves (B, D) of HTb300-derived activated carbons.

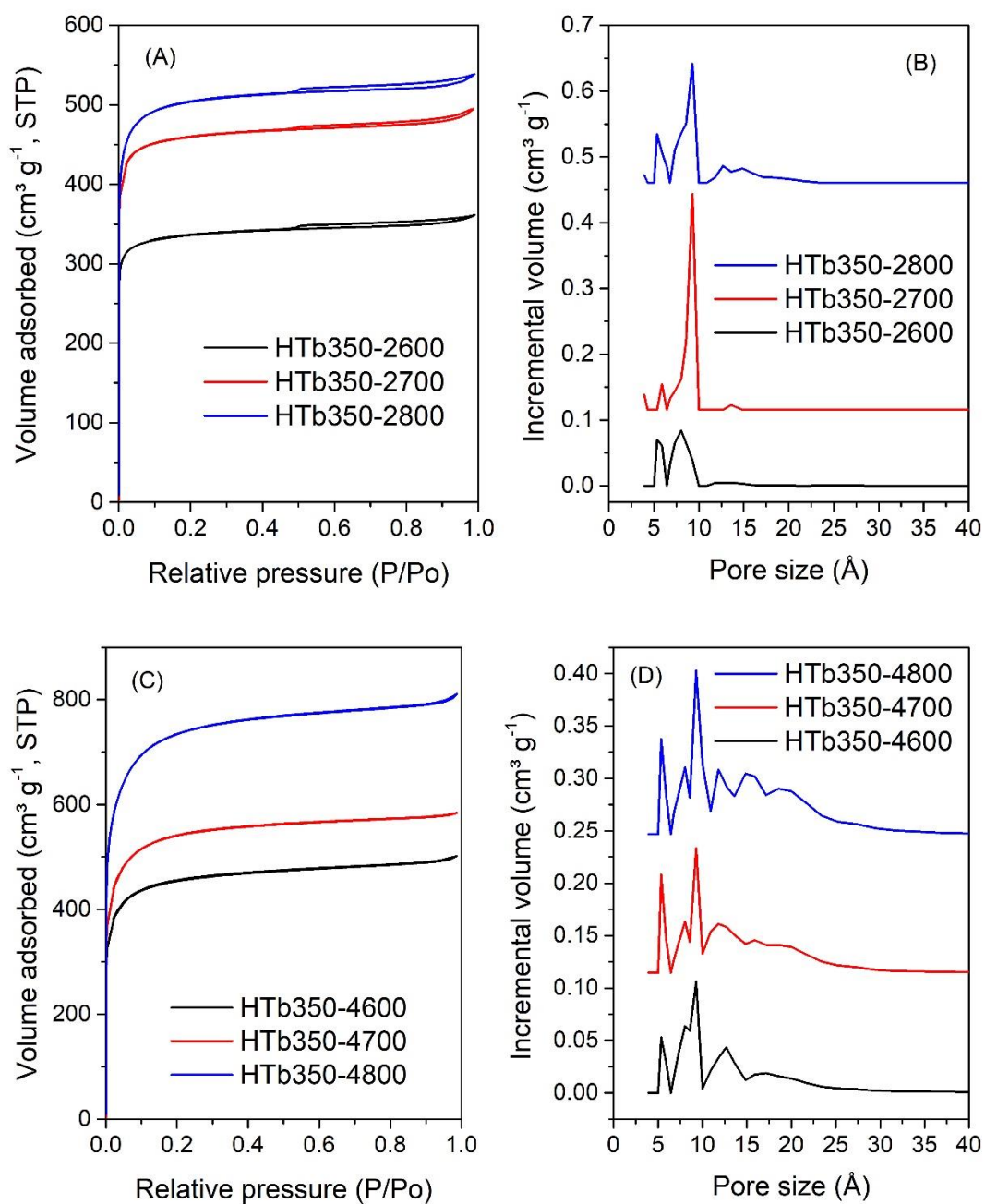


Figure 3.12. Nitrogen sorption isotherms (A, C) and corresponding pore size distribution curves (B, D) of HTb350-derived activated carbons.

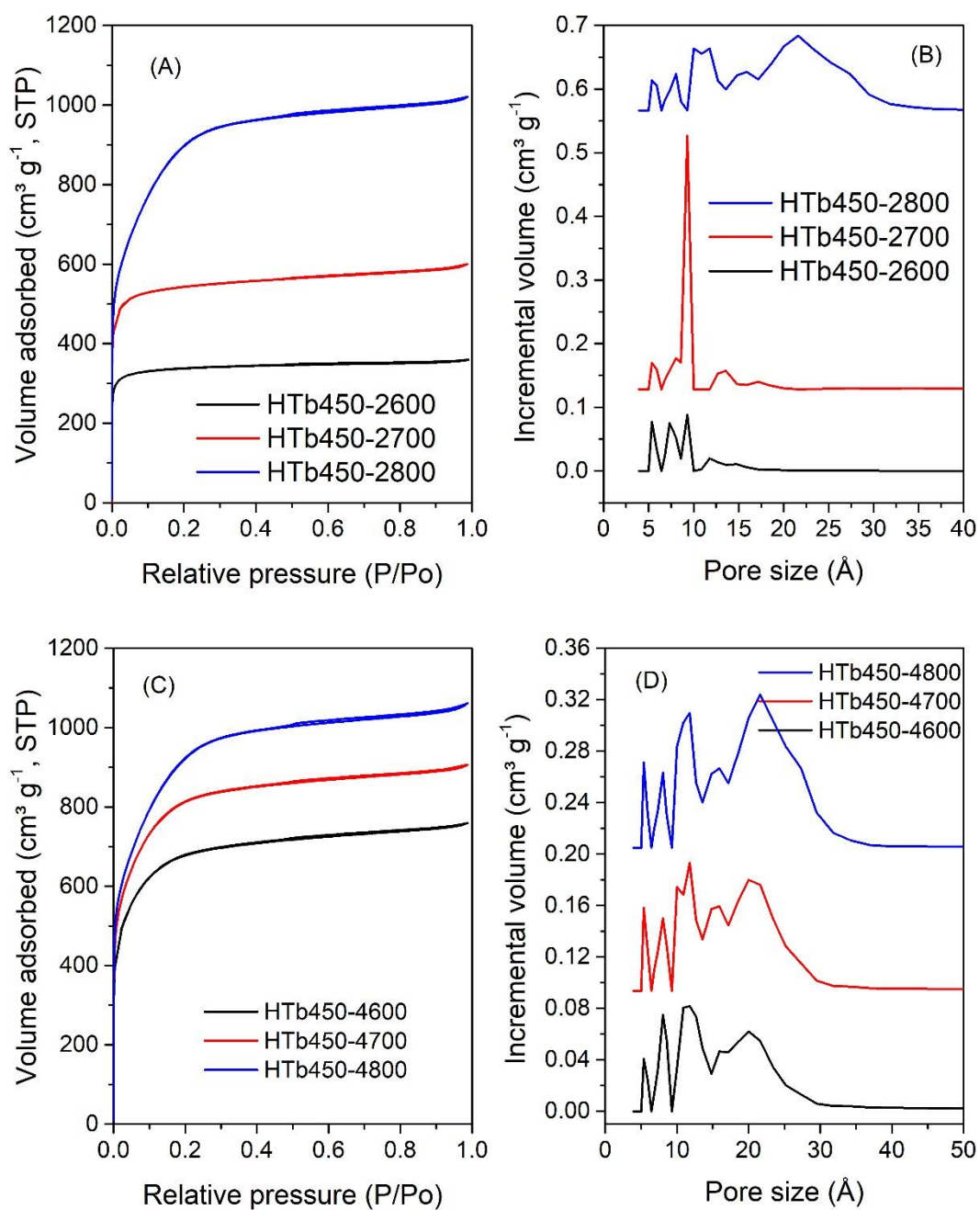


Figure 3.13. Nitrogen sorption isotherms (A, C) and corresponding pore size distribution curves (B, D) of HTb450-derived activated carbons.

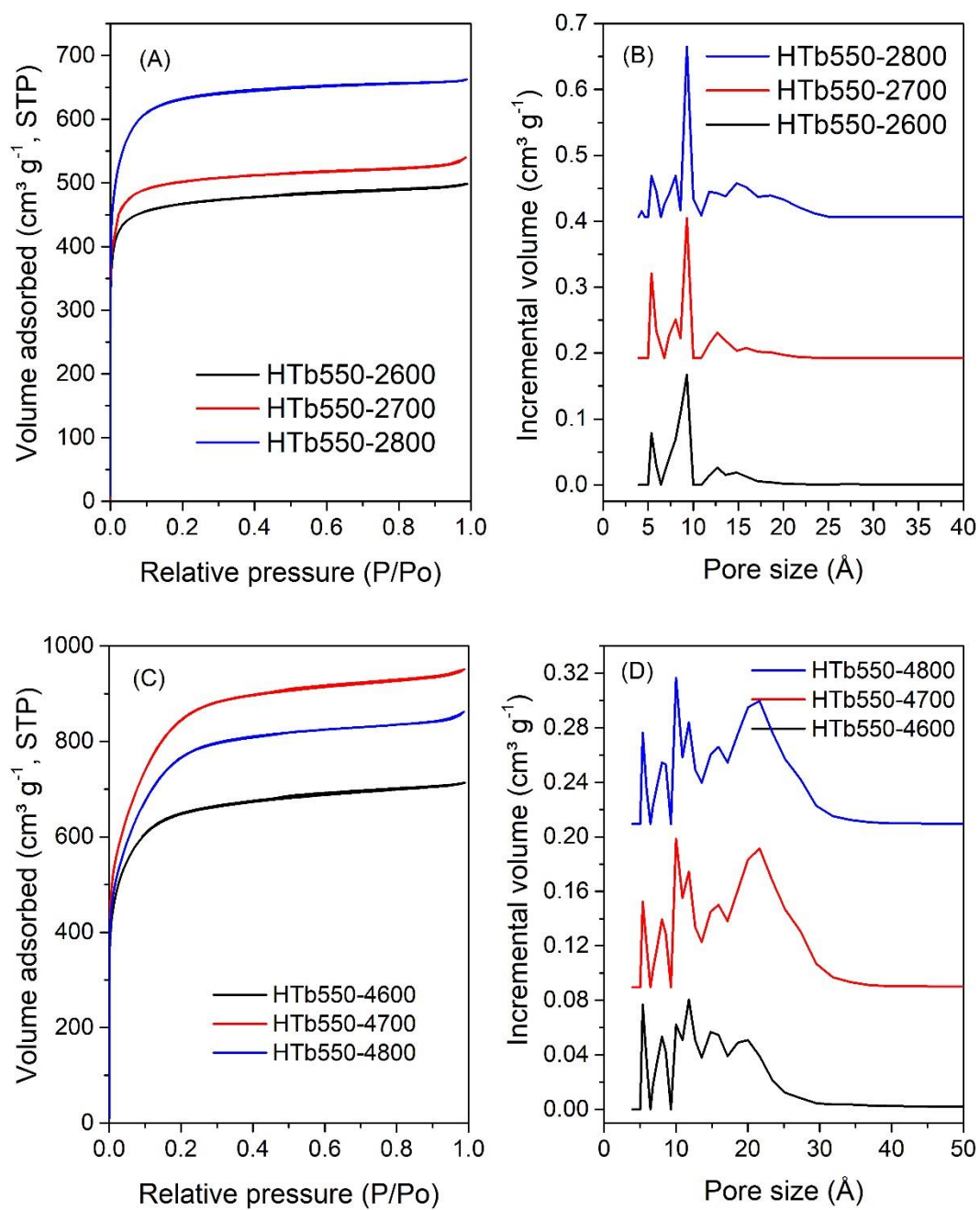


Figure 3.14. Nitrogen sorption isotherms (A, C) and corresponding pore size distribution curves (B, D) of HTb550-derived activated carbons.

Pore size distribution (PSD) curves provide further insight into the pore size of the activated carbons as shown in **Figure 3.11**, **Figure 3.12**, **Figure 3.13** and **Figure 3.14**. The pore size distribution of the activated carbons shifts towards larger pore sizes with increase in the air-carbonisation temperature and/or activation severity. Specifically, the PSD curves for HTb300-activated carbons (**Figure 3.11B** and **D**) exhibit a sharp peak centered at ~ 5 Å, indicating the presence of ultramicropores. Upon increasing the activation temperature for samples HTb300-2T (from 600 to 800 °C), a second peak is observed at ~ 9 Å following by collapsing in the wider pore for samples HTb300-4T with broader peaks ranging from 10 to 30 Å at higher severity activation. Increasing the carbonisation temperature to 350 °C, cause a peak to appear in other position in the PSD curves at ~ 9 Å, indicating the presence of supermicroporous features, which further broadening up to 20 Å at higher activation conditions (**Figure 3.12B** and **D**). The HTb450 and HTb550 activated carbons (**Figure 3.13** and **Figure 3.14**, **B** and **D**) exhibit a much broader PSD curve, with two distinct peaks centered at ~ 9 Å and ~ 30 Å, depending on the severity of the activation indicating the presence of both micropores and mesopores.

Table 3.2 presents the textural properties of HTbx-derived activated carbons. In general, the textural properties of the resulting activated carbons are strongly influenced by the carbonisation temperature. The total surface area and total pore volume typically increase with rising carbonisation temperature to a maximum at 450 °C and then slightly decrease for activated carbons produced from HTb550. Sample HTb450-4800 has the highest surface area and pore volume of $3413 \text{ m}^2 \text{ g}^{-1}$ and $1.65 \text{ cm}^3 \text{ g}^{-1}$, respectively. The surface area of the HTb300-yT series of sample (derived from HTb300), was found to range from 402 to $2253 \text{ m}^2 \text{ g}^{-1}$, which range increased to 1338 to $2799 \text{ m}^2 \text{ g}^{-1}$ for the HTb350-yT series carbons. The surface area of the HTb450-yT series carbons varied between 1320 and $3413 \text{ m}^2 \text{ g}^{-1}$, while for HTb 550-yT series carbons the surface area range was 1805 to $3123 \text{ m}^2 \text{ g}^{-1}$. Thus as the carbonisation temperature rises, the highest surface area attained by the activated carbons increased from $2253 \text{ m}^2 \text{ g}^{-1}$ for the HTb300-yT series to $3413 \text{ m}^2 \text{ g}^{-1}$ for the HTb450-yT series before a slightly decreasing to $3123 \text{ m}^2 \text{ g}^{-1}$, for the HTb550-yT series carbons. **Figure 3.15** illustrates the influence of carbonisation temperatures on the surface area of activated carbon that were prepared under similar conditions. As the carbonisation temperature increases, the surface area generally rises; for example,

for samples activated at KOH/HTbx ratio of 2 and 800 °C, the trend is HTb300-2800 ($1424 \text{ m}^2 \text{ g}^{-1}$) < HTb350-2800 ($1957 \text{ m}^2 \text{ g}^{-1}$) < HTb450-2800 ($3318 \text{ m}^2 \text{ g}^{-1}$). However, for the HTb550-derived sample, there is a slight decrease in surface area for HTb550-2800 to $2439 \text{ m}^2 \text{ g}^{-1}$. As stated above, a similar trend is evident activation at at KOH/HTbx ratio of 4 and 800 °C, i.e., HTb300-4800 ($2253 \text{ m}^2 \text{ g}^{-1}$) < HTb350-4800 ($2799 \text{ m}^2 \text{ g}^{-1}$) < HTb450-4800 ($3413 \text{ m}^2 \text{ g}^{-1}$) > HTb550-4800 ($2855 \text{ m}^2 \text{ g}^{-1}$), as depicted on **Table 3.2**. This trend may be attributed to the effect of a combination of factors including the O/C ratio and ash content of the HTbx precursors. The O/C ratio is inversely proportional to the ease of activation of the HTbx precursors, while the amount of ash acts in a converse manner. Indeed the ash in the HTbx precursors may contain metal residues that may also act as activators.³⁸

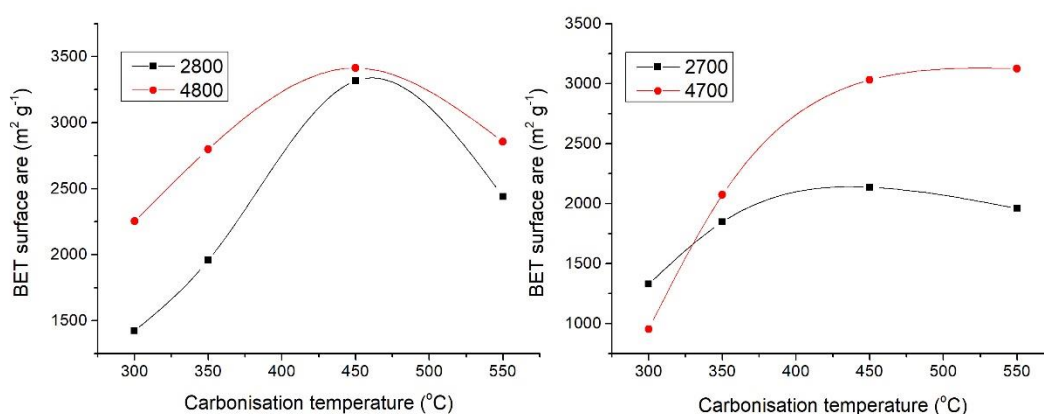


Figure 3.15. The effect of carbonisation temperature on surface area for activated carbons prepared under similar activation conditions.

The trend of pore volume of the activated carbons is also related to the carbonisation temperature. The HTb300-yT series has pore volume in the range of 0.18 to $1.08 \text{ cm}^3 \text{ g}^{-1}$, which range increases to 0.56 to $1.26 \text{ cm}^3 \text{ g}^{-1}$ for the HTb350-yT series, while HTb450-yT series shows an even higher range of 0.56 to $1.65 \text{ cm}^3 \text{ g}^{-1}$. In line with trends in surface area, a slight decrease in pore volume is observed for the HTb550-yT series with pore volume in the range of 0.77 to $1.48 \text{ cm}^3 \text{ g}^{-1}$. Thus, in line with the trend in surface area, the pore volume generally increases with carbonisation temperature. Specifically, the pore volume of samples activated under similar conditions significantly varies depending on carbonisation temperature, which emphasises the role of the later (carbonisation temperature) in modulating the textural

properties of the activated carbons. For example, the pore volume of HTb300-2800 is $0.61 \text{ cm}^3 \text{ g}^{-1}$, while for HTb550-2800 it is $1.03 \text{ cm}^3 \text{ g}^{-1}$. Regarding the nature of porosity generated, it is noteworthy that activated carbons prepared at KOH/HTbx ratio of 2 exhibit a significant proportion of micropore surface area and pore volume, notwithstanding the increase in overall surface area resulting from the rise in carbonisation temperature. For example, for HTb300-2T samples, ca. 90% of the surface area and 80% of the pore volume arise from micropores. This decreases for HTb300-4T samples to 45 – 85% of the surface area and 36 – 75% of the pore volume arising from micropores. Similarly, HTb350-2T samples have a high proportion of micropore surface area at 90%, with the micropore pore volume ranging between 84% and 90%. Overall, the HTb350-2T samples maintain high levels of micropore surface area and pore volume, with values of 74 – 80% and 71 – 64%, respectively, even at the severest activation conditions. Indeed, more generally, for activation at a KOH/HTbx ratio of 2, the percentage of surface area and pore volume arising from micropores is high at ca. 85 – 90% for surface area and 77 – 82% for pore volume. However, with increase in amount of KOH used (KOH/HTbx ratio of 4), and especially at higher activation temperature, the activated carbons also show some mesoporosity, resulting in a decrease in the proportion of microporosity. In this way the overall proportion of microporosity is lower; 28 – 60% for micropore surface area and 20 – 51% for micropore volume for HTb450-4T samples, and 38 – 69% and 30 – 60%, respectively for HTb550-4T samples.

The foregoing discussion highlights the significant impact of carbonisation temperature on the textural properties of activated carbons derived from HTbx. Overall, the porosity analysis indicates that the textural properties are dependent on both the carbonisation temperature of the precursor and the activation conditions. Increasing the carbonisation temperature and severity of activation generates carbons with higher overall porosity, with a varying mix of microporosity and mesoporosity. The observed trend is consistent with previous studies on the effect of carbonisation temperature on the porosity and textural properties of activated carbons derived from various biomass sources.^{18-20, 36, 39}

Table 3.2. Textural properties of HTbx-derived activated carbons (x = carbonisation temperature). The values in parenthesis are the percentage of surface area or pore volume arising from micropores.

Sample	BET surface area $\text{m}^2 \text{g}^{-1}$		Pore Volume $\text{cm}^3 \text{g}^{-1}$		Surface area density ($\text{m}^2 \text{cm}^{-3}$)
	Total	Micro	Total	Micro	
HTb300-2600	402	375 (93)	0.18	0.14 (78)	2233
HTb300-2700	1330	1221 (92)	0.57	0.47 (83)	2333
HTb300-2800	1424	1233 (87)	0.61	0.49 (80)	2334
HTb300-4600	460	389 (85)	0.20	0.15 (75)	2300
HTb300-4700	953	708 (74)	0.43	0.28 (65)	2216
HTb300-4800	2253	1008 (45)	1.08	0.39 (36)	2086
HTb350-2600	1338	1220 (91)	0.56	0.47 (84)	2389
HTb350-2700	1847	1692 (92)	0.77	0.65 (84)	2399
HTb350-2800	1957	1747 (89)	0.84	0.69 (82)	2330
HTb350-4600	1742	1387 (80)	0.78	0.55 (71)	2233
HTb350-4700	2073	1588 (77)	0.91	0.62 (67)	2278
HTb350-4800	2799	2066 (74)	1.26	0.81 (64)	2221
HTb450-2600	1320	1185 (90)	0.56	0.46 (82)	2338
HTb450-2700	2137	1862 (87)	0.93	0.72 (77)	2298
HTb450-2800	3318	940 (28)	1.58	0.33 (21)	2100
HTb450-4600	2530	1518 (60)	1.18	0.60 (51)	2144
HTb450-4700	3031	1633 (54)	1.41	0.63 (45)	2150
HTb450-4800	3413	960 (28)	1.65	0.33 (20)	2069
HTb550-2600	1805	1589 (88)	0.77	0.63 (82)	2344
HTb550-2700	1960	1744 (89)	0.84	0.68 (81)	2333
HTb550-2800	2439	2069 (85)	1.03	0.82 (80)	2368
HTb550-4600	2458	1685 (69)	1.11	0.66 (60)	2214
HTb550-4700	3123	1198 (38)	1.48	0.45 (30)	2110
HTb550-4800	2855	1160 (41)	1.34	0.43 (32)	2131

Previous studies have found that the surface area density (SAD) of activated carbons, which is the ratio of total surface area to total pore volume, correlates with the balance between microporosity and mesoporosity, with the former favouring high SAD values. The SAD may in turn be used to predict the packing density of activated carbons.^{9, 11, 16} As can be seen from **Table 3.2** the SAD of the present carbons is within a narrow range of 2086–2399 m² cm⁻³, and generally higher than that reported for most activated carbons.^{6, 15, 33, 35, 40} Specifically, the SAD range of the HTb300-yT series is between 2086 and 2334 m² cm⁻³, while that of HTb350-yT series is between 2221 and 2399 m² cm⁻³. The SAD range of the HTb450-yT series is between 2069 and 2338 m² cm⁻³, and that of HTb550-yT series is between 2110 and 2344 m² cm⁻³. Given their high SAD, these carbons are expected to have a high packing density. To get more insight, the packing density was measured for activated carbons obtained under similar activation conditions (KOH/HTbx ratio and activation temperatures) but generated at varying carbonisation temperatures. To facilitate an interesting comparison, only samples with high overall surface area (i.e., HTbx2800 and HTbx4800 carbons) that may be suitable for methane storage were considered for further investigation

3.3.4 Gas uptake measurements

To further study the effect of air-carbonisation temperatures on the pore development, surface area and packing density of the resulting activated carbons, their performance was explored for CO₂ uptake and methane storage.

3.3.4.1 CO₂ uptake

The CO₂ uptake isotherms of the HTbx-yT samples are shown in **Figure 3.16**, **Figure 3.17**, **Figure 3.18**, **Figure 3.19**, and **Table 3.3** summarises the uptake capacity at 0.15 bar, 1 bar and 20 bar. The CO₂ uptake at 0.15 bar is a critical measure of likely performance for capturing CO₂ from post-combustion flue gas streams from fossil fuel power stations, which typically contain ca. 15% CO₂, along with N₂ (70-75%) and water (5-7%). In general, the CO₂ uptake isotherms of HTbx-2T carbons demonstrate saturation at 20 bar, while HTbx-4T samples show no sign of saturation at 20 bar, suggesting they have the potential for higher storage capacity at higher pressures. As

discussed above, the porosity of HTbx-2T carbons is primarily characterised by micropores, while the HTbx-4T samples have larger micropores and small mesopores of size up to ca. 30 Å depending on the carbonisation temperature of the precursor from which they are derived. Analysis of the porosity data and CO₂ uptake indicates that the CO₂ uptake at low pressures (0.15 and 1 bar) is largely influenced by pore size, rather than total surface area. The uptake data confirms that activated carbons with narrow micropores are more effective at creating strong interactions between CO₂ molecules and the adsorbents, resulting in higher uptake compared to those with larger micropores and mesopores.^{1, 7, 41} The CO₂ uptake of HTbx-2T carbons at 1 bar varies between 3.1 and 4.9 mmol g⁻¹ for HTb300-2T, is in the range of 4.8 – 5.2 mmol g⁻¹ for HTb350-2T, 3.5 to 4.9 mmol g⁻¹ for HTb450-2T, and between 4.2 and 4.7 mmol g⁻¹ for HTb550-2T. It is clear that the CO₂ uptake at 1 bar is affected by the carbonisation temperatures of the carbonaceous matter (HTbx), i.e., for samples activated under the same activation conditions (amount of KOH and temperature) but generated from carbonaceous matter carbonised at different temperatures, the CO₂ uptake at 1 bar varies. The CO₂ uptake at 1 bar for the sample obtained at the lowest carbonisation temperature (HTb300-2700) is 4.9 mmol g⁻¹, which increases to 5.2 mmol g⁻¹ upon increasing the carbonisation temperature (HTb350-2700). Further increases in carbonisation temperature result in a slight decrease in the uptake to 5.0 mmol g⁻¹ for HTb450-2700 and 4.6 mmol g⁻¹ for HTb550-2700. These findings show that since the porosity of the carbons is largely influenced by the carbonisation temperature, the later can be used as a tool to enhance the CO₂ uptake. The uptake of 5.2 mmol g⁻¹ at 1 bar and 25 °C for HTb350-2700 is amongst the highest ever reported for activated carbons.^{10, 16, 21, 42-57} Interestingly, the uptake of HTb350-yT samples for any given activation conditions is the highest suggesting that carbonisation at 350 °C is conducive for targeting high performance for low pressure CO₂ uptake. It is clear to see that the enhanced performance of the HTb350-yT samples is due to their high proportion of microporosity as shown in **Table 3.2**. Overall, the activated carbons described in this chapter demonstrate exceptional performance in terms of gravimetric CO₂ uptake at 1 bar and 25 °C, which is comparable or even superior to that of the current standard porous carbons.^{10, 16, 21, 42-57} However, the HTbx-derived carbons have the added advantage of being produced at a lower and milder carbonisation temperature, and using a low cost precursor (waste tobacco), which adds to their attraction with respect to being environmentally friendly.

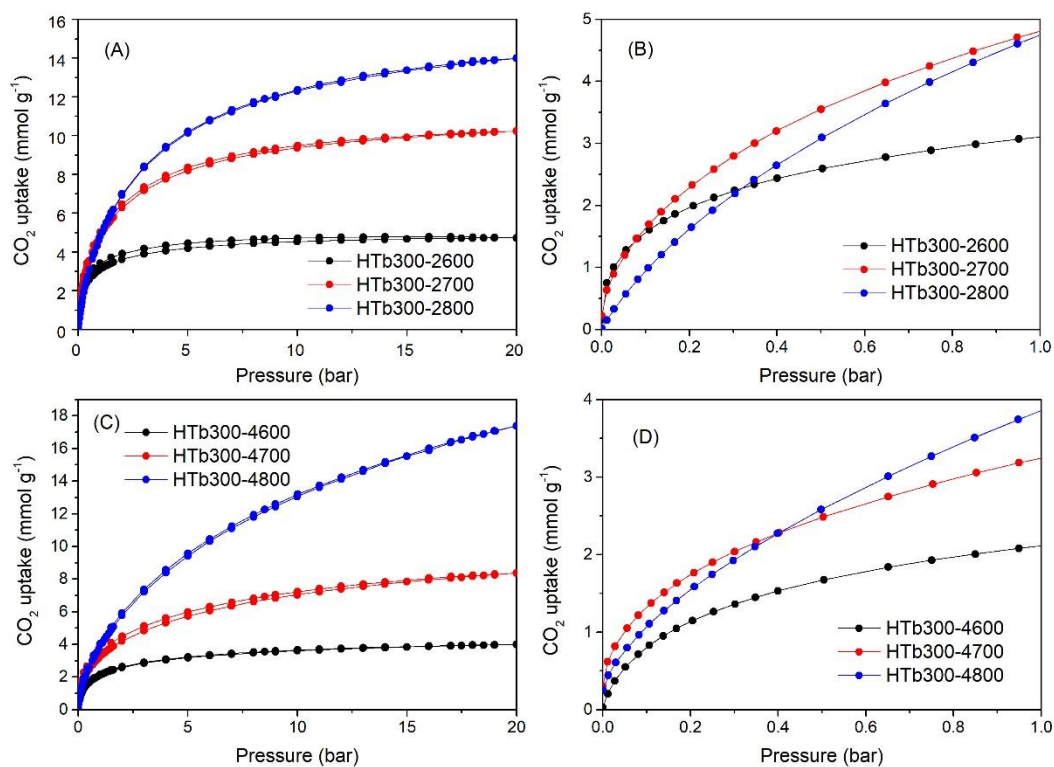


Figure 3.16. CO₂ uptake isotherms at 25 °C of HTb300-derived activated carbons prepared at KOH/HTb300 ratio of 2 (A and B) or 4 (C and D).

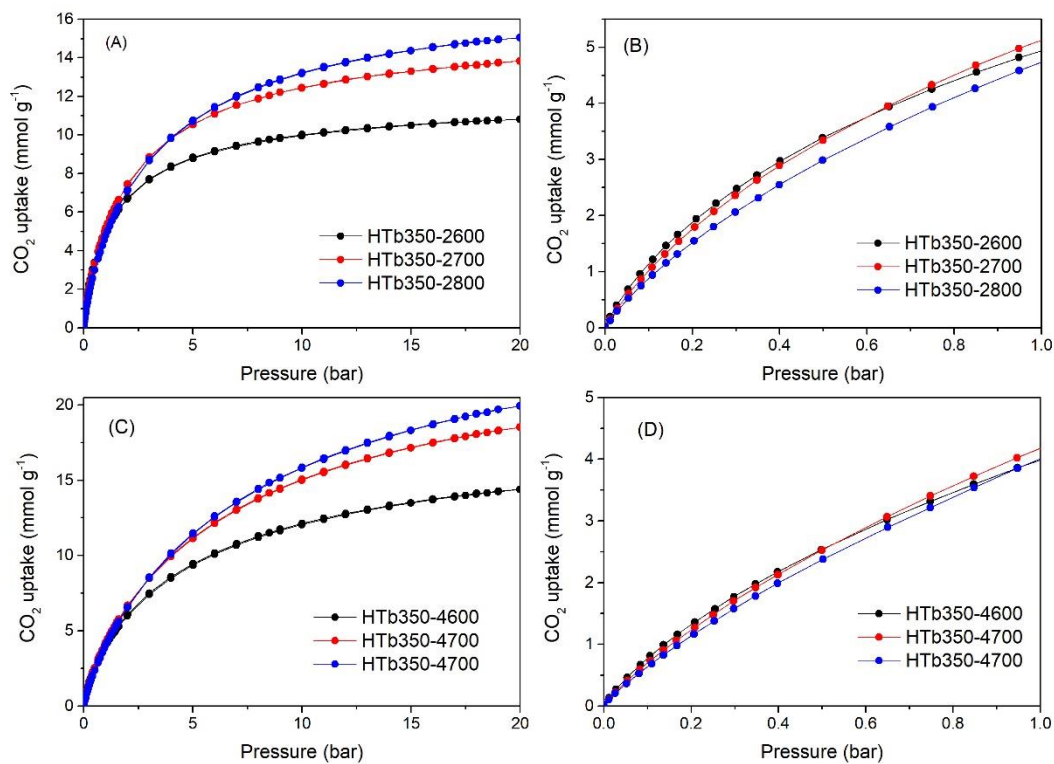


Figure 3.17. CO₂ uptake isotherms at 25 °C of HTb350-derived activated carbons prepared at KOH/HTb350 ratio of 2 (A and B) or 4 (C and D).

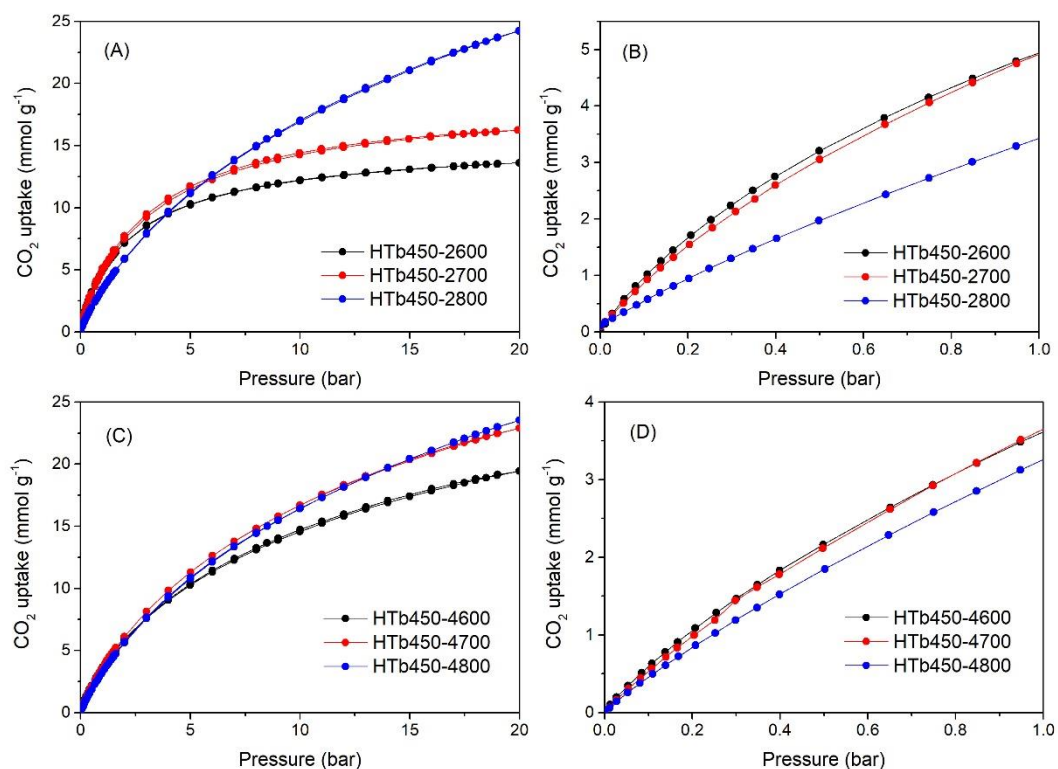


Figure 3.18. CO₂ uptake isotherms at 25 °C of HTb450-derived activated carbons prepared at KOH/HTb450 ratio of 2 (A and B) or 4 (C and D).

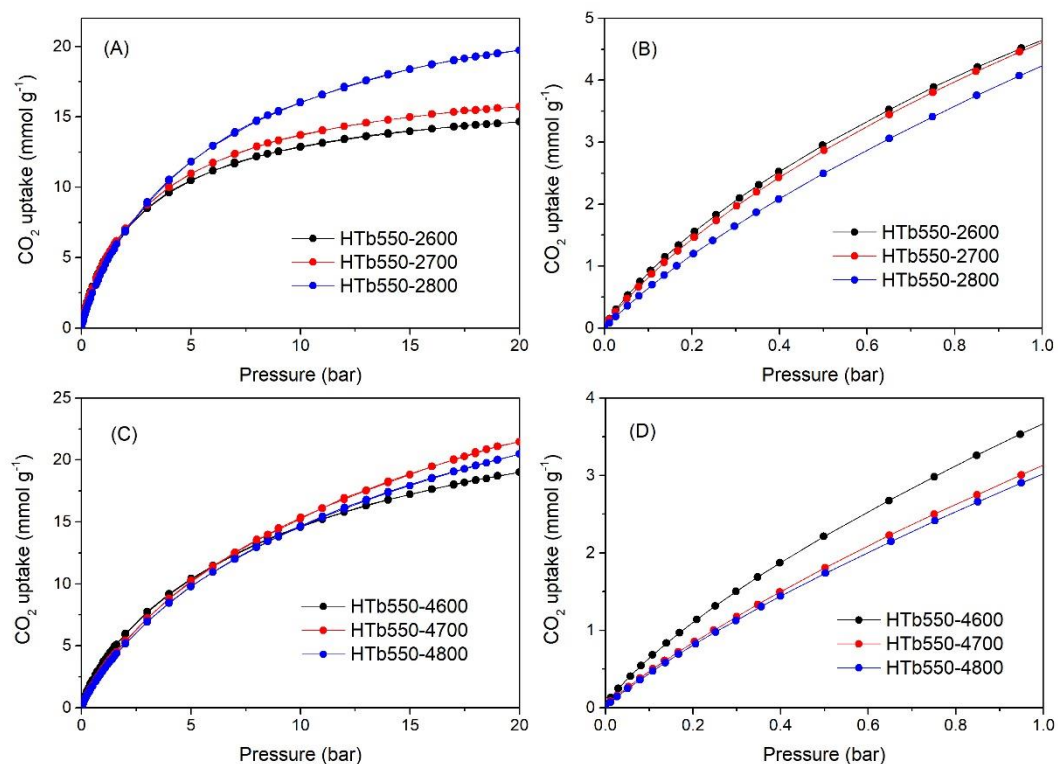


Figure 3.19. CO₂ uptake isotherms at 25 °C of HTb550-derived activated carbons prepared at KOH/HTb550 ratio of 2 (A and B) or 4 (C and D).

Table 3.3. CO₂ uptake isotherms at 25 °C of HTbx-derived activated carbons.

Sample	CO ₂ uptake (mmol g ⁻¹)		
	0.15 bar	1 bar	20 bar
HTb300-2600	1.8	3.1	4.7
HTb300-2700	2.0	4.9	10.2
HTb300-2800	1.3	4.8	13.9
HTb300-4600	1.0	2.1	4.0
HTb300-4700	1.6	3.3	8.4
HTb300-4800	1.3	3.9	17.4
HTb350-2600	1.6	5.0	10.8
HTb350-2700	1.4	5.2	13.8
HTb350-2800	1.2	4.8	15.1
HTb350-4600	1.1	4.1	14.4
HTb350-4700	1.0	4.2	18.5
HTb350-4800	0.9	4.0	20.0
HTb450-2600	1.3	4.9	13.6
HTb450-2700	1.2	5.0	16.2
HTb450-2800	0.8	3.5	24.3
HTb450-4600	0.8	3.7	19.4
HTb450-4700	0.8	3.7	22.9
HTb450-4800	0.7	3.3	23.5
HTb550-2600	1.2	4.7	14.7
HTb550-2700	1.2	4.6	15.7
HTb550-2800	0.9	4.2	19.7
HTb550-4600	0.9	3.7	19.2
HTb550-4700	0.7	3.1	21.5
HTb550-4800	0.6	3.0	20.5

At a lower pressure of 0.15 bar, which is particularly relevant as indicator for performance in capturing CO₂ from post-combustion flue gas streams, the HTbx-2T carbons exhibit remarkable performance with uptake ranging from 0.8 to 2.0 mmol g⁻¹ depending on the carbonisation temperature. Carbons activated at 800 °C show the lowest uptake, which is consistent with the trend of decreasing uptake as pore size increases, regardless of variations in total surface area and pore volume. The CO₂ uptake of samples produced from carbonaceous matter carbonised at lower temperatures of 300 and 350 °C, with a KOH/HTbx ratio of 2, exhibit remarkable performance due to the abundance of micropores. The uptake of HTb300-2T carbons is as follows: 1.8, 2.0, and 1.3 mmol g⁻¹ for HTb300-2600, HTb300-2700, and HTb300-2800, respectively, while the uptake of HTb350-2T carbons is 1.6, 1.4, and 1.2 mmol g⁻¹ for HTb350-2600, HTb350-2700, and HTb350-2800, respectively. Carbons produced from carbonaceous matter carbonised at higher temperatures of 450 and 550 °C, which have a higher surface area and slightly larger pore size, exhibit lower CO₂ uptake at 0.15 bar within the range of 0.75 – 1.34 mmol g⁻¹ for HTb450-2T and between 0.93 and 1.22 mmol g⁻¹ for HTb550-2T carbons. In general, the activated carbons obtained from low carbonisation temperature carbonaceous matter tend to be highly microporous with pores of size 5 – 8 Å and thus exhibit exceptional CO₂ uptake at 0.15 bar of 1.8 mmol g⁻¹ for HTb300-2600, 2.0 mmol g⁻¹ for HTb300-2700, 1.6 mmol g⁻¹ for HTb350-2600, and 1.4 mmol g⁻¹ for HTb350-2700. Such CO₂ uptake is exceptional and comparable or higher than most reported porous materials.^{4, 7, 10, 12, 16, 21, 33-36, 40, 42-60}

The uptake of HTb300-2700 and HTb350-2700 is exceptionally high, making them some of the best carbons for low pressure CO₂ uptake at ambient temperature. The CO₂ uptake at 0.15 bar and 1 bar for HTb300-2700 and HTb350-2700 samples, respectively, with values of 2.0 and 1.4 mmol g⁻¹ at 0.15 bar and 4.9 and 5.2 mmol g⁻¹ at 1 bar and 25 °C, is exceptional and placing them at the very upper limit of observed CO₂ uptake for all porous materials.^{4, 7, 10, 12, 16, 21, 33-36, 40, 42-60} The reason behind this is the high level of microporosity (92% of surface area and 84% of pore volume) and a relatively high surface area for such highly microporous materials. This combination of porosity is unique and is rarely seen in porous carbons, which usually have low uptake values at low pressures. The samples have uptake as high as 2.0 mmol g⁻¹ at 0.15 bar and 5.2 mmol g⁻¹ at 1 bar, which matches the best reported values to date,

namely, 5.4 mmol g⁻¹ for HCC2700,¹⁶ 5.8 mmol g⁻¹ for compactivated carbons derived from sawdust,⁵⁵ 5.67 mmol g⁻¹ for fern-derived carbons,⁵⁶ and 5.5 mmol g⁻¹ for compactivated carbons derived from polypyrrole.⁵⁷ However, samples with the highest surface area capture the largest amounts of CO₂ at 20 bar. Therefore, HTb450-2800 and HTb450-4800, with surface area of 3318 and 3413 m² g⁻¹, respectively, show impressive CO₂ uptake of 24.3 and 23.5 mmol g⁻¹ at 20 bar. Interestingly, the high uptake at 20 bar is accompanied by attractive storage capacity at lower pressures of 0.8 mmol g⁻¹ at 0.15 bar and 3.6 mmol g⁻¹ at 1 bar for HTb450-2800, and 0.7 mmol g⁻¹ (0.15 bar) and 3.3 mmol g⁻¹ (1 bar) for HTb450-4800.

The overall picture that emerges is that the present activated carbons demonstrate excellent performance in terms of gravimetric CO₂ uptake, which comparable or superior to that of the current benchmark porous carbons, with the added advantage of being prepared at a lower and milder carbonisation temperature and from waste biomass. This work highlights the significance of carbonisation temperature in enhancing pore characteristics and the feasibility of tailoring pores to achieve an optimal size for gas uptake applications.

3.3.4.2 Methane storage

Methane storage isotherms of the HTbx-yT samples were obtained and analysed to gain insights into the relationship between the air-carbonisation temperature, pore structure, packing density, and the methane storage capacity. In general, activated carbons with a high surface area and well-developed microporosity along with some level of mesoporosity exhibit better methane storage performance at moderate to high pressure (35–100 bar).^{9, 11, 16, 36, 61-65} A high volume of micropores is crucial for effective adsorption of methane molecules, while some level of mesoporosity contributes to efficient sorption kinetics. The mix of porosity exhibited by some of the HTbx-derived activated carbons appears to be suitable for achieving considerable methane storage at medium pressures. Taking into account the importance of overall surface area, pore volume, and packing density in determining methane uptake, this study focused on HTbx-2800 and HTbx-4800 set samples. The methane uptake measurements provided a direct determination of the excess uptake in mmol g⁻¹. By considering the methane density at specific temperatures and pressures, as well as the total pore volume of the adsorbent, the total storage capacity of methane was calculated as detailed in the preceding chapters.

Figure 3.20 displays the excess methane uptake isotherms of the HTbx-2800 and HTbx-4800 carbons. The methane storage capacity of the activated carbons at 35, 65, and 100 bar is summarised in **Table 3.4**. At low pressure, the methane uptake typically increases with increasing pressure, reaching a saturation point at ca. 80 bar. It was observed that the HTbx-2800 samples, characterised by their high microporosity, demonstrated superior methane storage capacity at low pressure compared to the HTbx-4800 samples, which have a combination of larger micropores and mesopores. The excess methane uptake follows the trend in surface area for both the HTbx-2800 and HTbx-4800 carbons, i.e., HTb300-2800 < HTb350-2800 < HTb450-2800 > HTb550-2800 for the HTbx-2800 samples, and HTb300-4800 < HTb350-4800 < HTb450-4800 > HTb550-4800 for the HTbx-4800 samples. Essentially, the excess methane uptake increases with carbonisation temperatures between 300 °C and 450 °C, and then decreases for carbons generated from carbonaceous matter carbonised at 550 °C. This can be attributed to the effect of air-carbonisation temperature, which leads to an enhancement in the overall textural properties and an increase in surface area as the air-carbonisation temperature increases up to 450 °C.

Upon further increase in air-carbonisation temperature to 550 °C, a slight decrease in excess methane uptake is observed. The excess methane uptake at 35 bar of the HTbx-2800 carbons is in the range of 8.6 – 13.1 mmol g⁻¹, and increased to the range of 9.3 – 15.3 mmol g⁻¹ at 65 bar, and rose further to 9.3 – 15.9 mmol g⁻¹ at 100 bar. While that of HTbx-4800 carbons is between 8.6 and 12.1 mmol g⁻¹ at 35 bar, 10.1 – 14.3 mmol g⁻¹ at 65 bar, and 10.6 – 14.9 mmol g⁻¹ at 100 bar. The HTb450-2800 and HTb450-4800 carbons displayed the highest excess methane uptake at 100 bar of 15.9 and 14.9 mmol g⁻¹, respectively, owing to their high surface area. This suggests that for our synthesis conditions, carbonisation at 450 °C may be considered as optimal with respect to generating carbons with enhanced methane storage.

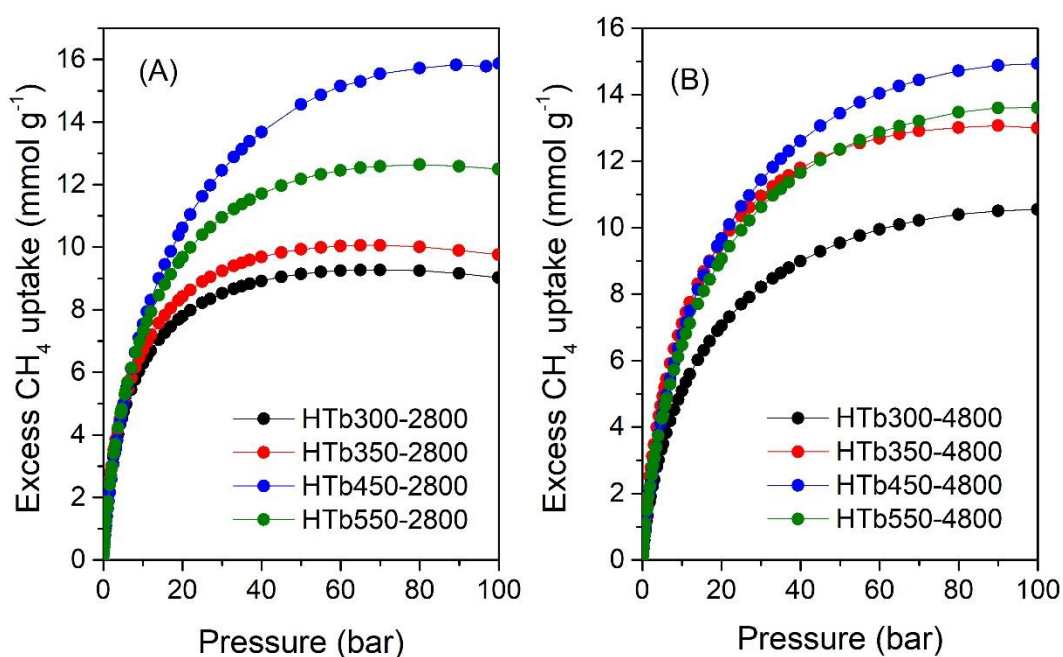


Figure 3.20. Excess gravimetric methane uptake isotherms at 25 °C of HTbx-2800 and HTbx-4800 activated carbons.

Table 3.4. Excess gravimetric methane uptake of HTbx-2800 and HTbx-4800 activated carbons.

Sample	Density (g cm ⁻³)	Excess gravimetric uptake (mmol g ⁻¹) or (g g ⁻¹) ^a		
		35 bar	65 bar	100 bar
HTb300-2800	0.786	8.6 (0.14)	9.3 (0.15)	9.0 (0.15)
HTb350-2800	0.754	9.5 (0.15)	10.1 (0.16)	9.8 (0.16)
HTb450-2800	0.465	13.1 (0.21)	15.3 (0.25)	15.9 (0.26)
HTb550-2800	0.715	11.4 (0.18)	12.5 (0.20)	12.5 (0.20)
HTb300-4800	0.587	8.6 (0.14)	10.1 (0.16)	10.6 (0.17)
HTb350-4800	0.526	11.4 (0.18)	12.8 (0.21)	13.0 (0.21)
HTb450-4800	0.452	12.1 (0.19)	14.3 (0.23)	14.9 (0.24)
HTb550-4800	0.495	11.2 (0.18)	13.1 (0.21)	13.6 (0.22)

^aThe values in parenthesis are the excess gravimetric methane uptake donated as g g⁻¹

Figure 3.21 displays the total gravimetric methane uptake isotherms of the HTbx-2800 and HTbx-4800 carbons, and the uptake at 35, 65, and 100 bar is summarised in **Table 3.5**. The uptake of the HTbx-2800 carbons ranges from 9.7 to 15.5 mmol g⁻¹ at 35 bar, 11.2 to 19.9 mmol g⁻¹ at 65 bar, and 11.9 to 23.4 mmol g⁻¹ at 100 bar. Whereas, the uptake of the HTbx-4800 carbons is as follows: 10.3 – 14.5 mmol g⁻¹ at 35 bar, 13.3 – 19.1 mmol g⁻¹ at 65 bar, and 15.7 – 22.7 mmol g⁻¹ at 100 bar. These values correspond to g g⁻¹ uptake at 100 bar of 0.19, 0.22, 0.38, and 0.28 for HTb300-2800, HTb350-2800, HTb450-2800, and HTb550-2800, respectively, and 0.25, 0.31, 0.37, and 0.32 for HTb300-4800, HTb350-4800, HTb450-4800, and HTb550-4800, respectively. It is worth noting that, at 100 bar, the g g⁻¹ uptake approaches the US DOE target of 0.5 g g⁻¹, particularly for samples HTb450-2800 and HTb450-4800. This remarkable total gravimetric uptake is comparable to, or even surpasses, that of the best benchmark materials reported to date.^{11, 16, 36, 62-64, 66-78} These results further emphasise the critical role of air-carbonisation temperature in fine-tuning and modulating the textural properties of the adsorbents, thereby enhancing their performance in gas uptake applications.

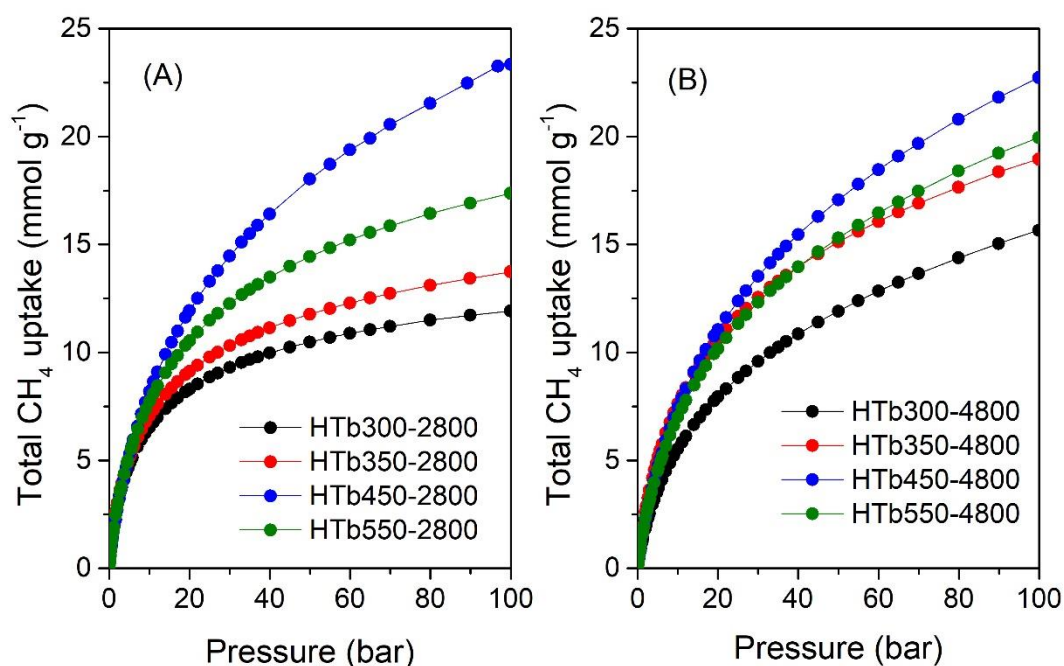


Figure 3.21. Total gravimetric methane uptake isotherms at 25 °C of HTbx-2800 and HTbx-4800 activated carbons.

Table 3.5. Total gravimetric methane uptake of HTbx-2800 and HTbx-4800 activated carbons.

Sample	Density (g cm ⁻³)	Total gravimetric uptake (mmol g ⁻¹) or (g g ⁻¹) ^a		
		35 bar	65 bar	100 bar
HTb300-2800	0.786	9.7 (0.16)	11.1 (0.18)	11.9 (0.19)
HTb350-2800	0.754	10.8 (0.17)	12.5 (0.20)	13.7 (0.22)
HTb450-2800	0.465	15.5 (0.25)	19.9 (0.32)	23.4 (0.38)
HTb550-2800	0.715	12.9 (0.21)	15.6 (0.25)	17.4 (0.28)
HTb300-4800	0.587	10.3 (0.16)	13.3 (0.21)	15.7 (0.25)
HTb350-4800	0.526	13.3 (0.21)	16.5 (0.27)	19.0 (0.31)
HTb450-4800	0.452	14.5 (0.23)	19.1 (0.31)	22.7 (0.37)
HTb550-4800	0.495	13.2 (0.21)	17.0 (0.27)	20.0 (0.32)

^aThe values in parenthesis are the total gravimetric methane uptake donated as g g⁻¹.

The quantity of methane adsorbed per unit volume (volumetric methane uptake) is a crucial parameter when considering methane gas storage applications. The US DOE has established a volumetric methane uptake target of $263 \text{ cm}^3 \text{ (STP) cm}^{-3}$ at 25°C and moderate pressure, ranging from 35 to 100 bar. The packing density of an adsorbent, in conjunction with its gravimetric uptake, significantly influence the volumetric uptake. A high packing density allows for more adsorbent material to be compacted within a limited storage space, such as a tank, effectively increasing the volumetric uptake. Due to the variability of the textural properties and the packing density of the present activated carbons, which are modulated by changes in air-carbonisation temperatures, they should exhibit excellent performance due to optimised balance between packing density, pore volume, and a mix of porosity. A high pore volume and a mix of porosity, resulting from optimal air-carbonisation, provides more space for methane molecules to adsorb, thereby contributing to the overall storage capacity and enabling efficient adsorption/desorption kinetics. However, it is essential to maintain a balance between microporosity and mesoporosity, as a combination of both types of pores contributes to efficient sorption kinetics and volumetric methane storage.⁷⁹ **Figure 3.22** shows the volumetric methane storage isotherms, and **Table 3.6** provides a summary of the uptake at various pressures. Additionally, **Table 3.6** presents the working capacity, which is the deliverable methane calculated as the difference in uptake between 5 bar and the storage pressure (35, 65, or 100 bar). Notably, the volumetric uptake isotherms of the activated carbons in **Figure 3.22** display no saturation at 100 bar, suggesting that these carbons may store even greater quantities of methane at pressures exceeding 100 bar. The exception is for the HTb300-2800 and HTb350-2800 carbons, which appear to approach saturation due to their relatively lower surface area. In general, the non-saturated isotherms of these carbons contrasts with most benchmark MOFs, which usually reach saturation at ca. 80 bar.^{71, 80} The activated carbons, despite variations in their surface areas, demonstrate exceptional volumetric methane storage capacity at 100 bar and 25°C , as shown in **Table 3.6**. The capacities are 210, 232, 243, and $278 \text{ cm}^3 \text{ (STP) cm}^{-3}$ for HTb300-2800, HTb350-2800, HTb450-2800, and HTb550-2800, respectively, and 206, 224, 230, and $221 \text{ cm}^3 \text{ (STP) cm}^{-3}$ for HTb300-4800, HTb350-4800, HTb450-4800, and HTb550-4800, respectively, as shown in **Table 3.6**. The data demonstrates the impact of air-carbonisation temperature on the packing density of the resulting activated carbons. The packing density of the present carbons critically

contributes to achieving high volumetric uptake, even for carbons with moderate surface area. Specifically, carbons derived from low carbonisation temperature precursors (HTb300-2800, HTb350-2800, HTb300-4800, and HTb350-4800) exhibit high packing density, as shown in **Table 3.6**, resulting in excellent volumetric uptake of 210, 232, 206, and 224 cm^3 (STP) cm^{-3} , respectively, despite their moderate surface area of 1424, 1957, 2253, and 2799 $\text{m}^2 \text{g}^{-1}$, respectively. This is ascribed to a positive effect of limiting the mesoporosity of the carbons, which in turn results in an increase in the packing density. On the other hand, the volumetric uptake of activated carbons obtained from high carbonisation temperature precursors (HTb450-2800, HTb550-2800, HTb450-4800, and HTb550-4800) falls within a range that is similar to those derived from low temperature precursors, being 243, 278, 230, and 221 cm^3 (STP) cm^{-3} , respectively, despite their higher surface area of 3318, 2439, 3413, and 2855 $\text{m}^2 \text{g}^{-1}$. This is attributed to the balance achieved between surface area and packing density in these carbons, which is essential for efficient methane sorption kinetics and volumetric methane storage. The volumetric uptake observed for the present carbons, which takes into account the packing density that experimentally determined, is one of the highest reported to date for both carbon and MOF materials.^{9,}

38, 61-64, 72, 74, 78, 79, 81-87

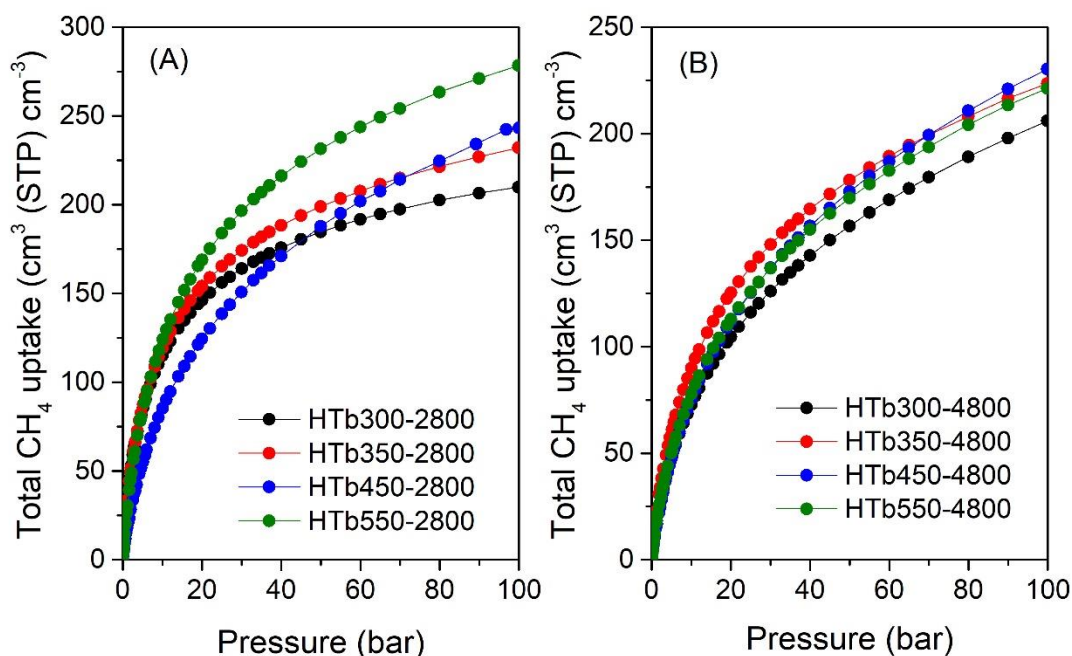


Figure 3.22. Total volumetric methane uptake at 25 °C of HTbx-2800 and HTbx-4800 activated carbons.

Table 3.6. Total volumetric methane uptake and working capacity of HTbx-2800 and HTbx-4800 activated carbons.

Sample	Density (g cm ⁻³)	Total volumetric uptake (cm ³ (STP) cm ⁻³)		
		35 bar	65 bar	100 bar
HTb300-2800	0.79	170 (84)	195 (109)	210 (124)
HTb350-2800	0.75	182 (94)	212 (124)	232 (145)
HTb450-2800	0.47	162 (106)	208 (152)	243 (188)
HTb550-2800	0.72	207 (117)	249 (159)	278 (189)
HTb300-4800	0.59	135 (86)	174 (125)	206 (157)
HTb350-4800	0.53	157 (96)	195 (133)	224 (162)
HTb450-4800	0.45	147 (100)	193 (145)	230 (182)
HTb550-4800	0.50	146 (95)	188 (137)	221 (170)

The volumetric working capacity in parenthesis (i.e., deliverable methane), is calculated as the difference in storage capacity at 5 bar and the uptake pressure (35, 65 or 100 bar).

The working capacity is an important measure for efficient methane uptake, which is the efficiency of materials to deliver the stored gas between two finite pressures. The working capacity is influenced by the porosity of the adsorbent. While the microporosity is important for achieving high packing density and thus high volumetric uptake, it also favours high methane uptake at low pressure, potentially reducing the deliverable methane. Therefore, to achieve high working capacity, a combination of microporosity and mesoporosity is essential, along with high packing density. **Table 3.6** summarises the volumetric working capacity, of the HTbx-2800 and HTbx-4800 carbons. For a 100 to 5 bar pressure swing, the capacities are 124, 145, 188, and 189 cm³ (STP) cm⁻³ for HTb300-2800, HTb350-2800, HTb450-2800, and HTb550-2800, respectively, and 157, 162, 182, and 170 cm³ (STP) cm⁻³ for HTb300-4800, HTb350-4800, HTb450-4800, and HTb550-4800, respectively. The increase in the overall working capacity is also in the line with increasing carbonisation temperature, which is due to enhancement in mesoporosity of the carbons. This finding reveals a further role of carbonisation temperature in modulating the porosity of the activated carbons towards efficient methane uptake, and deliverable methane.

3.4 Conclusion

The effect of air-carbonisation temperature of hookah tobacco (HTb) derived carbonaceous matter (HTbx, where x is carbonisation temperature) on the textural properties of HTbx-derived activated carbons, along with their performance toward gas adsorption, was investigated. The investigation involved modifying the following parameters: i) carbonisation temperature ($T = 300, 350, 450$ and $550\text{ }^{\circ}\text{C}$), ii) amount of activating agent amount (KOH/HTbx, mass ratio of 2 or 4), and iii) activating temperatures ($T = 600, 700$ or $800\text{ }^{\circ}\text{C}$). The HTbx carbonaceous matter displayed high C content that increased with the carbonisation temperature ranging from 63 to 77 wt%, while the oxygen content decreased, resulting in varying O/C ratios of between 0.245 and 0.37. These variations on the O/C were reflected in the textural properties of the activated carbons and their performance in gas storage. The carbons have surface area ranging from 402 to $3413\text{ m}^2\text{ g}^{-1}$ and pore volume in the range of $0.18 - 1.65\text{ cm}^3\text{ g}^{-1}$ with porosity that can be tailored for suitability in various applications. The activated carbons derived from low carbonisation temperature are dominated by a highly microporous ($5\text{--}20\text{ \AA}$) structure, which is suitable for capturing CO_2 from post-combustion at low pressure at $25\text{ }^{\circ}\text{C}$, with uptake of up to 2.0 and 5.2 mmol g^{-1} at 0.15 and 1 bar, respectively. Due to the possibility of controlling the O/C ratio of the precursors, activated carbons with tailored properties (i.e., high surface area, high packing density and mix of microporosity and mesoporosity) were synthesised for enhanced methane CH_4 storage. A good balance between gravimetric methane uptake and volumetric uptake was achieved with uptake of 0.37 g g^{-1} and $278\text{ cm}^3\text{ (STP) cm}^{-3}$, respectively. This indicates that air-carbonisation temperature can be a crucial factor in modulating the porosity of activated carbons. Overall, the findings demonstrate the potential of flash air-carbonisation as a simple and sustainable method for producing high-quality activated carbon from biomass sources, and provides new insights into the role of carbonisation temperature in controlling the porosity of activated carbons.

References

1. L. S. Blankenship and R. Mokaya, *Materials Advances*, 2022, **3**, 1905-1930.
2. M. Sevilla, A. S. M. Al-Jumialy, A. B. Fuertes and R. Mokaya, *ACS Applied Materials & Interfaces*, 2018, **10**, 1623-1633.
3. W. Sangchoom, D. A. Walsh and R. Mokaya, *Journal of Materials Chemistry A*, 2018, **6**, 18701-18711.
4. E. A. Hirst, A. Taylor and R. Mokaya, *Journal of Materials Chemistry A*, 2018, **6**, 12393-12403.
5. T. S. Blankenship and R. Mokaya, *Energy & Environmental Science*, 2017, **10**, 2552-2562.
6. N. Balahmar, A. S. Al-Jumialy and R. Mokaya, *Journal of Materials Chemistry A*, 2017, **5**, 12330-12339.
7. E. Haffner-Staton, N. Balahmar and R. Mokaya, *Journal of Materials Chemistry A*, 2016, **4**, 13324-13335.
8. M. Sevilla and R. Mokaya, *Energy & Environmental Science*, 2014, **7**, 1250-1280.
9. A. Altwala and R. Mokaya, *Journal of Materials Chemistry A*, 2022, **10**, 13744-13757.
10. A. Altwala and R. Mokaya, *RSC Advances*, 2022, **12**, 20080-20087.
11. A. Altwala and R. Mokaya, *Energy & Environmental Science*, 2020, **13**, 2967-2978.
12. N. Balahmar and R. Mokaya, *Journal of Materials Chemistry A*, 2019, **7**, 17466-17479.
13. M. Cox and R. Mokaya, *Sustainable Energy & Fuels*, 2017, **1**, 1414-1424.
14. L. S. Blankenship, N. Balahmar and R. Mokaya, *Nature Communications*, 2017, **8**, 1545.
15. M. Sevilla, A. B. Fuertes and R. Mokaya, *Energy & Environmental Science*, 2011, **4**, 1400-1410.
16. I. Alali and R. Mokaya, *Energy & Environmental Science*, 2022, **15**, 4710-4724.
17. Z. Zhang, D. Luo, G. Lui, G. Li, G. Jiang, Z. P. Cano, Y.-P. Deng, X. Du, S. Yin and Y. Chen, *Carbon*, 2019, **143**, 531-541.

18. H. M. Lee, D. C. Chung, S. C. Jung, K. H. An, S. J. Park and B. J. Kim, *Chemical Engineering Journal*, 2019, **377**, 120836.
19. O. Üner and Y. Bayrak, *Microporous and Mesoporous Materials*, 2018, **268**, 225-234.
20. W. Li, K. B. Yang, J. H. Peng, L. B. Zhang, S. H. Guo and H. Y. Xia, *Industrial Crops and Products*, 2008, **28**, 190-198.
21. M. Sevilla and A. B. Fuertes, *Energy & Environmental Science*, 2011, **4**, 1765-1771.
22. M. Sevilla and A. B. Fuertes, *Carbon*, 2009, **47**, 2281-2289.
23. M. Sevilla, J. A. Maciá-Agulló and A. B. Fuertes, *Biomass and Bioenergy*, 2011, **35**, 3152-3159.
24. M. Fang, D. Shen, Y. Li, C. Yu, Z. Luo and K. Cen, *Journal of Analytical and Applied Pyrolysis* 2006, **77**, 22-27.
25. A. Demirbas and G. Arin, *Energy Sources* 2002, **24**, 471-482.
26. A. V. Bridgwater, D. Meier and D. Radlein, *Organic Geochemistry* 1999, **30**, 1479-1493.
27. J. M. Encinar, F. J. Beltrán, J. F. González and M. J. Moreno, *Journal of Chemical Technology & Biotechnology*, 1997, **70**, 400-410.
28. A. C. Gonçalves Jr, J. Zimmermann, D. Schwantes, V. H. D. de Oliveira, F. da Cunha Dudczak, C. R. T. Tarley, M. C. Prete and A. Snak, *Journal of Analytical and Applied Pyrolysis* ,2023, **171**, 105965.
29. J. Rouquerol, P. Llewellyn and F. Rouquerol, *Studies in Surface Science and Catalysis*, 2006, **160**, 49-56.
30. A. Galarneau, D. Mehlhorn, F. Guenneau, B. Coasne, F. Villemot, D. Minoux, C. Aquino and J. P. Dath, *Langmuir*, 2018, **34**, 14134-14142.
31. M. Thommes, K. Kaneko, A. V. Neimark, J. P. Olivier, F. Rodriguez-Reinoso, J. Rouquerol and K. S. W. Sing, *Pure and Applied Chemistry*, 2015, **87**, 1051-1069.
32. M. Forster, C. Liu, M. G. Duke, K. G. McAdam and C. J. Proctor, *Chemistry Central Journal*, 2015, **9**, 1-10.
33. A. M. Aljumaily and R. Mokaya, *Materials Advances*, 2020, **1**, 3267-3280.
34. B. Adeniran, E. Masika and R. Mokaya, *Journal of Materials Chemistry A*, 2014, **2**, 14696-14710.

-
35. H. M. Coromina, D. A. Walsh and R. Mokaya, *Journal of Materials Chemistry A*, 2016, **4**, 280-289.
 36. I. Alali and R. Mokaya, *Journal of Materials Chemistry A*, 2023, **11**, 6952-6965.
 37. E. Masika and R. Mokaya, *RSC Advances*, 2013, **3**, 17677-17681.
 38. P. N. Quirant, C. Cuadrado-Collados, A. J. Romero-Anaya, J. S. Albero and M. M. Escandell, *Industrial & Engineering Chemistry Research*, 2020, **59**, 5775-5785.
 39. M. Dizbay-Onat, U. K. Vaidya and C. T. Lungu, *Industrial Crops and Products*, 2017, **95**, 583-590.
 40. W. Sangchoom and R. Mokaya, *ACS Sustainable Chemistry & Engineering*, 2015, **3**, 1658-1667.
 41. L. S. Blankenship, N. Albeladi, T. Alkhaldi, A. Madkhali and R. Mokaya, *Energy Advances*, 2022, **1**, 1009-1020.
 42. J. Silvestre-Albero, A. Wahby, A. Sepúlveda-Escribano, M. Martínez-Escandell, K. Kaneko and F. Rodríguez-Reinoso, *Chemical Communications*, 2011, **47**, 6840-6842.
 43. N. P. Wickramaratne and M. Jaroniec, *ACS Applied Materials & Interfaces*, 2013, **5**, 1849-1855.
 44. N. P. Wickramaratne and M. Jaroniec, *Journal of Materials Chemistry A*, 2013, **1**, 112-116.
 45. J. Wang, A. Heerwig, M. R. Lohe, M. Oschatz, L. Borchardt and S. Kaskel, *Journal of Materials Chemistry*, 2012, **22**, 13911-13913.
 46. X. Q. Fan, L. X. Zhang, G. B. Zhang, Z. Shu and J. L. Shi, *Carbon*, 2013, **61**, 423-430.
 47. M. Sevilla, P. Valle-Vigon and A. B. Fuertes, *Advanced Functional Materials*, 2011, **21**, 2781-2787.
 48. W. Xing, C. Liu, Z. Zhou, L. Zhang, J. Zhou, S. Zhuo, Z. Yan, H. Gao, G. Wang and S. Z. Qiao, *Energy & Environmental Science*, 2012, **5**, 7323-7327.
 49. Y. D. Xia, R. Mokaya, G. S. Walker and Y. Q. Zhu, *Advanced Energy Materials*, 2011, **1**, 678-683.
 50. Y. Zhao, L. Zhao, K. X. Yao, Y. Yang, Q. Zhang and Y. Han, *Journal of Materials Chemistry*, 2012, **22**, 19726-19731.

-
51. Z. Zhang, J. Zhou, W. Xing, Q. Xue, Z. Yan, S. Zhuo and S. Z. Qiao, *Physical Chemistry Chemical Physics*, 2013, **15**, 2523-2529.
 52. M. Nandi, K. Okada, A. Dutta, A. Bhaumik, J. Maruyama, D. Derks and H. Uyama, *Chemical Communications*, 2012, **48**, 10283-10285.
 53. D. Lee, C. Zhang, C. Wei, B. L. Ashfeld and H. Gao, *Journal of Materials Chemistry A*, 2013, **1**, 14862-14867.
 54. M. Sevilla, C. Falco, M.-M. Titirici and A. B. Fuertes, *RSC Advances*, 2012, **2**, 12792-12797.
 55. N. Balahmar, A. C. Mitchell and R. Mokaya, *Advanced Energy Materials*, 2015, **5**, 1500867.
 56. J. Serafin, K. Kiełbasa and B. Michalkiewicz, *Chemical Engineering Journal*, 2022, **429**, 131751.
 57. B. Adeniran and R. Mokaya, *Nano Energy*, 2015, **16**, 173-185.
 58. A. B. Fuertes and M. Sevilla, *Carbon*, 2015, **94**, 41-52.
 59. A. Altwala and R. Mokaya, *Energy Advances*, 2022, **1**, 216-224.
 60. M. Sevilla and A. B. Fuertes, *Journal of Colloid and Interface Science*, 2012, **366**, 147-154.
 61. Y. He, W. Zhou, G. Qian and B. Chen, *Chemical Society Reviews*, 2014, **43**, 5657-5678.
 62. T. A. Makal, J. R. Li, W. Lu and H. C. Zhou, *Chemical Society Reviews*, 2012, **41**, 7761-7779.
 63. J. A. Mason, M. Veenstra and J. R. Long, *Chemical Science*, 2014, **5**, 32-51.
 64. B. Li, H. M. Wen, W. Zhou, J. Q. Xu and B. L. Chen, *Chem*, 2016, **1**, 557-580.
 65. F. Gándara, H. Furukawa, S. Lee and O. M. Yaghi, *Journal of the American Chemical Society*, 2014, **136**, 5271-5274.
 66. T. Tian, Z. Zeng, D. Vulpe, M. E. Casco, G. Divitini, P. A. Midgley, J. Silvestre-Albero, J. C. Tan, P. Z. Moghadam and D. Fairen-Jimenez, *Nature Materials*, 2018, **17**, 174-179.
 67. E. Masika and R. Mokaya, *Energy & Environmental Science*, 2014, **7**, 427-434.
 68. Y. C. Lin, C. L. Kong, Q. J. Zhang and L. Chen, *Advanced Energy Materials*, 2017, **7**, 1601296.
 69. D. Lozano-Castello, D. Cazorla-Amoros, A. Linares-Solano and D. Quinn, *Carbon*, 2002, **40**, 989-1002.

-
70. Z. Chen, P. Li, R. Anderson, X. Wang, X. Zhang, L. Robison, L. R. Redfern, S. Moribe, T. Islamoglu, D. A. Gomez-Gualdron, T. Yildirim, J. F. Stoddart and O. K. Farha, *Science*, 2020, **368**, 297-303.
71. Y. Peng, V. Krungleviciute, I. Eryazici, J. T. Hupp, O. K. Farha and T. Yildirim, *Journal of the American Chemical Society*, 2013, **135**, 11887-11894.
72. K. V. Kumar, K. Preuss, M. M. Titirici and F. Rodriguez-Reinoso, *Chemical Reviews*, 2017, **117**, 1796-1825.
73. T. A. Rash, A. Gillespie, B. P. Holbrook, L. H. Hiltzik, J. Romanos, Y. C. Soo, S. Sweany and P. Pfeifer, *Fuel*, 2017, **200**, 371-379.
74. D. A. Gómez-Gualdrón, C. E. Wilmer, O. K. Farha, J. T. Hupp and R. Q. Snurr, *Journal of Physical Chemistry C*, 2014, **118**, 6941-6951.
75. H. Nishihara and T. Kyotani, *Chemical Communications*, 2018, **54**, 5648-5673.
76. H. Wu, W. Zhou and T. Yildirim, *Journal of the American Chemical Society*, 2009, **131**, 4995-5000.
77. J. Jiang, H. Furukawa, Y. B. Zhang and O. M. Yaghi, *Journal of the American Chemical Society*, 2016, **138**, 10244-10251.
78. J. Romanos, S. Sweany, T. Rash, L. Firlej, B. Kuchta, J. C. Idrobo and P. Pfeifer, *Adsorption Science & Technology*, 2014, **32**, 681-691.
79. M. E. Casco, M. Martínez-Escandell, E. Gadea-Ramos, K. Kaneko, J. Silvestre-Albero and F. Rodríguez-Reinoso, *Chemistry of Materials*, 2015, **27**, 959-964.
80. S. Bracco, D. Piga, I. Bassanetti, J. Perego, A. Comotti and P. Sozzani, *Journal of Materials Chemistry A*, 2017, **5**, 10328-10337.
81. P. Pfeifer, L. Aston, M. Banks, S. Barker, J. Burrell, S. Carter, J. Coleman, S. Crockett, C. Faulhaber, J. Flavin, M. Gordon, L. Hardcastle, Z. Kallenborn, M. Kemiki, C. Lapilli, J. Pobst, R. Schott, P. Shah, S. Spellerberg, G. Suppes, D. Taylor, A. Tekeci, C. Wexler, M. Wood, P. Buckley, T. Breier, J. Downing, S. Eastman, P. Freeze, S. Graham, S. Grinter, A. Howard, J. Martinez, D. Radke, T. Vassalli and J. Ilavsky, *Chaos: An Interdisciplinary Journal of Nonlinear Science*, 2007, **17**, 041108.
82. C. M. Simon, J. Kim, D. A. Gomez-Gualdron, J. S. Camp, Y. G. Chung, R. L. Martin, R. Mercado, M. W. Deem, D. Gunter, M. Haranczyk, D. S. Sholl, R. Q. Snurr and B. Smit, *Energy & Environmental Science*, 2015, **8**, 1190-1199.

-
83. M. E. Casco, M. Martinez-Escandell, K. Kaneko, J. Silvestre-Albero and F. Rodriguez-Reinoso, *Carbon*, 2015, **93**, 11-21.
 84. S. Choi, M. A. Alkhabbaz, Y. G. Wang, R. M. Othman and M. Choi, *Carbon*, 2019, **141**, 143-153.
 85. B. M. Connolly, M. Aragoes-Anglada, J. Gandara-Loe, N. A. Danaf, D. C. Lamb, J. P. Mehta, D. Vulpe, S. Wuttke, J. Silvestre-Albero, P. Z. Moghadam, A. E. H. Wheatley and D. Fairen-Jimenez, *Nature Communications*, 2019, **10**, 2345.
 86. B. M. Connolly, D. G. Madden, A. E. H. Wheatley and D. Fairen-Jimenez, *Journal of the American Chemical Society*, 2020, **142**, 8541-8549.
 87. V. Rozyyev, D. Thirion, R. Ullah, J. Lee, M. Jung, H. Oh, M. Atilhan and C. T. Yavuz, *Nature Energy*, 2019, **4**, 604-611.

Chapter 4

Modulating The Porosity of N-doped Carbon Materials for Enhanced CO₂ Capture and Methane Uptake

Abstract

N-doped carbons with judiciously modulated porosity have been successfully prepared via the addition of melamine or urea as a N source to an activation mixture containing biomass-derived carbonaceous matter of low O/C ratio (air-carbonised date seed, *Phoenix dactylifera*, ACDS), and potassium hydroxide (KOH) as an activating agent. To access a broad range of surface area and mix of porosity characteristics, a series of carbons were prepared by varying the following; (i) the amount of added N-containing melamine or urea (at melamine or urea/ACDS ratio of 1 or 2), (ii) the KOH/ACDS ratio (2 or 4), and (iii) activation temperature (600, 700, or 800 °C). We found that the N added to the activation mix acts both as an N-dopant and porogen, with the later effect enabling formation of larger pores, which extended the pore size distribution into the mesopore region. Furthermore, the presence of N acts to increase the surface area and provides carbons with tuneable porosity (with respect to the mix of microporosity and mesoporosity) and variable packing density, all of which may be tailored towards suitability of the carbons for enhanced uptake of CO₂ and methane. The activated carbons have significant N content of up to 18 wt%, surface area of up to 3646 m² g⁻¹, and pore volume that reaches 2.1 cm³ g⁻¹. Depending on the preparation conditions and resulting mix of micro/mesoporosity, the carbons show excellent low pressure CO₂ capture at 25 °C of 1.7 mmol g⁻¹ at 0.15 bar and 4.7 mmol g⁻¹ at 1 bar. The porosity and packing density of the carbons may also be directed towards excellent methane storage; gravimetric uptake of up to 0.42 g g⁻¹ at 25 °C and 100 bar, volumetric storage capacity of up to 266 cm³ (STP) cm⁻³ at 25 °C and 100 bar, and a working capacity (for 100 to 5 bar pressure swing) of 196 cm³ (STP) cm⁻³.

4.1 Introduction

The surface area and overall porosity of any adsorbent are important factors by which the total amount of gas adsorbed can be determined. Hence, exploring new approaches for the synthesis of porous carbons has been a long-term goal in preparing activated carbons with the properties desired to exhibit good performance in energy-related applications. It is well-established that the textural properties and elemental composition of activated carbons are greatly influenced by the type and amount of the activating agent, activation temperature, and the nature and elemental composition of the carbonaceous precursor.¹

Among the various chemical activation agents, KOH is widely used due to its effectiveness in controlling the surface area and porosity of the resulting carbon via adjustment of the activation conditions, namely the amount of KOH and the activation temperature.²⁻⁵ Carbons obtained via this method can exhibit high surface area ($> 2800 \text{ m}^2 \text{ g}^{-1}$), and their pore size can be tuned between ultramicropores/micropores and small mesopores.^{6, 7} However, although these carbons have shown advantages in certain applications, especially at low-pressure adsorption, their use in energy-related applications at high-pressures remains limited, due to limits on their mesoporosity.^{8, 9} Only a few examples of precursors, such as polypyrrole,⁹ imidazolium-based ionic liquids,¹⁰ zeolite-templated carbons,¹¹ or graphene,¹² have shown activated materials with a high level of mesoporosity when activated with KOH. For example, Sevilla, *et al.* reported ultra-high surface area carbons ($3000\text{-}3500 \text{ m}^2 \text{ g}^{-1}$) derived from direct activation of polypyrrole (PPy) with varying amounts of potassium hydroxide (KOH).⁹

Regarding the role of the elemental composition of precursors in tailoring the surface area and porosity of activated carbons, researchers in the Mokaya group have demonstrated that it is possible to customise the porosity through a systematic selection of precursors based on their chemical composition.^{4, 13, 14} For instance, Balahmar and Mokaya explored the use of pre-mixed precursors (PPy and sawdust) to control, tailor and enhance the porosity of activated carbons.⁴ Highly porous carbons were prepared with surface area higher than that achievable from the single use of any of the precursors (PPy or sawdust). This is directly linked to the modification of the O/C ratio and the incorporation of nitrogen from polypyrrole. For example, Altwala and Mokaya

synthesised activated carbons from air-carbonised date seeds (with a very low O/C ratio of 0.156) and investigated their textural properties and methane uptake.¹⁵ They found that precursors with a low O/C ratio have a high resistance to activation and therefore tend to yield significant microporosity and high packing density. However, such low O/C ratio precursors are only able to generate activated carbons with relatively low surface area due to their high resistance to activation. This means that the gravimetric methane uptake of activated carbons derived from such precursors tends to be low since methane storage at moderate to high pressure (35 to 100 bar) is very dependent on surface area. However, despite their low gravimetric uptake, their high packing density (arising from their highly microporous nature) means that they have attractive methane volumetric uptake of up to 222 cm³ (STP) cm⁻³ at 25 °C and 35 bar.¹⁵ This finding was explored further in a study that showed a greater degree of control over porosity and surface area by premixing of polypyrrole (PPy), which readily activates, with precursors of different O/C ratios, which are resistant to activation, namely, air carbonised date seed, ACDS, (O/C ratio of 0.156) and so-called CNL carbon (O/C ratio of 0.185).¹³ The premixing of precursors enabled the preparation of carbons with simultaneously optimum porosity and high packing density making them suitable for methane uptake to the extent that they achieved attractive combinations of gravimetric and volumetric methane uptake; 0.36 g g⁻¹ and 260 cm³ (STP) cm⁻³ and 0.46 g g⁻¹ and 229 cm³ (STP) cm⁻³, at 25 °C and 100 bar.¹³ The careful mixing of the PPy with ACDS or CNL plays a key role in influencing the ratio of microporosity to mesoporosity in the resultant carbons. More specifically it was found that the level of mesoporosity was proportional of the amount of PPy (N-containing) in the mixture during the activation step whereas the mesopore size increased with the PPy/ACDS or PPy/CNL ratio.¹³ On other hand, having higher amounts of CNL or ACDS than PPy (for example at ratio 2:1) resulted in a decrease in the mesoporosity on the carbons and their surface area.¹³

Given the behaviour of PPy under activation conditions (i.e., susceptibility to activation), it is now apparent that the presence of N in the framework of carbonaceous matter plays an important role towards achieving high surface area. The surface area and porosity of activated carbons can be increased further by adding so-called mediators, such as melamine and urea, to the precursors, before activation.^{7, 16, 17} For example, Fuertes and Sevilla prepared high-surface area carbons via the KOH-

activation of hydrochar, using melamine as a mediator.¹⁸ The use of melamine generated mesoporosity, which in turn contributed to increasing the surface area of the resulting carbons.¹⁸ While a large surface area is important for high-pressure gas storage, the materials must exhibit other characteristics to be suitable for methane uptake. For instance, when materials have a high surface area and pore volume, the packing density decreases, causing a decrease in volumetric gas uptake.¹⁹ Hence, in order to obtain a material with suitable properties for methane adsorption, the adsorbent should exhibit a balance between possessing a high surface area, mix of microporosity/mesoporosity, and a high packing density.

The primary objective of the work presented in this chapter was to synthesise activated carbons with judiciously modulated porosity, appropriate for methane storage, by adding a mediator, specifically a N-containing additive to the precursor during activation. In an attempt to enhance both the porosity and packing density, a precursor with a low O/C ratio, namely air-carbonised date seeds (*Phoenix dactylifera*), designated as ACDS, which is known to be resistant to activation, was utilised.¹⁵ The low oxygen content of the ACDS carbon was expected to favour activated carbons with a high packing density, while the presence of a N-containing additive would work to increase the surface area. This combination is expected to generate activated carbons with high surface area, tuneable porosity (micropore/mesopore mix), and variable packing density. The interplay between these three factors was expected to yield carbons with a range of desirable properties suited for CO₂ and/or methane storage.

4.2 Experimental Section

4.2.1 Synthesis of N-doped carbons

Air carbonisation. Date seeds (*Phoenix dactylifera*) were used as the starting material for this study. Before use, the date seeds were washed with deionized water and dried in an oven at 80 °C. 5 g of the washed date seeds were placed in an alumina boat and introduced to a horizontal tube furnace, which was then heated to 400 °C at a heating ramp rate of 10 °C min⁻¹ under 100 cm³ min⁻¹ flow of nitrogen atmosphere. Once at 400 °C, the date seeds were exposed to a flow of air for 5 minutes, and then the furnace was allowed to cool down under a flow of nitrogen gas. The carbonaceous material obtained by this process was collected and ground with a mortar and designed as ACDS (air-carbonised date seeds).

Chemical activation. The air-carbonised date seed (ACDS) carbon was chemically activated with KOH in the presence of melamine as a N source. In a typical procedure, the ACDS carbon was thoroughly mixed in an agate mortar with appropriate amounts of KOH (at KOH/ACDS weight ratio of 2 or 4) and melamine (at melamine/ACDS weight ratio of 1 or 2). Subsequently, the mixture was placed in an alumina boat and heated in a horizontal furnace to the desired temperatures of (600, 700 or 800 °C) at a heating ramp rate of 3 °C min⁻¹ under a nitrogen gas flow and held at the target temperature for 1 h, following which the samples were allowed to cool down to room temperature under a nitrogen atmosphere. The resulting activated carbons were then thoroughly washed by stirring in an aqueous solution of HCl (10%) at room temperature to remove any residual inorganic salts. *Note, precautions should be taken when washing a nitrogen-containing precursor and potassium salts, as hazardous amount of toxic potassium cyanate (KOCN) or potassium cyanide (KCN) could be produced.* The carbons were then repeatedly washed with deionised water until neutral pH (pH ~ 7) was achieved for the filtrate, and then dried overnight at 100 °C in an oven. The activated carbons are denoted as DSMxT-y, where x is the KOH/ACDS weight ratio, T is the activation temperatures (600, 700 or 800 °C), and y is the melamine/ACDS weight ratio. For comparison purposes, two activated carbons were produced in the presence of urea (at urea/ACDS weight ratio of 1 or 2) instead of melamine at KOH/ACDS ratio of 4 and 800 °C. These activated carbons were designated as DSU4800-1 or DSU4800-2, where U indicates use of urea, 4 is the KOH/ACDS ratio, 800 is the activation temperature (800 °C), and 1 or 2 are the urea/ACDS ratio. It is important to note that activation of melamine and urea was attempted, and that they yielded no activated carbons, as shown in **Figure 4.1**.

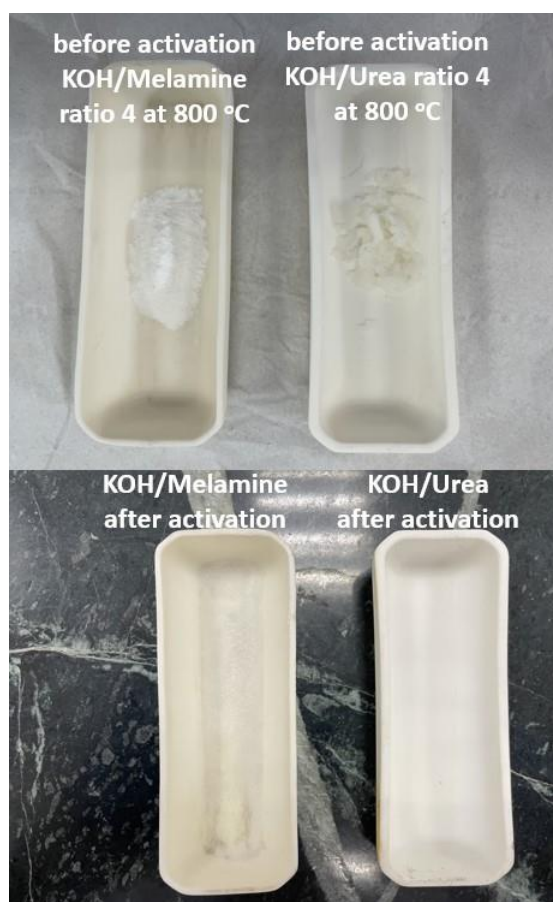


Figure 4.1. Photograph of the attempted activation of melamine and urea.

4.2.2 Materials Characterisation

An Exeter Analytical CE-440 Elemental Analyser Instrument was used for CHN elemental analysis. A TA Instruments SDT Q600 analyser were used to perform Thermogravimetric analysis (TGA) in ambient air (100 mL/min) conditions at heating ramp rate of 10 °C min⁻¹. Powder XRD analysis was performed using a PANalytical X'Pert PRO diffractometer with a Cu-K α light source (40 kV, 40 mA), a step size of 0.021, and step time of 50 s. Porosity analysis and textural properties of the activated carbons were determined using nitrogen sorption analysis (at -196 °C) using a Micromeritics 3FLEX sorptometer. The samples were degassed under vacuum for 16 h at 240 °C prior to analysis. The surface area was calculated using the Brunauer–Emmett–Teller (BET) method applied to nitrogen sorption isotherms according to Rouquerol rules, in the relative pressure (P/P_0) range of 0.02–0.22. The relative pressure range used to calculate surface area was maintained so that the multipoint BET fitting produced a positive y-axis intercept (i.e., $C > 0$) and $V_{ads}(1 - P/P_0)$

increased with P/Po. The total pore volume was determined from the total nitrogen adsorbed at a relative pressure near saturation ($P/P_o \approx 0.99$). The micropore surface area and micropore volume were obtained via t -plot analysis. The pore size distributions (PSDs) were determined by applying the Non-local density functional theory (NL-DFT) method to the nitrogen adsorption data with the assumption of a slit pore model. Scanning electron microscopy (SEM) images were obtained using a JEOL 7000F FEG-SEM microscope. Transmission electron microscopy (TEM) images were obtained using a JEOL 2100F instrument operating at 200 kV and equipped with a Gatan Orius CCD for imaging. Prior to analysis, the carbon samples were suspended in distilled water and dispersed onto lacey carbon support films.

4.2.3 Gas (CO₂ & CH₄) Uptake Measurements

Using a Hiden Isochema Intelligent Gravimetric Analyser (IGA-003), CO₂ uptake measurements of the carbons were determined in the pressure range of 0–20 bar at room temperature. The methane uptake was determined using a Hiden Isochema XEMIS analyser at 25 °C and a pressure range of 0–100 bar. In all cases, the carbons were degassed at 240 °C for several hours before performing the measurement of the gas uptake.

4.3 Results and Discussion

4.3.1 Yield and elemental compositions of N-doped carbons

The yields and elemental composition of the raw date seeds, air carbonised date seeds (ACDS), and activated carbons are summarised in **Table 4.1** and **Table 4.2**. The elemental composition of the raw date seeds reveals a high C content and relatively low O content with an O/C ratio of ~ 0.66 , which is one of the lowest observed for biomass sources where typical values are between 0.75 and 1.0.¹⁵ When biomass is subjected to air-carbonisation (AC), the O/C ratio of the resulting carbonaceous matter is reduced to a greater extent than for other carbonisation methods, namely, hydrothermal carbonisation (HTC) or conventional pyrolysis.³ For this reason we adopted flash air-carbonisation to convert the raw date seeds to carbonaceous matter (ACDS). Following air-carbonisation, the C content increased from 49.4 wt% for the raw date seeds to 76.7 wt% for the ACDS carbon. On the other hand, the apparent O content decreased from 43.5 wt% for the raw date seeds to 17.5 wt% for the ACDS

carbon, while the H content decreased from 6 wt% to 3.8 wt%. Thus the O/C ratio of the ACDS is 0.171, which is on the very low end for biomass-derived carbonaceous matter.¹⁵

Table 4.1. Yield and elemental composition of raw date seeds, air-carbonised date seeds (ACDS) and N-doped activated carbons prepared at melamine or urea/ACDS ratio of 1.

Sample	Yield [wt%]	C [%]	H [%]	N [%]	O [%]	(O/C) ^a	(N/C) ^a
Raw DS	-	49.4	6.0	1.1	43.5	0.660	0.019
ACDS	50	76.7	3.8	2.0	17.5	0.171	0.022
DSM-1	-	51.5	4.0	36.0	8.5	0.124	0.599
DSU-1	-	46.1	5.3	26.2	22.4	0.364	0.487
DSM2600-1	40	73.4	1.5	8.4	16.7	0.171	0.098
DSM2700-1	31	78.6	0.9	7.2	13.3	0.127	0.079
DSM2800-1	25	86.9	0.1	2.5	10.5	0.091	0.025
DSM4600-1	32	74.8	0.5	4.6	20.1	0.202	0.053
DSM4700-1	28	78.0	0.3	3.8	17.9	0.172	0.042
DSM4800-1	16	90.0	0.0	0.8	9.2	0.077	0.008
DSU4800-1	21	92.6	0.1	0.5	6.8	0.055	0.005

Table 4.2. Yield and elemental composition of raw date seeds, air-carbonised date seeds (ACDS) and N-doped activated carbons prepared at melamine or urea/ACDS ratio of 2.

Sample	Yield [wt%]	C [%]	H [%]	N [%]	O [%]	(O/C) ^a	(N/C) ^a
Raw DS	-	49.4	6.0	1.1	43.5	0.660	0.019
ACDS	50	76.7	3.8	2.0	17.5	0.171	0.022
DSM-2	-	43.7	4.2	47.5	4.6	0.079	0.932
DSU-2	-	38.2	5.8	33.6	22.4	0.440	0.754
DSM2600-2	33	67.7	1.5	18.0	12.8	0.142	0.228
DSM2700-2	28	72.5	0.9	14.9	11.7	0.121	0.176
DSM2800-2	23	77.3	0.7	10.1	11.9	0.115	0.112
DSM4600-2	25	74.7	1.3	7.4	16.6	0.167	0.085
DSM4700-2	18	76.0	0.6	7.0	16.4	0.162	0.079
DSM4800-2	10	89.6	0.2	1.2	9.2	0.077	0.012
DSU4800-2	9	90.5	0.0	0.5	8.9	0.074	0.005

Another important aspect to consider is the chemical composition of the pre-mixed precursor material following addition of melamine or urea to the ACDS. As shown in **Table 4.1** and **Table 4.2** the elemental composition of the premixed precursors changes drastically compared to the ACDS. The nominal N content increases significantly as expected, meaning that the proportion of C and O reduce. For the activated carbons, at melamine/ACDS ratio of 1, is between 0.8 and 8.4 wt% depending on the severity of activation. At melamine/ACDS ratio of 2, the activated carbons have N content of between 1.2 to 18.0 wt%, which is remarkably high. The N content of the activated carbons decreases with rise in activation temperature and/or amount of KOH used. For example, the N content of DSM2600-1 is 8.4 wt%, which reduces to 2.5 wt% for DSM2800-1, and 4.6 wt% for DSM4600-1. In this way, the N/C ratio decreases at higher activation temperature as shown in **Figure 4.2**. In

general, the C content of the activated carbons increases compared to that of the precursor, which is accompanied by a decrease in N, H and O, except that some samples activated at the lowest temperature show a decrease in their C content associated with their very high N content. Thus, the C content of activated carbons derived from DSM-1 increased from 73.4 wt% for DSM2600-1 to 90.0 wt% for DSM4800-1 wt%, while the H and O contents decreased from 1.5 and 16.7 wt% to 0 and 9.2 wt%, respectively. For DSM-2 derived carbons, the C content increases from 67.7 wt% (DSM2600-2) to 89.6 wt% (DSM4800-2), while the H content decreases from 1.5 to 0.2 wt% and the O content lowers from 12.8 to 9.2 wt%.

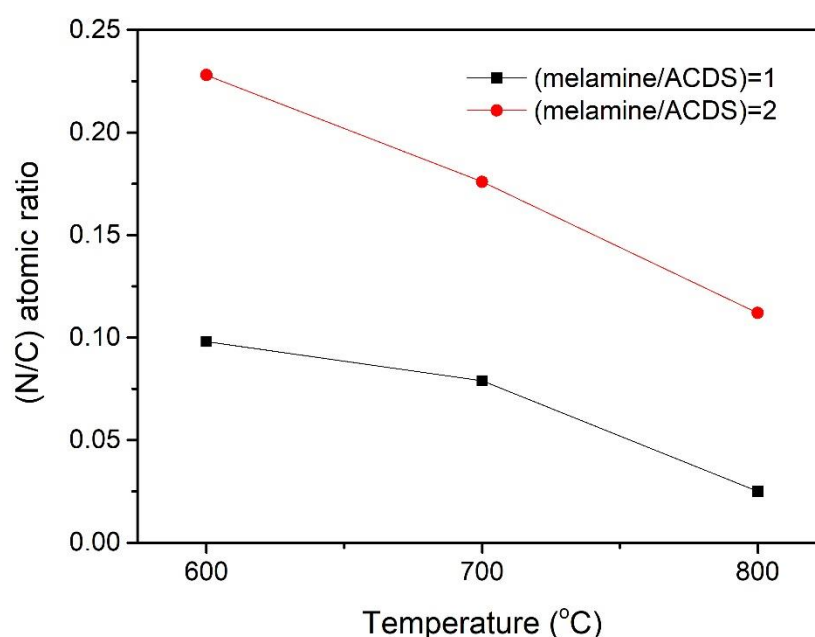
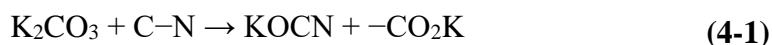


Figure 4.2. The N/C atomic ratio of activated carbons as a function of the activation temperature.

The yields of the samples are summarised in **Table 4.1** and **Table 4.2**. The flash air-carbonisation of raw date seeds resulted in a 50% yield of carbonaceous matter (i.e., ACDS carbon). On the other hand, when melamine is added to the KOH/ACDS mixture, the yield of activated carbon decreased. For the carbons obtained DSM-1, the yield is between 16 and 40 wt% and for those derived from DSM-2, the yield is between 10 and 33 wt%. The lower yield, especially at high activation temperature may be ascribed to the decomposition of endogenic carbon nitride. The presence of melamine during the activation increased the susceptibility of the ACDS carbon to

activation, meaning that the mechanism of activation is likely different from that of N-free precursors.^{7, 17, 20-22} In contrast to the N-free pathway, different behaviour is usually observed when N heteroatoms are present in the precursor. At elevated temperatures, the K^+ salts etch N species, resulting in N loss from the surface by the formation of inorganic salts (KOCN or KCN) according to (Eq. (4-1 and (4-2)).^{21, 22} The strength of interaction between N and K^+ depends on how much of each is present in the precursor. This is consistent with the elemental compositions of the activated carbons and shows that the overall loss of N, especially for high temperature activation, is related to the K/melamine ratio (N: K^+) during the activation process.



Altogether, it appears that K^+ attacks surface N species easily and preferentially, even when there are large amounts of surface O.²¹ This provides further evidence that the activation mechanism involves a surface-mediated etching reaction which has the effect of decreasing the overall yield of the carbons.

4.3.2 TGA analysis and the morphology of N-doped carbons

TGA was carried out to ascertain the purity of the carbons and their thermal stability. The TGA curves of the activated carbons are displayed in **Figure 4.3** and **Figure 4.4**, and as can be seen, the carbons are stable up to temperatures of 500 °C. All samples show an initial weight loss below 100 °C, which is attributed to the evaporation of adsorbed moisture. This is followed by a significant weight loss in a single step as a result of carbon combustion. In general, the carbons have residual mass close to nil, indicating that they are mostly composed of carbonaceous material with minimal, trace or nil amounts of inorganic material.

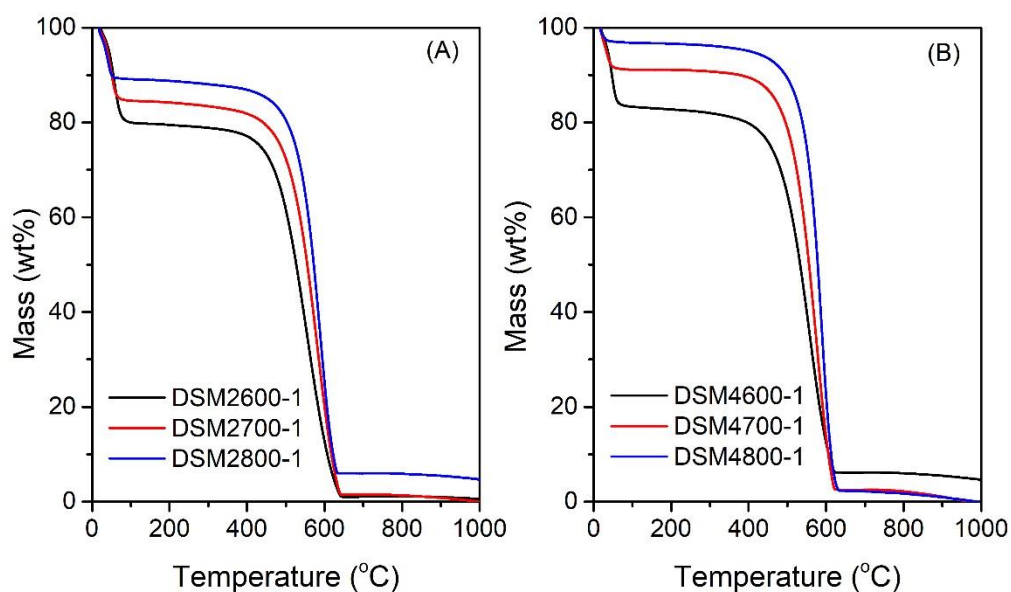


Figure 4.3. TGA curves of N-doped activated carbons prepared at KOH/ACDS ratio of 2 or 4 at 600, 700 or 800 °C and melamine/ACDS ratio of 1.

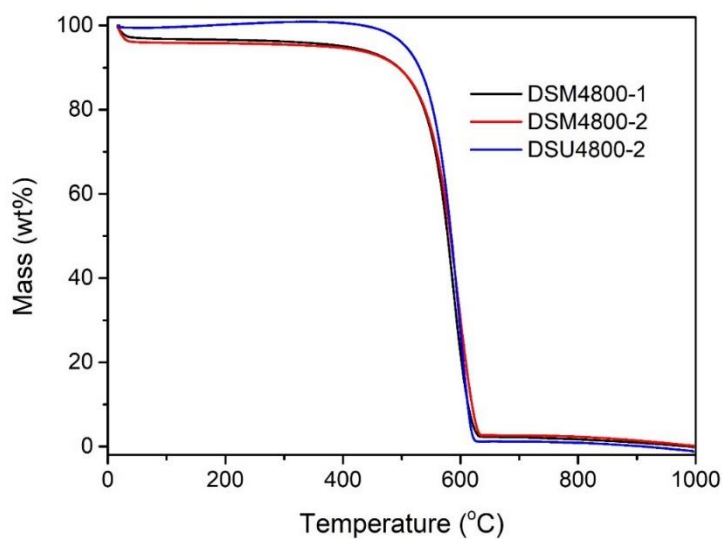


Figure 4.4. TGA curves of N-doped activated carbons prepared at 800 °C and KOH/ACDS ratio of 4 and various amounts of melamine or urea.

The X-ray diffraction (XRD) patterns of the samples are displayed in **Figure 4.5** and **Figure 4.6**. The XRD patterns show the typical broad peak at $\theta = 24.7^\circ$ and at $\theta = 43^\circ$ assigned to (002) and (100) diffractions of graphitic carbon, respectively. The intensity of these broad peaks reduced when the amount of activating agent was increased, as shown in **Figure 4.6(D)**, which supports the fact that the K^+ favoured to attack the N atoms present in the samples, which leads to greater amorphisation. The morphology of the N-doped carbons was analysed by scanning electron microscopy (SEM) and high-resolution transition electron microscopy (HRTEM). The SEM images of representative N-doped activated carbons are shown in **Figure 4.7**. The images of carbons obtained at a low ratio of KOH/ACDS ratio reveal a conchoidal morphology. Carbons prepared at higher KOH/ACDS have rough-surfaced morphology. The HRTEM images (**Figure 4.8**) reveal a disordered porous structure, which is typical for activated carbons.

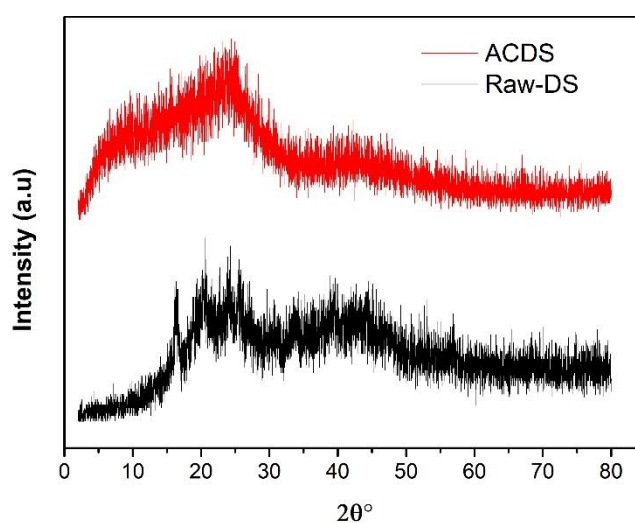


Figure 4.5. Powder XRD patterns of raw date seeds (Raw-DS) and air-carbonised dated seeds (ACDS).

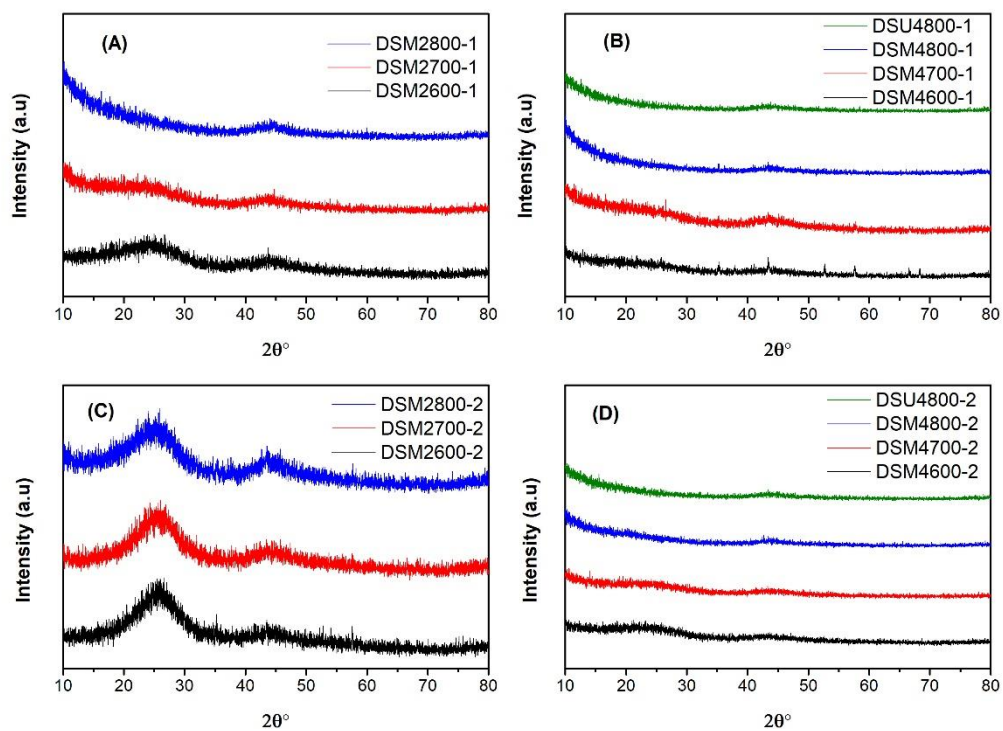


Figure 4.6. Powder XRD patterns of N-doped carbons activated at KOH/ACDS ratio 2 or 4 with melamine or urea as dopants.

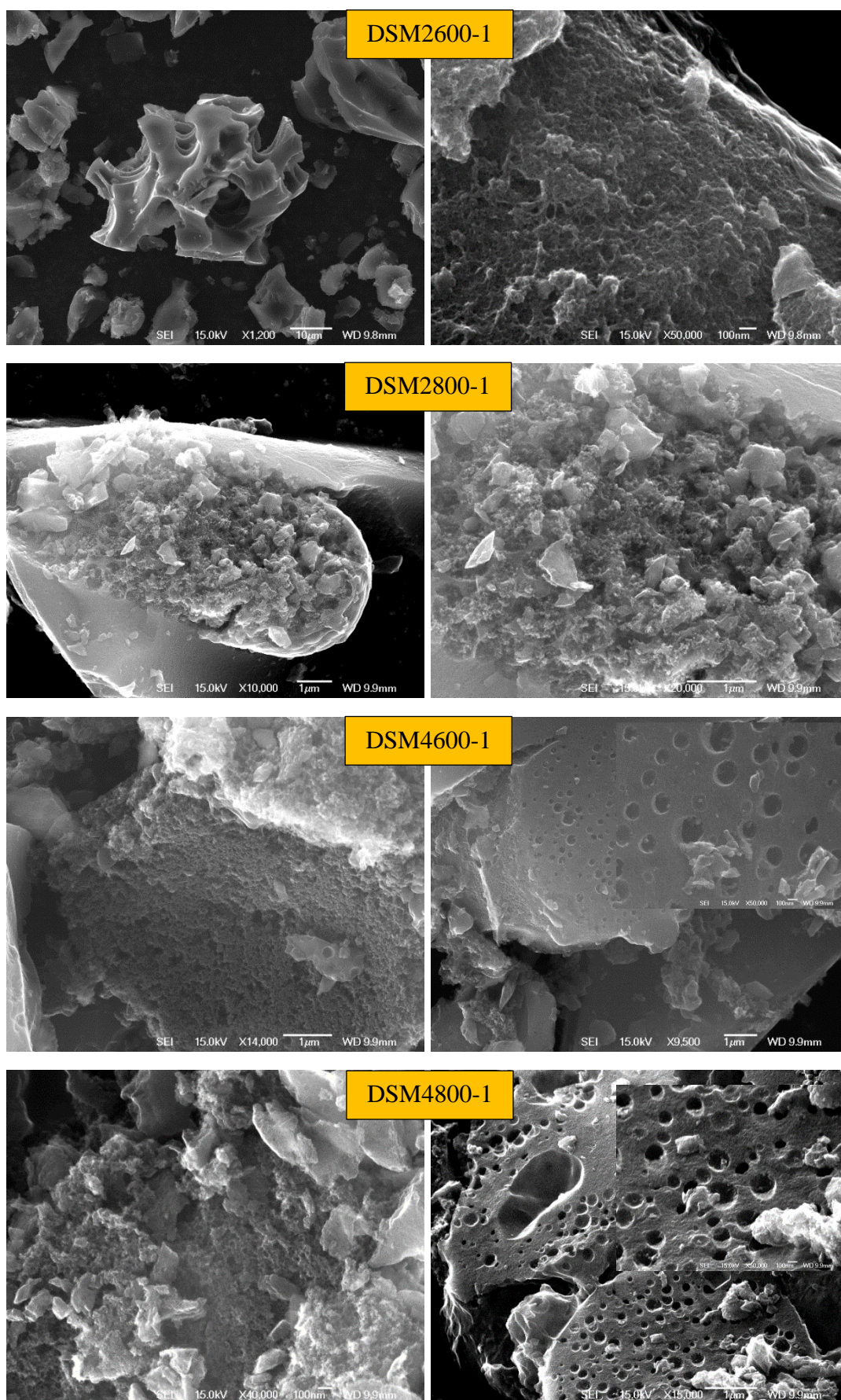


Figure 4.7. SEM images of selected N-doped activated carbons.

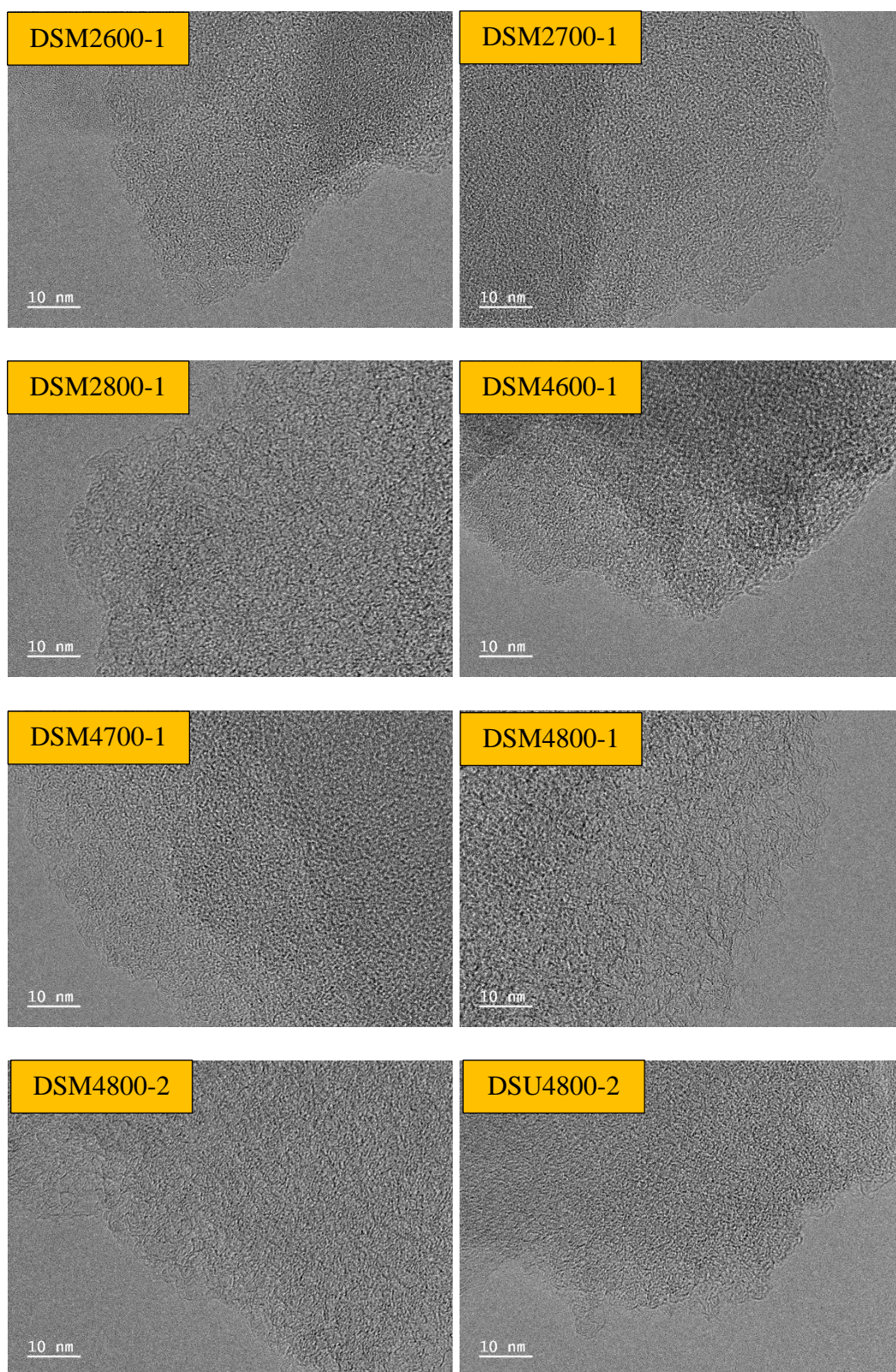


Figure 4.8. TEM images of selected N-doped activated carbons.

4.3.3 Porosity and textural properties

The nitrogen sorption isotherms and corresponding pore size distribution (PSD) curves of activated carbons prepared at melamine or urea/ACDS ratio of 1 are shown in **Figure 4.9** and **Figure 4.10**. The type of isotherms of this set of samples appeared to depend on the amount of the activation agent (KOH/ACDS) and/or the activation temperature. Thus, as shown in **Figure 4.9**, carbons obtained at a KOH/ACDS ratio of 2 exhibit type I isotherms indicative of microporosity but with a broader adsorption “knee” for samples prepared at higher activation temperature (e.g. DSM2800-1). The broadening in the adsorption knee indicates the presence of larger pores (micropores and small mesopores), as confirmed by the PSD curves in **Figure 4.9B**. The isotherms of samples prepared at KOH/ACDS ratio of 4 are either type I (DSM4600-1 and DSM4700-1) or show a greater proportion of mesoporosity at higher activation temperature (DSM4800-1) as shown in **Figure 4.10**. The isotherms of DSM4600-1 and DSM4700-1 are primarily type I but with a broader adsorption knee, indicating the presence of larger micropores. Upon increasing the temperature to 800 °C, the isotherm shape and quantity of nitrogen adsorbed for samples (DSM4800-1 and DSU4800-1) altered from type I (microporous) to type IV (mesoporous nature). Interestingly, the isotherms of DSM4800-1 and DSU4800-1 even though they were prepared from different additives, melamine and urea, respectively. The near mesoporous nature of DSM4800-1 and DSU4800-1 contrasts with the microporous nature of carbons prepared from activation of ACDS alone.³⁷ Clearly, the presence of melamine and urea, which introduce N to the activation mix, has the effect of increasing the susceptibility of the ACDS carbon to activation thus generating larger pores with dimensions in the large micropore and small mesopore range as shown in **Figure 4.10B**.

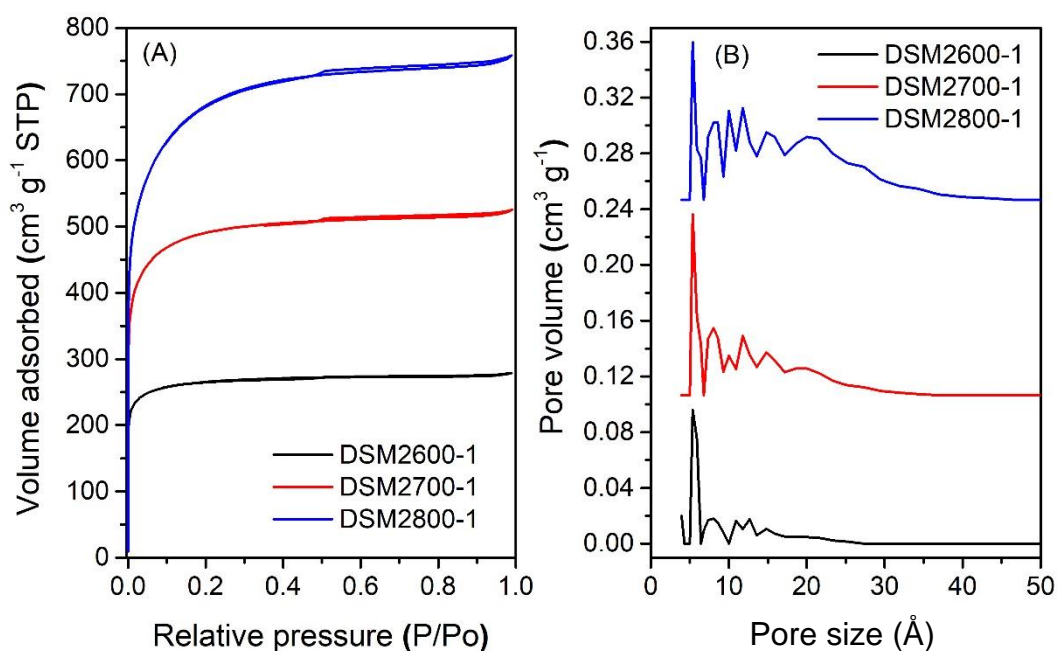


Figure 4.9. Nitrogen sorption isotherms (A) and pore size distribution curves (B) of N-doped activated carbons prepared at melamine/ACDS ratio of 1 and KOH/ACDS ratio of 2.

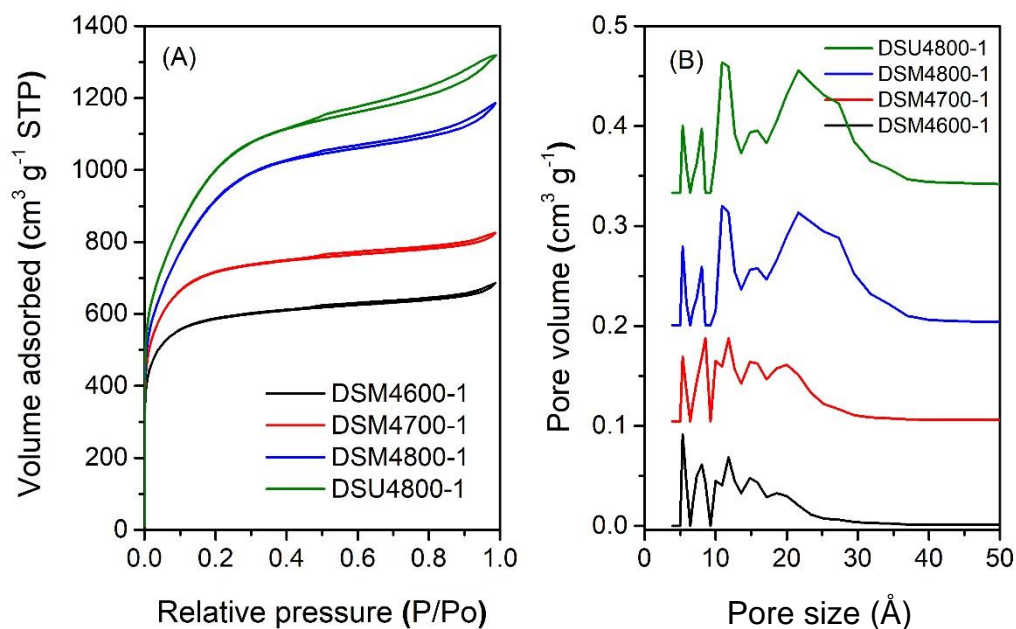


Figure 4.10. Nitrogen sorption isotherms (A) and pore size distribution curves (B) of N-doped activated carbons prepared at melamine or urea/ACDS ratio of 1 and KOH/ACDS ratio of 4.

The nitrogen sorption isotherms and PSD curves of activated carbons prepared at melamine or urea/ACSD ratio of 2 are shown in **Figure 4.11** and **Figure 4.12**. In general, except for samples generated at a high severity of activation (DSM4800-2 and DSU4800-2), all samples show a type I isotherm, typical of microporous materials, with most nitrogen adsorption occurring at very low relative pressure ($P/P_o < 0.01$). The total amount of nitrogen adsorbed (i.e., level of porosity) rises as (i) activation temperature increases from 600 to 800 °C, and/or (ii) the amount of KOH increases from KOH/ACDS ratio of 2 to 4. Carbons prepared at a KOH/ACDS ratio of 2 (**Figure 4.11**) are microporous although with a broad knee for DSM2800-2. For the carbons prepared at KOH/ACDS ratio of 4 (**Figure 4.12**), the isotherms for DSM4600-2 and DSM4700-2 are typically microporous while those for DSM4800-2 and DSU4800-2, on the other hand, shift towards significant mesoporosity (i.e., isotherms of type IV-character). Overall, the isotherms of carbons generated at a melamine/ACDS ratio of 1 are very similar to those generated at melamine/ACDS ratio of 2, although the former suggest higher levels of porosity. This suggest that use of excessive amounts of N-dopants, i.e., melamine/ACDS ratio beyond 1, does not significantly alter the porosity.

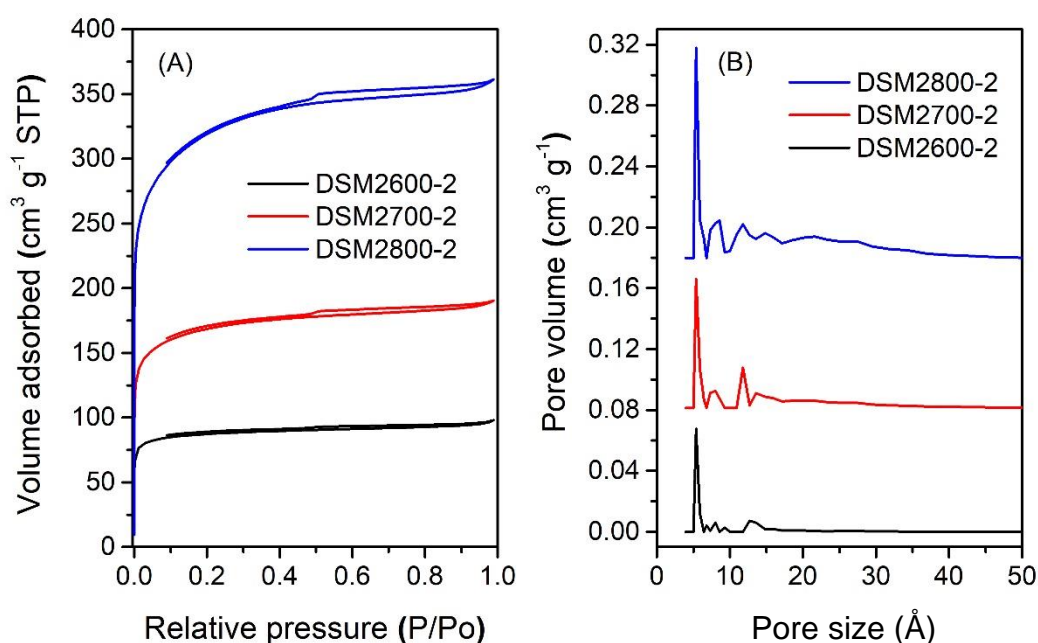


Figure 4.11. Nitrogen sorption isotherms (A) and pore size distribution curves (B) of N-doped activated carbons prepared at melamine/ACDS ratio of 2 and KOH/ACDS ratio of 2.

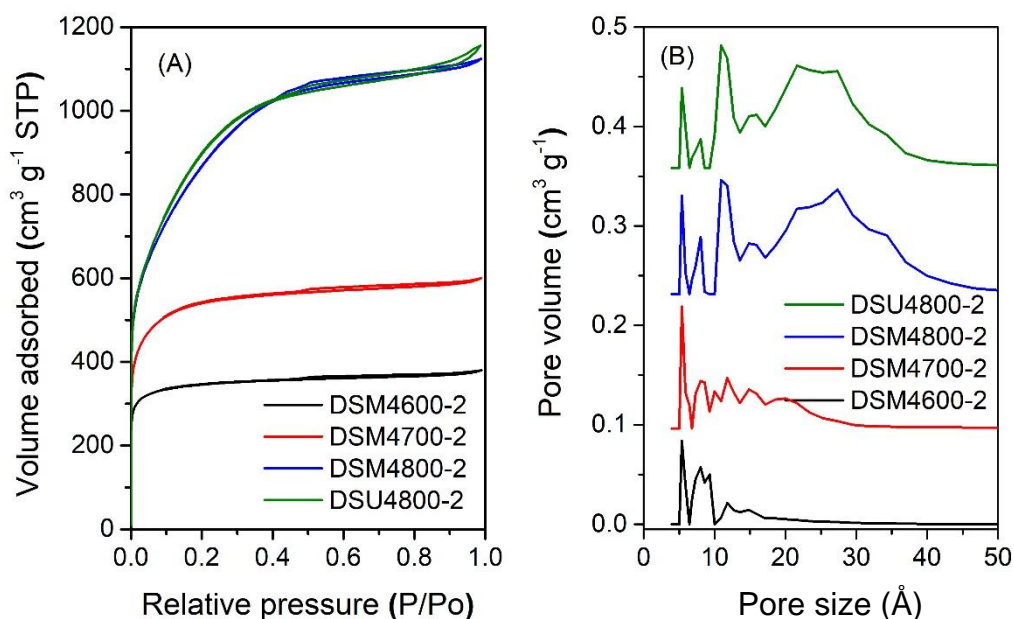


Figure 4.12. Nitrogen sorption isotherms (A) and pore size distribution curves (B) of N-doped activated carbons prepared at melamine or urea/ACDS ratio of 2 and KOH/ACDS ratio of 4.

The porosity depicted in **Figure 4.9(B)** and **Figure 4.12(B)** clearly shows that the N:K ratio plays an important role in pore formation (porogenesis) of the resulting carbons. For the DSMxT-1 carbons, porosity levels range from microporous to mesoporous depending on the amount of KOH and activating temperature. For samples DSM2600-1, DSM2700-1 and DSM2800-1, the porosity falls in between micro/supermicroporous to small mesoporous (1.0–2.5 nm pores), with moderate N content retained in the carbons. For samples activated with higher amounts of KOH (KOH/precursor a ratio of 4), there was a greater loss in N content accompanied by the formation of larger pores. Bimodal pore size distributions are seen in these samples, with a smaller percentage of micropores centred at ca. 0.8 nm and 1.1 nm and a much greater proportion of mesopores centred at ca. 2.5 nm, as shown in **Figure 4.9(B)**. Thus the proportion of mesopores in DSM2T-1 carbons is lower than for DSM4T-1 samples, which may be ascribed to greater formation of K_2CO_3 (see **equations 4-1 and 4-2 in page 130**) leading to more etching out of N species with the overall effect of increasing the porosity generated.

On the other hand, at melamine/ACDS ratio of 2, there is an increase in the N content relative to the K in the mixture (i.e., rise in N/K ratio), meaning that there is in effect an excess amount of N, which is then retained in the activated carbon at amounts of up to 18 wt% as shown in **Table 4.2**. A higher amount of N can also lead to the formation of KCN, which is an unreacted species.²¹ This unreacted species can result in a decrease in porosity at apparently high N content.²¹ The resulting carbons, DSM2600-2, DSM2700-2, and DSM2800-2, have ultra-microporous characteristics with pores centred at 0.5 to 1.1 nm and hardly any pores larger than 2 nm. At melamine/ACDS ratio of 2, and higher KOH, the lowering in the N:K ratio resulted in the removal of more N species from the carbons for samples DSM4T-2. For activation at 600 °C and 700 °C, samples DSM4600-2 and DSM4700-2 reveal a micro- and supermicropore structure with a size distribution dominated by 1.2 nm pores and some small mesopores. Samples DSM4800-2 and DSU4800-2, on the other hand, exhibit a pore size distribution very comparable to DSM4800-1 and DSU4800-1, with mesopores centred at 2.7 nm. It appears that when higher amounts of melamine are used, KOH serves as the limiting agent and as a result significant N content was retained in the carbons, which limited the overall porosity.

The level of porosity in the resulting carbons can be interpreted as follows: The decomposition of KOH to K_2CO_3 occurs at high temperatures. When N heteroatoms are present during the synthesis of the activated carbons, different pathway is taken during the activation process. As shown in **equation (4-1)**, the K_2CO_3 attacks the N-C on the surface of the ACDS carbon, resulting in the formation of N adducts (KOCN) at ca. 600 °C and the formation of some porosity. Sevilla, *et al.* found that the intermediate KOCN is a reactive form, and upon further heating, the KOCN works as an oxidising agent and can create significant porosity, as seen in **equation (4-2)**. Thus, the enhancement observed in the mesopore region takes place at 700 °C, which is the temperature at which the decomposition of K_2CO_3 with N-C occurs. This is accompanied by a decrease in the yield of product, from 40% at 600 °C (sample DSM2600-1) to 31% at 700 °C (sample DSM2700-1), and a reduction in N content (**Table 4.1**). Further increase in activation temperature from 700 to 800 °C largely enhances the proportion of pores of size ~ 3 nm, accompanied by a drop in the carbon yield to 16% for DSM4800-1. As more N atoms are involved in the reaction and removed by the etching reaction with K_2CO_3 , larger pores are generated alongside with

small proportion of micropores. However, when the N content is very high and a low amount of KOH is used (DSM2T-2), the amount of generated K_2CO_3 works as a limiting agent, resulting in excess N content remaining in the resulting carbons. Altogether, in this way, the melamine acts as both an N-dopant and a structure-directing agent (porogen) by extending the size distribution of the pores into the mesopore region.

The textural properties of the N-doped activated carbons are given in **Table 4.3**, and show that the surface area and pore volume range from moderate to ultra-high depending on the amount of N-dopant and the severity of activation. For samples prepared at a melamine/ACDS ratio of 1, the surface area ranges from $1029 \text{ m}^2 \text{ g}^{-1}$ for DSM2600-1 to $2536 \text{ m}^2 \text{ g}^{-1}$ for DSM2800-1, and from $2226 \text{ m}^2 \text{ g}^{-1}$ for DSM4600-1 to $3360 \text{ m}^2 \text{ g}^{-1}$ for DSM4800-1, while the equivalent sample prepared in presence of urea (DSU4800-1) has the highest surface area of $3646 \text{ m}^2 \text{ g}^{-1}$. A similar patterns is observed for the pore volume, varying from 0.43 to $1.18 \text{ cm}^3 \text{ g}^{-1}$ for DSM2T-1 samples, 1.06 to $1.84 \text{ cm}^3 \text{ g}^{-1}$ for DSM4T-1 samples, and reaching $2.05 \text{ cm}^3 \text{ g}^{-1}$ for DSU4800-1. When the amount of melamine was increased, the surface area and pore volume decreased at any given activation conditions. DSM2T-2 carbons have surface areas ranging from $340 \text{ m}^2 \text{ g}^{-1}$ for DSM2600-2 to $1161 \text{ m}^2 \text{ g}^{-1}$ for DSM2800-2 and pore volume of $0.15 \text{ cm}^3 \text{ g}^{-1}$ and $0.56 \text{ cm}^3 \text{ g}^{-1}$, respectively. Carbons prepared with a high amount of KOH (DSM4T-2) had a larger surface area and pore volume of $1322 \text{ m}^2 \text{ g}^{-1}$ and $0.59 \text{ cm}^3 \text{ g}^{-1}$ for DSM4600-2, which increased to $3138 \text{ m}^2 \text{ g}^{-1}$ and $1.75 \text{ cm}^3 \text{ g}^{-1}$ for DSM4800-2. Sample DSU4800-2, which was prepared in the presence of urea, has the highest surface area ($3270 \text{ m}^2 \text{ g}^{-1}$) and pore volume ($1.79 \text{ cm}^3 \text{ g}^{-1}$) in this group of samples. In general, the samples prepared in the presence of urea (DSU4800-y) generated carbons with a higher surface area than their counterparts (DSM4800-y), prepared with melamine. This is because melamine has a bulk N content of $\sim 67 \text{ wt\%}$ compared to 46 wt\% for urea, meaning a higher N/K ratio for the former. It is noteworthy that the retained N content follows the trend $\text{DSM4800-2} > \text{DSU4800-2} > \text{DSM4800-1} > \text{DSU4800-1}$, which is consistent with their surface areas of 3138 , 3270 , 3360 and $3646 \text{ m}^2 \text{ g}^{-1}$. Thus DSU4800-1 has the lowest N/K ratio among all samples in this study and the highest surface area and pore volume, which may be attributed to the ideal ratio of N/K where significant amount of N are consumed during the activation. Interestingly, the significant increase in the surface area from

modest to ultra-high is consistent with the decreasing N content (N/C) in the samples, which, as described above, means more N was involved in the creation of the surface area and porosity.^{21, 22}

The surface area density (SAD) of the carbons, defined as the ratio of surface area to pore volume, is shown in **Table 4.3**. The SAD shows a clear correlation with the nature of porosity, and decreases at higher levels of mesoporosity. For melamine/ACDS ratio of 1, the SAD ranges between 2393 and 2149 m² cm⁻³ for DSM2T-1 carbons, and between 2100 m² cm⁻³ and 1826 m² cm⁻³ for DSM4T-1 carbons. For melamine/ACDS ratio of 2, the SAD ranges from 2267 to 2073 m² cm⁻³ for DSM2T-2 carbons and 2241 to 1793 m² cm⁻³ for DSM4T-2 samples. The DSU4800-1 sample, which has the highest surface area, had surface area density of 1779 m² cm⁻³, which is the lowest observed in this study due to a high level of mesoporosity.

Table 4.3. Textural properties of N-doped activated carbons prepared at melamine or urea/ACDS ratio of 1 or 2, KOH/ACDS ratio of 2 or 4, and activation temperature of 600, 700, or 800 °C.

Sample	BET surface area / m ² g ⁻¹		Pore Volume / cm ³ g ⁻¹		Surface area density ^c (m ² cm ⁻³)	Packing density ^d (g cm ⁻³)	Volumetric surface area ^f (m ² cm ⁻³)
	Total	Micro (%) ^a	Total	Micro (%) ^b			
DSM2600-1	1029	891 (87)	0.43	0.35 (82)	2393	0.89	916
DSM2700-1	1859	1441 (78)	0.82	0.58 (71)	2267	0.74	1376
DSM2800-1	2536	1513 (60)	1.18	0.60 (57)	2149	0.65	1648
DSM4600-1	2226	1690 (76)	1.06	0.67 (63)	2100	0.68	1514
DSM4700-1	2672	1712 (64)	1.28	0.68 (53)	2088	0.59	1577
DSM4800-1	3360	510 (15)	1.84	0.15 (8)	1826	0.45	1512
DSU4800-1	3646	578 (16)	2.05	0.19 (9)	1779	0.41	1495
DSM2600-2	340	295 (87)	0.15	0.12 (80)	2267	-	-
DSM2700-2	635	484 (76)	0.30	0.20 (67)	2117	-	-
DSM2800-2	1161	756 (65)	0.56	0.32 (57)	2073	-	-
DSM4600-2	1322	1113 (84)	0.59	0.44 (75)	2241	-	-
DSM4700-2	1989	1383 (70)	0.93	0.57 (61)	2139	-	-
DSM4800-2	3138	400 (13)	1.75	0.14 (8)	1793	0.43	1349
DSU4800-2	3270	366 (11)	1.79	0.11 (6)	1827	0.41	1341

^aThe values in parentheses represent the proportion of micropores, and ^b is the proportion of micropore volume. Surface area density (SAD)^c defined as the ratio of surface area to pore volume. To calculate the packing density^d, a known quantity of carbon was compressed in a 1.3 cm die at 7 MPa for 10 minutes. Multiplying the surface area by the packing density yields the volumetric surface area^f.

4.3.4 Gas uptake

4.3.4.1 CO₂ uptake

Given the broad range of porosity for the present carbons, their potential use as stores for carbon capture and storage (CCS) was investigated at 25 °C and a pressure range of 0–20 bar. **Figure 4.13** and **Figure 4.14** show the CO₂ uptake isotherms for DSMxT-1 carbons along with sample DSU4800-1, and **Table 4.4** summarises the CO₂ uptake (mmol g⁻¹) at various pressures (0.15 bar, 1 bar and 20 bar). The CO₂ uptake at 1 bar (**Figure 4.13B**) for DSM2T-1 carbons is very attractive and ranges from 4.3 mmol g⁻¹ (DSM2600-1) to 4.6 mmol g⁻¹ (DSM700-1) with a decrease to 4.1 mmol g⁻¹ for DSM2800-1. For DSM4T-1 carbons (**Figure 4.14B**), the CO₂ uptake is lower and in the range 3.2–4.1 mmol g⁻¹ as a consequence of lower levels of microporosity. This trend confirms that the CO₂ uptake at low pressure is dependent on the pore size of the adsorbent rather than the overall surface area, which is in line with previous reports that low pressure CO₂ uptake is determined by the preponderance of narrow micropores.²³⁻²⁵ At uptake pressure of 20 bar, however, the situation is reversed, and the CO₂ storage capacity of DSM4T-1 carbons is higher due to the greater dependence of uptake on the total surface area. The CO₂ uptake of DSM4800-1 and DSU4800-1 at 20 bar is as high as 24.9 and 24.7 mmol g⁻¹, but still not at saturation point, meaning that these samples can store more CO₂ at higher pressures (**Figure 4.13**, **Figure 4.14** and **Table 4.4**). At uptake pressure of 0.15 bar, DSM2T-1 carbons show attractive CO₂ uptake of 1.67 mmol g⁻¹ for DSM2600-1, 1.37 mmol g⁻¹ for DSM2700-1 and 0.97 mmol g⁻¹ for DSM2800-1 as shown in **Figure 4.13** and **Table 4.4**. The trend to lower CO₂ uptake for DSM2800-1 is due to pore widening. It is worth noting that CO₂ uptake at 25 °C and 0.15 bar of 1.67 mmol g⁻¹ for DSM2600-1 is among the highest reported for any porous material.^{24, 26-43} The uptake for DSM4T-1 samples is lower and ranges between 0.63 and 1.05 mmol g⁻¹, which is to be expected due to their lower levels of microporosity. Overall, the uptake of CO₂ at low pressures of 0.15 bar and 1 bar is strongly affected by the pore size, with the narrow microporous carbons exhibiting higher uptake.

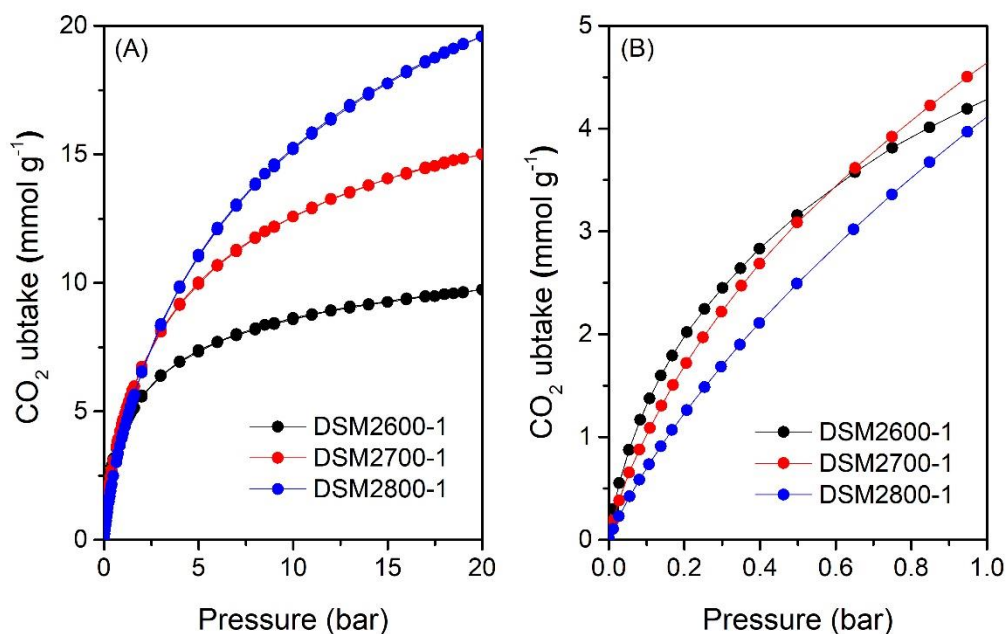


Figure 4.13. CO₂ uptake isotherms at 25 °C of N-doped activated carbons prepared at melamine/ACDS ratio of 1 and KOH/ACDS ratio of 2.

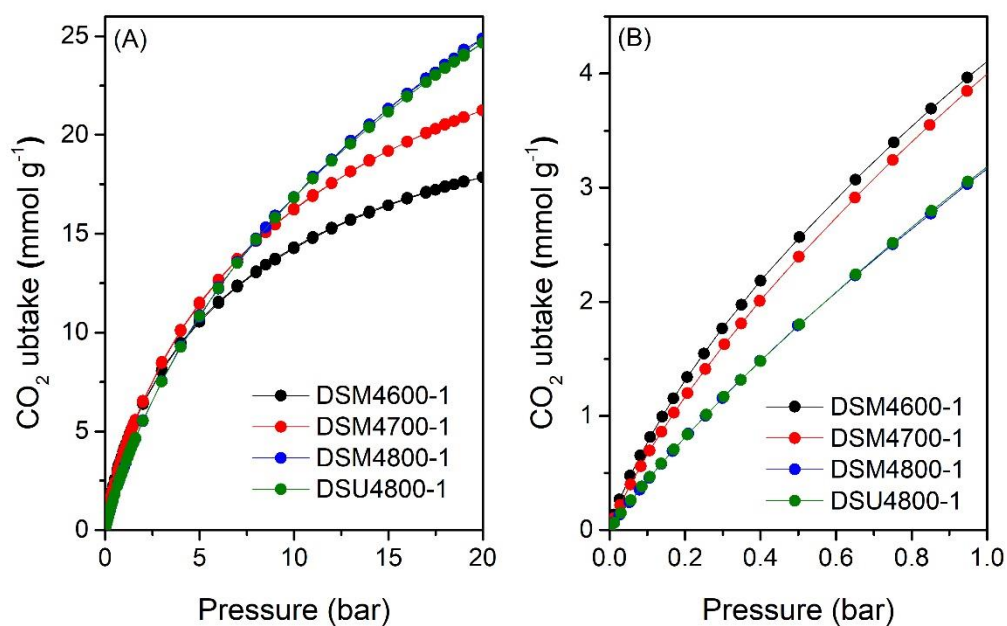


Figure 4.14. CO₂ uptake isotherms at 25 °C of N-doped activated carbons prepared at melamine or urea/ACDS ratio of 1 and KOH/ACDS ratio of 4.

Table 4.4. CO₂ uptake at 25 °C and various pressures (0.15, 1 and 20 bar) of N-doped activated carbons prepared at melamine or urea/ACDS ratio of 1 and KOH/ACDS ratio of 2 or 4.

Sample	CO ₂ uptake (mmol g ⁻¹)		
	0.15 bar	1 bar	20 bar
DSM2600-1	1.67	4.3	9.8
DSM2700-1	1.37	4.6	15.0
DSM2800-1	0.97	4.1	19.6
DSM4600-1	1.05	4.1	17.9
DSM4700-1	0.92	4.0	21.3
DSM4800-1	0.63	3.2	24.9
DSU4800-1	0.63	3.2	24.7

The CO₂ uptake isotherms of DSMxT-2 carbons and DSU4800-2 are shown in **Figure 4.15** and **Figure 4.16**. **Table 4.5** summarises the CO₂ storage capacity of these samples at various pressures (0.15, 1 and 20 bar). At 1 bar (**Figure 4.15B** and **Figure 4.16B**), the storage capacity of DSM2T-2 carbons increases from 2.5 mmol g⁻¹ for DSM2600-2 to 3.4 mmol g⁻¹ for DSM2800-2, whereas carbons derived from harsh activation conditions (DSM4T-2) show uptake of ~3.2 mmol g⁻¹ for DSM4800-2 and DSU4800-2, which rises to 4.7 and 4.3 mmol g⁻¹ for samples obtained at lower activation temperatures of 600 °C and 700 °C, respectively. The highest uptake at 1 bar and 25 °C of 4.7 mmol g⁻¹ is observed for DSM4600-2. All the samples approach saturation at 20 bar (**Figure 4.15A** and **Figure 4.16A**) with the exception of DSM4800-2 and DSU4800-2. The lower uptake for some samples at 20 bar is attributed to the use of a higher amount of melamine, which leads to the generation of N-rich carbons, which is accompanied by lowering the surface area and narrower pores.²² On the other hand, the CO₂ uptake at very low pressure of 0.15 bar (**Figure 4.15B** and **Figure 4.16B**) is very attractive and in a narrow range between 1.22 and 1.32 mmol g⁻¹ for DSM2T-2 carbons, with the highest uptake registered for the sample DSM2700-2. It is interesting to note that the uptake for samples prepared with a KOH/ACDS ratio of 2 was nearly matched regardless of activation temperature and N content. The CO₂ uptake for

samples activated at a KOH/ACDS ratio of 4 is more varied; 1.58 mmol g⁻¹ for DSM4600-2 and 1.20 mmol g⁻¹ for DSM4700-2, and decreases to between 0.69 and 0.65 mmol g⁻¹ for DSM4800-2 and DSU4800-2, respectively. The lowering in the uptake for DSM4800-2 and DSU4800-2 is expected due to their wider porosity, which is evidence that the uptake at low pressure is not determined by the surface area but mainly by the pore size of the adsorbent. Notably, DSM4600-2 had the highest CO₂ uptake at 0.15 and 1 bar of 1.58 and 4.7 mmol g⁻¹, respectively. This uptake is amongst the highest ever reported for N-doped carbon materials, which show a great promise as post-combustion CO₂ storage materials.^{24, 26-43}

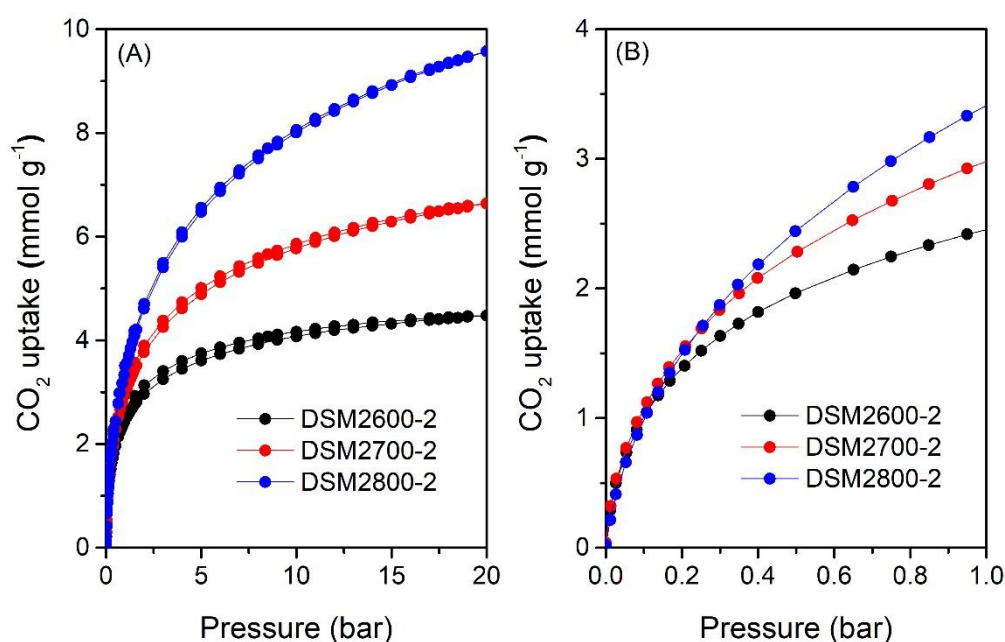


Figure 4.15. CO₂ uptake isotherms at 25 °C of N-doped activated carbons prepared at melamine/ACDS ratio of 2 and KOH/ACDS ratio of 2.

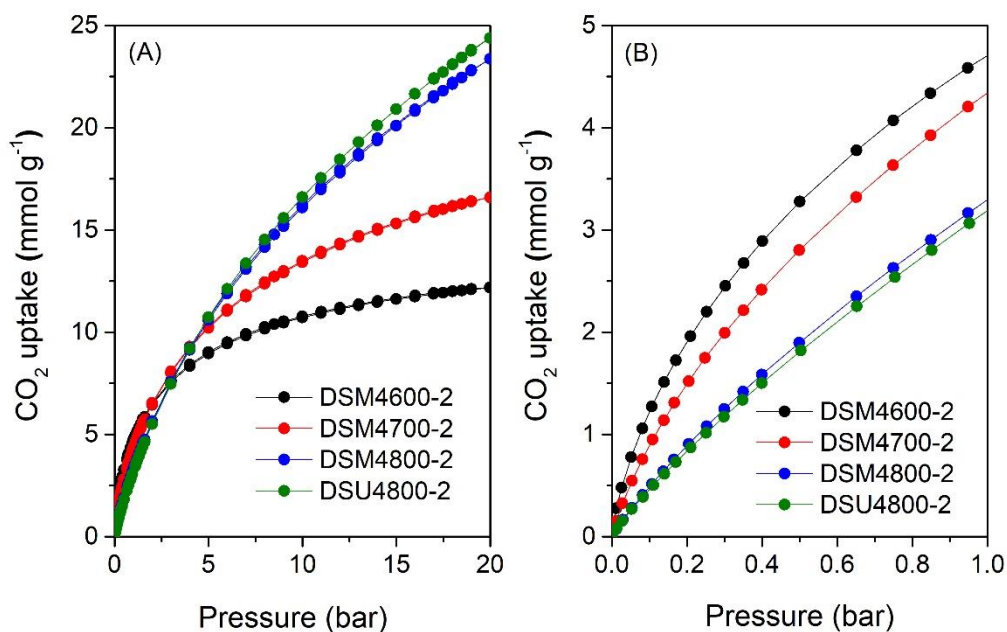


Figure 4.16. CO₂ uptake isotherms at 25 °C of N-doped activated carbons prepared at melamine or urea/ACDS ratio of 2 and KOH/ACDS ratio of 4.

Table 4.5. CO₂ uptake at 25 °C and various pressures (0.15, 1 and 20 bar) of N-doped activated carbons prepared at melamine or urea/ACDS ratio of 2 and KOH/ACDS ratio of 2 or 4.

Sample	CO ₂ uptake (mmol g ⁻¹)		
	0.15 bar	1 bar	20 bar
DSM2600-2	1.22	2.5	4.5
DSM2700-2	1.32	3.0	6.6
DSM2800-2	1.26	3.4	9.6
DSM4600-2	1.58	4.7	12.2
DSM4700-2	1.20	4.3	16.0
DSM4800-2	0.69	3.3	23.4
DSU4800-2	0.65	3.2	24.4

4.3.4.2 Methane storage

Porous materials must possess the appropriate combination of micro- and mesoporosity, large surface area, and high packing density in order to effectively store methane at moderate to high pressure (35-100 bar). The presence of optimal microporosity is important to enhance the packing density, which is key for enhanced volumetric methane uptake, while mesoporosity is essential for facilitating the sorption kinetics and improving the working capacity or deliverable methane for pressure swing processes.^{1, 13, 15, 25, 44-48} The high surface area of the present carbons (**Table 4.3**), and the mix of their microporosity and mesoporosity suggest that they may be suitable stores for methane. The excess methane uptake was directly determined at pressures between 0 and 100 bar and 25 °C. The uptake at pressures of 35, 65 and 100 bar was the emphasis as they offer a practical measure of performance that has been extensively used in earlier research, which therefore simplifies direct comparisons to the current state-of-the-art materials.^{1, 13, 15, 25, 44-48} The total methane uptake capacity was calculated from the excess data by considering the methane density and the total pore volume of the adsorbing carbons according to the following equation:

$$\theta_T = \theta_{Exc} + d_{CH_4} \times V_T \quad (4-3)$$

Where: θ_T is total methane uptake (g g⁻¹), θ_{Exc} is excess methane uptake (g g⁻¹), d_{CH_4} is methane density (g cm⁻³) at any given pressure at 25 °C, and V_T is total pore volume (cm³ g⁻¹) of the activated carbon. The density of methane (d_{CH_4}) was obtained from the National Institute of Standards and Technology (NIST) website (<https://www.nist.gov/>).

Figure 4.17 shows the excess CH₄ uptake isotherms at 25 °C for a selection of samples, and the methane storage capacity at 35, 65, and 100 bar is summarised in **Table 4.6**. In general, the excess methane uptake is proportional to the surface area, and the isotherms are completely reversible with no hysteresis. It is apparent that the excess uptake sharply increased at low pressure and then shows a gradual increase at pressures above 60 bar, which indicates that storage capacity approaches saturation at pressure of ca. 60 bar. **Figure 4.17A** shows the uptake of representative DSMxT-1 carbons that have sufficiently high surface area to be of interest as methane stores. These samples have high methane storage capacity, with greater storage for

samples that have higher surface area, i.e., DSM2700-1 < DSM4600-1 < DSM2800-1 < DSM4700-1. For instance, the excess uptake at 35 bar is in the range of 8.5-10.9 mmol g⁻¹, and increased to 9.5-12.4 and 9.8-12.7 mmol g⁻¹ at pressures of 65 and 100 bar, respectively. On the other hand, the excess methane uptake of samples obtained under severe activation conditions (DSM4800-1, DSM4800-2, DSU4800-1 and DSU4800-2), show higher methane uptake, as shown in **Figure 4.17B** and **Table 4.6**. The methane storage capacity of these carbons is in a very narrow range. For example at 35 bar, the uptake is between 12.2 and 13.0 mmol g⁻¹, and ranges from 14.5 to 15.5 mmol g⁻¹ at 65 bar, which further increases to between 14.8 and 16.3 mmol g⁻¹ at 100 bar. The excess methane uptake of 13.0 mmol g⁻¹ at 25 °C and 35 bar DSU4800-1 is among the highest ever reported for any porous materials and demonstrates the capability of the present carbons for methane storage at moderate pressure.^{13, 15, 25, 44-54} Generally, the highest excess methane uptake at 25 °C and 100 bar is for the samples with the highest surface area (DSU4800-1 and DSM4800-1) at 16.3 and 15.5 mmol g⁻¹, respectively. It can be inferred from the excess uptake that samples prepared with a low N/K ratio store more methane than those prepared at higher ratio. This is an indication that the strategy of adding N-containing additives, as structure-directing agents, to the ACDS precursor enhances the methane storage capacity.

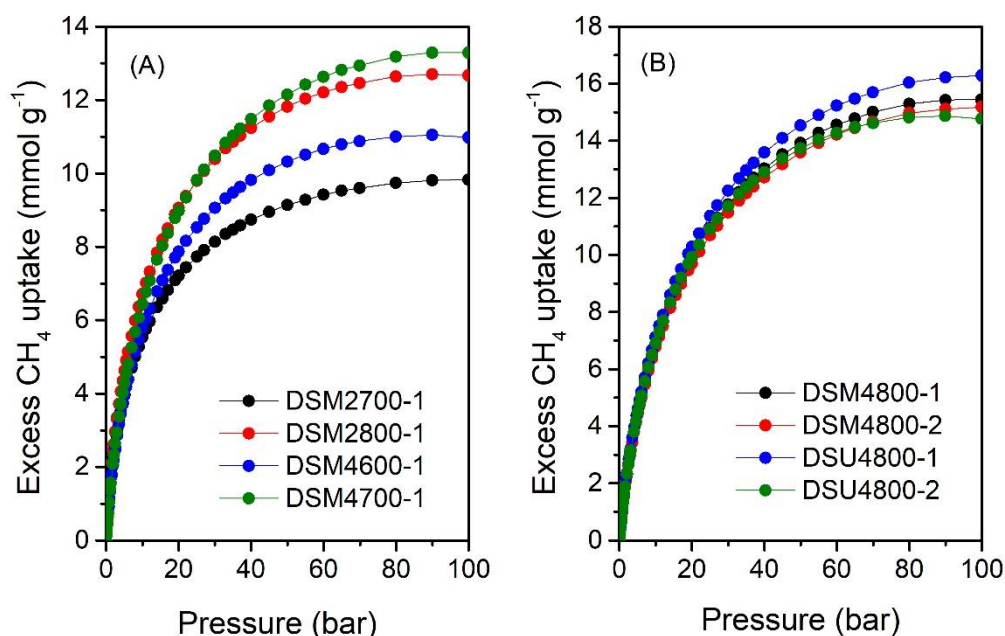


Figure 4.17. Excess gravimetric methane uptake isotherms at 25 °C of N-doped activated carbons prepared at KOH/ACDS ratio of 2 or 4 and melamine or urea/ACDS ratio of 1 or 2.

Table 4.6. Excess gravimetric methane uptake at 25 °C and pressures of 35, 65 and 100 bar of N-doped activated carbons prepared at KOH/ACDS ratio of 2 or 4 and melamine or urea/ACDS ratio of 1 or 2.

Sample	Excess gravimetric methane uptake (mmol g ⁻¹) or (g g ⁻¹) ^a		
	35 bar	65 bar	100 bar
DSM2700-1	8.5 (0.14)	9.5 (0.15)	9.8 (0.16)
DSM2800-1	10.9 (0.17)	12.4 (0.20)	12.7 (0.21)
DSM4600-1	9.5 (0.15)	10.8 (0.17)	11.0 (0.18)
DSM4700-1	11.1 (0.18)	12.8 (0.21)	13.3 (0.22)
DSM4800-1	12.5 (0.20)	14.8 (0.24)	15.5 (0.25)
DSM4800-2	12.2 (0.19)	14.5 (0.23)	15.2 (0.24)
DSU4800-1	13.0 (0.21)	15.5 (0.25)	16.3 (0.26)
DSU4800-2	12.4 (0.20)	14.5 (0.23)	14.8 (0.24)

^aThe values in parenthesis are the excess gravimetric methane uptake donated as (g g⁻¹).

Figure 4.18 shows the total gravimetric methane uptake isotherms of samples DSM2700-1, DSM2800-1, DSM4600-1, DSM4700-1, DSM4800-1, and DSM4800-2, as well as those of DSU4800-1 and DSU4800-2 that were prepared with added urea. **Table 4.7** provides a summary of the total gravimetric methane uptake at 35, 65, and 100 bar. The total methane storage for carbons produced at milder conditions was 9.7, 12.6, 11.1 and 13.0 mmol g⁻¹ (at 35 bar), 11.9, 15.8, 13.9 and 16.6 mmol g⁻¹ (at 65 bar), and 13.7, 18.3, 16.0 and 19.4 mmol g⁻¹ (at 100 bar), respectively, for DSM2700-1, DSM2800-1, DSM4600-1 and DSM4700-1. At 35 bar, the total methane uptake of carbons produced under harsher activation conditions is 15.3 and 14.8 mmol g⁻¹ for DSM4800-1 and DSM4800-2, respectively, while for DSU4800-1 and DSU4800-2, the total uptake is 16.1 and 15.1 mmol g⁻¹, respectively. At 65 bar, the total methane uptake is 20.2 and 19.6 mmol g⁻¹ for DSM4800-1 and DSM4800-2, respectively, and increases further to 24.2 and 23.5 mmol g⁻¹ at 100 bar. While the total uptake is 21.5 and 19.7 mmol g⁻¹ at 65 bar, and 26.0 and 23.4 mmol g⁻¹ at 100 bar for DSU4800-1 and DSU4800-2, respectively. At 100 bar and 25 °C, the uptake of some carbons (0.39 and 0.38 g g⁻¹ for DSM4800-1 and DSM4800-2, and 0.42 and 0.37 g g⁻¹ for DSU4800-1 and DSU4800-2, respectively, is close to the DOE target. The N-doping process results in carbons with remarkable gravimetric methane adsorption that either matches or exceeds those previously reported to date for carbon or MOF materials.^{13, 15, 44-48, 50, 51, 54-61} Furthermore, the gravimetric uptake of all the present carbons is higher than that of carbons prepared from ACDS only.¹⁵

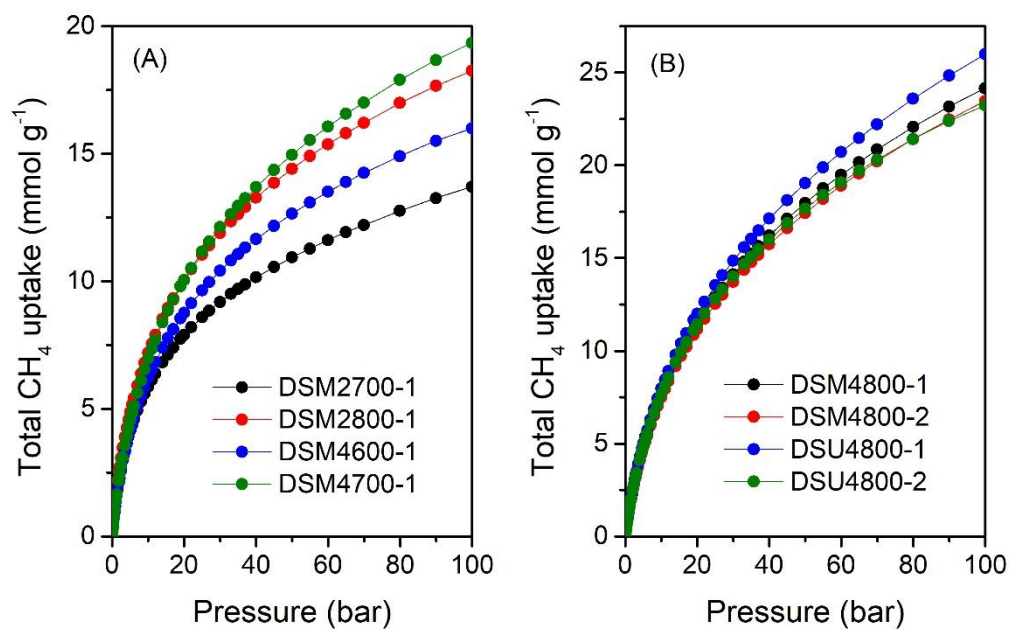


Figure 4.18. Total gravimetric methane uptake isotherms at 25 °C of N-doped activated carbons prepared at KOH/ACDS ratio of 2 or 4 and melamine or urea/ACDS ratio of 1 or 2.

Table 4.7. Total gravimetric methane uptake at 25 °C and pressures of 35, 65 and 100 bar of N-doped activated carbons prepared at KOH/ACDS ratio of 2 or 4 and melamine or urea/ACDS ratio of 1 or 2.

Sample	Total gravimetric methane uptake (mmol g ⁻¹) or (g g ⁻¹) ^a		
	35 bar	65 bar	100 bar
DSM2700-1	9.7 (0.16)	11.9 (0.19)	13.7 (0.22)
DSM2800-1	12.6 (0.20)	15.8 (0.25)	18.3 (0.29)
DSM4600-1	11.1 (0.18)	13.9 (0.22)	16.0 (0.26)
DSM4700-1	13.0 (0.21)	16.6 (0.27)	19.4 (0.31)
DSM4800-1	15.3 (0.25)	20.2 (0.32)	24.2 (0.39)
DSM4800-2	14.8 (0.24)	19.6 (0.31)	23.5 (0.38)
DSU4800-1	16.1 (0.26)	21.5 (0.35)	26.0 (0.42)
DSU4800-2	15.1 (0.24)	19.7 (0.32)	23.4 (0.37)

^aThe values in parenthesis are the total gravimetric methane uptake donated as (g g⁻¹).

In addition to the impressive gravimetric methane storage capacity achieved, the volumetric uptake (i.e., cm³ (STP) cm⁻³), which is the amount of methane that can be held by the adsorbent per unit of tank volume, is an important parameter for methane storage performance from a practical perspective. The volumetric uptake is largely determined by the packing density of the adsorbent and the gravimetric uptake. If an adsorbent has a higher packing density, it could potentially allow more of it to be filled in a given tank, which in turn increases the volumetric capacity. The United States Department of Energy (U.S. DOE) has established a goal for volumetric methane uptake at 25 °C and pressure (i.e., 35–100 bar) of 263 cm³ (STP) cm⁻³ to facilitate widespread use. The total volumetric methane uptake isotherms are shown in **Figure 4.19**, and **Table 4.8** provides a summary of the uptake at pressures of 35, 65 and 100 bar. It is interesting to note that the volumetric uptake isotherms do not show any saturation at 100 bar. This indicates that the present carbons might be able to store considerably more methane at pressures higher than 100 bar. In contrast, it has been found that most benchmark MOFs reach saturation at pressures of ca. 80 bar.^{57, 62} This could be explained by the fact that the presence of mesopores in these carbons facilitates enhanced gas uptake at higher pressures and also allows for rapid adsorption

and desorption rates.⁶² For the carbons obtained at milder activation conditions (DSM2700-1, DSM2800-1, DSM4600-1 and DSM4700-1), at 35 bar, the total volumetric methane uptake ($\text{cm}^3 \text{ (STP) cm}^{-3}$) varies from 161 to 184, while it is between 154 and 138 for those obtained under harsher conditions (DSM4800-y and DSU4800-y). The highest volumetric methane uptake capacity at 35 bar, observed for DSM2800-1 at $184 \text{ cm}^3 \text{ (STP) cm}^{-3}$, is amongst the best reported for porous materials.^{13, 48, 63-65} At 65 bar, the uptake is between 198 and 230 for DSM2700-1, DSM2800-1, DSM4600-1 and DSM4700-1, and in the range of 181 to 203 for DSM4800-y and DSU4800-y. At 100 bar, DSM2700-1, DSM2800-1, DSM4600-1, and DSM4700-1 carbons have total methane uptake of 227, 266, 244, and $256 \text{ cm}^3 \text{ (STP) cm}^{-3}$, respectively, and DSM4800-1, DSM4800-2, and DSU4800-1 and DSU4800-2 have total methane uptake of 244, 226, 239, and $214 \text{ cm}^3 \text{ (STP) cm}^{-3}$. The best volumetric uptake performance at 100 bar is observed for sample DSM2800-1 at $266 \text{ cm}^3 \text{ (STP) cm}^{-3}$, which exceeds the DOE target and outperforms or is comparable to the best porous materials (activated carbons or MOFs).^{13, 47, 48, 51} On the other hand, it is interesting to note that, at 25°C and 100 bar the volumetric uptake of the DSU4800-1 carbon is just $\sim 9\%$ lower than that of the target uptakes (0.5 g g^{-1} and $263 \text{ cm}^3 \text{ (STP) cm}^{-3}$) for gravimetric and volumetric uptake, i.e., 0.42 g g^{-1} and $239 \text{ cm}^3 \text{ (STP) cm}^{-3}$, respectively. The outstanding performance of DSU4800-1 samples can be attributed to a well-balanced combination of porosity and packing density as a result of an optimal N:K ratio during synthesis. Overall, however, the volumetric uptake obtained by the activated carbons in this study is among the highest values recorded for carbons or MOF materials so far, based on experimentally obtained packing density values.^{13, 44-46, 48-50, 52-54, 63-70}

The working capacity, i.e., the efficacy of materials to deliver the stored gas between two finite pressures, is more important than the total storage capacity. The efficiency of this process is largely dependent on the type of porosity. Highly microporous materials are expected to absorb a large amount of methane at lower pressures (e.g., 5 bar), thereby reducing their working capacity. Thus, to achieve high working capacity, the mix microporosity and mesoporosity is important; the former is critical for high packing density, while the latter plays an important role in minimising the uptake at lower pressure, leading to an increase in the working capacity of the materials. Deliverable methane, or volumetric working capacity, calculated by

subtracting the storage at release pressure of 5 bar from the uptake at 35, 65 or 100 bar, is given in **Table 4.8**. The volumetric working capacity, for a 100 to 5 bar pressure swing, reaches 196, 195, 195, and 193 cm^3 (STP) cm^{-3} for samples DSM4700-1, DSM2800-1, DSM4800-1 and DSU4800-1, respectively. It's interesting that the volumetric capacities of DSM4800-1 and DSU4800-1 are almost the same as for DSM2800-1, even though the later has the highest total volumetric uptake of 266 cm^3 (STP) cm^{-3} . This is ascribed to the presence of greater mesoporosity in DSM4800-1 and DSU4800-1, which lowers the uptake at 5 bar.⁶² It is noteworthy that the present carbons have volumetric working capacities approaching the values of the best MOFs (i.e., monolithic monoHKUST1 and monoUiO-66_D), which are considered to be 50% better than any powder MOF.^{47, 68}

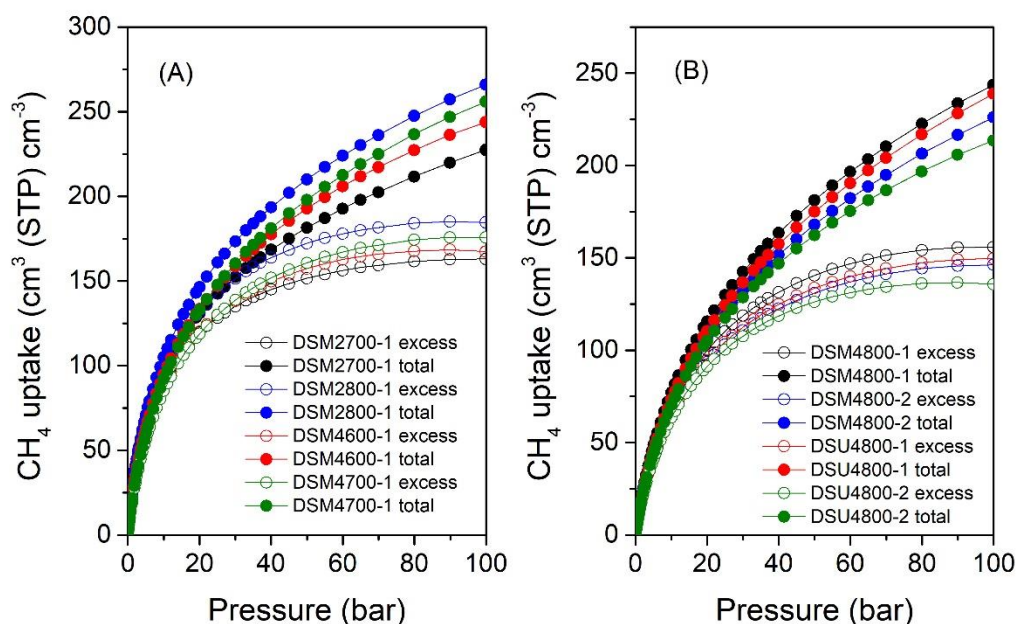


Figure 4.19. Excess and total volumetric methane uptake isotherms at 25 °C of N-doped activated carbons prepared at KOH/ACDS ratio of 2 or 4 and melamine or urea/ACDS ratio of 1 or 2.

Table 4.8. Total volumetric methane uptake and working capacity of N-doped activated carbons prepared at KOH/ACC ratio of 2 or 4 and melamine or urea/ACDS ratio of 1 or 2.

Sample	Total volumetric methane uptake (cm^3 (STP) cm^{-1})		
	35 bar	65 bar	100 bar
DSM2700-1	161 (92)	198 (129)	227 (158)
DSM2800-1	184 (113)	230 (159)	266 (195)
DSM4600-1	169 (105)	212 (148)	244 (180)
DSM4700-1	171 (111)	219 (159)	256 (196)
DSM4800-1	154 (105)	203 (154)	244 (195)
DSM4800-2	143 (97)	189 (143)	226 (180)
DSU4800-1	148 (102)	197 (151)	239 (193)
DSU4800-2	138 (93)	181 (136)	214 (169)

The values in parentheses are volumetric working capacity (i.e., deliverable methane), which is calculated by subtracting the storage pressure at 5 bar.

4.4 Conclusion

N-doped carbons with well controlled porosity were achieved through the addition of N-containing additives (melamine or urea) to an activation mixture containing KOH as an activating agent and carbonaceous matter derived from biomass, i.e., air-carbonised date seed, *Phoenix dactylifera*, ACDS. Depending on the preparation conditions and by varying the amount of melamine or urea, the amount of activating agent, and the activation temperature, carbons with a wide range of surface area and porosity properties were generated. The activated carbons feature a large N content, which can reach up to 18 wt%, with surface area of between 340 to 3646 m² g⁻¹ and pore volume in the range of 0.15 to 2.1 cm³ g⁻¹. It was observed that the N added to the activation mix serves as both an N-dopant and a structure-directing agent (porogen) by extending the size of pores generated into the mesopore region. This study provides evidence that N-containing additives can play a key role determining the structural properties of the resulting carbons, and their use during activation acts to increase the susceptibility of the ACDS carbon to activation. It appears that K⁺ from the KOH reacts with surface N species readily, leading to a significant increase in the surface area, which is accompanied with a lowering of the N content of the carbons. Furthermore, the presence of N provides activation pathways to carbons with a unique combination of textural properties (surface area, mix of microporosity and mesoporosity and packing density) that can be tuned for towards suitability for enhanced uptake of CO₂ and methane. Depending on the preparation conditions and resulting mix of micro/mesoporosity, the carbons show excellent low pressure CO₂ capture at 25 °C of 1.7 mmol g⁻¹ at 0.15 bar and 4.7 mmol g⁻¹ at 1 bar. At 25 °C and 100 bar the methane uptake of one of the best performing carbons (DSU4800-1) is only ca. 9% lower than the target uptakes (0.5 g g⁻¹ and 263 cm³ (STP) cm⁻³) at 0.42 g g⁻¹ and 239 cm³ (STP) cm⁻³, respectively. The impressive performance is attributed to the balanced combination of porosity and packing density as a result of an optimal ratio of N:K during the activation process.

References

1. L. S. Blankenship and R. Mokaya, *Materials Advances*, 2022, **3**, 1905-1930.
2. N. Balahmar, A. S. Al-Jumialy and R. Mokaya, *Journal of Materials Chemistry A*, 2017, **5**, 12330-12339.
3. E. A. Hirst, A. Taylor and R. Mokaya, *Journal of Materials Chemistry A*, 2018, **6**, 12393-12403.
4. N. Balahmar and R. Mokaya, *Journal of Materials Chemistry A*, 2019, **7**, 17466-17479.
5. E. Masika and R. Mokaya, *Energy & Environmental Science*, 2014, **7**, 427-434.
6. M. Sevilla and R. Mokaya, *Energy & Environmental Science*, 2014, **7**, 1250-1280.
7. M. Sevilla, W. Sangchoom, N. Balahmar, A. B. Fuertes and R. Mokaya, *ACS Sustainable Chemistry & Engineering*, 2016, **4**, 4710-4716.
8. M. E. Casco, M. Martinez-Escandell, J. Silvestre-Albero and F. Rodriguez-Reinoso, *Carbon*, 2014, **67**, 230-235.
9. M. Sevilla, R. Mokaya and A. B. Fuertes, *Energy & Environmental Science*, 2011, **4**, 2930-2936.
10. M. H. Kim, S. Yun, H. S. Park, J. T. Han, K. B. Kim and K. C. Roh, *Journal of Materials Chemistry A*, 2015, **3**, 2564-2567.
11. M. Sevilla, N. Alam and R. Mokaya, *Journal of Physical Chemistry C*, 2010, **114**, 11314-11319.
12. Y. Zhu, S. Murali, M. D. Stoller, K. J. Ganesh, W. Cai, P. J. Ferreira, A. Pirkle, R. M. Wallace, K. A. Cychosz, M. Thommes, D. Su, E. A. Stach and R. S. Ruoff, *Science*, 2011, **332**, 1537-1541.
13. A. Altwala and R. Mokaya, *Journal of Materials Chemistry A*, 2022, **10**, 13744-13757.
14. A. M. Aljumialy and R. Mokaya, *Materials Advances*, 2020, **1**, 3267-3280.
15. A. Altwala and R. Mokaya, *Energy & Environmental Science*, 2020, **13**, 2967-2978.
16. M. Sevilla, G. A. Ferrero, N. Diez and A. B. Fuertes, *Carbon*, 2018, **131**, 193-200.

-
17. M. Sevilla, A. S. M. Al-Jumaily, A. B. Fuertes and R. Mokaya, *ACS Applied Materials & Interfaces*, 2018, **10**, 1623-1633.
 18. A. B. Fuertes and M. Sevilla, *Carbon*, 2015, **94**, 41-52.
 19. M. Cox and R. Mokaya, *Sustainable Energy & Fuels*, 2017, **1**, 1414-1424.
 20. A. B. Fuertes, G. A. Ferrero and M. Sevilla, *Journal of Materials Chemistry A*, 2014, **2**, 14439-14448.
 21. J. V. Guerrero, J. N. Burrow, J. E. Eichler, M. Z. Rahman, M. V. Namireddy, K. A. Friedman, S. S. Coffman, D. C. Calabro and C. B. Mullins, *Energy & Fuels*, 2020, **34**, 6101-6112.
 22. J. E. Eichler, J. N. Burrow, Y. Wang, D. C. Calabro and C. B. Mullins, *Carbon*, 2022, **186**, 711-723.
 23. E. Haffner-Staton, N. Balahmar and R. Mokaya, *Journal of Materials Chemistry A*, 2016, **4**, 13324-13335.
 24. M. Sevilla and A. B. Fuertes, *Energy & Environmental Science*, 2011, **4**, 1765-1771.
 25. I. Alali and R. Mokaya, *Energy & Environmental Science*, 2022, **15**, 4710-4724.
 26. M. Sevilla and A. B. Fuertes, *Journal of Colloid and Interface Science*, 2012, **366**, 147-154.
 27. G. Srinivas, V. Krungleviciute, Z.-X. Guo and T. Yildirim, *Energy & Environmental Science*, 2014, **7**, 335-342.
 28. J. Silvestre-Albero, A. Wahby, A. Sepúlveda-Escribano, M. Martínez-Escandell, K. Kaneko and F. Rodríguez-Reinoso, *Chemical Communications*, 2011, **47**, 6840-6842.
 29. N. P. Wickramaratne and M. Jaroniec, *ACS Applied Materials & Interfaces*, 2013, **5**, 1849-1855.
 30. N. P. Wickramaratne and M. Jaroniec, *Journal of Materials Chemistry A*, 2013, **1**, 112-116.
 31. G. P. Hao, W. C. Li, D. Qian, G. H. Wang, W. P. Zhang, T. Zhang, A. Q. Wang, F. Schuth, H. J. Bongard and A. H. Lu, *Journal of the American Chemical Society*, 2011, **133**, 11378-11388.
 32. J. Wang, A. Heerwig, M. R. Lohe, M. Oschatz, L. Borchardt and S. Kaskel, *Journal of Materials Chemistry*, 2012, **22**, 13911-13913.

-
33. X. Q. Fan, L. X. Zhang, G. B. Zhang, Z. Shu and J. L. Shi, *Carbon*, 2013, **61**, 423-430.
34. M. Sevilla, P. Valle-Vigon and A. B. Fuertes, *Advanced Functional Materials*, 2011, **21**, 2781-2787.
35. W. Xing, C. Liu, Z. Zhou, L. Zhang, J. Zhou, S. Zhuo, Z. Yan, H. Gao, G. Wang and S. Z. Qiao, *Energy & Environmental Science*, 2012, **5**, 7323-7327.
36. Y. D. Xia, R. Mokaya, G. S. Walker and Y. Q. Zhu, *Advanced Energy Materials*, 2011, **1**, 678-683.
37. Y. Zhao, L. Zhao, K. X. Yao, Y. Yang, Q. Zhang and Y. Han, *Journal of Materials Chemistry*, 2012, **22**, 19726-19731.
38. Z. Zhang, J. Zhou, W. Xing, Q. Xue, Z. Yan, S. Zhuo and S. Z. Qiao, *Physical Chemistry Chemical Physics*, 2013, **15**, 2523-2529.
39. M. Nandi, K. Okada, A. Dutta, A. Bhaumik, J. Maruyama, D. Derks and H. Uyama, *Chemical Communications*, 2012, **48**, 10283-10285.
40. M. Saleh, J. N. Tiwari, K. C. Kemp, M. Yousuf and K. S. Kim, *Environmental Science & Technology* 2013, **47**, 5467-5473.
41. D. Lee, C. Zhang, C. Wei, B. L. Ashfeld and H. Gao, *Journal of Materials Chemistry A*, 2013, **1**, 14862-14867.
42. M. Sevilla, C. Falco, M.-M. Titirici and A. B. Fuertes, *RSC Advances*, 2012, **2**, 12792-12797.
43. A. Altwala and R. Mokaya, *Energy Advances*, 2022, **1**, 216-224.
44. K. V. Kumar, K. Preuss, M. M. Titirici and F. Rodriguez-Reinoso, *Chemical Reviews*, 2017, **117**, 1796-1825.
45. T. A. Makal, J. R. Li, W. Lu and H. C. Zhou, *Chemical Society Reviews*, 2012, **41**, 7761-7779.
46. B. Li, H. M. Wen, W. Zhou, J. Q. Xu and B. L. Chen, *Chem*, 2016, **1**, 557-580.
47. T. Tian, Z. Zeng, D. Vulpe, M. E. Casco, G. Divitini, P. A. Midgley, J. Silvestre-Albero, J. C. Tan, P. Z. Moghadam and D. Fairen-Jimenez, *Nature Materials*, 2018, **17**, 174-179.
48. J. A. Mason, M. Veenstra and J. R. Long, *Chemical Science*, 2014, **5**, 32-51.
49. S. Dutta, A. Bhaumik and K. C. W. Wu, *Energy & Environmental Science*, 2014, **7**, 3574-3592.
50. Y. He, W. Zhou, G. Qian and B. Chen, *Chemical Society Reviews*, 2014, **43**, 5657-5678.

-
51. Z. Chen, P. Li, R. Anderson, X. Wang, X. Zhang, L. Robison, L. R. Redfern, S. Moribe, T. Islamoglu, D. A. Gomez-Gualdron, T. Yildirim, J. F. Stoddart and O. K. Farha, *Science*, 2020, **368**, 297-303.
52. P. Pfeifer, L. Aston, M. Banks, S. Barker, J. Burrell, S. Carter, J. Coleman, S. Crockett, C. Faulhaber, J. Flavin, M. Gordon, L. Hardcastle, Z. Kallenborn, M. Kemiki, C. Lapilli, J. Pobst, R. Schott, P. Shah, S. Spellerberg, G. Suppes, D. Taylor, A. Tekeci, C. Wexler, M. Wood, P. Buckley, T. Breier, J. Downing, S. Eastman, P. Freeze, S. Graham, S. Grinter, A. Howard, J. Martinez, D. Radke, T. Vassalli and J. Ilavsky, *Chaos: An Interdisciplinary Journal of Nonlinear Science*, 2007, **17**, 041108.
53. J. Romanos, S. Sweany, T. Rash, L. Firlej, B. Kuchta, J. C. Idrobo and P. Pfeifer, *Adsorption Science & Technology*, 2014, **32**, 681-691.
54. D. A. Gómez-Gualdrón, C. E. Wilmer, O. K. Farha, J. T. Hupp and R. Q. Snurr, *Journal of Physical Chemistry C*, 2014, **118**, 6941-6951.
55. H. Nishihara and T. Kyotani, *Chemical Communications*, 2018, **54**, 5648-5673.
56. Y. C. Lin, C. L. Kong, Q. J. Zhang and L. Chen, *Advanced Energy Materials*, 2017, **7**, 1601296.
57. Y. Peng, V. Krungleviciute, I. Eryazici, J. T. Hupp, O. K. Farha and T. Yildirim, *Journal of the American Chemical Society*, 2013, **135**, 11887-11894.
58. D. Lozano-Castello, D. Cazorla-Amoros and A. Linares-Solano, *Energy & Fuels*, 2002, **16**, 1321-1328.
59. T. A. Rash, A. Gillespie, B. P. Holbrook, L. H. Hiltzik, J. Romanos, Y. C. Soo, S. Sweany and P. Pfeifer, *Fuel*, 2017, **200**, 371-379.
60. J. Jiang, H. Furukawa, Y. B. Zhang and O. M. Yaghi, *Journal of the American Chemical Society*, 2016, **138**, 10244-10251.
61. H. Wu, W. Zhou and T. Yildirim, *Journal of the American Chemical Society*, 2009, **131**, 4995-5000.
62. S. Bracco, D. Piga, I. Bassanetti, J. Perego, A. Comotti and P. Sozzani, *Journal of Materials Chemistry A*, 2017, **5**, 10328-10337.
63. S. Choi, M. A. Alkhabbaz, Y. G. Wang, R. M. Othman and M. Choi, *Carbon*, 2019, **141**, 143-153.
64. M. E. Casco, M. Martinez-Escandell, K. Kaneko, J. Silvestre-Albero and F. Rodriguez-Reinoso, *Carbon*, 2015, **93**, 11-21.

-
65. M. E. Casco, M. Martínez-Escandell, E. Gadea-Ramos, K. Kaneko, J. Silvestre-Albero and F. Rodríguez-Reinoso, *Chemistry of Materials*, 2015, **27**, 959-964.
 66. B. M. Connolly, D. G. Madden, A. E. H. Wheatley and D. Fairen-Jimenez, *Journal of the American Chemical Society*, 2020, **142**, 8541-8549.
 67. V. Rozyyev, D. Thirion, R. Ullah, J. Lee, M. Jung, H. Oh, M. Atilhan and C. T. Yavuz, *Nature Energy*, 2019, **4**, 604-611.
 68. B. M. Connolly, M. Aragonés-Anglada, J. Gandara-Loe, N. A. Danaf, D. C. Lamb, J. P. Mehta, D. Vulpe, S. Wuttke, J. Silvestre-Albero, P. Z. Moghadam, A. E. H. Wheatley and D. Fairen-Jimenez, *Nature Communications*, 2019, **10**, 2345.
 69. C. M. Simon, J. Kim, D. A. Gomez-Gualdron, J. S. Camp, Y. G. Chung, R. L. Martin, R. Mercado, M. W. Deem, D. Gunter, M. Haranczyk, D. S. Sholl, R. Q. Snurr and B. Smit, *Energy & Environmental Science*, 2015, **8**, 1190-1199.
 70. P. N. Quirant, C. Cuadrado-Collados, A. J. Romero-Anaya, J. S. Albero and M. M. Escandell, *Industrial & Engineering Chemistry Research*, 2020, **59**, 5775-5785.

Chapter 5

Ultra-high surface area ionic-liquid-derived carbons that meet both gravimetric and volumetric methane storage targets

Abstract

Natural gas, whose main ingredient is methane, is an alternative fuel for vehicular transport due to its lower carbon emission compared to petroleum based fuels. Methane storage for vehicular use may be achieved in porous materials, but to date, there is no material that meets the required gravimetric and volumetric targets for such use. To address this challenge, we explore carbonised N-rich and O-poor (i.e. low O/C ratio) crosslinkable imidazolium-based ionic liquids as precursors for porous carbons. On activation, the carbonised ionic liquid yields activated carbons with surface area and pore volume of up to $\sim 4000 \text{ m}^2 \text{ g}^{-1}$ and $3.3 \text{ cm}^3 \text{ g}^{-1}$, respectively, along with high packing density. Here we show that the carbons have excellent methane uptake of up to 0.53 g g^{-1} and $289 \text{ cm}^3 \text{ (STP) cm}^{-3}$, respectively, at 25°C and 100 bar , which surpasses both gravimetric and volumetric storage targets required for vehicular transport.

5.1 Introduction

5.1.1 Ionic liquids as carbon precursors

Recently, ionic liquids (ILs), which consist of an organic cation and an inorganic anion, have gained much attention as a new class of carbon precursors owing to their combination of remarkable physicochemical properties.¹⁻⁴ Since ionic liquids are composed entirely of ions and coupled with their carbon-rich nature, they are becoming very promising candidates as carbon precursors with the following advantages. First, due to their ionic structure and high electrostatic interaction between charges, ILs exhibit negligible vapor pressure and high thermal stability, significantly reducing mass loss during carbonisation processes.^{5, 6} Second, in comparison to polymer precursors (e.g., polyacrylonitrile⁷, poly(furfuryl alcohol), and phenolic resins) that require long scale and complicated synthesis beside their limited solubility and solid-state, the carbonisation of a small amount of ILs is simple and easy to handle.⁸ This facilitates the carbonisation process, leading to reduced time consumption and lower costs. Third, the homogeneous incorporation of nitrogen and carbon atoms in situ into the carbon materials (when using some nitrogen-containing ILs) eliminates the need for doping agents.³ Fourth, the low melting points of ILs under atmospheric conditions (i.e., below 100 °C or even below room temperature) and their liquid state enable them to wet most surfaces effectively and form seamless and homogeneous carbon films, suitable for various applications.⁵ Fifth, one key advantage of ionic liquids is the structural diversity that can be tweaked to meet different requirements by a smart selection of ILs cation and anion offering additional possibilities for controlling over structures and properties of carbon materials at the molecular level.⁹

For instance, IL with nitrogen-containing cations and Cl^- or BF_4^- anion results in a hydrophilic IL, but its combination with PF_6^- results in a hydrophobic IL.¹⁰ The unusual compositions with different properties of ILs have led to an explosion in their use in many different potential applications, including as green ionic solvents in green chemistry and clean technology, in electrochemical applications such as (Li-ion batteries⁶, supercapacitors¹¹, sensors, solar panel, and fuel cells)¹², catalysts or catalyst supports, and recently as a new family of precursors for carbon-based materials.^{1, 3, 4,}

8, 12-15

5.1.2 Previous studies of ionic liquids as carbon precursors

Typically, conventional carbon materials are in a solid-state which rising up the difficulty of using them as a coating agent on substrates. Furthermore, non-polymer liquid molecules could be used as an alternative method, but due to the low yield obtained and their high volatility, they might not be suitable. To overcome these difficulties, ILs, which are liquid at room temperature, are being used as a relatively new method for the synthesis of carbon materials. The presence of certain functional groups into ILs precursors is a fundamental structural prerequisite that enables cross-linking during thermal treatment.

There have been several successful instances where cyano- or nitrile-functionalised ionic liquids have improved carbon yields. For example, Lee, *et al.* attempted to develop IL-based carbon precursor by adding nitrile functionality onto imidazolium backbones.² For this purpose: 1-cyanomethyl-3-methylimidazolium ([MCNIm]⁺) and 1,3-bis(cyanomethyl)imidazolium ([BCNIm]⁺) have been prepared. It was found that the thermal stability of this class of ILs strongly depends on the nature of the anion, and significant yields were observed for all nitrile-functionalised ionic liquids.² Further, they demonstrated that carbonaceous materials derived from bulky anions feature high surface areas suggesting the key role of the anion on the structural morphology. For example, the surface area of [BCNIm]Cl precursor is only 15.5 m² g⁻¹, while for the same cation paired with [Tf₂N]⁻ and [beti]⁻ anions possessed high surface areas (640 m² g⁻¹ & 662 m² g⁻¹, respectively).² In a later study, Lee, *et al.* and his team focused on anions because they are more easily designed to bear multiple crosslinkable components.¹ They used for this study [C(CN)₃]⁻ anion, which is expected to be more favourable to undergo crosslinking reactions during the carbonisation process than those from cations. The [C(CN)₃]⁻ anion was introduced to three different types of cations, which are (1-ethyl-3-methylimidazolium [EMIm]⁺, 1-butyl-3-methylimidazolium [BMIm]⁺, and 1-decyl-3-methylimidazolium [C10MIm]⁺).¹ Significant carbonisation yields were achieved for all these three studied precursors.

In another study, Fulvio, *et al.* reported a mixture of two ILs containing different anions namely: 1-butyl-3-methylimidazolium tricyanomethanide ([BMIm][C(CN)₃]) and 1-ethyl-3-methylimidazolium tetracyanoborate ([EMIm][B(CN)₄]).¹⁶ The

porosity and surface area of the carbonaceous matter were controlled proportionally to reach the maximum surface area of $528 \text{ m}^2 \text{ g}^{-1}$. However, the nitrogen content found to decrease to 4.0 wt%.¹⁶

To enrich this, the study conducted by Zhang, *et al.* need to be included in this discussion.¹³ In this study, N-doped mesoporous porous carbon material has been prepared and originated from ionic liquid, 1-cyanomethyl-3-methylimidazolium bis(trifluoromethylsulfonyl) imide ($[\text{MCNIm}]^+[\text{Nf}_2\text{T}]^-$) via carbonisation method.¹³ It was found that the ionic liquid does not only act as a precursor for carbon materials, but also as a nitrogen source for the prepared carbon materials. The materials showed a high nitrogen-content of 18 wt% and a surface area of $865 \text{ m}^2 \text{ g}^{-1}$.

Based on this discussion, all authors attempted to study the use of ionic liquids as a new class for nitrogen-rich carbon precursors from various perspective. However, no study has shown that or attempted to investigate the activation effect on the ionic liquid precursors. In this chapter, we will study and investigate the carbonisation and activation effect on chosen IL (1-butyl-3-methylimidazolium tricyanomethanide ($[\text{BMIm}][\text{C}(\text{CN})_3]$) precursor and its potential applications for methane capture and storages.

5.2 Ionic liquid-derived activated carbon for methane storage

The continuous emission of greenhouse gases into the atmosphere, largely driven by rapid global development that has relied on the accelerated use of fossil fuels, has raised concerns over the impact on the environmental, and on climate and global ecosystems. In particular, the concentration of CO_2 , the largest contributor to global warming, has reached unprecedented levels in the atmosphere.¹⁷ The need for alternative fuels to enable a transition away from conventional petroleum is becoming more urgent in order to meet the mitigation target set by international pledges, such as the Paris Agreement, to reduce atmospheric CO_2 levels.¹⁸ Efforts are currently focussed on the development of environmentally-friendly and low cost technology that will enable both the remediation of environmental damage caused by rising CO_2 levels and the transition to cleaner fuels.¹⁹⁻²² An example of an alternative fuel is natural gas (NG), which primarily consists of methane ($\sim 70\%$). NG has recently received a great deal of interest as an alternative fuel for vehicular transport due to its abundance and lower carbon emissions.^{22, 23} However, the use of NG as fuel for mobile applications

faces challenges associated with storage and transportation due to a gaseous nature under ambient conditions.^{21, 24-26} Conventionally, NG is stored as compressed natural gas (CNG) in high-pressure vessels (> 250 bar), which pose safety concerns. NG may also be stored as liquefied natural gas (LNG) under cryogenic conditions. However, LNG technology is limited by high costs of compression and is therefore impractical for use in vehicles. On the other hand, adsorbed natural gas (ANG) technology, which involves adsorption onto solid materials, is promising and can circumvent the difficulties of CNG and LNG by combining much lower pressures than those needed for CNG along with the possibility of achieving sufficient storage at room temperature, unlike LNG. Successful application of ANG technology relies on the development of adsorbent materials that are effective for methane storage. In this regard, a variety of porous materials have been investigated, including metal-organic frameworks (MOFs)^{22, 27}, zeolites²⁸ and porous carbons.^{29, 30} The latter, particularly activated carbons, have gained increasing interest due to several factors, including low cost, excellent chemical and mechanical stability, and tunability of their textural properties.³¹⁻³⁴

The storage of methane in zeolites tends to be limited by their low to moderate surface area; they can store up to ca. 10 mmol g^{-1} of methane at 100 bar and 25°C .²⁸ On the other hand, due to their much higher surface area and pore volume, MOFs can achieve greater gravimetric methane uptake.^{22, 27} For example, at 23°C , it has been reported that methane storage in MOFs can reach 25 and 33 mmol g^{-1} at 65 and 100 bar, respectively.²⁷ However, the low packing density of MOFs means their volumetric uptake does not attain the required levels.^{22, 27} The packing density of MOFs may be increased via compaction, but such densification has deleterious effects on the gravimetric storage capacity and consequently does not improve the volumetric uptake.^{22, 27} Porous carbons, on the other hand, can achieve high surface area and, due to their high mechanical stability, can also be compacted without loss of porosity and gravimetric uptake capacity for methane. The ideal porous carbon would need to have both high porosity (Surface area and pore volume) and packing density. Such a combination, while possible for porous carbons, would be difficult to achieve for zeolites or MOFs.

The textural properties of activated carbons are determined by the type and amount of activating agent, the activation temperature, and the nature and elemental composition

of the carbonaceous precursor from which they are derived.³² Regarding the impact of the nature of the carbonaceous precursor, we have recently shown that it is possible to tailor the porosity of activated carbons by systematic selection of precursors on the basis of their elemental composition.^{29, 35, 36} We explored the use of pre-mixed precursors (e.g., polypyrrole and sawdust) to control, tailor and enhance the porosity of activated carbons.³⁵ More specifically, we have shown that the nature of the carbonaceous precursor and in particular the elemental composition can determine susceptibility to activation.^{29, 30, 32, 36} Knowledge of the link between the elemental composition of a carbon precursor and susceptibility to activation is important as it can enable predicting of the textural parameters of the resulting activated carbon (i.e., proportion and level of microporosity and mesoporosity). We have shown that the oxygen/carbon (O/C) atomic ratio of a precursor can play a role in determining susceptibility to pore formation following activation. Precursors with high O/C ratio are more susceptible to activation and may result in activated carbons with a high surface area but with greater levels of mesoporosity and wider pores. On the other hand, carbonaceous matter with a low O/C ratio have high resistance to so-called over-activation and thus offer more control over textural properties and favour the formation of micropores. However, such low O/C ratio precursors are only able to generate activated carbons with relatively low surface area due to their high resistance to activation. This means that the gravimetric gas (e.g., methane) uptake of activated carbons derived from such precursors tends to be low since gas storage at moderate to high pressure (35 to 100 bar) is very dependent on the surface area of the adsorbent.^{29, 30}

The presence of N in the framework of a carbonaceous precursor also plays a role in determining the textural properties of activated carbons. For example, it has been demonstrated that the porosity of activated carbons can be tuned by adding N-containing additives to carbonaceous precursors, in a manner that allows achievement of high surface area and tailoring of the balance between microporosity and mesoporosity.³⁷⁻⁴⁰ The presence of N in precursors can therefore function as an in-situ porogen and favour generation of carbons with high mesoporosity and high surface area but which have low packing density. In a sense the presence of N can have the opposite effect to that of low O/C ratio. While the presence of N favours generation of high mesoporosity and high surface area, a low O/C ratio acts in a reverse manner and

favours the formation of microporous carbons with moderate surface area but high packing density. In order to optimise both the gravimetric and volumetric uptake of methane, a suitable carbon material would ideally have high surface area, a mix of mesoporosity and microporosity, and as high a packing density as possible. Such a mix of properties is most likely to be achieved from a precursor that contains high amounts of N along with a low O/C ratio.

In this work we show that by careful selection of a suitable precursor it is possible to prepare activated carbons with a combination of attractive properties not previously achieved without the need to premix precursors or the use of added doping agents. We report on a class of carbon precursor, derived from ionic liquids, that allows for porosity control towards high surface area but without excessive diminution of microporosity and packing density. Recently, ionic liquids (ILs), which consist of an organic cation and an inorganic anion, have gained much attention as a new class of carbon precursors.^{2, 3, 15, 41, 42} Since ionic liquids are composed entirely of ions, coupled with their carbon-rich nature, they are very promising candidates as carbon precursors with the following advantages: i) because of their structure and high electrostatic interaction between electrical charges, they exhibit negligible vapour pressure and high thermal stability leading to reduced mass loss during carbonisation processes, ii) the homogeneous incorporation of nitrogen and carbon atoms in situ into the carbon materials when using ILs with N-containing motifs, which eliminates the need for using doping agents, and iii) structural diversity that can be modified to meet various requirements by the smart selection of IL cation and anion thus offering additional possibilities for control over structures and properties of carbon materials at the molecular level. We show that careful carbonisation of ILs can yield carbonaceous matter that possesses a significant amount of N and in addition has a low O/C ratio. We explore the porosity of the carbons prepared from the IL-derived carbonaceous matter using carefully selected protocols, and probe the impact of the presence of N on both the storage capacity and manner of methane adsorption. The expectation, which is proven here, is that such precursors can generate porous carbons with both high porosity and high packing density, a combination that is suitable for optimising both the gravimetric and volumetric storage of methane.

5.3 Experimental section

5.3.1 Materials

The following chemicals were used as received, 1-butyl-3-methylimidazolium tricyanomethanide, ([BMIm][C(CN)₃]), (TCI), and potassium hydroxide (KOH), (Sigma-Aldrich). Ionic liquid-derived activated carbons (IL-ACs) were thermally prepared in two steps, namely, carbonisation followed by activation. Firstly, for the carbonisation, the required amount of [BMIm][C(CN)₃], in an alumina boat, was placed in a horizontal tube furnace and heated, at a heating ramp rate of 10 °C min⁻¹, to 800 °C and held for 1 h under an inert (N₂ gas) atmosphere. The furnace was then allowed to cool to room temperature under a flow of N₂ gas. The resulting carbonaceous matter was designated as IL-C (IL = ionic liquid, and C = carbonised). Secondly, the IL-C carbon was chemically activated as follows; IL-C was added to KOH at KOH/IL-C ratio of 2, 4, or 6 in an agate mortar and thoroughly mixed. The mixture was then placed in an alumina boat and heated in a furnace under a flow of N₂ gas (100 mL min⁻¹) at ramp rate of 5 °C min⁻¹ to the target temperature (700, 800, or 900 °C) and held for 1 h. The furnace was then allowed to cool to room temperature under a flow of N₂ gas. The resulting activated carbons were washed with 1 M HCl by stirring at room temperature, followed by washing with deionised water until the filtrate achieved neutral pH (i.e., pH ~ 7). The carbons were then dried in oven at 120 °C. The activated carbons were designated as (IL-AC_xT, where x is the KOH/IL-C mass ratio, and T is the activation temperature (in °C)). Thus, a carbon activated at a KOH/IL-C ratio of 4 and at 800 °C is designated as IL-AC4800. The packing density of the carbons was determined by pressing a known amount of carbon in a 1.3 cm die at pressure of 7 MPa for 5 min. The packing density was then calculated from the mass and volume of the resulting pellet/disc.

5.3.2 Materials Characterisation

Thermogravimetric analysis (TGA) was performed using a TA Instruments SDT Q600 analyser under flowing air or N₂ conditions (100 ml min⁻¹) and heating ramp rate of 10 °C min⁻¹. Powder XRD patterns were obtained using a PANalytical X'Pert PRO diffractometer with Cu-K α radiation (λ = 1.5418 Å) (40 kV, 40 mA), 0.02 step size and 5 s step time between 2° and 80°. Elemental analysis (CHN) was performed on an

Exeter Analytical CE-440 Elemental Analyser. Nitrogen sorption (at -196 °C) isotherms and textural properties of the activated carbons were determined using a Micromeritics 3Flex sorptometer. Prior to analysis, the carbons were degassed at 300 °C for 16 h under vacuum. The surface areas were calculated using the Brunauer–Emmett–Teller (BET) method using the nitrogen adsorption data in the relative pressure (P/P_0) range between 0.05–0.30. Total pore volume was determined from the amount of nitrogen adsorbed at a relative pressure of 0.99. The micropore surface area and micropore volume were estimated by t-plot analysis. The porosity measures (surface area and pore volume) were also calculated using the Non-Local Density Functional Theory (NLDFT) model. Furthermore, to ensure consistency of the porosity measures, BET surface identification (BETSI) was also performed for which the minimum number of points in the linear region was 10, with a minimum r^2 of 0.995, and Rouquerol criterion maximum error of 20%.⁴³⁻⁴⁵ More details about the BETSI method can be found at <https://github.com/fairen-group/betsi-gui>. The PSDs were calculated using the SAIEUS software and the 2D-NLDFT heterogeneous surface kernel with a fitting parameter, λ of 5 for all isotherms.

Infra-red spectroscopy (FTIR) was performed using a Bruker ALPHA FTIR Spectrometer. Scanning electron microscopy (SEM) images were obtained using a JEOL 7000F FEG-SEM microscope. Transmission electron microscopy (TEM) images were obtained using a JEOL 2100F instrument operating at 200 kV and equipped with a Gatan Orius CCD for imaging. Prior to analysis, the carbon samples were suspended in distilled water and dispersed onto lacey carbon support films. For X-ray photoelectron spectroscopy (XPS), a Kratos AXIS ULTRA with a monochromated Al K X-ray source (1486.6 eV) was used at 10 mA emission current and 12 kV anode potential. To avoid surface charging, a charge neutralizer filament was utilised. The analysis chamber pressure was lower than 5×10^{-9} Torr. Each sample was analysed in three different areas. XPS spectra were analysed using CasaXPS™ software (version 2.3.22PR1.0), with the Kratos sensitivity factors to derive atomic percentage values from the peak regions. The binding energies of the high-resolution spectra were calibrated by setting C-1s to 284.6 eV.

5.3.3 Methane uptake measurements

Methane uptake was determined using a Hiden Isochema XEMIS Analyser. Sample masses were at least 30 mg, and the mass measurement precision of XEMIS is 0.1 μg with a mass stability of 1 μg . CH_4 (BOC, purity 99.9995%) isotherms were measured up to 100 bar. The pressure precision for any isotherm point is 0.02% at any point, and the base vacuum pressure is $< 1 \times 10^{-6}$ mbar. Equilibrium uptake was determined by identifying the asymptote of rate of change in uptake after a relaxation of 99% (tolerance 2%). Data was sampled at an interval of 1 s. Prior to isotherm measurement, samples were degassed in-situ at 240 $^{\circ}\text{C}$ (ramp rate 10 $^{\circ}\text{C min}^{-1}$) for at least 4 h until sample mass was stable.

Isosteric enthalpies Q_{st} of adsorption were calculated from the methane uptake isotherms using the Whittaker method,⁴⁶ for which a specific python module was created in pyGAPS.⁴⁷ Owing to the PointIsotherm and ModelIsotherm classes in pyGAPS, calculations requires only an isotherm as an input because physical parameters (such as critical point, triple point, and saturation pressures) are automatically calculated from the identity of the adsorbate and analysis temperature. In the case of a supercritical isotherm, a pseudo-saturation pressure is calculated. Due to the fact that the Whittaker method requires determination of enthalpy of vaporisation of the adsorbate, the module returns the values of Q_{st} only at loadings corresponding to pressures between the critical and saturation pressures. For convenience, the module can also output a plot of Q_{st} vs loading. For this work, Toth was found to fit the isotherms best so this model was used in the Whittaker Q_{st} calculations.

5.4 Results and discussion

5.4.1 Nature of ionic and composition of liquid-derived carbons

The ionic liquid, 1-butyl-3-methylimidazolium tricyanomethanide (**Figure 5.1**) was chosen as starting material due to a combination of factors so as to achieve the desired properties in the carbonisation products. The ionic liquid is rich in N ($\text{C}_{12}\text{H}_{15}\text{N}_5$), and the high electrostatic interaction between the ions leads to negligible vapour pressure and high thermal stability, minimising mass loss during carbonisation. The imidazolium based-cation can induce high surface area in any resulting carbons, while

the nitrile group (tricyanomethanide) favours the formation of 3D-connected frameworks via cross-linking during pyrolysis. The yield and elemental composition of the samples are summarized in **Table 5.1**. We first noticed that, due to the high thermal stability of the [BMIm][C(CN)₃] ionic liquid, the carbonaceous matter has a graphite-like appearance and feel (**Figure 5.2**). This is attributed to the presence of the [C(CN)₃] anion, which does not decompose completely at high temperature showing a yield for IL-C of ~30 wt%. This yield is comparable to that of biomass following hydrothermal carbonisation.^{35, 36, 40} The molar N/C ratio of the ionic liquid is 0.42 with N content of 30 wt%, which is consistent with the molecular formula (C₁₂H₁₅N₅). After carbonisation at 800 °C, the N content of IL-C remains high at 19.3 wt%. The C content increases from ca. 62 wt% for the IL to 69 wt% for IL-C, while the O content rises from 2.1 wt to 10.7 wt%. The H content decreases drastically from 6.6 wt% for the IL to 0.9 wt% for IL-C. It is interesting to note that the O/C ratio of IL-C is, therefore, very low at 0.116, which is one of the lowest reported for any activatable carbonaceous precursor.^{29, 30} This means that IL-C achieves the unusual elemental composition of having both a high N content (19.3 wt%) and very low O/C ratio (0.116). We are not aware of any previous study that has deliberately targeted such carbonaceous matter as precursor for activated carbons or conducted a systematic exploration of its activation.

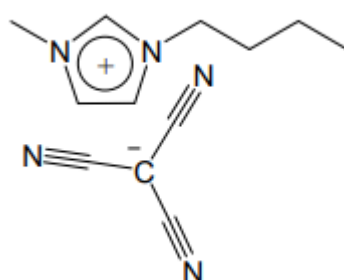


Figure 5.1. The chemical structure of butyl-3-methylimidazolium tricyanomethanide (C₁₂H₁₅N₅), CAS number 878027-73-7.



Figure 5.2. Photograph of the IL after carbonisation at 800 °C.

Table 5.1. Yield and elemental composition of ionic liquid (IL), carbonised ionic liquid (IL-C), and corresponding IL-C-derived activated carbons (IL-ACxT).

Sample	Yield [wt%]	C [%]	H [%]	N [%]	O [%]	(O/C) ^a	(N/C) ^a
IL	-	61.6	6.6	29.7	2.1	0.026	0.482
IL-C	28	69.1	0.9	19.3	10.7	0.116	0.279
IL-AC2700	46	72.2	0.6	6.7	20.5	0.213	0.093
IL-AC2800	33	87.9	0.5	1.6	10.0	0.085	0.018
IL-AC2900	17	90.0	0.2	0.3	9.5	0.079	0.004
IL-AC4700	34	83.2	0.8	2.3	13.7	0.124	0.027
IL-AC4800	29	93.6	0.1	0.5	5.8	0.047	0.005
IL-AC4900	16	92.9	0.0	0.4	6.7	0.054	0.004
IL-AC6700	23	86.6	0.4	2.3	10.7	0.093	0.027
IL-AC6800	18	90.3	0.8	0.2	8.7	0.072	0.002
IL-AC6900	13	96.0	0.0	0.2	3.8	0.030	0.001

^aAtomic ratio.

In general, the yields of the activated carbons depend on the amount of KOH and the activation temperature such that for samples activated at 900 °C, the yields vary from 17 to 13%, while at 700 °C the yield is between 46 and 23%. For samples activated at 800 °C the yield is in the range of 33 to 18 wt%. The activated samples show a high C content, which increases from ca. 69 wt% for IL-C to between 72 and 96 wt% for IL-ACs. The highest C content (96 wt%) was observed for the most severely activated sample (IL-AC6900), while the lowest (72 wt%) was for the least severely activated (IL-AC2700). The N content of the activated carbons decreases as the activation temperature or amount of KOH rises, and ranges from 6.7 wt% for the sample activated under the mildest conditions (IL-AC2700) to 0.2 wt% for the most severely activated carbons (IL-AC6800 and IL-AC6900). These results indicate that a high amount of N is lost during activation, which can be attributed to the fact that N is oxidised and

eliminated more readily than carbon during the activation process, which is the genesis of its action as in-situ porogen.⁴⁸ The H and O content vary less drastically on activation but generally decrease with increasing severity of activation.

The thermal stability of the IL, IL-C, and the IL-AC activated carbons was probed via TGA, and the resulting curves are shown in **Figure 5.3**. The IL was thermally treated at 800 °C with a ramp rate of 10 °C min⁻¹ under an inert atmosphere of (N₂ flow of 100 ml min⁻¹) for 1 h. The TGA curve of the IL are consistent with the carbonisation yield of ca. 30 wt%. The purity (in terms of being purely carbonaceous with no inorganic components) and thermal stability of IL-C and IL-ACs were probed under air flow of 100 ml min⁻¹. The TGA curves indicates high thermal stability up to at least 500 °C, followed by almost complete mass loss between 500 – 750 °C, due to combustion of carbon. The IL-ACs burn off at roughly the same temperature, indicating that they are similar in terms of the nature of their carbon. The activated carbons were burnt off with hardly any residual mass, which indicates that they are fully carbonaceous.

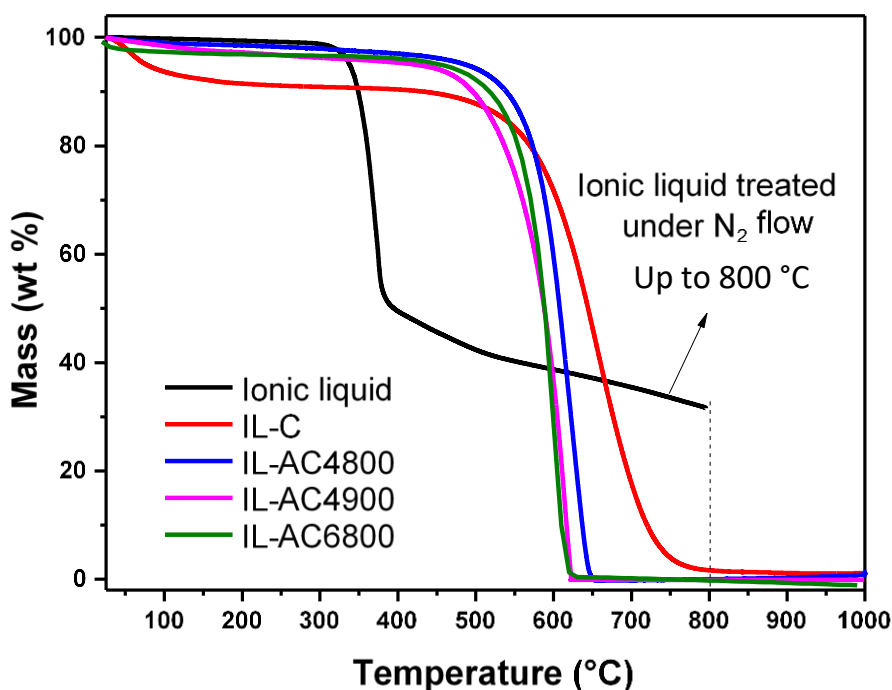


Figure 5.3. Thermal stability and purity of ionic liquid, IL-C and activated carbons. TGA curves of the ionic liquid (thermally treated under N₂ gas), and IL-C and some IL-C derived activated carbons (IL-ACxT), which were thermally treated in air.

Powder X-ray diffraction was used to study the structure and purity (in terms of absence of any crystalline inorganic phases) of IL-C and activated carbons. The XRD pattern of IL-C (**Figure 5.4**) shows a well-developed graphitic stacking peak at 2θ of $\sim 26^\circ$, which is assigned to the (002) diffraction of graphitic carbon. A further weak peak is observed at 2θ of $\sim 44^\circ$ which is the (100) diffraction arising from graphene stacks. The intensity of these peaks reduced greatly on activation of IL-C (**Figure 5.4**). Carbons activated under milder conditions (e.g., IL-AC2700) still show the peaks, which are much broader. For the other samples, no graphitic peaks were observed, which indicates that the nature of the carbon is amorphous. This is consistent with the expectation that activation should break up any graphitic domains.

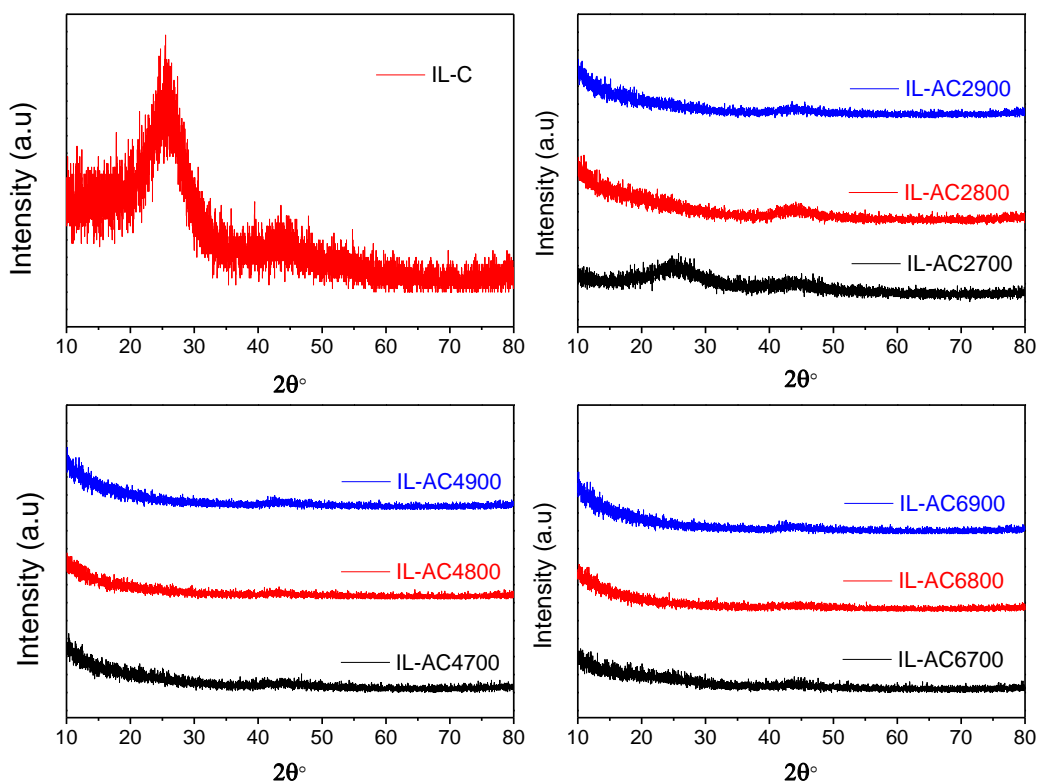


Figure 5.4. Powder XRD patterns of carbonised ionic liquid (IL-C) and IL-AC_xT activated carbons prepared at KOH/IL-C ratio of 2, 4 or 6, and activation temperature of 700, 800 or 900 °C. (x = KOH/IL-C ratio, T is activation temperature).

The surface structure and morphology of IL-C and IL-AC carbons were explored using scanning electron microscopy (SEM) so as to illustrate the structural transformation following carbonisation and activation. The SEM images of IL-C appear to show a non-porous surface morphology (**Figure 5.5**), which agrees with the expected low porosity of the carbonised product. In contrast, the SEM images for IL-AC carbons (**Figure 5.6** and **Figure 5.7**) suggest well developed porous structures. Transmission electron microscopy (TEM) was used to further probe the microstructural differences between IL-C and IL-ACs. The TEM images of IL-C reveal a graphitic structure (**Figure 5.8**) which agrees well with the XRD pattern (**Figure 5.4**). The formation of a graphitic carbon can be attributed to the dynamic trimerization of nitrile group based-anion during carbonisation.⁴⁹ On the other hand, the TEM images of IL-ACs (**Figure 5.9**) are similar to each other and reveal amorphous carbon structures, which is consistent with the XRD patterns and the expected break up of graphitic domains during activation. Overall, however, the morphology of the IL-AC carbons is similar to that previously reported for activated carbons.³¹⁻³⁶

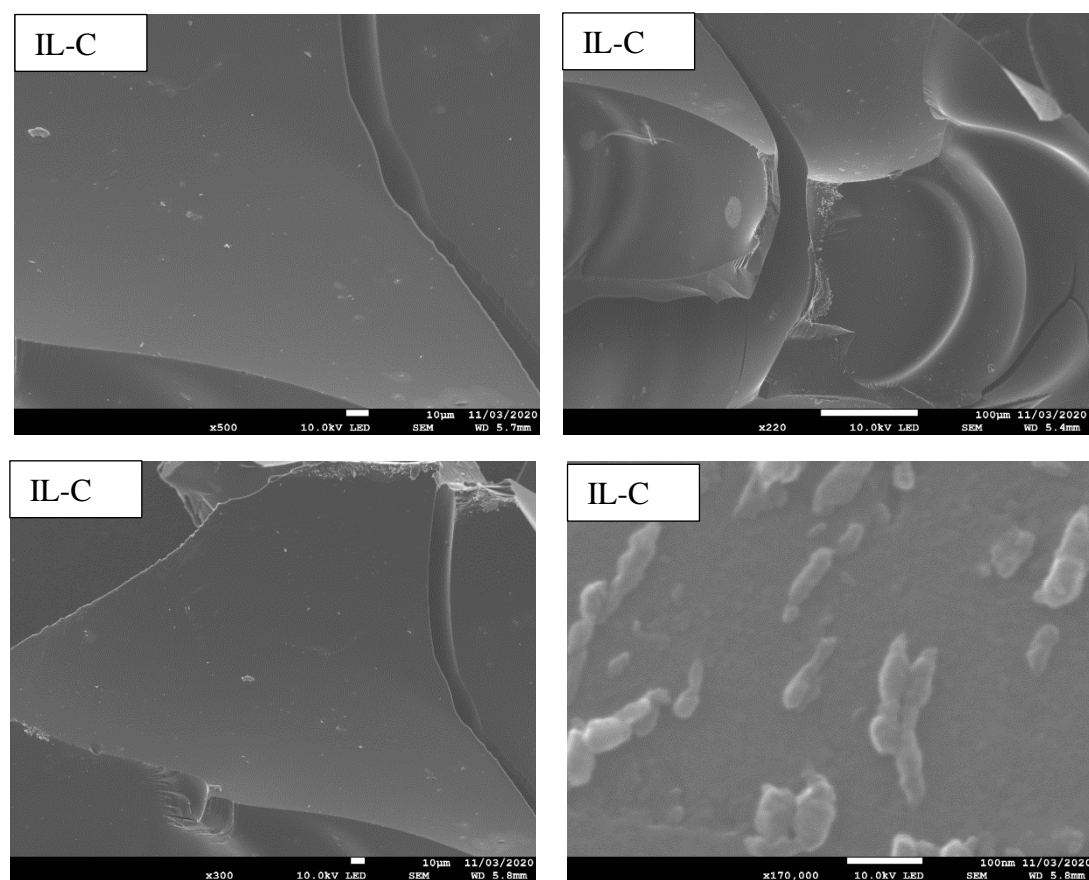


Figure 5.5. SEM images of the carbonised ionic liquid (IL-C).

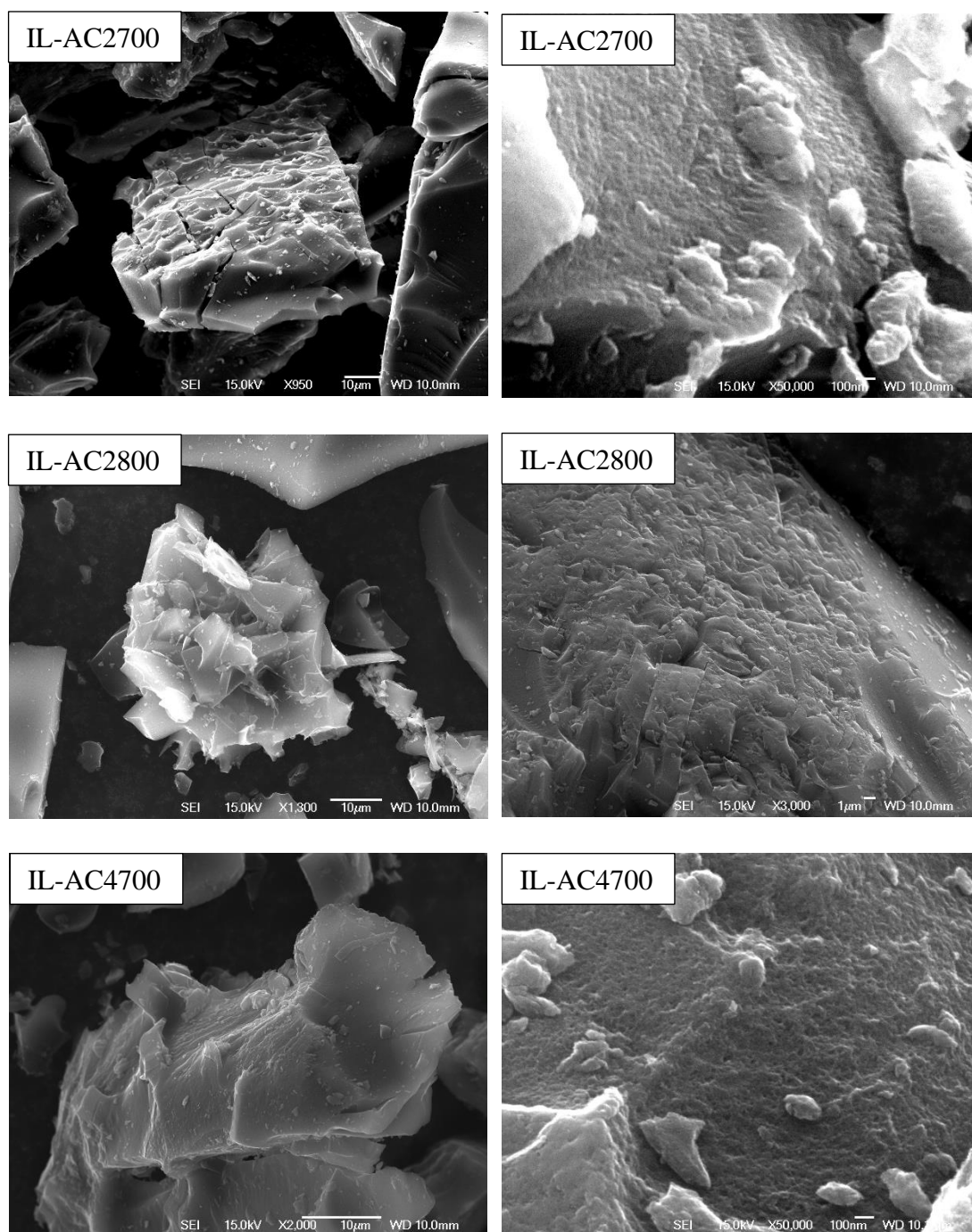


Figure 5.6. SEM images of the ionic liquid-derived activated carbons; IL-AC2700, IL-AC2800 and IL-AC4700.

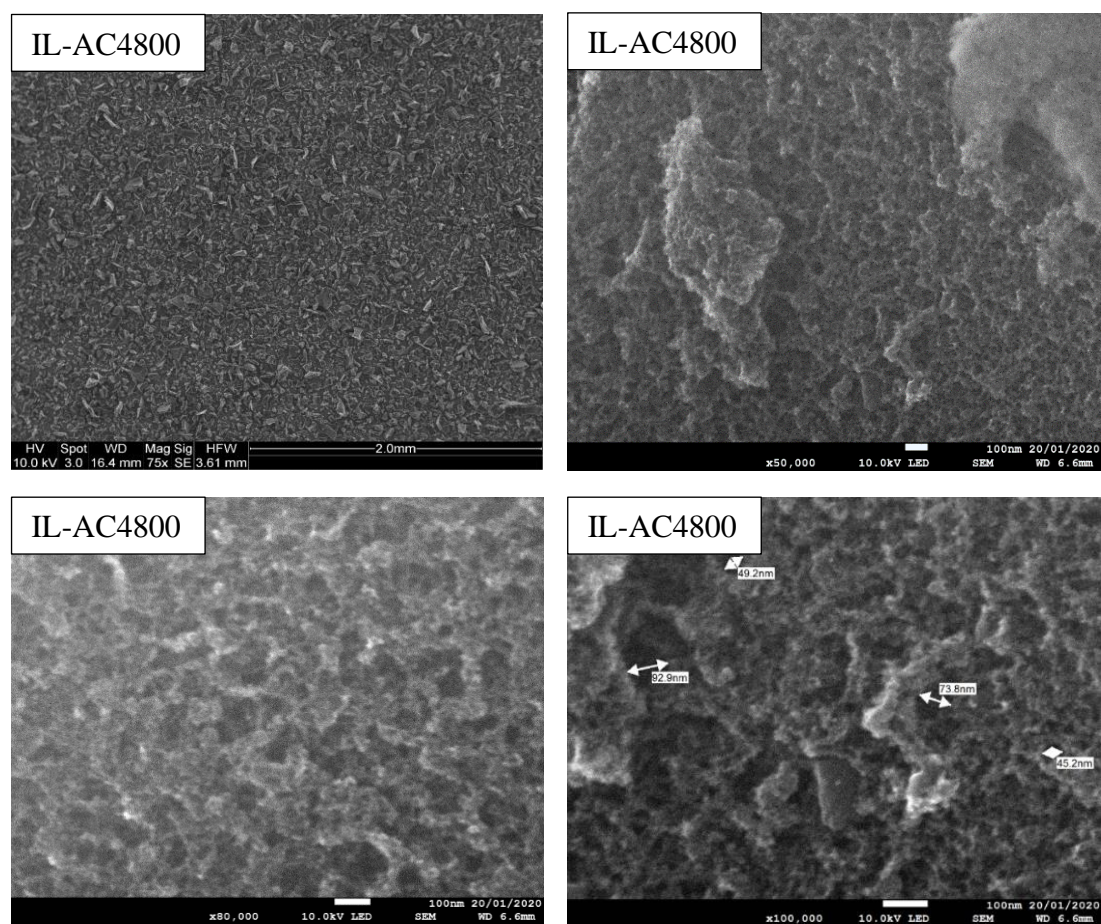


Figure 5.7. SEM images of the ionic liquid-derived activated carbon IL-AC4800.

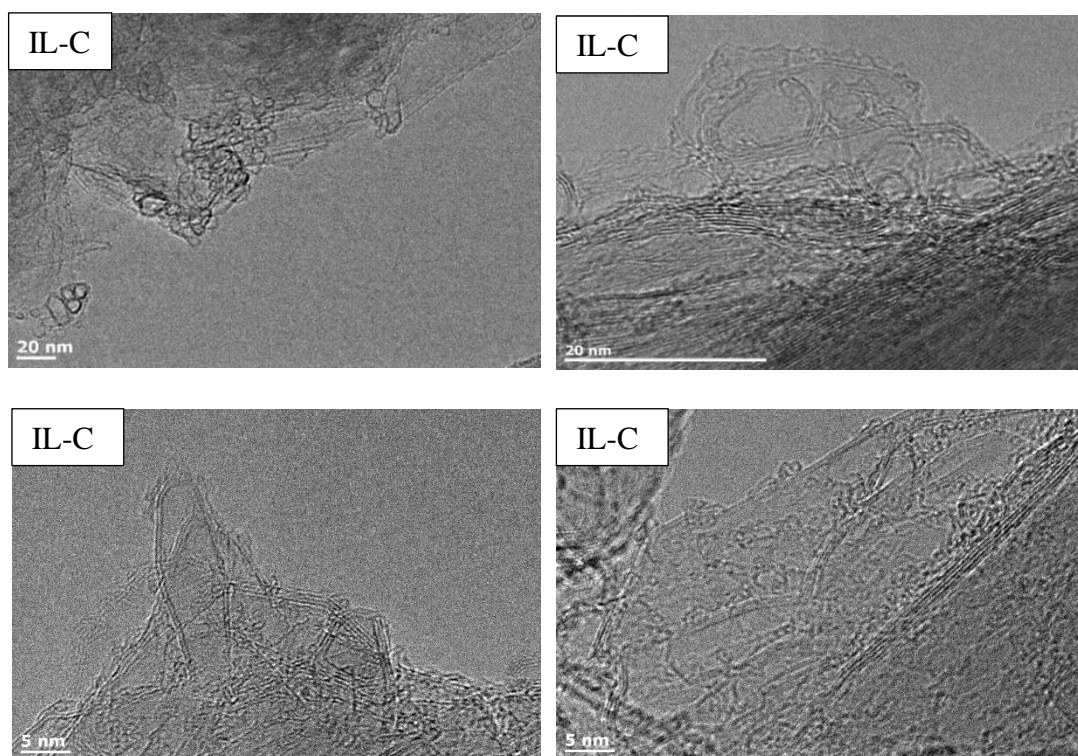


Figure 5.8. TEM images of carbonised ionic liquid (IL-C).

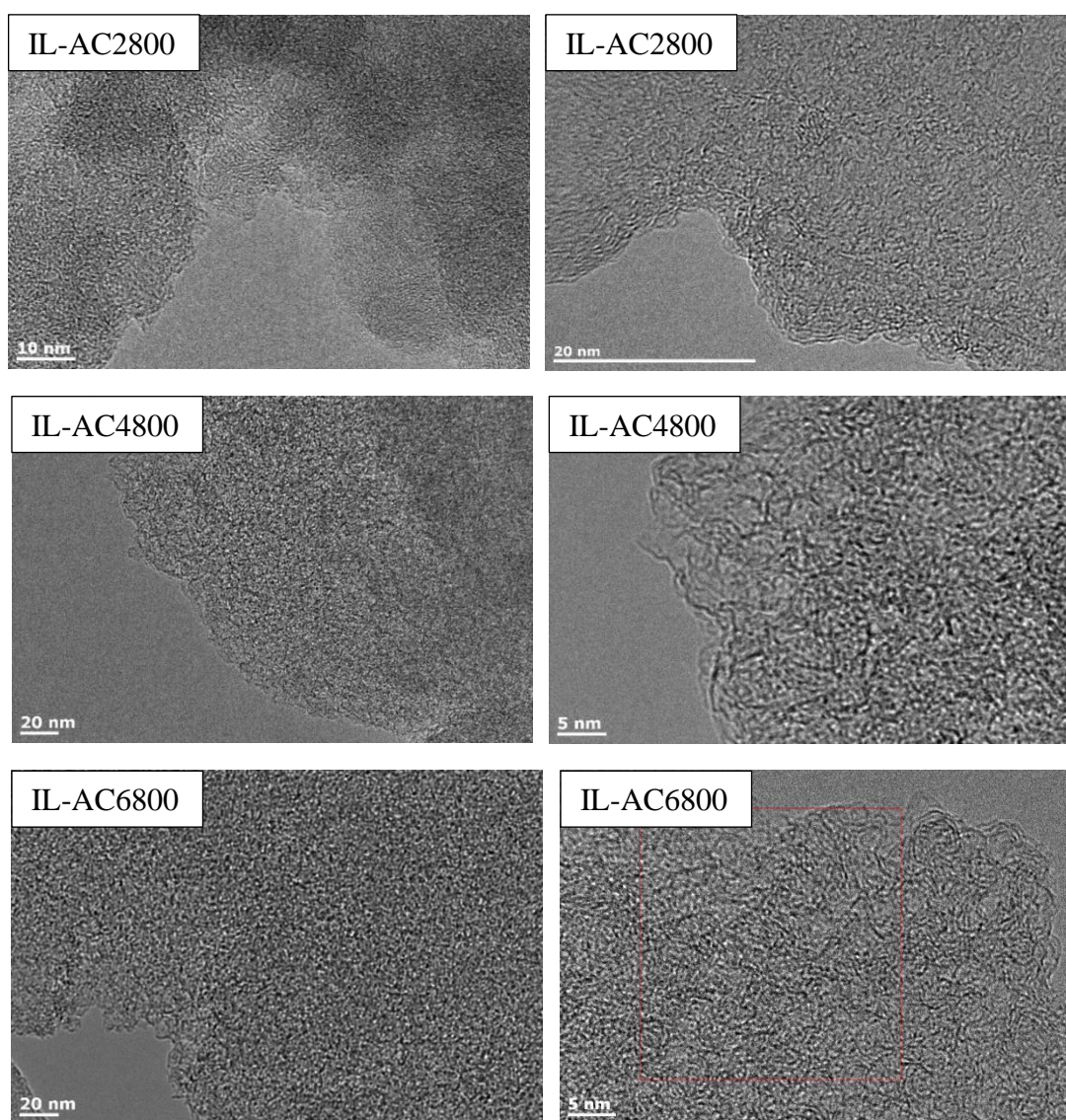


Figure 5.9. TEM images of activated carbons IL-AC2800, IL-AC4800 and IL-AC6800.

X-ray photoelectron spectroscopy (XPS) is useful in determining the elemental composition of a material and the chemical state of any elements present. The XPS wide scan spectra of IL-ACxT carbons and IL-C are compared in **Figure 5.10**. The spectrum of IL-C revealed a high N content, which is consistent with the elemental composition (**Table 5.1**). The content of N reduced after activation and the reduction was greater at higher activation temperature/and or amounts of KOH. The high resolution N1s-XPS spectra (**Figure 5.11**) show that the N has the following bonding: The N environment in IL-C is dominated by pyridine-N (peak at 398.4 eV) and quarternary-graphitic N (peak at 401.0 eV).⁵⁰ For IL-AC2700 (**Figure 5.11**) there are three peaks ascribed to pyridinic N (N-6 at 398.9 eV), quaternary N (N-Q at 401.1 eV) and oxidized N (N-X at 405.3 eV). The intensity of N-6 peak decreased after activation, which is in agreement with previous reports.⁵¹ It is likely that the activation is responsible for generating the oxidised-N group. The XPS spectrum of IL-AC4900, which was prepared under harsh conditions, appeared to show no N content in agreement with the elemental composition data (**Table 5.1**).

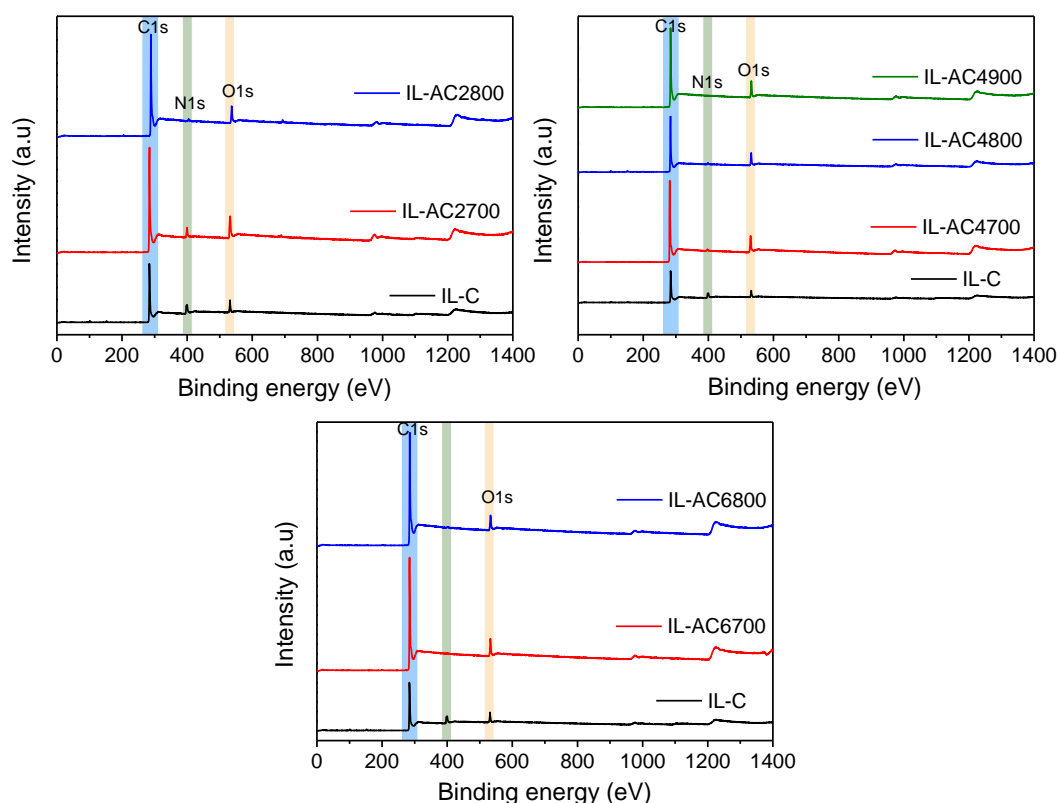


Figure 5.10. X-ray photoelectron spectroscopy (XPS) of IL-C and activated carbons. Wide scan XPS spectra of carbonised ionic liquid (IL-C) and IL-ACxT activated carbons.

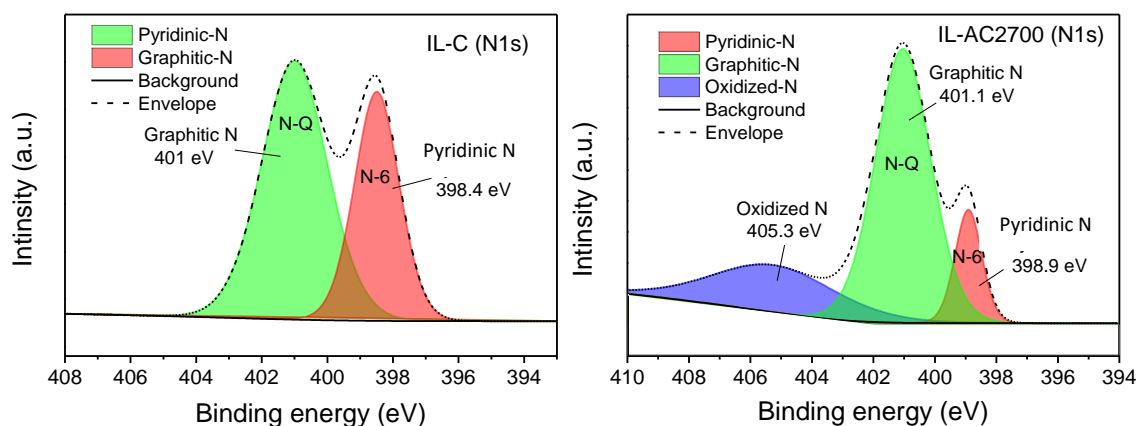


Figure 5.11. High-resolution XPS spectra showing N 1s peaks for carbonised ionic liquid (IL-C), and IL-AC2700 activated carbon.

In order to clarify on the mechanism underlying the conversion of the IL to IL-C and finally to the activated carbons, we performed Fourier transform Infra-red spectroscopy (FTIR) of all the respective species in the transformation chain. The IR spectrum of the 1-butyl-3-methylimidazolium tricyanomethanide ionic liquid (**Figure 5.12**) exhibits peaks at 2960 cm^{-1} and 2870 cm^{-1} , which arise from C-H stretching vibrations of the alkyl chain. The peak at ca. 3100 cm^{-1} can be attributed to the stretching mode of the aromatic C-H bonds of the imidazolium cation. The strong peak at 2156 cm^{-1} arises from stretching vibrations of the $\text{C}\equiv\text{N}$ bonds of the tricyanomethanide moiety. The peaks within the fingerprint region ($600 - 1500\text{ cm}^{-1}$) can be attributed to the imidazolium ring, i.e., stretching and bending vibrations of the aromatic structure. The peaks at 1570 cm^{-1} and 1450 cm^{-1} are due to C=C and C=N stretching, while those at 750 cm^{-1} and 620 cm^{-1} are due to C-N stretching. Interestingly, the spectra of IL-C (**Figure 5.12**) shows some retained features in the fingerprint region due to retention of the imidazolium backbone in the carbonaceous matter. Interestingly, these ‘imidazolium backbone’ features are transferred to the IL-ACxT activated carbons (**Figure 5.13**). Importantly, however, the spectra of IL-C and the IL-ACxT activated carbons do not show the sharp tricyanomethanide ($\text{C}\equiv\text{N}$) peak expected at 2156 cm^{-1} . These observations are important in clarifying the mechanism of conversion of the IL to the IL-C carbonaceous matter and finally to the IL-ACxT activated carbons especially with regard to role of the imidazolium backbone and the N in the anionic fragments. The IR spectra are consistent with the assumption that the N in the anionic fragments serves as a source of N within the carbonised IL (IL-C),

which is then available to influence the nature of porosity developed in the activated carbons. On the other hand, the imidazolium backbone serves as a main C source for the activated carbons along with any carbon arising from the alkyl chains.

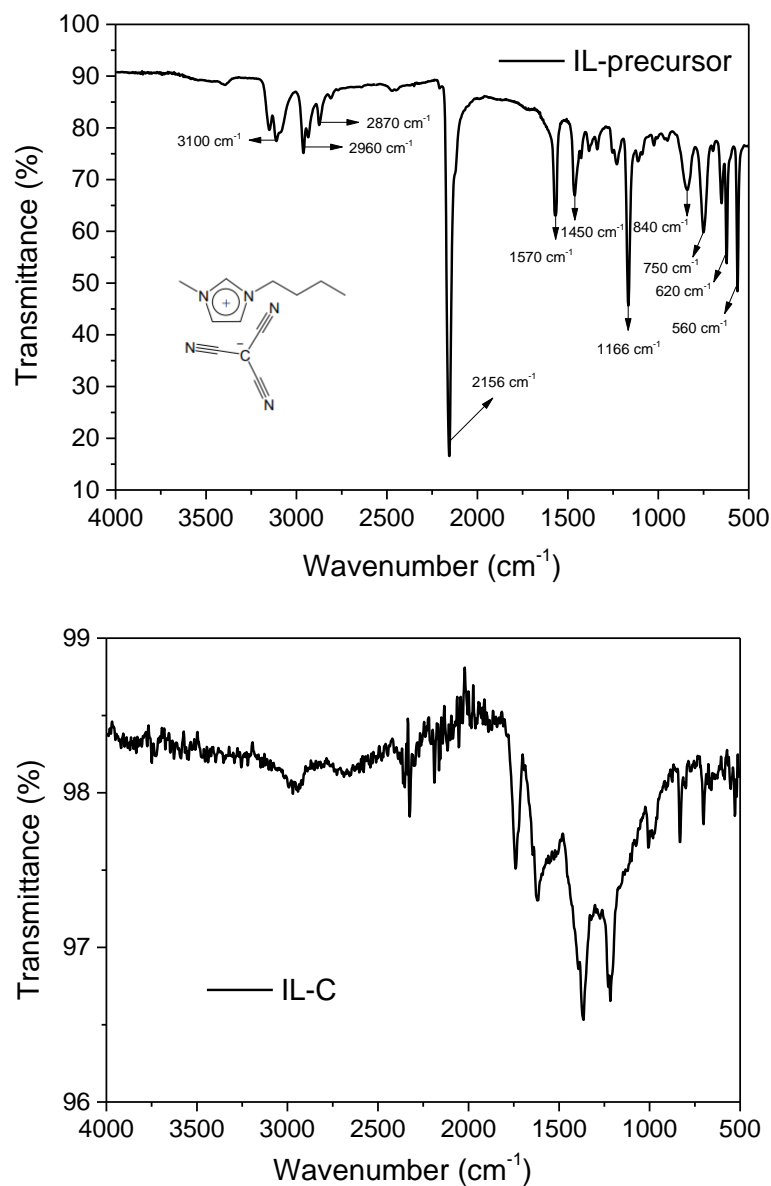


Figure 5.12. IR spectra of (top) 1-butyl-3-methylimidazolium tricyanomethanide ionic liquid, and (bottom) the carbonised ionic liquid (IL-C).

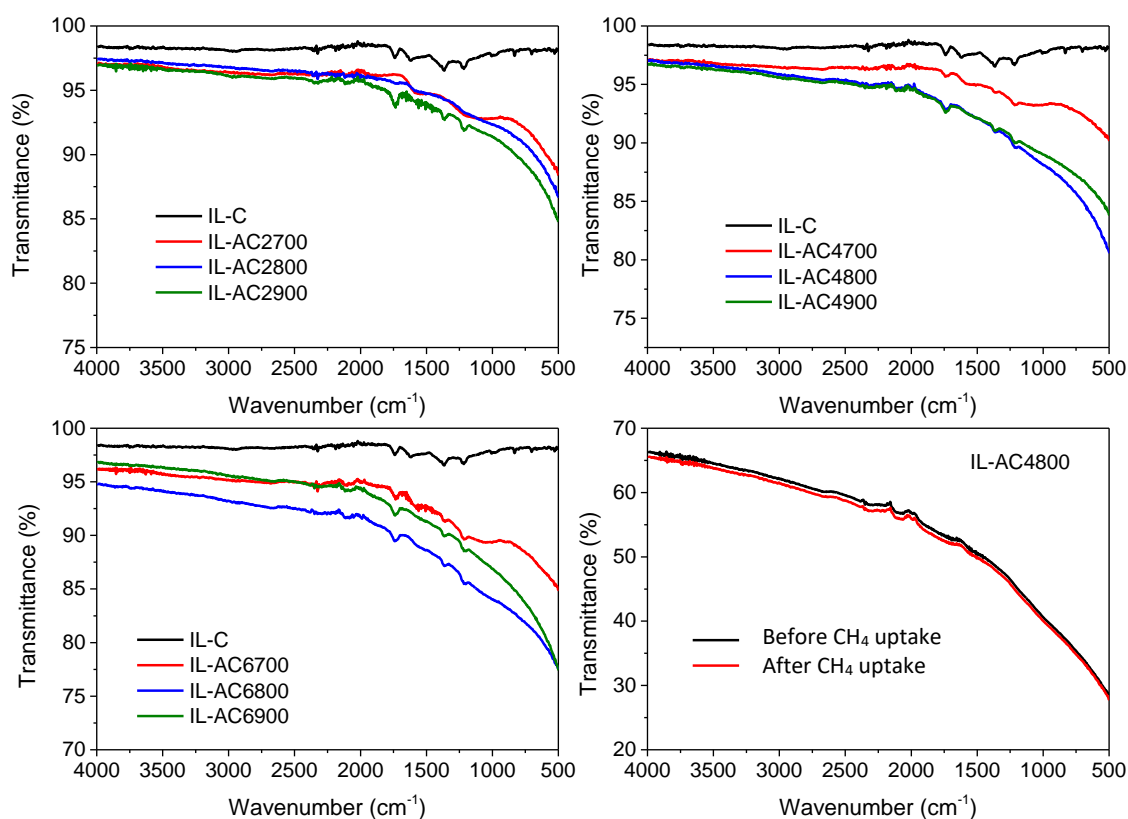


Figure 5.13. IR spectra of carbonised ionic liquid, IL-C, compared to that of IL-C derived activated carbon, IL-AC_xT, where x is KOH/IL-C ratio (2,4 or 6), and T is activation temperature (700, 800 or 900 °C). A comparison of the IR spectra of sample IL-AC4800 before and after methane uptake is also shown.

5.4.2 Porosity of ionic-liquid derived activated carbons

The IL-C carbon had limited porosity with surface area and pore volume of $40 \text{ m}^2 \text{ g}^{-1}$ and $0.03 \text{ cm}^3 \text{ g}^{-1}$, respectively. The nitrogen sorption isotherm and pore size distribution of IL-C (**Figure 5.14**) confirm that the IL-C carbon is very lowly porous with hardly any developed pores. The nitrogen sorption isotherms and corresponding pore size distribution (PSD) curves of the activated carbons are shown in **Figure 5.15**. For IL-AC2T, the isotherm changes from type I (microporous) to type IV (mesoporous) with increase in activation temperature. This change is reflected in the pore structure of the activated carbons by the formation of wider pores as shown by the PSD curves (**Figure 5.15** and **Figure 5.16**), which indicate the presence of micropores and small mesopores. For KOH/IL-C ratio of 4 or 6 (**Figure 5.15** and **Figure 5.16**), predominantly mesoporous carbons with isotherm type IV are produced at all activation temperatures. Thus, unlike IL-AC2T carbons, the IL-AC4T and IL-AC6T samples are predominantly mesoporous but with a significant proportion of microporosity. The adsorbed nitrogen levels, as per the isotherms, are significantly higher than the average for activated carbons.^{34, 52, 53} We attribute the enhanced porosity to the presence of N in the IL-C precursor. However, it is also noticeable that despite the enhanced porosity, the isotherms and PSD curves still show that some microporosity is retained even under the harshest activating conditions. We attribute the retention of some microporosity to the mitigating effect of the low O/C ratio of IL-C. The mix of microporosity and mesoporosity is also reflected in whether the isotherms show hysteresis. The isotherms of IL-AC2700, IL-AC2800, IL-AC4700 and IL-AC6700, which are the relatively more microporous samples, do not show any hysteresis loop. The rest of the samples show type H2 hysteresis loop, which can arise from hierarchical porosity, which is consistent with their higher level of mesoporosity accompanied with a significant proportion of microporosity. The size of the hysteresis loops appears to increase with the level of mesoporosity. Overall, the hysteresis loops are consistent with slit-shaped pores and the nature of connectivity expected for activated carbons.

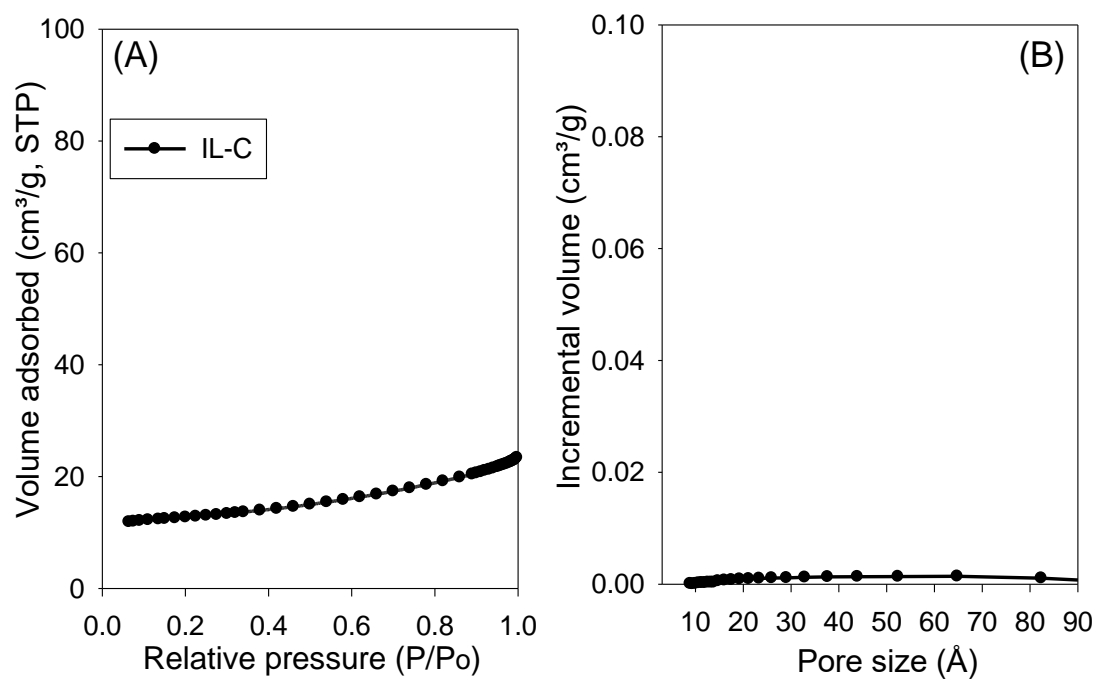


Figure 5.14. Nitrogen sorption isotherm (A) and pore size distribution curve (B) of carbonised ionic liquid (IL-C).

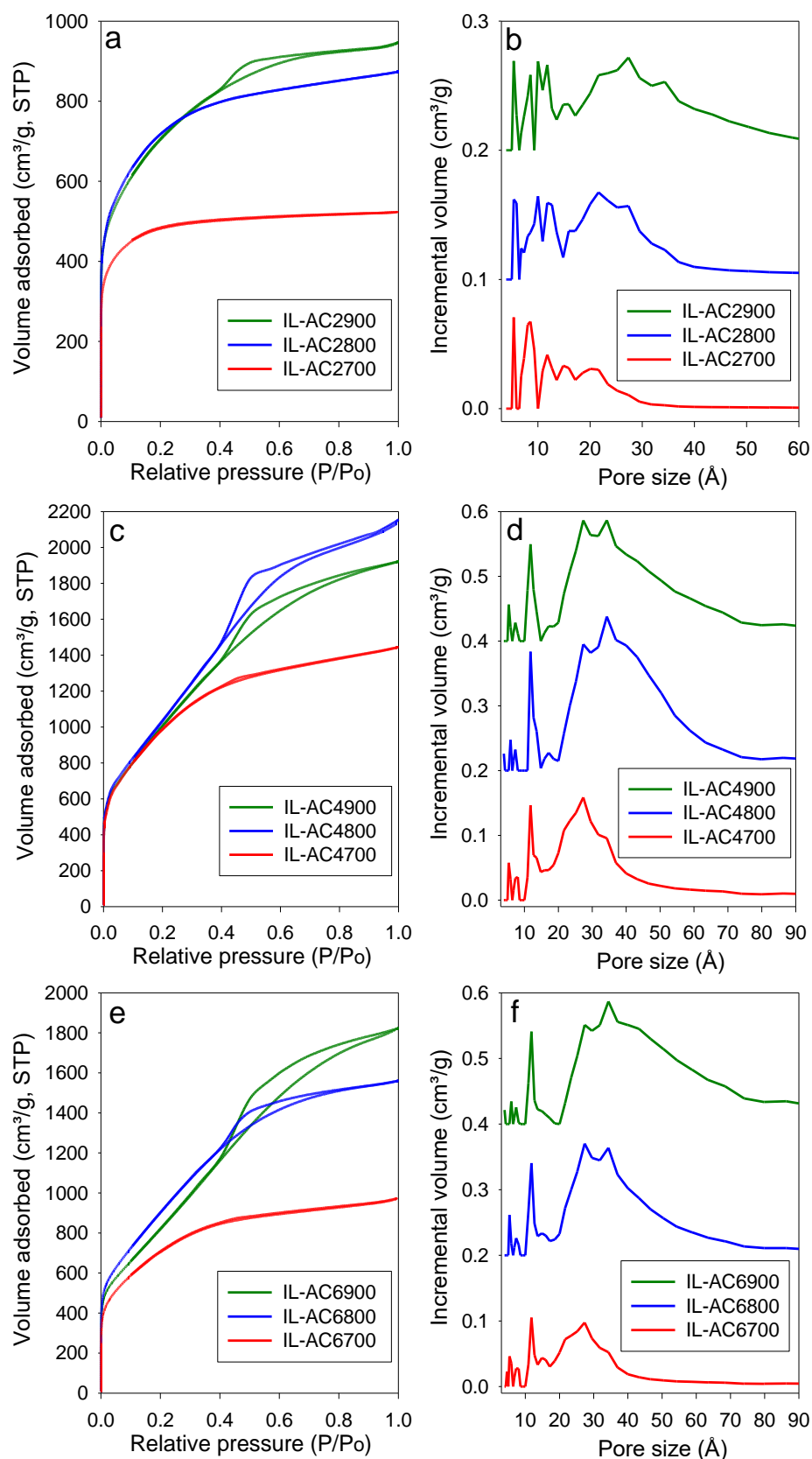


Figure 5.15. Porosity of IL-ACxT activated carbons. (a, c and e) Nitrogen sorption isotherms of IL-AC2T, IL-AC4T and IL-AC6T carbons, respectively. (b, d and f) Pore size distribution (PSD) curves of IL-AC2T, IL-AC4T and IL-AC6T carbons, respectively.

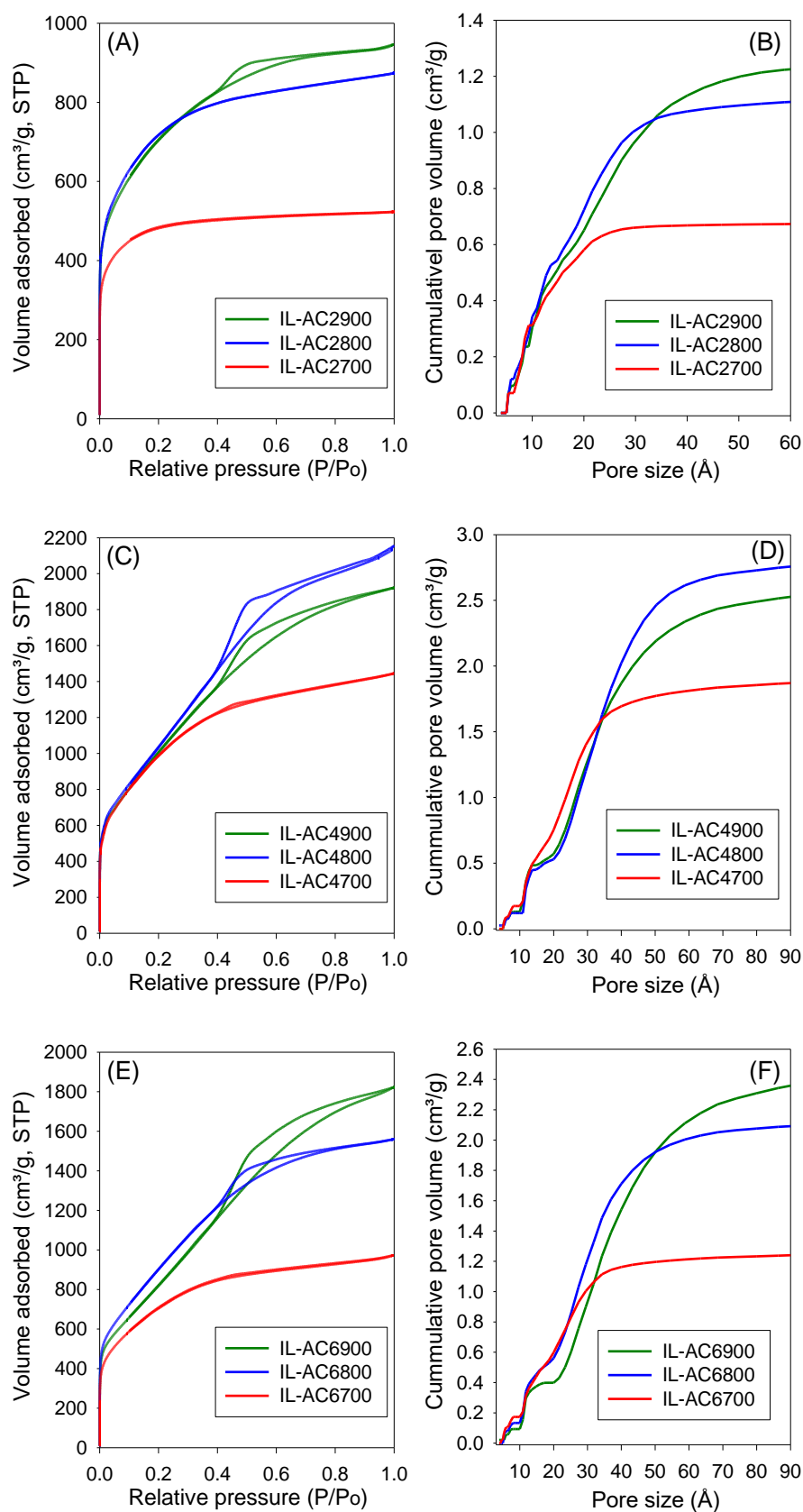


Figure 5.16. Nitrogen sorption isotherms (A, C and E) and cumulative pore size distribution curves (B, D and F) of IL-AC_xT carbons prepared at KOH/IL-C ratio of 2 (A, B), 4 (C, D) and 6 (E, F).

Table 5.2 summarises the textural parameters of the activated carbons. The surface area of the activated carbons is high to ultra-high in the range 1803 to 3995 m² g⁻¹, depending on the severity of activation. In general, the surface area rises when the activation temperature increases from 700 to 800 °C, followed by a slight reduction at 900 °C, which is in line with the "overactivation" concept.³¹ The surface area for IL-AC2T (IL-AC2700, IL-AC2800 and IL-AC2900) carbons is 1803, 2619 and 2534 m² g⁻¹, respectively, which shows a clear impact of the activation temperature and that 800 °C offers the optimum conditions for maximising the surface area. For IL-AC4T carbons (IL-AC4700, IL-AC4800 and IL-AC4900) the surface area increased to 3662, 3995 and 3818 m² g⁻¹, respectively. Further increase in amount of KOH resulted in decrease in surface area to 2567, 3394 and 3135 m² g⁻¹, respectively for IL-AC6700, IL-AC6800 & IL-AC6900 carbons. The carbons have high pore volume that ranges from 1.35 to 3.3 cm³ g⁻¹, except the sample IL-AC2700 (0.81 cm³ g⁻¹). The surface area and pore volume are amongst the highest ever reported for any precursor under any given activation conditions. Indeed, to the best of our knowledge, IL-AC4800 has one of the highest surface areas of any activated carbons reported to date.^{29, 40, 52-58} The level of microporosity in the carbons depends on the severity of activation, and generally decreases at higher activation temperature and KOH/IL-C ratio. Thus, whilst IL-AC2T carbons are predominantly microporous (57 – 79% of surface area and 45 – 72% of pore volume arising from micropores), IL-AC4T show a mix of micro and mesoporosity, and IL-AC6T are mesoporous in nature. Similar to recently described polypyrrole-derived carbons, IL-C appears to be susceptible to the creation of larger pores and mesoporosity, suggesting that, despite having a low O/C ratio, it is considerably less resistant to activation due to a high N content.^{34, 53, 54}

Table 5.2. Textural properties of ionic liquid-derived IL-ACxT activated carbons.

Sample	Surface area (m ² g ⁻¹)	Micropore surface area ^a (m ² g ⁻¹)	Pore volume (cm ³ g ⁻¹)	Micropore volume ^b (cm ³ g ⁻¹)	Surface area density ^c (m ² cm ⁻³)	Packing density ^d (g cm ⁻³)	Volumetric surface area ^e (m ² cm ⁻³)
IL-AC2700	1803	1424 (79)	0.81	0.58 (72)	2226	0.76	1370
IL-AC2800	2619	1853 (71)	1.35	0.80 (60)	1940	0.50	1310
IL-AC2900	2524	1433 (57)	1.46	0.66 (45)	1729	0.39	984
IL-AC4700	3662	1745 (48)	2.23	0.79 (35)	1642	0.49	1794
IL-AC4800	3995	1523 (38)	3.30	0.81 (25)	1210	0.39	1558
IL-AC4900	3817	1172 (31)	2.97	0.64 (22)	1285	0.31	1183
IL-AC6700	2567	1322 (52)	1.50	0.6 (40)	1711	0.56	1438
IL-AC6800	3394	1305 (38)	2.40	0.71 (30)	1414	0.37	1256
IL-AC6900	3135	876 (28)	2.81	0.61 (22)	1116	0.31	972

^aValues in parenthesis are % of surface area from micropores. ^bValues in parenthesis are % of pore volume from micropores. ^cSurface area density is obtained as ratio of total surface area to total pore volume. ^dThe packing density was determined by pressing a given amount of carbon in a 1.3 cm die at pressure of 7 MPa for 5 min. ^eVolumetric surface area determined as surface area x packing density.

Recently, there has been some discussion on the effectiveness of the use of the BET equation in reproducibly calculating the surface area of porous materials.⁵⁵ A round-robin study involving a large number of research groups found significant variability in the BET surface area calculated from identical nitrogen sorption isotherms.⁵⁵ To address such variability, the study developed a computational method, namely BET surface identification (BETSI), that was claimed to more accurately and unambiguously determine the BET surface area of porous materials.⁵⁵ Therefore, to ensure consistency of our porosity measures, we calculated the surface area of the activated carbons using the BETSI method wherein the minimum number of points in the linear region was 10, with a minimum r^2 of 0.995, and Rouquerol criterion

maximum error of 20% (**Table 5.3**). For completeness, we also analysed the porosity and calculated the porosity measures (surface area and pore volume) using the Non-Local Density Functional Theory (NLDFT) model. The comparative porosity data from BET, BETSI and NLDFT analysis (**Table 5.4**) shows that our BET values are very close to the BETSI derived surface area, which signifies their veracity. Most of our BET values are within 1% of the BETSI surface areas, which validates our porosity calculation protocols. The surface area obtained via the NLDFT method is lower than that of from BET and BETSI methods. However, the trends in surface area are retained.

Table 5.3. Parameters for the determination of BETSI surface area for IL-ACxT carbons.

Sample	BETSI surface area (m ² g ⁻¹)	Points	r ²	Slope	Intercept	C	Qm (cm ³ g ⁻¹ STP)
IL-AC2700	1783	10	0.9998	0.002436	5.005×10^{-6}	488	410
IL-AC2800	2519	10	0.9991	0.001724	4.964×10^{-6}	348	579
IL-AC2900	2521	10	0.9999	0.001716	1.154×10^{-5}	149	579
IL-AC4700	3545	10	0.9976	0.001215	1.334×10^{-5}	92	814
IL-AC4800	3978	10	0.9995	0.001069	2.469×10^{-5}	44	914
IL-AC4900	3748	10	0.9985	0.001141	2.005×10^{-5}	58	861
IL-AC6700	2545	10	0.9998	0.001691	1.923×10^{-5}	89	585
IL-AC6800	3405	10	0.9998	0.001252	2.639×10^{-5}	49	782
IL-AC6900	3156	10	0.9996	0.001347	3.275×10^{-5}	42	725

Table 5.4. Measures of porosity of IL-ACxT carbons. Classical measures (BET surface area (A_{BET}) and pore volume (V_{sp})), and NLDFT measurements, (NLDFT surface area (A_{NLDFT}) and NLDFT pore volume (V_{NLDFT})) are accompanied, in parenthesis, by the surface area or pore volume arising from micropores and the proportion taken up by micropores as a percentage of the total. The middle column shows the BETSI surface area.

Sample	A_{BET} ($\text{m}^2 \text{g}^{-1}$)	V_{sp} ($\text{cm}^3 \text{g}^{-1}$)	BETSI surface area ($\text{m}^2 \text{g}^{-1}$)	A_{NLDFT} ($\text{m}^2 \text{g}^{-1}$)	V_{NLDFT} ($\text{cm}^3 \text{g}^{-1}$)
IL-AC2700	1803 (1424, 79%)	0.81 (0.58, 72%)	1783	1489 (1421, 95%)	0.74 (0.65, 88%)
IL-AC2800	2619 (1853, 71%)	1.35 (0.80, 60%)	2519	1993 (1727, 87%)	1.23 (0.86, 70%)
IL-AC2900	2524 (1433, 57 %)	1.46 (0.66, 45%)	2521	1915 (1528, 80%)	1.33 (0.77, 58%)
IL-AC4700	3662 (1745, 48%)	2.23 (0.79, 35%)	3545	2391 (1661, 70%)	2.04 (0.96, 47%)
IL-AC4800	3995 (1223, 31%)	3.30 (0.81, 25%)	3978	2647 (1266, 48%)	3.07 (0.72, 24%)
IL-AC4900	3817 (1172, 31%)	2.97 (0.64, 22%)	3748	2547 (1365, 54%)	2.75 (0.76, 28%)
IL-AC6700	2567 (1322, 52%)	1.50 (0.60, 40%)	2545	1837 (1404, 76%)	1.37 (0.74, 54%)
IL-AC6800	3394 (1305, 38%)	2.40 (0.71, 30%)	3405	2244 (1280, 57%)	2.22 (0.73, 33%)
IL-AC6900	3135 (876, 28%)	2.81 (0.61, 22%)	3156	2131 (976, 46%)	2.63 (0.54, 21%)

Recent reports have shown that there is a link between the ratio of surface area to pore volume ratio, i.e., the surface area density (SAD), and the tendency to generate micropores rather than larger pores.^{30, 35} Microporous materials have high SAD, which can then reduce with the introduction of mesopores. A strong linear correlation has been demonstrated between the O/C of a precursor ratio and surface area density of the resulting carbons.³⁰ This means that SAD is a good indicator of the susceptibility or resistance to activation of any carbonaceous precursor.^{30, 35} The SAD of the IL-ACxT carbons (**Table 5.2**) covers a wide range from 1116 to 2226 $\text{m}^2 \text{cm}^{-3}$, and is dependent on the activation conditions (KOH/IL-C ratio and activation temperature). To further clarify on the contrasting effects of the presence of N and low O/C ratio on the activation behavior of IL-C, we compared it with other forms of carbonaceous matter that have been used as starting material for activated carbons (**Table 5.5**). The carbonaceous matter include air-carbonised carbon from biomass (date seed,³⁰ CNL1 carbon,⁵⁹

cloves,⁶⁰ sawdust⁶¹), hydrothermally carbonised hydrochar from biomass (starch,⁶² cellulose hydrochar,^{62, 63} sawdust,^{35, 62} lignin,⁶⁴ jujun grass,⁶⁵ *Camellia Japonica*,⁶⁵ cloves⁶⁰), hydrochar from fresh cigarette filters,⁵⁶ hydrochar from smoked cigarette filters,⁵⁶ raw sawdust,⁶⁶ hydrochar from cellulose acetate,⁶³ and also carbon nanotube composites,⁶⁷ and polypyrrole.³⁴ It is interesting to note that IL-C has the lowest O/C ratio amongst the wide range of carbonaceous matter (**Table 5.5**), which suggests that IL-ACxT carbons should exhibit comparatively high SAD. Thus, we compared (**Table 5.6** and **Table 5.7**) the SAD of selected IL-AC carbons with that of similarly activated (in terms of KOH/precursor ratio and activation temperature) carbons from the other carbonaceous matter (**Table 5.5**). The expectation is that the IL-AC carbons should have the highest SAD under any given activations conditions on account of their low O/C ratio. In general, there is a clear linear relationship between the O/C ratio and SAD as has previously been demonstrated.³⁰ However, the IL-AC samples, both IL-AC4700 and IL-AC4800, do not follow this trend (**Figure 5.17** and **Figure 5.18**). Whilst the expectation is that the IL-AC samples should have the highest SAD amongst the suite of carbons, the reality is that their SAD is much lower. This anomalous behavior is explained by the counter effect of the high N content in IL-C. This behavior reveals the unique nature of the IL-C carbon, which is the genesis for generating ultra-high surface area carbons that still possess significant microporosity. These observations confirm that careful selection of the carbonaceous precursor can allow tailoring of the porosity of activated carbons. In the present case, it is clear that knowledge of the link between N-content and O/C ratio of a precursor and SAD can be a basis for the preparation of carbons with tailored or targeted porosity for specific applications.

The packing density of the IL-AC carbons (**Table 5.2**) reflects their micro/mesoporous nature. The packing density reduces as the overall porosity rises but still remains comparatively high. The volumetric surface area (defined as surface area x packing density) of the carbons in **Table 5.2** shows some interesting trends. The volumetric surface areas of IL-AC2T carbons is in the range 984 and 1370 m² cm⁻³ and for IL-AC4T it is between 1183 and 1794 m² cm⁻³ while for IL-AC6T carbons it ranges from 972 to 1438 m² cm⁻³. The volumetric surface area of IL-AC2T carbons is limited by their relatively low surface area, while that of IL-AC6T is limited by low packing density. On the other hand, samples IL-AC4700 and IL-AC4800 have the highest

volumetric surface area of, respectively, 1794 and 1558 m² cm⁻³, due to their high surface area and moderate packing density. Such volumetric surface area is amongst the highest reported for any porous materials.^{30, 35, 68-73} Although some MOFs such as NU-1501-Al have been reported to have volumetric surface area as high as 2060 m² cm⁻³, it is likely that such values are overestimated due to the fact that they are calculated using the crystallographic density of the MOFs instead of the packing density.⁷³ The performance of porous materials in gas storage, and especially methane uptake, has recently been linked to their volumetric surface area.^{29, 30, 60, 68} The expectation, therefore, is that the IL-AC samples that have high volumetric surface area (e.g. IL-AC4700 and IL-AC4800) would exhibit attractive methane uptake at pressures of 35 to 100 bar on both a gravimetric basis (due to high surface area and pore volume) and volumetric basis (due to enhanced packing density and volumetric surface area).

Table 5.5. Elemental composition of IL-C carbon compared to other carbonaceous precursors, namely, flash air-carbonised date seed (ACDS), flash air-carbonised sawdust (ACSD), flash air-carbonised cloves (ACSD), CNL1 carbon (CNL1), raw sawdust (SDD), cloves hydrochar (HCC), sawdust hydrochar (SD), lignin hydrochar (LAC), jujun grass hydrochar (ACGR), *Camelia Japonica* hydrochar (ACCA), cellulose hydrochar (C), cellulose acetate hydrochar (CA), starch hydrochar (S), fresh cigarette filter hydrochar (FF)), smoked cigarette filter hydrochar (SF), carbon nanotube composites (CN) and polypyrrole (Py).

Carbonaceous precursor	C [%]	H [%]	O [%]	(O/C) ^a	Reference
IL-C ^b	69.1	0.9	10.7	0.116	This work
Flash air carbonised date seed (ACDS)	78.5	4.0	16.3	0.156	14
Flash air carbonised sawdust (ACSD)	72.4	3.2	24.2	0.251	48
Flash air carbonised cloves (ACC)	66.1	4.3	27.7	0.310	47
CNL1 carbon (CNL1)	77.7	3.1	19.2	0.185	46
Raw sawdust (SDD)	46.4	5.8	47.8	0.773	53
Cloves hydrochar (HCC)	62.1	6.3	30.1	0.360	47
Sawdust hydrochar (SD)	57.4	5.6	37.0	0.483	19,49
Lignin hydrochar (LAC)	66.6	5.1	28.3	0.319	51
Jujun grass hydrochar (AGGR)	55.8	5.7	38.5	0.517	52
<i>Camellia Japonica</i> hydrochar (ACCA)	49.1	5.2	45.7	0.698	52
Cellulose hydrochar (C)	69.5	6.2	24.4	0.263	49,50
Cellulose acetate hydrochar (CA)	66.2	3.9	29.9	0.339	50
Starch hydrochar (S)	68.8	6.6	24.6	0.269	49
Fresh cigarette filter hydrochar (FF)	63.6	4.2	32.2	0.380	43
Smoked cigarette filter hydrochar (SF) ^c	68.5	5.7	24.8	0.272	43
Carbon nanotube composites (CN) ^d	45.1	1.5	52.6	0.875	54
Polypyrrole (Py) ^{e,f}	44.5	3.0	39.9	0.672	18

^aAtomic ratio. ^bIL-C contains 19.3 wt% N. ^cSmoked cigarette filter hydrochar contains 1 wt% N. ^dThe CNT composites contained 0.8 wt% N, and therefore a nominal O content of 52.6% obtained as $O = 100 - C - H - N$, which gives O/C ratio of 0.875. ^ePolypyrrole contained 12.6 wt% N. ^fPolypyrrole has nominal O content of 39.9% obtained as $O = 100 - C - H - N$, which gives O/C ratio of 0.672.

Table 5.6. Textural properties and surface area density of IL-AC carbons activated at 800 °C and KOH/IL-C ratio of 4 compared to similarly activated carbons derived from a variety of carbonaceous precursors. See **Table 5.5** for description of the precursors.

Precursor	Sample	Surface area ^a (m ² g ⁻¹)	Pore volume ^b (cm ³ g ⁻¹)	Surface area density (m ² cm ⁻³)	O/C ratio of precursor	Reference
IL-C	IL-AC4800	3995 (1223)	3.30 (0.81)	1211	0.116	This work
ACDS	ACDS4800	2609 (1825)	1.10 (0.70)	2372	0.156	14
ACSD	ACSD-4800	2610 (1892)	1.15 (0.74)	2270	0.251	48
ACC	ACC4800	3175 (2568)	1.65 (1.17)	1924	0.310	47
CNL1	CNL1-4800	2183 (1886)	1.05 (0.84)	2079	0.185	46
SDD	SD4800D	2980 (478)	2.10 (0.30)	1419	0.773	53
HCC	HCC4800	3116 (2190)	1.75 (0.98)	1781	0.360	47
SD	SD4800	2783 (694)	1.80 (0.36)	1546	0.483	19,49
LAC	LAC4800	3235 (1978)	1.77 (0.93)	1828	0.319	51
ACGR	ACGR4800	2957 (1578)	1.72 (0.75)	1719	0.517	52
ACCA	ACCA4800	3537 (2557)	1.85 (1.21)	1912	0.698	52
C	C-4800	2125 (1707)	0.98 (0.74)	2168	0.263	49,50
CA	CA-4800	2864 (2662)	1.32 (1.17)	2170	0.339	50
FF	FF-4800	4113 (2075)	1.87 (0.79)	2199	0.380	43
SF	SF-4800	2393 (1810)	1.09 (0.70)	2195	0.272	43
CN	CN4800	3802 (33)	2.98 (0.22)	1276	0.875	54
Py	Py4800	3450 (1910)	2.57 (1.22)	1342	0.672	18

The values in the parenthesis refer to: ^amicropore surface area and ^bmicropore volume.

Table 5.7. Textural properties and surface area density of IL-AC carbons activated at 700 °C and KOH/IL-C ratio of 4 compared to similarly activated carbons derived from a variety of carbonaceous precursors. See **Table 5.5** for description of the precursors.

Precursor	Sample	Surface area ^a (m ² g ⁻¹)	Pore volume ^b (cm ³ g ⁻¹)	Surface area density (m ² cm ⁻³)	O/C ratio of precursor	Reference
IL-C	IL-AC4700	3662 (1745)	2.23 (0.79)	1642	0.116	This work
ACDS	ACDS4700	2192 (1871)	0.93 (0.74)	2357	0.156	14
ACC	ACC4700	2773 (2431)	1.42 (1.01)	1953	0.310	47
CNL1	CNL1-4700	1280 (1191)	0.65 (0.56)	1969	0.185	46
HCC	HCC4700	2743 (2267)	1.35 (1.05)	2032	0.360	47
SD	SD4700	2252 (2088)	1.03 (0.91)	2186	0.483	19,49
LAC	LAC4700	2038 (1832)	1.00 (0.84)	2028	0.319	51
ACGR	ACGR4700	3144 (2753)	1.56 (1.23)	2015	0.517	52
ACCA	ACCA4700	2983 (2500)	1.50 (1.14)	1987	0.698	52
C	C-4700	2370 (2201)	1.08 (0.94)	2194	0.263	49,50
CA	CA-4700	3771 (3484)	1.75 (1.54)	2155	0.339	50
S	S4700	2194 (2082)	1.01 (0.92)	2172	0.269	49
FF	FF-4700	2803 (1901)	1.23 (0.73)	2279	0.380	43
SF	SF-4700	2512 (2019)	1.20 (0.91)	2093	0.272	43
CN	CN4700	3202 (1106)	2.14 (0.20)	1496	0.875	54
Py	Py4700	3568	2.46 (0.28)	1450	0.672	18

The values in the parenthesis refer to: ^amicropore surface area and ^bmicropore volume.

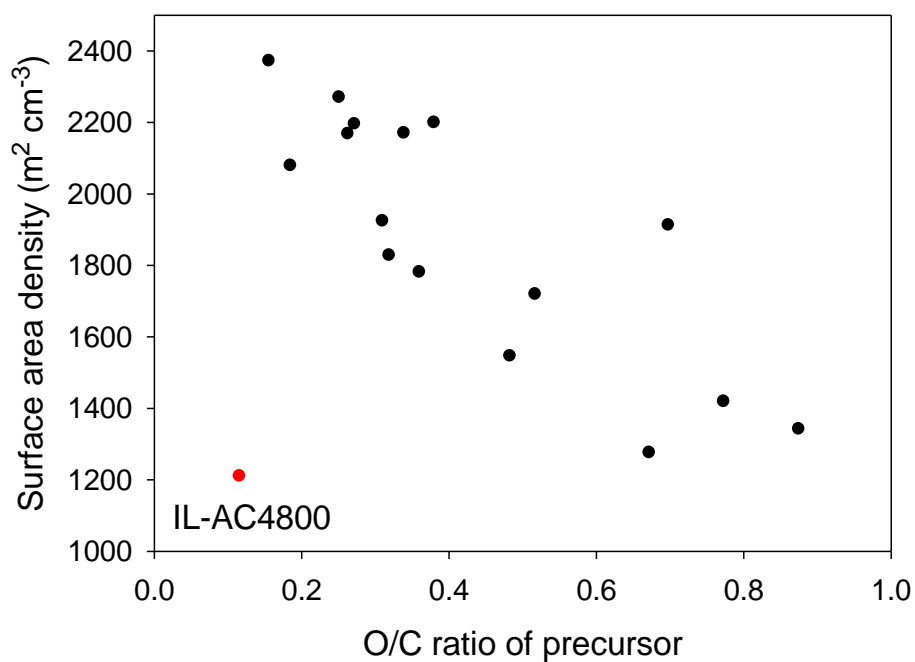


Figure 5.17. Surface area density of activated carbons as a function of the O/C ratio of the precursor carbonaceous matter. All activations were performed at 800 °C at KOH/precursor ratio of 4.

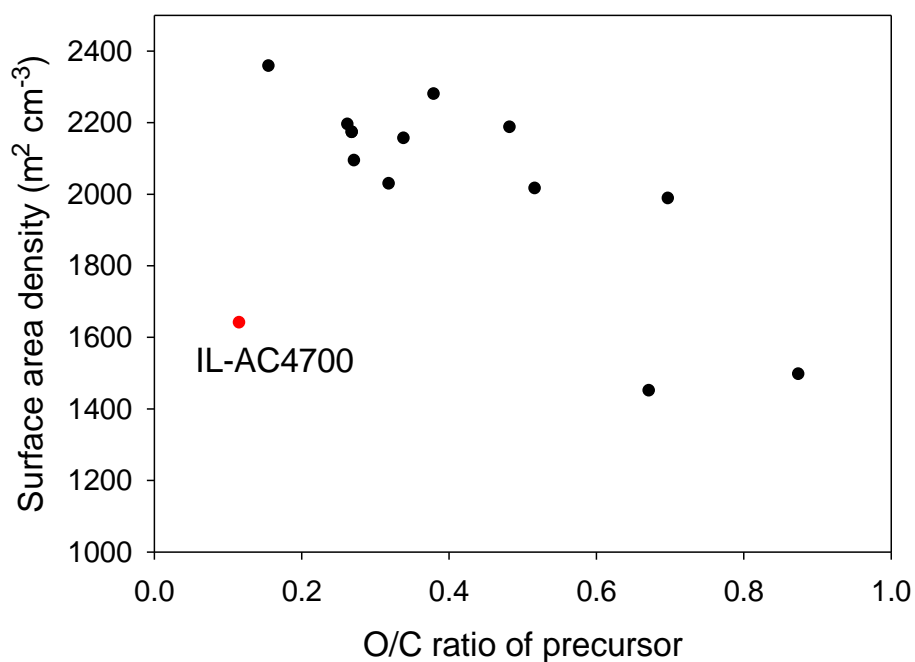


Figure 5.18. Surface area density of activated carbons as a function of the O/C ratio of the precursor carbonaceous matter. All activations were performed at 700 °C at KOH/precursor ratio of 4.

5.4.3 Methane storage of ionic-liquid derived activated carbons

To achieve efficient methane storage at medium to high pressures (35 – 100 bar), porous materials should possess a combination of micropores and mesopores and have high surface area. Given their unique properties with regard to porosity and packing density, the IL-AC carbons are potentially excellent candidates for achieving substantial methane storage at moderate to high pressures. The methane storage capacity was measured at 25 °C and pressures ranging from 0 to 100 bar. Uptake at 35, 65, and 100 bar was the main focus of this study since these pressures have been used to evaluate performance of porous materials in many earlier research efforts and therefore provide a convenient basis for comparing the performance of the present carbons to that of the state-of-the-art materials.^{22, 24, 26, 29, 68, 70-75} The methane uptake measurements determined the excess storage capacity. The total methane storage capacity was then calculated from the excess uptake data by taking into account the total pore volume of the activated carbon, along with the density of methane at any given temperature and pressure. The following equation was applied:

$$\theta_T = \theta_{Exc} + (d_{CH_4} \times V_T)$$

Where, θ_T is the total methane uptake (g g^{-1}), θ_{Exc} is excess methane uptake (g g^{-1}), d_{CH_4} is methane density (g cm^{-3}) at any given pressure and prevailing temperature (25 °C or 0 °C), and V_T is total pore volume ($\text{cm}^3 \text{g}^{-1}$) of the activated carbon. The density of methane (d_{CH_4}) under any given temperature and pressure conditions was obtained from the National Institute of Standards and Technology (NIST) website (<https://www.nist.gov/>).

Figure 5.19 shows the excess gravimetric methane uptake isotherms of the activated carbons. The excess methane storage capacity at 35, 65, and 100 bar is summarised in **Table 5.8**. The excess gravimetric uptake shows the following trends; (i) increases as KOH/IL-C ratio rises from 2 to 4 and then reduces for samples prepared at a ratio of 6, and (ii) increases as the activating temperature rises from 700 °C to 800 °C and then slightly decreases for carbons prepared at 900 °C. For example, at 35 bar, the excess methane uptake of samples IL-AC2700, IL-AC2800 and IL-AC2900 is 8.1, 12.5 and 11.1 mmol g^{-1} , respectively, whereas IL-AC4700, IL-AC4800 and IL-AC4900 exhibited higher methane uptake of 11.6, 12.7 and 12.5 mmol g^{-1} , respectively. For IL-AC6700, IL-AC6800 and IL-AC6900, uptake was 9.7, 12.1 and 12.3 mmol g^{-1} ,

respectively. Excess methane uptake of IL-AC4800 (12.7 mmol g^{-1}) at 25°C and 35 bar is among the best reported for any porous material.^{22, 24, 26, 29, 68, 70-75} At higher pressures of 65 and 100 bar, the excess methane uptake ranges from 9.5 to 15.7 mmol g^{-1} and 10.1 to 17.2 mmol g^{-1} , respectively, with IL-AC4T samples possessing the highest methane storage capacity. In general, the performance of the IL-AC4T samples is superior to the IL-AC2T or IL-AC6T series, which is in line with the trend in surface area and volumetric surface area (**Table 5.2**).

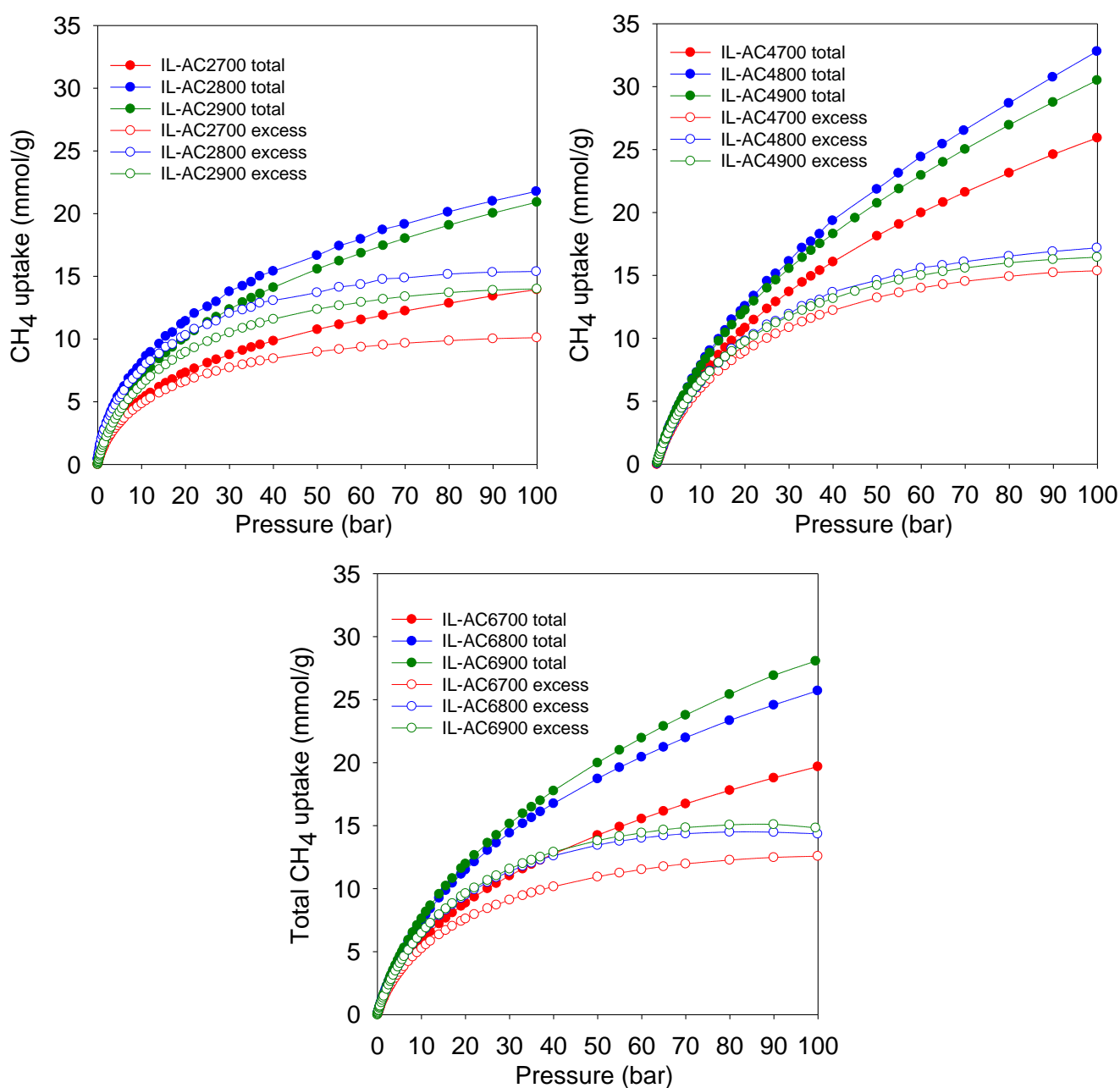


Figure 5.19. Gravimetric methane uptake isotherms. Excess and total gravimetric methane uptake at 25°C for IL-AC_xT activated carbons.

Table 5.8. Total and excess gravimetric methane uptake of IL-ACxT carbons at 25 °C.

Sample	Gravimetric methane uptake					
	35 bar		65 bar		100 bar	
	(mmol g ⁻¹)	(g g ⁻¹)	(mmol g ⁻¹)	(g g ⁻¹)	(mmol g ⁻¹)	(g g ⁻¹)
IL-AC2700	9.3 (8.1)	0.15 (0.13)	11.9 (9.5)	0.19 (0.15)	13.9 (10.1)	0.23 (0.16)
IL-AC2800	14.6 (12.5)	0.23 (0.20)	18.8 (14.9)	0.30 (0.24)	21.8 (15.4)	0.35 (0.25)
IL-AC2900	13.3 (11.1)	0.21 (0.18)	17.5 (13.2)	0.28 (0.21)	20.9 (14.0)	0.34 (0.22)
IL-AC4700	14.9 (11.6)	0.24 (0.19)	20.8 (14.3)	0.33 (0.23)	25.9 (15.4)	0.42 (0.25)
IL-AC4800	17.7 (12.7)	0.28 (0.20)	25.4 (15.7)	0.41 (0.25)	32.8 (17.2)	0.53 (0.28)
IL-AC4900	17.0 (12.5)	0.27 (0.20)	24.0 (15.3)	0.39 (0.25)	30.5 (16.5)	0.49 (0.26)
IL-AC6700	11.9 (9.7)	0.19 (0.16)	16.2 (11.8)	0.26 (0.19)	19.7 (12.6)	0.32 (0.20)
IL-AC6800	15.6 (12.1)	0.25 (0.19)	21.2 (14.2)	0.34 (0.23)	25.7 (14.4)	0.41 (0.23)
IL-AC6900	16.5 (12.3)	0.26 (0.20)	22.9 (14.7)	0.37 (0.24)	28.1 (14.8)	0.45 (0.24)

The total gravimetric methane uptake isotherms are shown in **Figure 5.19**. **Table 5.8** shows a summary of the total gravimetric uptake at 35, 65, and 100 bar. The total methane uptake for IL-AC2T carbons is in the range of 9.3 – 14.6 mmol g⁻¹ (at 35 bar), 11.9 – 18.8 mmol g⁻¹ (at 65 bar) and 13.9 – 21.8 mmol g⁻¹ (at 100 bar), respectively. The total gravimetric methane uptake at 35 bar ranged from 14.9 to 17.7 mmol g⁻¹ for IL-AC4T carbons and from 11.9 to 16.5 mmol g⁻¹ for IL-AC6T samples. The total gravimetric methane uptake by the IL-AC4T carbons is, in particular, higher than that of other reported carbon materials.^{28, 29, 76, 77} Additionally, the total gravimetric methane uptake of IL-AC4T carbons at 65 bar ranges from 20.8 to 25.4 mmol g⁻¹, while that of IL-AC6T carbons ranges from 16.2 to 22.9 mmol g⁻¹. Total methane uptake for IL-AC4T carbons at 100 bar varies between 25.9 and 32.8 mmol g⁻¹, while for IL-AC6T samples, the range is 19.7 to 28.1 mmol g⁻¹. It is clear that the carbons prepared at KOH/IL-C, ratio 4 have the highest gravimetric uptake, which is in line

with their high surface area and pore volume. Indeed, the total gravimetric methane uptake of IL-AC4800 at 100 bar and 25 °C at 32.8 mmol g⁻¹ is one of the best for any carbon or MOF material.^{22, 24, 26, 28-30, 60, 70-72, 74-81}

The United States Department of Energy (DOE) has set a methane uptake target of 0.5 g g⁻¹ at 25 °C and pressure of 35 to 100 bar. The present IL-AC carbons have impressive gravimetric storage performance for methane storage, as shown in **Table 5.9**. In particular, the IL-AC4800 carbon surpasses the DOE gravimetric methane storage target with uptake of 0.53 g g⁻¹ at 100 bar and 25 °C. Such a high gravimetric absorption matches or exceeds that of the best benchmark materials reported to date.^{22, 24, 26, 28, 29, 60, 70-72, 74, 75, 77-81} Furthermore, other IL-AC samples (**Table 5.9**) also have gravimetric uptake that is very close to the DOE target; 0.42 g g⁻¹ (IL-AC4700), 0.49 g g⁻¹ (IL-AC4900), 0.41 g g⁻¹ (IL-AC6800) and 0.45 g g⁻¹ (IL-AC6900). As far as we are aware, these are the highest values ever reported for carbons and are comparable with the top values reported for MOFs.^{22, 24, 26, 28, 29, 60, 70-72, 74, 75, 77-81} If the high gravimetric uptake of the IL-ACxT activated carbons were accompanied with high volumetric uptake, it would provide unique and highly useful materials for methane storage.

Methane storage performance is often measured in terms of the volumetric uptake. The DOE has set a target of 263 cm³ (STP) cm⁻³ at 25 °C and moderate pressure (i.e., 35 – 100 bar), in addition to gravimetric uptake of at least 0.5 g g⁻¹. The gravimetric uptake and the packing density of an adsorbent are the two most important factors in determining volumetric uptake. **Figure 5.20** displays the excess and total volumetric methane uptake isotherms and **Table 5.9** summarises the total volumetric uptake and the working capacity (i.e., deliverable methane at 5 bar) for storage at 35, 65, and 100 bar. The working capacity is calculated as the difference between adsorption at 5 bar (delivery pressure) and at uptake pressure (35, 65 or 100 bar). For IL-AC2T carbons, the total volumetric uptake (cm³ (STP) cm⁻³) was in the range of 118 – 163, 156 – 211 and 187 – 244 at 35, 65 and 100 bar, respectively. For IL-AC6T carbons the uptake ranges between 115 and 151 at 35 bar, 159 and 205 at 65 bar, and 195 and 249 at 100 bar. The volumetric uptake of IL-AC4700, IL-AC4800 and IL-AC4900 carbons is even more attractive; 165, 156 and 116, respectively, at 35 bar, 230, 223 and 164, respectively, at 65 bar, and 287, 289 and 209, respectively, at 100 bar. The IL-AC4T carbons show no saturation at 100 bar in their total volumetric uptake, which suggests

that the carbons are capable of storing more methane at higher pressures. This contrasts with MOFs, which tend to show saturation at ca. 80 bar.^{82, 83} The volumetric uptake is amongst the best reported to date for carbon or MOF materials, and is crucially based on experimentally determined packing density.^{22, 24-26, 28-30, 60, 68, 70-73, 75-77, 82-85} The present carbons also show impressive performance in terms of their working capacity, which is higher than that of most porous materials; the highest deliverable methane for pressure swing of 100 to 5 bar at 25 °C is for IL-AC4700 and IL-AC4800 at 241 and 248 cm³ (STP) cm⁻³, respectively. More importantly, the present IL-AC carbons, and in particular sample IL-AC4800, are the first porous materials (carbon or MOF) to meet both gravimetric and volumetric storage targets at 25 °C.^{22, 24-26, 28-30, 60, 68, 70-77, 82-85} At 100 bar, the volumetric uptake capacity of IL-AC4700, IL-AC4800 and IL-AC4900 at, respectively, 287, 289 and 209 cm³ (STP) cm⁻³, coupled with their high gravimetric uptake of 0.42, 0.53 and 0.49 g g⁻¹, offer impressive storage combinations that are superior to any previous reports for porous carbon or MOF materials.^{22, 24-26, 28-30, 60, 68, 70-77, 82-85}

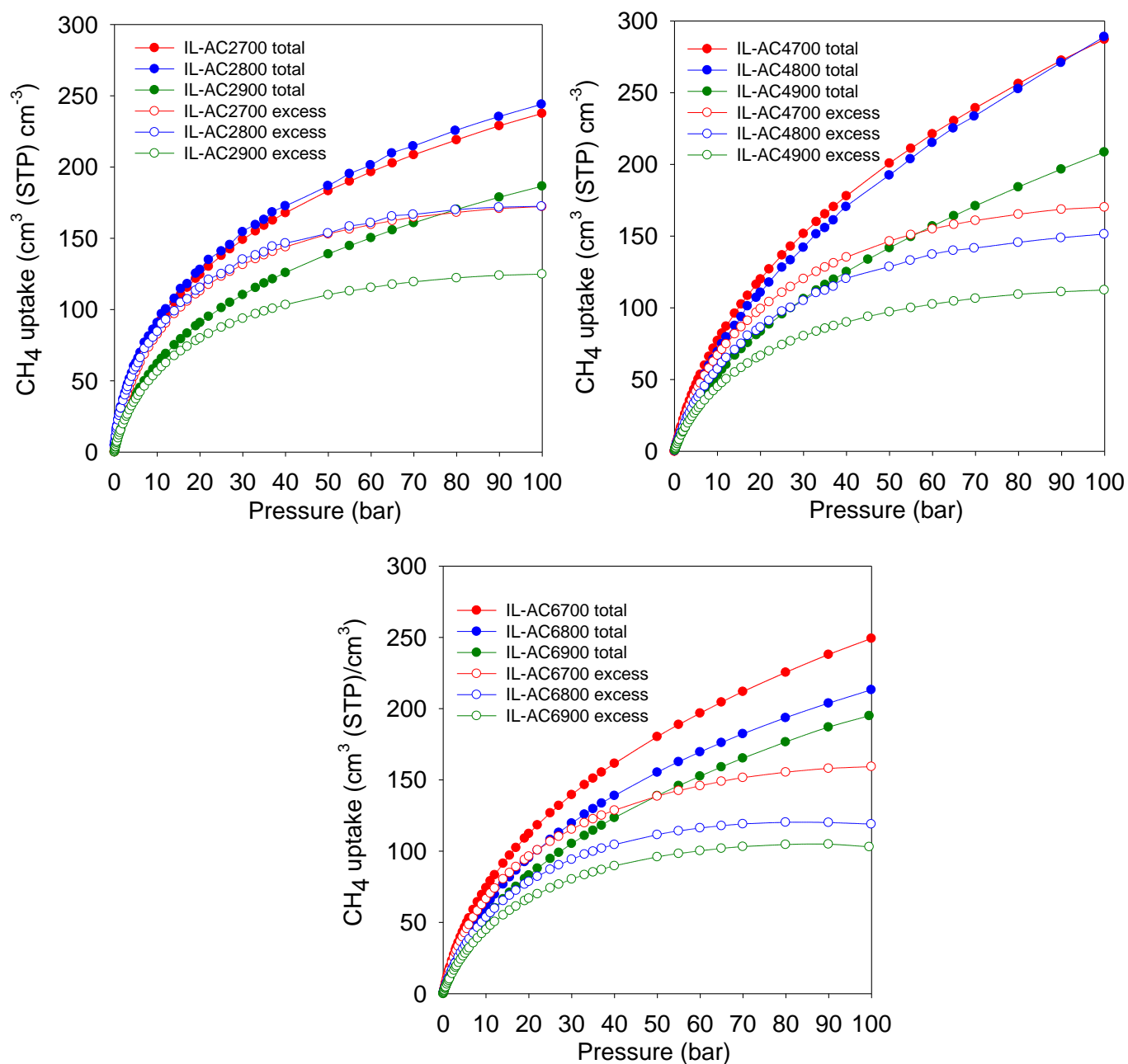


Figure 5.20. Volumetric methane uptake isotherms. Excess and total volumetric methane uptake at 25 °C for IL-ACxT activated carbons.

Table 5.9. Total volumetric methane uptake and working capacity of IL-ACxT activated carbons.

Sample	Total volumetric methane uptake ^a (cm ³ (STP) cm ⁻³)		
	35 bar	65 bar	100 bar
IL-AC2700	159 (100)	203 (144)	238 (179)
IL-AC2800	163 (101)	211 (149)	244 (182)
IL-AC2900	118 (78)	156 (116)	187 (147)
IL-AC4700	165 (119)	230 (184)	287 (241)
IL-AC4800	156 (115)	223 (182)	289 (248)
IL-AC4900	116 (84)	164 (132)	209 (177)
IL-AC6700	151 (105)	205 (159)	249 (203)
IL-AC6800	130 (93)	176 (139)	213 (176)
IL-AC6900	115 (83)	159 (127)	195 (163)

^aThe numbers in parentheses represent the volumetric working capacity (i.e., deliverable methane), which is the difference between the gas uptake at pressure of 5 bar and the specified pressure (35, 65, or 100 bar).

Regarding the nature of adsorption of methane, the FTIR spectra of IL-ACxT carbons (**Figure 5.13**) indicate that there are no functional groups on the activated carbons except those associated with remnants of the imidazolium backbone and which give rise to stretching and bending vibrations of the aromatic structure. FTIR spectra of an activated carbon taken before and after methane uptake (**Figure 5.13**) indicates that the sorption process does not cause any variation in the functional groups on the surface, i.e., IR spectra remains unchanged. This is consistent with the uptake being based on physisorption rather than any strong interaction with surface functional groups.

From the foregoing discussion, it is clear that the methane uptake is chiefly dependent on the porosity of the carbons. Further insights on the performance of the carbons may be obtained from the isosteric heat of adsorption (Qst). **Figure 5.21** shows the Qst of the carbons as a function of methane loading. The Qst is in the range of 23 to 13 kJ/mol for methane loading of up to 7 mmol g⁻¹. The Qst at low coverage, which is the best guide of the interaction between methane molecules and the carbons is in the range of 23 to 15 kJ/mol. This is within the range (10 - 25 kJ/mol) previously reported for activated carbons and other porous materials, including MOFs.^{24, 70} There seems to be a correlation between the Qst and pore size of the carbons meaning that the Qst order is IL-AC2T > IL-AC4T > IL-AC6T, except for sample IL-AC6700, which shows anomalously high Qst. The observed correlation between Qst and pore size is consistent with the fact that smaller pores can enhance the interaction between methane and the carbon pore walls. However, whilst a high Qst can favour enhanced methane storage capacity, it can also act to limit the working capacity (deliverable methane) due to high uptake at low pressure, i.e., the deliverable pressure of 5 bar. Indeed, a closer look at the data in **Table 5.9** indicates that the working capacity of IL-AC2T carbons is a lower proportion of the total uptake compared IL-AC4T and IL-AC6T carbons. For example, for a 35 to 5 bar swing the deliverable proportion is ca. 63% for IL-AC2T compared to at least 71% for IL-AC4T. For a 65 to 5 bar swing, the deliverable proportion is ca. 71% for IL-AC2T and 80% for IL-AC4T while for 100 to 5 bar it is 75% and 85% for IL-AC2T and IL-AC4T, respectively. This trend can be explained by the proportionately higher uptake at 5 bar for the IL-AC2T samples due to their higher Qst. In this regard, the porosity and Qst of the IL-AC4T carbons appears to offer a more optimised balance between low pressure uptake and total uptake, which translates to excellent working capacity.

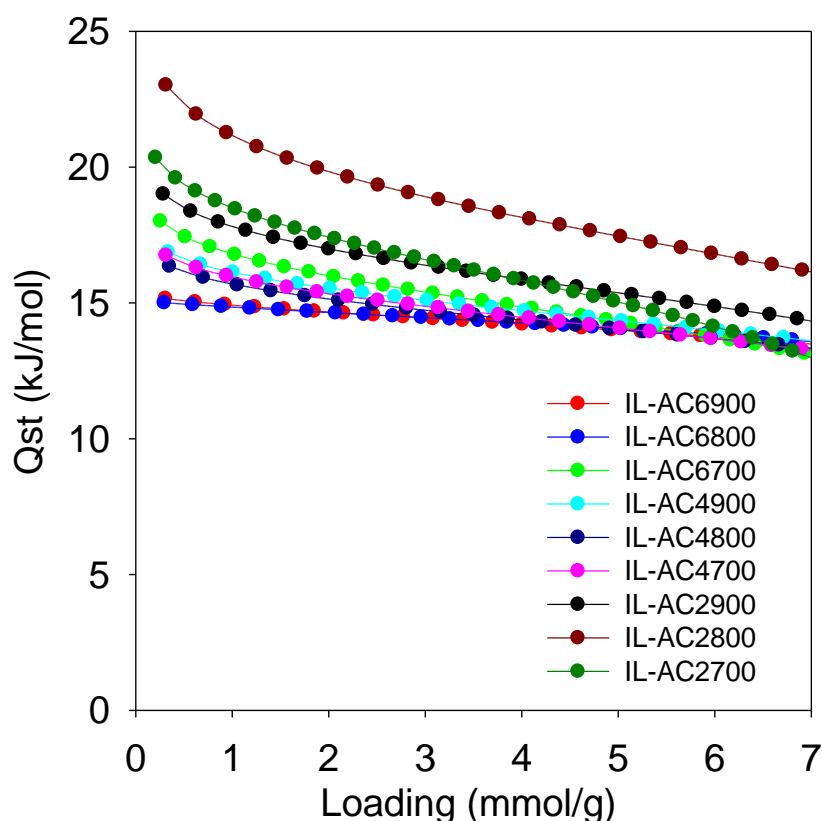


Figure 5.21. Isosteric heat of adsorption (Q_{st}) of methane. Q_{st} of methane on IL-ACxT carbons as a function of uptake, which is given as loading in mmol of methane per gram of carbon.

To be viable for methane storage, porous materials need to be used over several cycles, which means that cyclability is an important consideration. We therefore assessed the performance of one of the best performing carbons, IL-AC4800, over several cycles (**Figure 5.22**). The assessment also allowed us to clarify on any impact of compaction on the methane uptake. In this way, the first use (cycle 1) was measured for powdered IL-AC4800, i.e., before compaction, while the subsequent cycles (2, 3 and 4) were measured in pellet form after compaction of the activated carbon at 370 MPa for 10 min in a 1.3 cm (diameter) die. The uptake data over several cycles (**Figure 5.22**) show a high level of recyclability with no reduction in storage capacity. Furthermore, it is also clear that our compaction process had no impact of the methane uptake, which is consistent with previous reports on the mechanical stability of high surface area activated carbons.⁶⁰

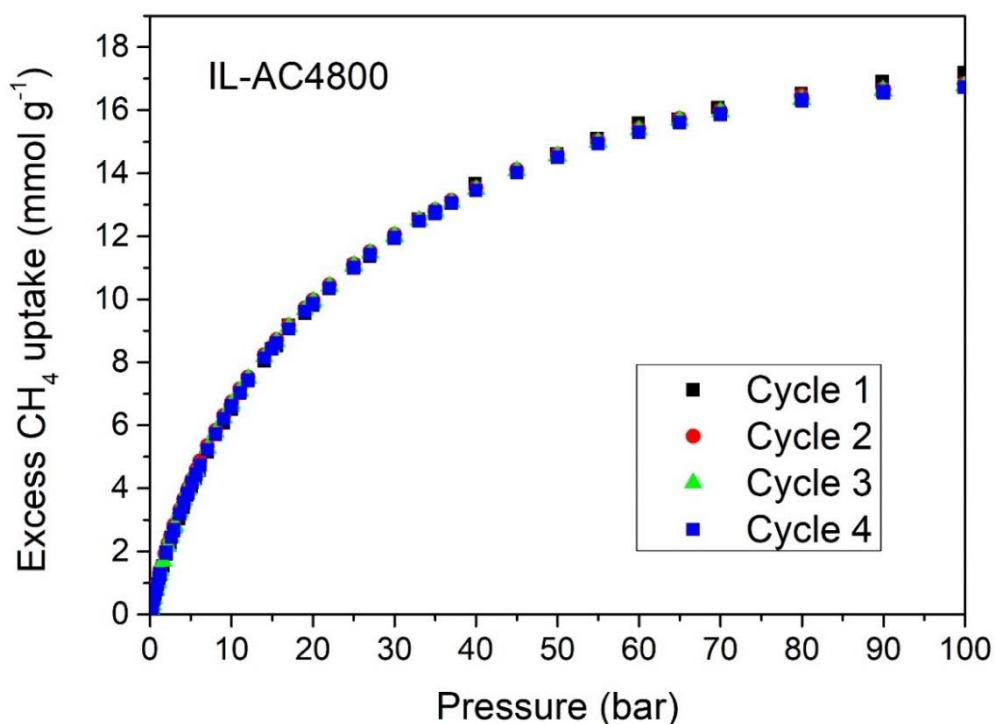


Figure 5.22. Cyclability of methane uptake and effect of compaction for sample IL-AC4800. Cycle 1 was measured for powdered IL-AC4800, i.e., before compaction, while cycle 2, 3 and 4 were measured after compaction at 370 MPa for 10 min in a 1.3 cm (diameter) die. The data shows a high level of recyclability, and furthermore that compaction has no impact of the methane uptake.

5.4.3.1 Comparison with benchmark materials

To gain a more complete picture of the performance of the IL-AC carbons, their methane-storage capacity is compared to that of state-of-the-art benchmark materials including Nu-1501-Al,⁷³ HKUST-1,⁷⁰ MOF-5,⁸⁵ Ni-MOF-74,⁷⁰ and PCN-14,^{86, 87} as shown in **Figure 5.23**. The methane storage capacity at 65, 80 and 100 bar, both in terms of total uptake (**Table 5.10**) and working capacity (**Table 5.11**) is also compared to other benchmark materials. What emerges from the comparisons is that the IL-AC carbons are unique in that they have very attractive uptake both on a gravimetric and volumetric basis. The performance of the IL-AC carbons stands out given that the apparently high volumetric uptake of MOFs is based on crystallographic density rather than packing density. It is known that the actual packing density of MOFs is much lower than their crystallographic density, meaning that the volumetric uptake implied

in (**Figure 5.23**, **Table 5.10** and **Table 5.11**) is likely to be overestimated. Reduction of the MOF values by at least 25% offers a more realistic estimate of their true performance (**Figure 5.24**). However, more recently, monolithic MOFs (monoHKUST-1 and monoUiO-66_D) have been reported that have high packing density and very attractive volumetric methane uptake.^{68, 79, 80} It is noteworthy that the volumetric uptake of the best IL-AC carbons is similar to that of the monolithic MOFs but the carbons have higher gravimetric uptake (**Figure 5.25**, **Table 5.10** and **Table 5.11**). We have previously reported on carbons that have higher volumetric uptake than the IL-AC samples but with lower gravimetric uptake that does not reach the DOE target of 0.5 g g^{-1} .^{29, 30, 60, 88} The best performance to date in terms of volumetric methane uptake at 25 °C and 100 bar is for compacted activated carbons derived from clove hydrochar (CHCC2800, CHCC4700 and CHCC4800) at 339, 334 and 309 $\text{cm}^3 \text{ (STP) cm}^{-3}$, respectively.⁶⁰ However, the overall performance of these clove-derived carbons is limited by their moderate gravimetric uptake.⁶⁰ Other carbons that perform well in terms of volumetric uptake, namely, CNL4800, ACDS4800, and PPYCNL124 with volumetric uptake of 291, 282 and 260 $\text{cm}^3 \text{ (STP) cm}^{-3}$ (at 25 °C and 100 bar) also have low to moderate gravimetric uptake of 0.31, 0.29 and 0.36 g g^{-1} , respectively.²⁹

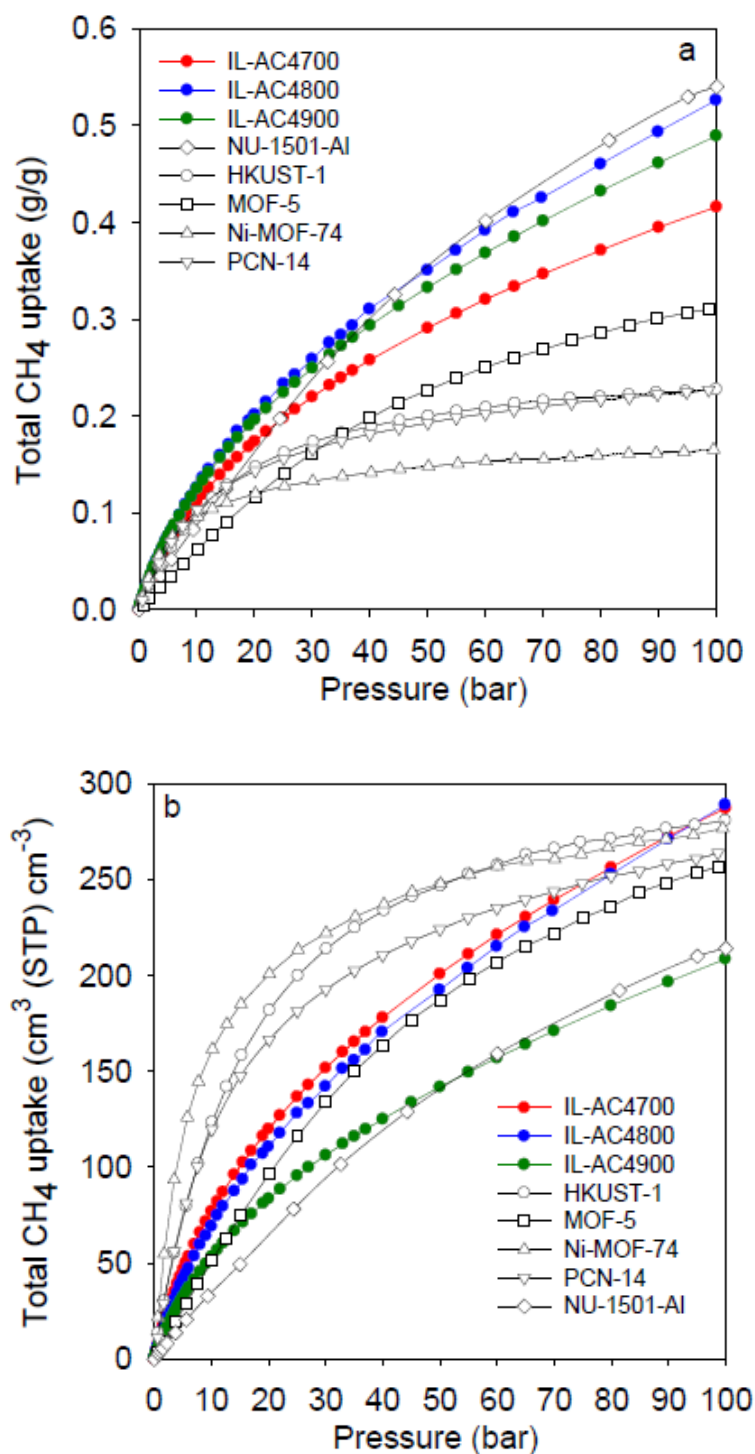


Figure 5.23. Comparative methane uptake of IL-AC4T activated carbons. (a) Total gravimetric methane uptake at 25 °C of IL-AC4T carbons compared to benchmark MOF materials. (b) Total volumetric methane storage capacity at 25 °C of IL-AC4T carbons compared to that of MOFs, for which the volumetric uptake was calculated using crystallographic density. Data for Nu-1501-A is from reference 60, HKUST-1 and Ni-MOF-74 from reference 57, MOF-5 from reference 72 and PCN-14 from references 73 and 74.

Table 5.10. Methane uptake of the best performing IL-AC carbons compared to selected benchmark MOFs and carbons. Volumetric uptake of powder MOFs is calculated based on crystallographic density rather than packing density. The references are listed below **Table 5.11**.

Sample	Density (g cm ⁻³)	65 bar (g g ⁻¹) (cm ³ cm ⁻³)		80 bar (g g ⁻¹) (cm ³ cm ⁻³)		100 bar (g g ⁻¹) (cm ³ cm ⁻³)		Reference
IL-AC4700	0.49	0.33	230	0.37	256	0.42	287	This work
IL-AC4800	0.39	0.41	223	0.46	253	0.53	289	This work
IL-AC4900	0.31	0.39	164	0.43	184	0.49	209	This work
CHCC2800	0.82	0.26	293	0.28	315	0.30	339	1
CHCC4700	0.75	0.27	282	0.29	306	0.32	334	1
CHCC4800	0.58	0.32	258	0.35	279	0.38	309	1
CNL4800	0.67	0.26	241	0.29	269	0.31	291	2
PPYCNL124	0.52	0.30	217	0.33	238	0.36	260	2
PPYCNL214	0.36	0.36	183	0.41	204	0.46	229	2
ACDS4800	0.69	0.25	243	0.27	262	0.29	282	2,3
PPYSD114	0.47	0.32	211	0.35	231	0.39	254	3
AX-21 carbon	0.487	0.30	203	0.33	222	0.35	238	4
HKUST-1	0.881	0.21	263	0.22	272	0.23	281	4
Ni-MOF-74	1.195	0.15	259	0.16	267	0.17	277	4
Al-soc-MOF-1	0.34	0.41	197	0.47	222			5
MOF-210	0.25	0.41	143	0.48	168			6
NU-1500-Al	0.498	0.29	200	0.31	216	0.34	237	7
NU-1501-Fe	0.299	0.40	168	0.46	193	0.52	218	7
NU-1501-Al	0.283	0.41	163	0.48	190	0.54	214	7
_{mono} HKUST-1	1.06	0.17	261	0.18	278	0.18	275	8
_{mono} UiO-66_D	1.05	0.14	210	0.17	245	0.20	296	9

Table 5.11. Methane uptake working capacity of the best performing IL-AC carbons compared to selected benchmark MOFs and carbons. The references are listed below.

Sample	65 bar		80 bar		100 bar		Reference
	(g g ⁻¹)	(cm ³ cm ⁻³)	(g g ⁻¹)	(cm ³ cm ⁻³)	(g g ⁻¹)	(cm ³ cm ⁻³)	
IL-AC4700	0.27	184	0.30	210	0.36	241	This work
IL-AC4800	0.34	182	0.39	212	0.46	248	This work
IL-AC4900	0.31	132	0.35	151	0.41	177	This work
CHCC2800	0.18	200	0.20	222	0.22	246	1
CHCC4700	0.20	210	0.22	234	0.25	262	1
CHCC4800	0.25	197	0.28	218	0.31	248	1
CNL4800	0.19	182	0.22	202	0.24	224	2
PPYCNL124	0.23	167	0.26	188	0.29	209	2
PPYCNL214	0.29	146	0.34	167	0.39	192	2
ACDS4800	0.18	171	0.20	189	0.22	209	2,3
PPYSD114	0.25	162	0.28	182	0.32	205	2
AX-21 carbon	0.23	155	0.26	174	0.28	190	4
HKUST-1	0.15	179	0.16	198	0.17	207	4
Ni-MOF-74	0.08	148	0.09	152	0.10	162	4
Al-soc-MOF-1	0.36	176	0.42	201			5
MOF-210	0.38	134	0.45	157			6
NU-1500-Al	0.24	165	0.26	181	0.29	202	7
NU-1501-Fe	0.36	151	0.42	176	0.48	201	7
NU-1501-Al	0.37	147	0.44	174	0.50	198	7
_{mono} HKUST-1	0.12	184	0.13	201	0.13	198	8
_{mono} UiO-66_D	0.11	167	0.14	202	0.17	253	9

References

1. I. Alali and R. Mokaya, *Energ Environ Sci*, 2022, **15**, 4710-4724.
2. A. Altwala and R. Mokaya, *J Mater Chem A*, 2022, **10**, 13744-13757.
3. A. Altwala and R. Mokaya, *Energ Environ Sci*, 2020, **13**, 2967-2978.
4. J. A. Mason, M. Veenstra and J. R. Long, *Chem Sci*, 2014, **5**, 32-51.
5. D. Alezi, Y. Belmabkhout, M. Suyetin, P. M. Bhatt, L. J. Weselinski, V. Solovyeva, K. Adil, I. Spanopoulos, P. N. Trikalitis, A. H. Emwas and M. Eddaoudi, *J Am Chem Soc*, 2015, **137**, 13308-13318.
6. H. Furukawa, N. Ko, Y. B. Go, N. Aratani, S. B. Choi, E. Choi, A. O. Yazaydin, R. Q. Snurr, M. O'Keeffe, J. Kim and O. M. Yaghi, *Science*, 2010, **329**, 424-428.

7. Z. Chen, P. Li, R. Anderson, X. Wang, X. Zhang, L. Robison, L. R. Redfern, S. Moribe, T. Islamoglu, D. A. Gomez-Gualdron, T. Yildirim, J. F. Stoddart and O. K. Farha, *Science*, 2020, **368**, 297-303.
8. T. Tian, Z. Zeng, D. Vulpe, M. E. Casco, G. Divitini, P. A. Midgley, J. Silvestre-Albero, J. C. Tan, P. Z. Moghadam and D. Fairen-Jimenez, *Nat Mater*, 2018, **17**, 174-179.
9. B. M. Connolly, M. Aragonés-Anglada, J. Gandara-Loe, N. A. Danaf, D. C. Lamb, J. P. Mehta, D. Vulpe, S. Wuttke, J. Silvestre-Albero, P. Z. Moghadam, A. E. H. Wheatley and D. Fairen-Jimenez, *Nat Commun*, 2019, **10**, 2345.

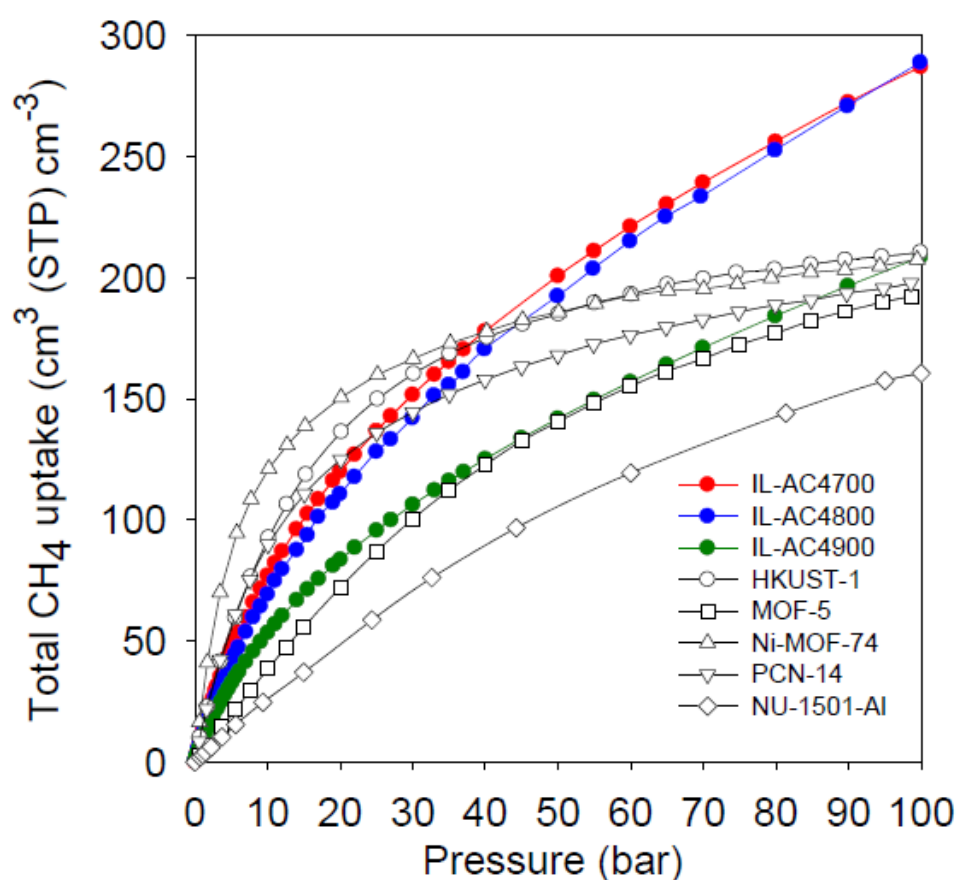


Figure 5.24. Total volumetric methane uptake at 25 °C of the best performing IL-AC carbons compared to benchmark MOF materials. The uptake of powder MOFs was calculated using crystallographic density and a reduction of 25% was applied to simulate more realistic packing density.

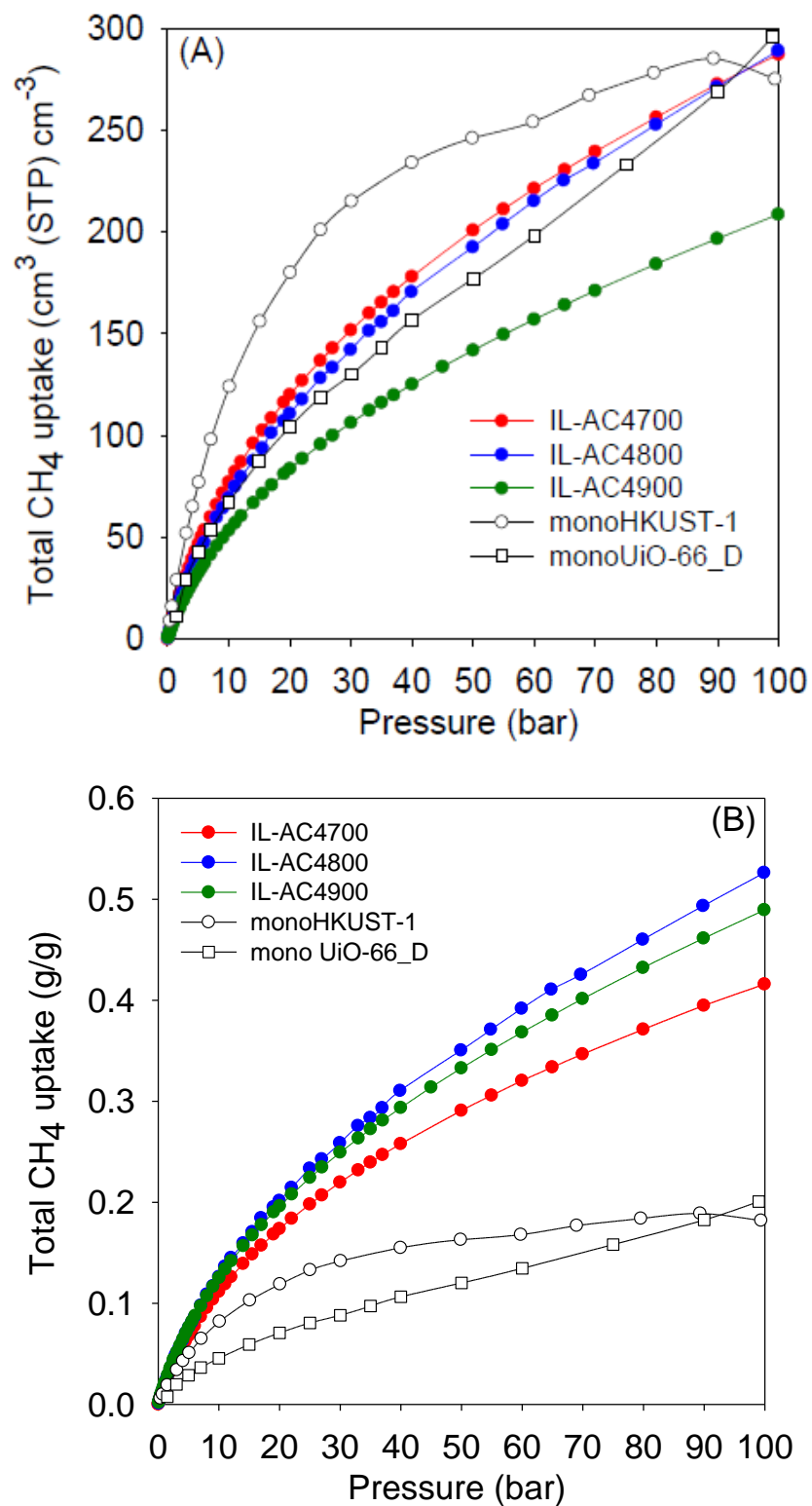


Figure 5.25. Total volumetric (A) and gravimetric (B) methane uptake at 25 °C of the best performing IL-AC carbons compared to monolithic MOF materials.

Most studies on methane storage in porous materials have been performed at ambient temperature (typically 25 °C), which is considered the most relevant for vehicular applications. However, other storage conditions have been explored. A notable study is that of Rozyyev and co-workers who reported on a flexible aromatic network porous polymer, COP-150, with attractive methane storage at 0 °C.⁸¹ The nature of COP-150 is such that it has very low volumetric and gravimetric uptake at 25 °C, which in combination with a relatively low packing density (0.34 g cm⁻³) mean that it is not competitive. However, due to flexible porosity, COP-150 has attractive gravimetric and volumetric methane storage capacity of 0.64 g g⁻¹ and 301 cm³ (STP) cm⁻³, respectively, at 0 °C and 100 bar. To have a fuller picture of the performance of the IL-AC carbons we measured the methane uptake for IL-AC4T samples at 0 °C (**Figure 5.26**). As expected the methane uptake at 0 °C is higher than that at 25 °C. At 100 bar, the total gravimetric methane uptake is 29.7 mmol g⁻¹ (0.48 g g⁻¹) for IL-AC4700, 37.3 mmol g⁻¹ (0.60 g g⁻¹) for IL-AC800, and 34.8 mmol g⁻¹ (0.56 g g⁻¹) for IL-AC4900. The volumetric uptake at 100 bar is, therefore, 329 cm³ (STP) cm⁻³ for IL-AC4700, 326 cm³ (STP) cm⁻³ for IL-AC4800 and 245 cm³ (STP) cm⁻³ for IL-AC4900. Thus, the storage capacity of IL-AC4800 matches that of COP-150 both in terms of gravimetric and volumetric uptake. The working capacity for IL-AC4800 for a pressure swing of 100 to 5 bar is 0.5 g g⁻¹ and 273 cm³ (STP) cm⁻³, which is comparable to that of COP-150.

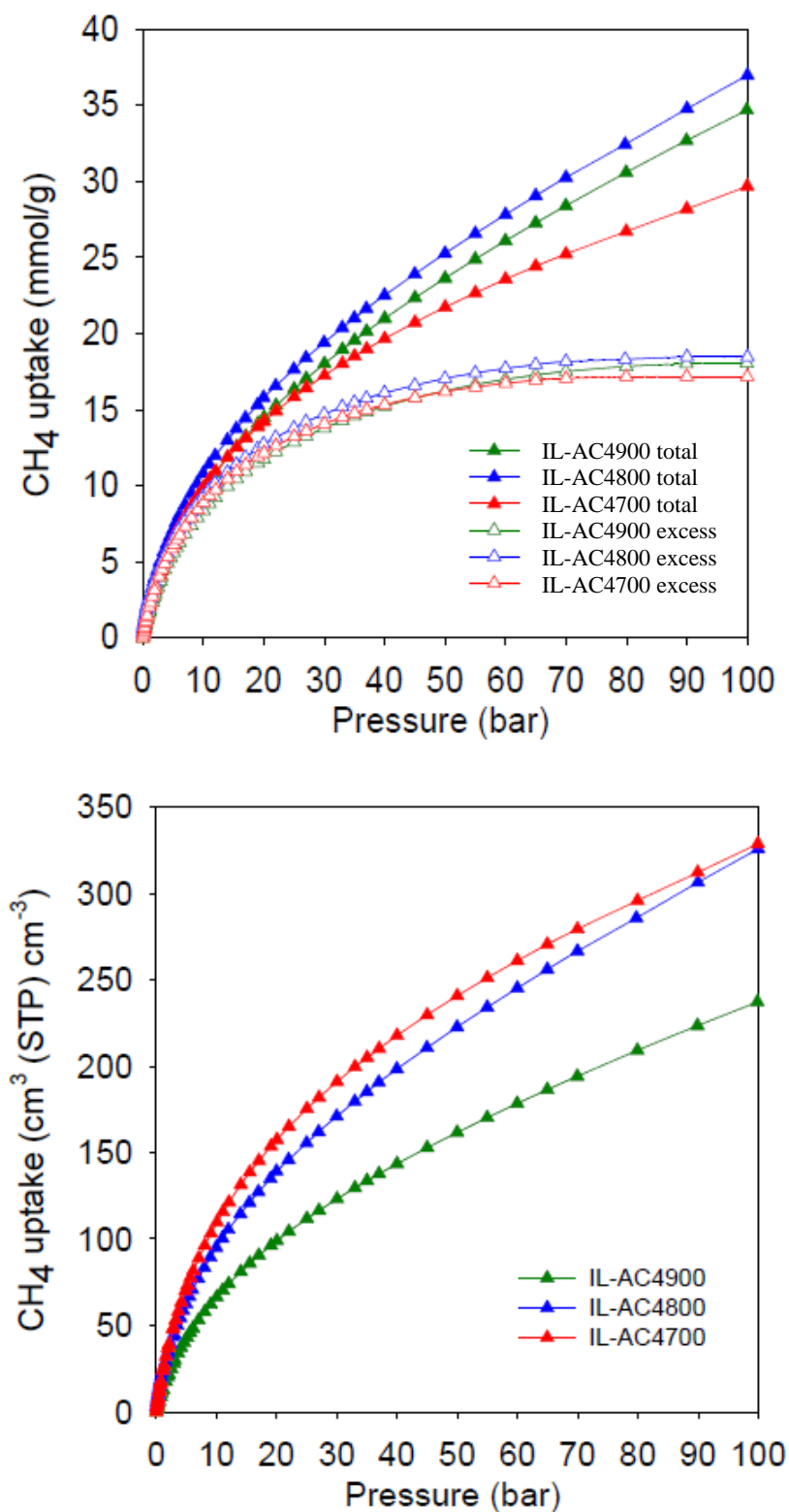


Figure 5.26. Excess and total gravimetric methane uptake (top) and total volumetric uptake (bottom) for IL-AC4T activated carbons at 0 °C.

5.4.3.2 Link between nature of precursor porosity and enhanced methane uptake

To clarify on the reasons for the high methane uptake of the IL-AC_xT carbons, we compared the porosity and packing density of the best performing sample (IL-AC4800) to similarly activated carbons from other types of precursors. The other precursors were chosen so as to represent either extreme when compared to IL-C with respect to elemental composition and in particular O/C ratio and presence of N. The selected precursors are air carbonised date seed (ACDS),³⁰ which has low O/C ratio and hardly any N, and polypyrrole (PPY) that has a higher O/C ratio and high N content.²⁹ The ACDS precursor has a low O/C ratio (0.156) that is comparable to that of IL-C (0.116) but hardly any N (**Table 5.12**). On the other hand, PPY has a higher O/C ratio (0.349) and high N content (16 wt%) that is comparable to that of IL-C (19.3 wt%). Thus, in terms of their elemental composition, and in particular O/C ratio and N content, the ACDS and PPY precursors may be considered as being end members when compared to IL-C. On activation at 800 °C and KOH/precursor ratio of 4, the ACDS precursor, which is resistant to activation, generates a predominantly microporous carbon (ACDS4800) that has high packing density of 0.67 g cm⁻³ and modest surface area and pore volume (**Figure 5.27** and **Table 5.13**).^{29, 30} On the other hand, PPY has greater susceptibility to activation and therefore yields a predominantly mesoporous carbon (PPY4800) that has low packing density of 0.37 g cm⁻³ but higher surface area and pore volume (**Figure 5.27** and **Table 5.13**). Precursors with low O content (low O/C ratio) are resistant to activation and mainly generate micropores as we have already demonstrated.¹⁴ On the other hand, the presence of N in a carbon framework introduces weak points and therefore greater susceptibility with respect to activation, which results in higher levels of activation and larger pores.^{29, 30} Clearly, the IL-AC4800 carbon achieves much higher porosity compared to both ACDS4800 and PPY4800 (**Figure 5.27** and **Table 5.13**). The high porosity is due to the unique elemental composition of the IL-C precursor that combines a low O/C ratio and high N content. It is interesting to note that despite having a much higher surface area and pore volume, the IL-AC4800 carbon retains a significant proportion of microporosity and moderate packing density of 0.39 g cm⁻³. Thus by deliberate choice of the precursor, we have succeeded in generating an activated carbon with a unique and difficult to achieve combination of ultra-high porosity and significant microporosity but without compromising the packing density.

Table 5.12. Elemental composition of carbonised ionic liquid (IL-C), air-carbonised date seed (ACDS) and polypyrrole (PPY).

Sample	C [%]	H [%]	N [%]	O [%]	(O/C) ^a	(C/N) ^a
IL-C	69.1	0.9	19.3	10.7	0.116	4.18
ACDS	78.5	4.0	2.1	16.3	0.156	43.6
PPY	55.5	2.7	16.0	25.8	0.349	4.04

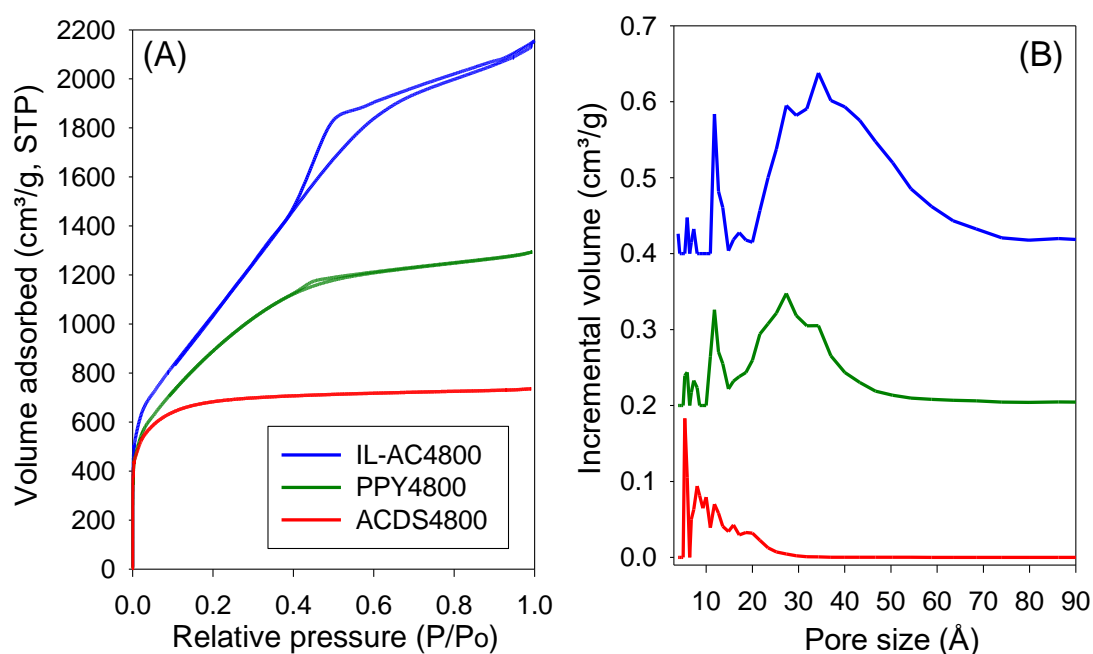
^aAtomic ratio.**Figure 5.27.** Nitrogen sorption isotherms (A) and corresponding pore size distribution curves (B) of IL-AC4800 compared to similarly activated carbons prepared from other precursors; ACDS4800 from air-carbonised date seed (ACDS) and PPY4800 from polypyrrole (PPY).

Table 5.13. Textural properties of IL-AC4800 compared to similarly activated carbons prepared from other precursors; ACDS4800 from air-carbonised date seed (ACDS) and PPY4800 from polypyrrole (PPY).

Sample	Surface area (m ² g ⁻¹)	Micropore surface area ^a (m ² g ⁻¹)	Pore volume (cm ³ g ⁻¹)	Micropore volume ^b (cm ³ g ⁻¹)	Packing density ^c (g cm ⁻³)
IL-AC4800	3995	1523 (38)	3.30	0.81 (25)	0.39
ACDS4800	2609	1825 (70)	1.10	0.70 (63)	0.69
PPY4800	3279	1320 (40)	2.00	0.62 (31)	0.37

^aValues in parenthesis are % of surface area from micropores. ^bValues in parenthesis are % of pore volume from micropores. ^cThe packing density was determined by pressing a given amount of carbon in a 1.3 cm die at pressure of 7 MPa for 5 min.

Next, we need to consider how the mix and level of porosity of the three samples affects their gravimetric methane uptake. This is best achieved by plotting the total gravimetric methane uptake (**Table 5.14**) at selected pressures (35, 65 and 100 bar) as a function of the surface area or pore volume of the carbons (**Figure 5.27**). The total gravimetric methane storage capacity at any uptake pressure increases linearly with both the surface area and pore volume. This finding indicates that the high gravimetric methane uptake of the IL-AC4800 carbon is due to its ultra-high porosity. Furthermore, the high gravimetric uptake when combined with the relatively undiminished packing density means that the IL-AC4800 carbon also exhibits very attractive volumetric methane storage capacity. On the other hand, ACDS4800 has high volumetric uptake due to its higher packing density but its overall storage performance is let down by low gravimetric uptake on account of lower surface area and pore volume. For PPY4800, the moderate gravimetric uptake translates to low or moderate volumetric uptake due to the diminished packing density. The unique nature of IL-AC4800, in terms of porosity and packing density, means that it achieves both high gravimetric and volumetric methane storage.

Table 5.14. Total gravimetric and volumetric methane uptake of IL-AC4800 compared to similarly activated carbons prepared from other precursors; ACDS4800 from air-carbonised date seed (ACDS) and PPY4800 from polypyrrole (PPY).

Sample	Total gravimetric (g g^{-1}) and volumetric (v/v) ^a methane uptake					
	35 bar		65 bar		100 bar	
	(g g^{-1})	(v/v)	(g g^{-1})	(v/v)	(g g^{-1})	(v/v)
IL-AC4800	0.28	156	0.41	223	0.53	289
ACDS4800	0.20	194	0.25	243	0.29	282
PPY4800	0.25	129	0.34	176	0.42	215

^a Volumetric uptake (v/v) is given as cm^3 (STP) cm^{-3} .

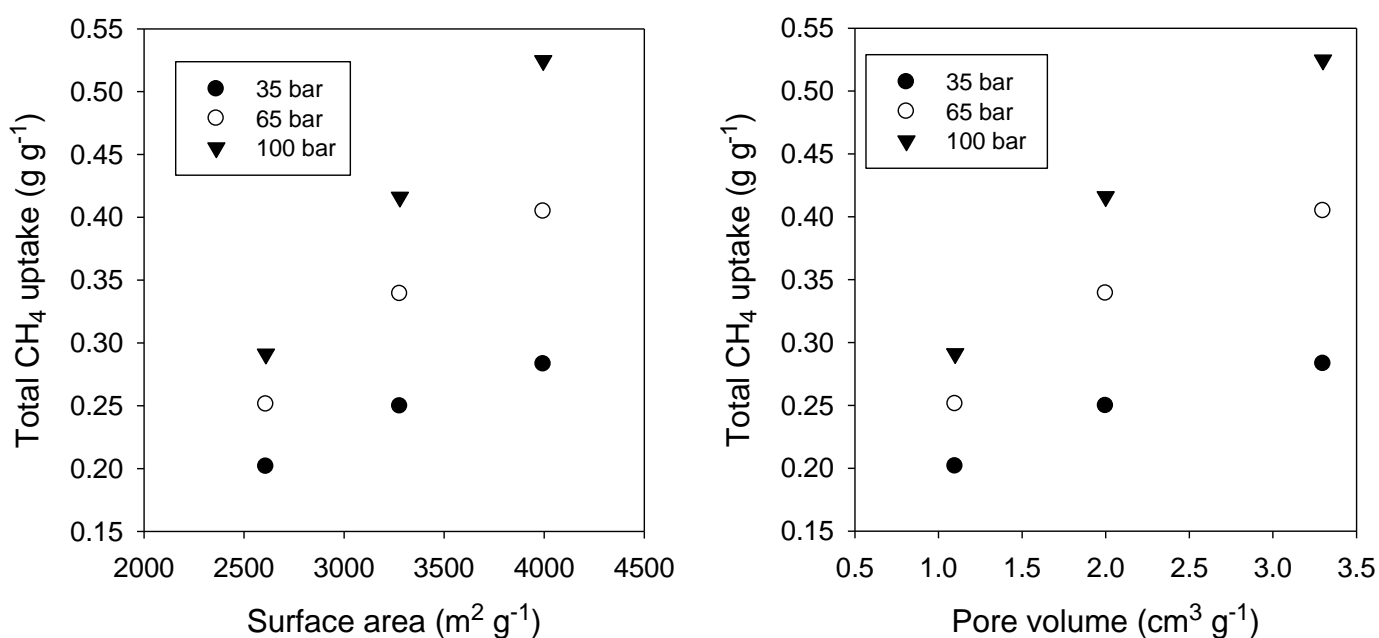


Figure 5.28. Total gravimetric methane storage capacity of IL-AC4800, ACDS4800 and PPY4800 carbons at 25 °C and various uptake pressures plotted as a function of surface area (left) or pore volume (right).

5.5 Conclusions

Activated carbons with high micro/mesoporosity have been prepared via carbonisation of an ionic liquid (1-butyl-3-methylimidazolium tricyanomethanide, [BMIm][C(CN)₃]) followed by chemical activation of the resulting carbonaceous matter with KOH. On carbonisation, the IL yields carbonaceous matter with the unusual combination of both a high N content and low O/C atomic ratio. On activation, the IL-derived carbonaceous matter (IL-C) generates activated carbons with a mix of micro and mesoporosity that have ultra-high surface area of up to $\sim 4000 \text{ m}^2 \text{ g}^{-1}$ and pore volume of up to $3.3 \text{ cm}^3 \text{ g}^{-1}$, along with comparatively high packing density. The porosity and packing density of the activated carbons is a consequence of the elemental composition of the IL-C precursor. In particular the low O/C ratio and high N content of the IL-C precursor play a role in determining the porosity. In this way, IL-C precursor shows anomalous activation behaviour when compared to other traditional carbonaceous matter. The IL-derived activated carbons are ideal for the storage of methane because of their well-balanced combination of microporosity and mesoporosity, high packing density, and large surface area. The best carbons achieve methane uptake of up to 0.53 g g^{-1} and $289 \text{ cm}^3 \text{ (STP) cm}^{-3}$ at 25°C and 100 bar. Such uptake exceeds the storage targets for both gravimetric and volumetric uptake set by the US Department of Energy of 0.5 g g^{-1} and $263 \text{ cm}^3 \text{ (STP) cm}^{-3}$, which would allow widespread use for vehicular transport and other purposes. In addition, the IL-derived carbons achieve attractive deliverable methane capacity (working capacity) of up to 0.46 g g^{-1} and $248 \text{ cm}^3 \text{ (STP) cm}^{-3}$ for a pressure swing of 100 to 5 bar at 25°C . The best performing IL-derived activated carbons meet both gravimetric and volumetric methane storage targets.

References

1. J. S. Lee, R. T. Mayes, H. M. Luo and S. Dai, *Carbon*, 2010, **48**, 3364-3368.
2. J. S. Lee, X. Wang, H. Luo, G. A. Baker and S. Dai, *Journal of the American Chemical Society*, 2009, **131**, 4596-4597.
3. J. P. Paraknowitsch, J. Zhang, D. Su, A. Thomas and M. Antonietti, *Advanced Materials*, 2010, **22**, 87-92.
4. O. Tzialla, G. Kakosimos, C. Athanasekou, E. Galata, G. E. Romanos, G. Pilatos, L. F. Zubeir, M. C. Kroon, B. Iliev, T. J. S. Schubert and K. G. Beltsios, *Microporous and Mesoporous Materials*, 2016, **223**, 163-175.
5. T. P. Fellingner, A. Thomas, J. Yuan and M. Antonietti, *Advanced Materials*, 2013, **25**, 5838-5854.
6. M. J. Xiao, Y. S. Meng, Y. Z. Li, X. L. Liu, X. Y. Ke, G. F. Ren and F. L. Zhu, *Applied Surface Science*, 2019, **494**, 532-539.
7. T. Kowalewski, N. V. Tsarevsky and K. Matyjaszewski, *Journal of the American Chemical Society*, 2002, **124**, 10632-10633.
8. S. G. Zhang, K. Dokko and M. Watanabe, *Chemistry of Materials*, 2014, **26**, 2915-2926.
9. Z. L. Xie and D. S. Su, *European Journal of Inorganic Chemistry*, 2015, 1137-1147.
10. H. Wang, J. Wang, S. Zhang and X. Xuan, *Journal of Physical Chemistry B*, 2008, **112**, 16682-16689.
11. H. M. Coromina, B. Adeniran, R. Mokaya and D. A. Walsh, *Journal of Materials Chemistry A*, 2016, **4**, 14586-14594.
12. D. R. MacFarlane, N. Tachikawa, M. Forsyth, J. M. Pringle, P. C. Howlett, G. D. Elliott, J. H. Davis, M. Watanabe, P. Simon and C. A. Angell, *Energy & Environmental Science*, 2014, **7**, 232-250.
13. L. Zhang, K. Cai, F. Zhang and Q. Yue, *Chemical Research in Chinese Universities*, 2015, **31**, 130-137.
14. P. F. Fulvio, P. C. Hillesheim, Y. Oyola, S. M. Mahurin, G. M. Veith and S. Dai, *Chemical Communications*, 2013, **49**, 7289-7291.
15. P. F. Fulvio, J. S. Lee, R. T. Mayes, X. Wang, S. M. Mahurin and S. Dai, *Physical Chemistry Chemical Physics*, 2011, **13**, 13486-13491.

-
16. P. F. Fulvio, J. S. Lee, R. T. Mayes, X. Q. Wang, S. M. Mahurin and S. Dai, *Physical Chemistry Chemical Physics*, 2011, **13**, 13486-13491.
 17. International Energy Agency (IEA), *Global CO₂ emissions rebounded to their highest level in history in 2021*, <https://www.iea.org/news/global-co2-emissions-rebounded-to-their-highest-level-in-history-in-2021>, (accessed 8th March, 2022).
 18. C. F. Schleussner, J. Rogelj, M. Schaeffer, T. Lissner, R. Licker, E. M. Fischer, R. Knutti, A. Levermann, K. Frieler and W. Hare, *Nature Climate Change*, 2016, **6**, 827-835.
 19. M. S. Dresselhaus and I. L. Thomas, *Nature*, 2001, **414**, 332-337.
 20. S. Choi, J. H. Drese and C. W. Jones, *ChemSusChem*, 2009, **2**, 796-854.
 21. U. Eberle, B. Muller and R. von Helmolt, *Energy & Environmental Science*, 2012, **5**, 8780-8798.
 22. K. V. Kumar, K. Preuss, M. M. Titirici and F. Rodriguez-Reinoso, *Chemical Reviews*, 2017, **117**, 1796-1825.
 23. I. Angelidaki, L. Treu, P. Tsapekos, G. Luo, S. Campanaro, H. Wenzel and P. G. Kougias, *Biotechnology Advances* 2018, **36**, 452-466.
 24. T. A. Makal, J.-R. Li, W. Lu and H.-C. Zhou, *Chemical Society Reviews*, 2012, **41**, 7761-7779.
 25. D. Lozano-Castello, J. Alcaniz-Monge, M. A. de la Casa-Lillo, D. Cazorla-Amoros and A. Linares-Solano, *Fuel*, 2002, **81**, 1777-1803.
 26. J. Romanos, S. Sweany, T. Rash, L. Firlej, B. Kuchta, J. C. Idrobo and P. Pfeifer, *Adsorption Science & Technology*, 2014, **32**, 681-691.
 27. D. Z. Li, L. Chen, G. Liu, Z. Y. Yuan, B. F. Li, X. Zhang and J. Q. Wei, *New Carbon Materials*, 2021, **36**, 468-492.
 28. A. Alonso, J. Moral-Vico, A. A. Markeb, M. Busquets-Fité, D. Komilis, V. Puentes, A. Sánchez and X. Font, *Science of the Total Environment* 2017, **595**, 51-62.
 29. A. Altwala and R. Mokaya, *Journal of Materials Chemistry A*, 2022, **10**, 13744-13757.
 30. A. Altwala and R. Mokaya, *Energy & Environmental Science*, 2020, **13**, 2967-2978.
 31. M. Sevilla and R. Mokaya, *Energy & Environmental Science*, 2014, **7**, 1250-1280.

-
32. L. S. Blankenship and R. Mokaya, *Materials Advances*, 2022, **3**, 1905-1930.
 33. Z. H. Hu, M. P. Srinivasan and Y. M. Ni, *Carbon*, 2001, **39**, 877-886.
 34. M. Sevilla, R. Mokaya and A. B. Fuertes, *Energy & Environmental Science*, 2011, **4**, 2930-2936.
 35. N. Balahmar and R. Mokaya, *Journal of Materials Chemistry A*, 2019, **7**, 17466-17479.
 36. A. M. Aljumialy and R. Mokaya, *Materials Advances*, 2020, **1**, 3267-3280.
 37. J. V. Guerrero, J. N. Burrow, J. E. Eichler, M. Z. Rahman, M. V. Namireddy, K. A. Friedman, S. S. Coffman, D. C. Calabro and C. B. Mullins, *Energy & Fuels*, 2020, **34**, 6101-6112.
 38. M. Sevilla, A. S. M. Al-Jumialy, A. B. Fuertes and R. Mokaya, *ACS Applied Materials & Interfaces*, 2018, **10**, 1623-1633.
 39. N. Tsubouchi, M. Nishio and Y. Mochizuki, *Applied Surface Science*, 2016, **371**, 301-306.
 40. M. Sevilla, W. Sangchoom, N. Balahmar, A. B. Fuertes and R. Mokaya, *ACS Sustainable Chemistry & Engineering*, 2016, **4**, 4710-4716.
 41. S. G. Zhang, K. Dokko and M. Watanabe, *Materials Horizons*, 2015, **2**, 168-197.
 42. J. S. Lee, X. Wang, H. Luo and S. Dai, *Advanced Materials*, 2010, **22**, 1004-1007.
 43. J. Rouquerol, P. Llewellyn and F. Rouquerol, *Studies in Surface Science and Catalysis*, 2006, **160**, 49-56.
 44. A. Galarneau, D. Mehlhorn, F. Guenneau, B. Coasne, F. Villemot, D. Minoux, C. Aquino and J. P. Dath, *Langmuir*, 2018, **34**, 14134-14142.
 45. M. Thommes, K. Kaneko, A. V. Neimark, J. P. Olivier, F. Rodriguez-Reinoso, J. Rouquerol and K. S. W. Sing, *Pure and Applied Chemistry*, 2015, **87**, 1051-1069.
 46. P. Iacomini and P. L. Llewellyn, *Adsorption*, 2019, **25**, 1533-1542.
 47. P. B. Whittaker, X. Wang, K. Regenauer-Lieb and H. T. Chua, *Physical Chemistry Chemical Physics*, 2013, **15**, 473-482.
 48. M. Sevilla, P. Valle-Vigón and A. B. Fuertes, *Advanced Functional Materials*, 2011, **21**, 2781-2787.
 49. J. Kim, J. H. Jeong, H. J. Ahn, J. S. Lee and K. C. Roh, *ChemElectroChem*, 2020, **7**, 2410-2417.

-
50. J. P. Paraknowitsch, A. Thomas and M. Antonietti, *Journal of Materials Chemistry*, 2010, **20**, 6746-6758.
 51. X. Zhang, D. Lin and W. Chen, *RSC Advances*, 2015, **5**, 45136-45143.
 52. B. Adeniran and R. Mokaya, *Nano Energy*, 2015, **16**, 173-185.
 53. M. Cox and R. Mokaya, *Sustainable Energy & Fuels*, 2017, **1**, 1414-1424.
 54. A. S. Jalilov, Y. L. Li, J. Tian and J. M. Tour, *Advanced Energy Materials*, 2017, **7**, 1600693.
 55. J. Osterrieth, J. Rampersad, D. G. Madden, N. Rampal, L. Skoric, B. Connolly, M. Allendorf, V. Stavila, J. Snider and R. Ameloot, *Advanced Materials*, 2021, **34**, 2201502.
 56. T. S. Blankenship and R. Mokaya, *Energy & Environmental Science*, 2017, **10**, 2552-2562.
 57. W. Sangchoom, D. A. Walsh and R. Mokaya, *Journal of Materials Chemistry A*, 2018, **6**, 18701-18711.
 58. J. J. He, J. W. F. To, P. C. Psarras, H. P. Yan, T. Atkinson, R. T. Holmes, D. Nordlund, Z. N. Bao and J. Wilcox, *Advanced Energy Materials*, 2016, **6**, 1502491.
 59. E. Haffner-Staton, N. Balahmar and R. Mokaya, *Journal of Materials Chemistry A*, 2016, **4**, 13324-13335.
 60. I. Alali and R. Mokaya, *Energy & Environmental Science*, 2022, **15**, 4710-4724.
 61. E. A. Hirst, A. Taylor and R. Mokaya, *Journal of Materials Chemistry A*, 2018, **6**, 12393-12403.
 62. M. Sevilla, A. B. Fuertes and R. Mokaya, *Energy & Environmental Science*, 2011, **4**, 1400-1410.
 63. L. S. Blankenship, N. Balahmar and R. Mokaya, *Nature Communications*, 2017, **8**, 1545.
 64. W. Sangchoom and R. Mokaya, *ACS Sustainable Chemistry & Engineering*, 2015, **3**, 1658-1667.
 65. H. M. Coromina, D. A. Walsh and R. Mokaya, *Journal of Materials Chemistry A*, 2016, **4**, 280-289.
 66. N. Balahmar, A. S. Al-Jumialy and R. Mokaya, *Journal of Materials Chemistry A*, 2017, **5**, 12330-12339.

-
67. B. Adeniran and R. Mokaya, *Journal of Materials Chemistry A*, 2015, **3**, 5148-5161.
68. T. Tian, Z. Zeng, D. Vulpe, M. E. Casco, G. Divitini, P. A. Midgley, J. Silvestre-Albero, J. C. Tan, P. Z. Moghadam and D. Fairen-Jimenez, *Nature Materials*, 2018, **17**, 174-179.
69. E. Masika and R. Mokaya, *Energy & Environmental Science*, 2014, **7**, 427-434.
70. J. A. Mason, M. Veenstra and J. R. Long, *Chemical Science*, 2014, **5**, 32-51.
71. B. Li, H. M. Wen, W. Zhou, J. Q. Xu and B. L. Chen, *Chem*, 2016, **1**, 557-580.
72. Y. He, W. Zhou, G. Qian and B. Chen, *Chemical Society Reviews*, 2014, **43**, 5657-5678.
73. Z. Chen, P. Li, R. Anderson, X. Wang, X. Zhang, L. Robison, L. R. Redfern, S. Moribe, T. Islamoglu, D. A. Gomez-Gualdrón, T. Yildirim, J. F. Stoddart and O. K. Farha, *Science*, 2020, **368**, 297-303.
74. P. Pfeifer, L. Aston, M. Banks, S. Barker, J. Burrell, S. Carter, J. Coleman, S. Crockett, C. Faulhaber, J. Flavin, M. Gordon, L. Hardcastle, Z. Kallenborn, M. Kemiki, C. Lapilli, J. Pobst, R. Schott, P. Shah, S. Spellerberg, G. Suppes, D. Taylor, A. Tekeci, C. Wexler, M. Wood, P. Buckley, T. Breier, J. Downing, S. Eastman, P. Freeze, S. Graham, S. Grinter, A. Howard, J. Martinez, D. Radke, T. Vassalli and J. Ilavsky, *Chaos: An Interdisciplinary Journal of Nonlinear Science*, 2007, **17**, 041108.
75. D. A. Gómez-Gualdrón, C. E. Wilmer, O. K. Farha, J. T. Hupp and R. Q. Snurr, *Journal of Physical Chemistry C*, 2014, **118**, 6941-6951.
76. M. E. Casco, F. Rey, J. L. Jorda, S. Rudic, F. Fauth, M. Martinez-Escandell, F. Rodriguez-Reinoso, E. V. Ramos-Fernandez and J. Silvestre-Albero, *Chemical Science*, 2016, **7**, 3658-3666.
77. M. E. Casco, M. Martinez-Escandell, K. Kaneko, J. Silvestre-Albero and F. Rodriguez-Reinoso, *Carbon*, 2015, **93**, 11-21.
78. C. M. Simon, J. Kim, D. A. Gomez-Gualdrón, J. S. Camp, Y. G. Chung, R. L. Martin, R. Mercado, M. W. Deem, D. Gunter, M. Haranczyk, D. S. Sholl, R. Q. Snurr and B. Smit, *Energy & Environmental Science*, 2015, **8**, 1190-1199.
79. B. M. Connolly, M. Aragonés-Anglada, J. Gandara-Loe, N. A. Danaf, D. C. Lamb, J. P. Mehta, D. Vulpe, S. Wuttke, J. Silvestre-Albero, P. Z. Moghadam,

-
- A. E. H. Wheatley and D. Fairen-Jimenez, *Nature Communications*, 2019, **10**, 2345.
80. B. M. Connolly, D. G. Madden, A. E. H. Wheatley and D. Fairen-Jimenez, *Journal of the American Chemical Society*, 2020, **142**, 8541-8549.
81. V. Rozyyev, D. Thirion, R. Ullah, J. Lee, M. Jung, H. Oh, M. Atilhan and C. T. Yavuz, *Nature Energy*, 2019, **4**, 604-611.
82. S. Bracco, D. Piga, I. Bassanetti, J. Perego, A. Comotti and P. Sozzani, *Journal of Materials Chemistry A*, 2017, **5**, 10328-10337.
83. Y. Peng, V. Krungleviciute, I. Eryazici, J. T. Hupp, O. K. Farha and T. Yildirim, *Journal of the American Chemical Society*, 2013, **135**, 11887-11894.
84. M. E. Casco, M. Martínez-Escandell, E. Gadea-Ramos, K. Kaneko, J. Silvestre-Albero and F. Rodríguez-Reinoso, *Chemistry of Materials*, 2015, **27**, 959-964.
85. H. Furukawa, N. Ko, Y. B. Go, N. Aratani, S. B. Choi, E. Choi, A. O. Yazaydin, R. Q. Snurr, M. O'Keeffe, J. Kim and O. M. Yaghi, *Science*, 2010, **329**, 424-428.
86. S. Ma, D. Sun, J. M. Simmons, C. D. Collier, D. Yuan and H.-C. Zhou, *Journal of the American Chemical Society*, 2008, **130**, 1012-1016.
87. S. Dutta, A. Bhaumik and K. C. W. Wu, *Energy & Environmental Science*, 2014, **7**, 3574-3592.
88. I. Alali and R. Mokaya, *Journal of Materials Chemistry A*, 2023, **11**, 6952-6965.

Chapter 6

Non-Hydroxide Activated Carbons Derived from Ionic Liquid Precursor for Enhanced CO₂ and Methane Storage

Abstract

Activated carbons were successfully prepared by carbonisation of crosslinkable Imidazolium-based ionic liquid, followed by chemical activation with potassium oxalate (PO), a non-hydroxide activating agent. Upon carbonisation, the structure and thermal stability of the ionic liquid, arising from its ionicity, led to the formation of a high-yield of graphitic carbonaceous matter (designated as IL-C) with a notable combination of a high N content of up to 18 wt% and low O/C atomic ratio of 0.116. The yield of activated carbons derived from IL-C varies with activation temperature but shows minimal change with the amount of PO used (as represented by PO/IL-C ratio), and ranges from 71% under the mildest conditions (lowest activation temperature, 700 °C) to 46% at the severest conditions (900 °C). Due to the low O/C ratio of IL-C, and gentler activation nature of PO, the generated activated carbons exhibit moderate to high surface area of 447 to 2202 m² g⁻¹, and pore volume of 0.27 to 1.08 cm³ g⁻¹, depending on the activation temperature. The porosity of the activated carbons can be tailored to exhibit a highly microporous structure with porosity suitable for post-combustion CO₂ uptake, showing CO₂ capacity of 1.6 and 4.2 mmol g⁻¹ at 25 °C and pressure of 0.15 and 1 bar, respectively. Furthermore, as a benefit of PO being a milder activating agent, the activated carbons have high packing density of up to 0.98 cm³ g⁻¹, which when combined with a high surface area density (typically > 2000 m² cm⁻³) translates to excellent volumetric methane gas uptake. At 100 bar and 25 °C, the carbons have a total volumetric uptake of 282 cm³ (STP) cm⁻³ along with excellent deliverable capacity of 200 cm³ (STP) cm⁻³ (for a pressure swing of 100 bar → 5 bar). The role of activation temperature and benefits of using PO as a milder and greener activating agent represent a significant step towards the application of ionic liquid-derived activated carbons in gas capture and storage, and offers a promising strategy for improving the performance of activated carbons for CH₄ storage.

6.1 Introduction

The properties of activated carbons are primarily determined by the materials from which they are derived and the activation conditions. Chemical activation, often employing inorganic acids, alkali hydroxides, or other agents like ZnCl_2 and K_2CO_3 , is a commonly used in the preparation of activated carbons.¹⁻³ Amongst various activation agents, KOH has been extensively studied and is known to generate activated carbon with defined pore size and high surface area from a wide range of carbonaceous starting materials (precursors).⁴⁻⁸ However, the toxic and corrosive nature of KOH presents some drawbacks. Therefore, milder activating agents (i.e., potassium oxalate, PO) that can yield carbons with comparable or superior textural properties to those activated with KOH are highly desirable.⁹⁻¹⁵ Previous studies on carbons prepared via PO activation have demonstrated that activated carbons with low to medium surface area (typically $<1500 \text{ m}^2 \text{ g}^{-1}$) are obtained for activation at 800°C or below.^{9, 12, 13} The mild nature of PO activation allows for fine tuning of properties, such as pore size distribution and surface area, which are critical for efficient CO_2 adsorption and/or methane storage.

The elemental composition and the nature of the carbonaceous precursor also play crucial roles in determining the properties of activated carbons. Altwala and Mokaya have synthesised activated carbon by from air-carbonised date seeds (*Phoenix dactylifera*), designated as ACDS using KOH and PO as activating agents.^{13, 16} They found that the ACDS, by dint of its nature and low O/C ratio, showed high resistance to activation for both activating agents. KOH activation yielded carbons with moderate surface area and high packing density suitable for methane uptake, while PO activated carbons yielded had porosity highly suited for low-pressure CO_2 storage (i.e., post-combustion CO_2 capture).^{13, 16} This suggests that the properties of activated carbons can be influenced by not only the choice of precursors but also the activating agents, which may allow for better targeting and tailoring of porosity for specific applications.

In this chapter, an ionic liquid was used as a precursor for activation carbon synthesis in a manner similar to that described in **Chapter 5** but with the use of use of PO as a milder activating agent.¹⁷⁻¹⁹ Ionic liquids, entirely composed of ions, are often characterised by low volatility, thermal stability, and a broad liquid range.¹⁷⁻¹⁹ In **Chapter 5**, it has been shown that the carbonisation of ionic liquid 1-butyl-3-

methylimidazolium tricyanomethanide generated carbonaceous matter (IL-C) with an exceptionally low O/C ratio of 0.116 and high N content of ca. 18 wt%. This unusual combination played a crucial role in determining the porosity of the resulting KOH activated carbons, endowing them with a high surface area and relatively high packing density. In this chapter, that work is extended to go beyond KOH activation by employing PO, a milder activating agent. This combination, i. e., low O/C ratio, high N content and milder activation, is anticipated to limit the level of activation and curb the formation of mesopores while still generating high yields of microporous activated carbons and high packing density suitable for CO₂ uptake and methane storage under specific conditions.

6.2 Experimental and Methodology

6.2.1 Materials preparation

The following chemicals were used as received: 1-butyl-3-methylimidazolium tricyanomethanide ([BMIm][C(CN)₃]), (TCI), and potassium oxalate monohydrate (K₂C₂O₄·H₂O, PO), (Sigma-Aldrich).

Ionic liquid-derived activated carbons (IL-ACs) were prepared in two steps. First, the required amount of [BMIm][C(CN)₃] (**Figure 6.1**) was thermally carbonised at 800 °C as described in details in **section 5.3**. The resulting carbonaceous matter was designated as IL-C (IL = ionic liquid, and C = carbonised). The IL-C was then chemically activated by mixing with PO at predetermined PO/IL-C ratios of 2, 4, or 6 in an agate mortar. The mixture was then placed in alumina boat and heated in a furnace under N₂ gas flow (100 mL min⁻¹), and ramp rate of 5 °C min⁻¹, to the target temperature of 700, 800, or 900 °C, and held for 1 h. The furnace was then allowed to cool down to room temperature under a flow of N₂ gas. The resulting activated carbons were collected and washed with HCl (1 M, 200 mL) by stirring at room temperature, following which the carbon was filtered and washed to pH ~ 7 (for the filtrate) with deionised water before drying in oven at 120 °C overnight. The activated carbons were designated as IL-AC_xT-PO, where x is the PO/IL-C mass ratio, T is the activation temperature (in °C), and the PO indicates potassium oxalate as activator. Thus, a carbon activated at a PO/IL-C carbon ratio of 4 and at 800 °C is designated as IL-AC4800-PO.

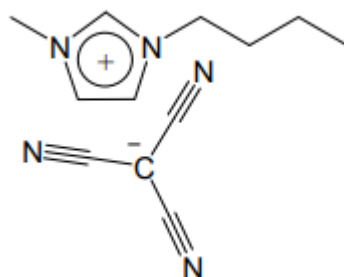


Figure 6.1. The chemical structure of 1-butyl-3-methylimidazolium tricyanomethanide.

6.2.2 Materials characterisation

In order to analyse the samples, various techniques were used, including thermogravimetric analysis (TGA), powder X-ray diffraction (XRD), elemental analysis (CHN), porosity analysis, and scanning electron microscopy (SEM). The TGA was performed using a TA Instruments SDT Q600 analyser under flowing air or N₂ conditions (100 ml min⁻¹) and heating ramp rate of 10 °C min⁻¹. Powder XRD analysis was carried out using a PANalytical X'Pert PRO diffractometer with a Cu-K α radiation (λ = 1.5418 Å) operating at 40 kV and 40 mA, 0.02 step size and 5 s step time and between 2° and 80° was 50 s. Elemental (CHN) analysis was performed using an Exeter Analytical CE-440 Elemental Analyser. The nitrogen sorption isotherms and textural characteristics of the activated carbons were determined using a Micromeritics 3FLEX sorptometer operating at -196 °C. Before analysis, the carbons were degassed at 300 °C for 16 h under vacuum. The surface area was calculated using the Brunauer–Emmett–Teller (BET) method applied to adsorption data within a relative pressure range (P/Po) in accordance to the Rouquerol Criterion, and the total pore volume was estimated from the amount of nitrogen adsorbed at close to saturation (P/Po \approx 0.99).²⁰⁻²² The micropore surface area and micropore volume were calculated using *t*-plot analysis. The pore size distribution (PSDs) were determined using the non-local density functional theory (NLDFT) model. The SEM images were obtained using a JEOL 7000F FEG-SEM microscope at an accelerating voltage of 15 kV.

6.2.3 Gas uptake measurements

The CO₂ uptake of the IL-ACxT-PO carbons were measured at room temperature and pressure range of 0 to 20 bar using a Hiden Isochema Intelligent Gravimetric Analyser (IGA-003). The methane uptake was determined using a Hiden Isochema XEMIS Analyser at 25 °C and a pressure range of 0 to 100 bar. In all cases, the carbons were degassed at 240 °C for several hours prior to the measurements of gas uptake.

6.3 Results and discussion

6.3.1 Nature of ionic liquid-derived carbons and elemental composition

The elemental composition of the ionic liquid (IL), and yield and elemental composition of the carbonised ionic liquid (IL-C), and the activated carbons (IL-ACxT-PO) are summarised in **Table 6.1**. It was first observed that due to the high chemical stability of ([BMIm][C(CN)₃]) ionic liquid precursor, arising from its structure, the carbonisation of ionic liquid yielded carbonaceous matter with a graphitic appearance and feel, as shown in **Figure 5.2**. This characteristic is ascribed to the presence of tricyanomethanide [C(CN)₃] anion, which has high thermal stability and does not completely decompose at elevated temperatures, leading to an IL-C yield of ca. 30 wt% at 800 °C. This finding agrees with the previous studies, which indicated that the ionic liquid cation paired with non-nitrile functional groups exhibits very low carbon yields.^{23, 24} Overall, the yield is comparable to that of hydrothermally carbonised biomass.^{6, 9, 25} The ionic liquid has N/C molar ratio of 0.482 with C and N contents of 62 wt% and 30 wt%, respectively, which is in line with its molecular formula (C₁₂H₁₅N₅). After carbonisation at 800 °C, IL-C maintains a high N content of 19.3 wt%, while the C content increases from 62 wt% to 69 wt%. The O content rises from 2.1 wt% to 10.7 wt%, and the H content significantly drops from 6.6 wt% to 0.9 wt%. Interestingly, the O/C ratio of 0.116 for the IL-C is remarkably low, and is one of the lowest values reported so far for any carbonaceous matter.^{16, 26}

Table 6.1. Elemental composition of ionic liquid (IL), and yield and elemental composition of carbonised ionic liquid (IL-C), and corresponding IL-C-derived activated carbons (IL-ACxT-PO).

Sample	Yield [wt%]	C [%]	H [%]	N [%]	O [%]	(O/C) ^a	(N/C) ^a
IL	—	61.6	6.6	29.7	2.1	0.026	0.482
IL-C	28	69.1	0.9	19.3	10.7	0.116	0.279
IL-AC2700-PO	71	64.2	1.4	11.1	23.3	0.272	0.173
IL-AC2800-PO	50	85.4	0.1	1.8	12.7	0.112	0.021
IL-AC2900-PO	46	89.4	0.0	1.1	9.5	0.079	0.012
IL-AC4700-PO	67	62.2	1.6	10.2	26.0	0.314	0.164
IL-AC4800-PO	50	79.7	0.3	2.0	18.0	0.169	0.025
IL-AC4900-PO	44	89.9	0.0	0.5	9.6	0.080	0.006
IL-AC6700-PO	66	66.1	1.1	11.8	21.0	0.238	0.179
IL-AC6800-PO	50	79.9	0.1	0.4	19.6	0.184	0.005
IL-AC6900-PO	46	85.2	0.0	0.6	14.2	0.125	0.007

^aAtomic ratio.

The overall yield of the activated carbons ranges from 66 wt% to 71 wt% for samples activated at 700 °C, a similar yield of 50 wt% for samples obtained at 800 °C, and between 44 wt% and 46 wt% for those activated at 900 °C. The yield is notably high compared to that observed for activated carbons derived from other sources of carbonaceous matter.^{9, 12, 13} It is noteworthy that at any given temperature, changing the PO/IL-C ratio from 2 to 6 does not appear to have a significant effect on the overall carbon yield. However, increasing the activation temperature leads to a lowering of carbon yield, meaning that the activation temperature is a critical factor that determines the carbon yield when using PO as an activating agent, unlike other hydroxide activating agents.^{13, 27} In general, this demonstrates the benefits of using PO as a milder and greener activating agent, along with low O/C ratio of the IL-C associated with resistance to activation, allowing for greater yields of carbon.

The elemental composition of the activated carbons, on the other hand, reveals an interesting trend. In general the C content ranges from 62.2 wt% to 89.9 wt% depending on the activating temperature. As indicated in **Table 6.1**, the amount of PO

does not directly influence the C content. The N content was found to depend on the activation temperature, and varied between 0.6 wt% and 12 wt%. For activation at 700 °C and any PO/IL-C ratio (2, 4, or 6), the activated carbons retain a high N content of ca. 12 wt%, which is significantly high, standing at ca. 60% of the N content of IL-C (19 wt%). The H content decreases after activation from 1.4 wt% for the IL-C to almost nil, while the O content rises to from 10 wt% for IL-C to between 9.7 and 26 wt% for the activated carbons. It is worth noting that with increase the amount of PO/IL-C used, the O content of the activated carbons also rises. This finding aligns with the established understanding that the amount of PO does not play a crucial role in determining the porosity. Therefore, it could be concluded that the PO exists in excess amounts, which contribute to the overall O content.

The nature and thermal stability of the IL, IL-C and IL-ACxT-PO carbons was probed using TGA, and the resulting curves are shown in **Figure 6.2**. The IL was thermally treated to 800 °C at a heating ramp rate of 10 °C min⁻¹ under an inert atmosphere (N₂ flow of 100 ml min⁻¹) for 1 h as depicted in **Figure 6.2A**. The TGA curve of the IL is consistent with the carbonisation yield of ca. 30 wt%. The purity (in terms of being purely carbonaceous with no inorganic components) and thermal stability were probed by TGA performed under air at a heating ramp rate of 10 °C min⁻¹ up to 1000 °C as shown in **Figure 6.2**. The TGA curves revealed high thermal stability of up to ca. 500 °C, followed by near complete mass loss between 500 °C and 750 °C, attributed to the combustion of carbon. Notably, the IL-ACxT-PO carbons exhibited similar burn-off temperatures, with greater stability observed for carbons prepared at higher activation temperature. The activated carbons burnt off with hardly any residual mass, indicating their predominantly carbonaceous composition.

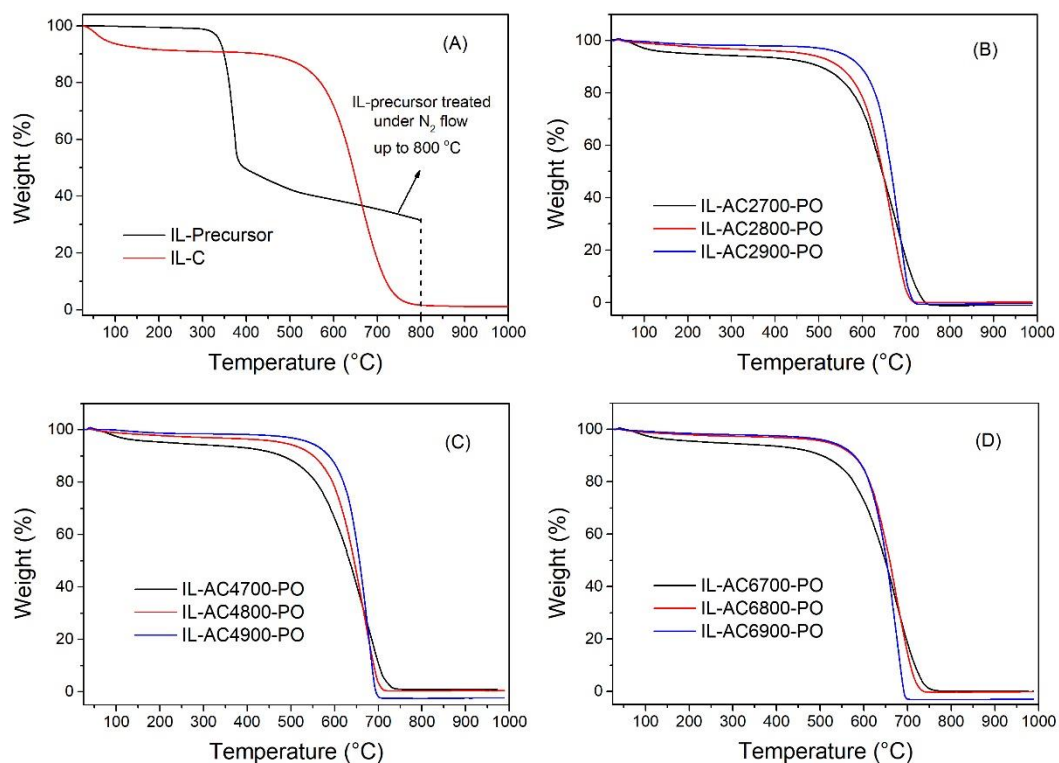


Figure 6.2. TGA curves of ionic liquid thermally treated under N_2 gas, carbonised ionic liquid (IL-C) and IL-derived activated carbons (IL-AC x T-PO), which were thermally treated in air.

The structure and purity (as evidenced by the absence of any crystalline inorganic phases) of IL-C and the activated carbons were examined using powder XRD. The XRD pattern of IL-C (**Figure 6.3**) exhibits a pronounced peak at a 2θ of $\sim 26^\circ$, assigned to the (002) diffraction of graphitic carbon. A further weak peak is observed at 2θ of $\sim 44^\circ$, corresponding to the (100) diffraction arising from graphene stacks. Upon activation of IL-C, the intensity of these peaks greatly reduced (**Figure 6.3B, C & D**). Carbons activated at 700°C (i.e., IL-AC x 700-PO) still display these peaks, but in a much broader form. No graphitic peaks were observed in the other samples, suggesting that the carbons are of an amorphous nature. These observations align with the fact that the activation process should disrupt any existing graphitic domains.

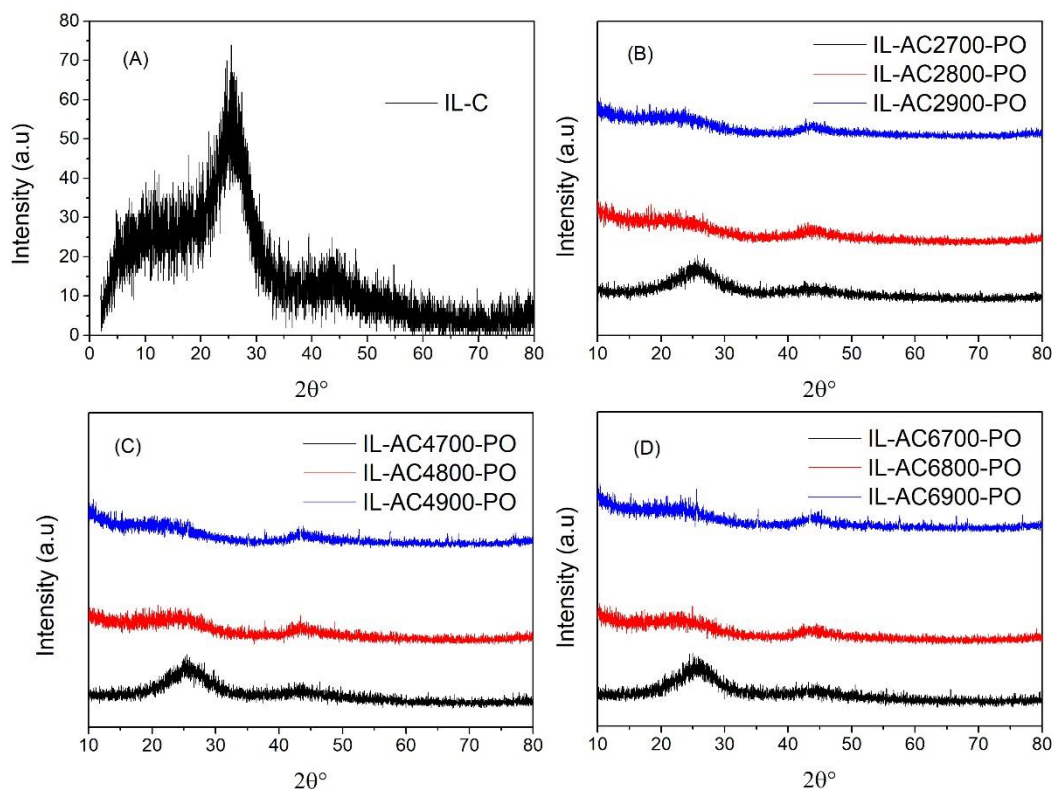
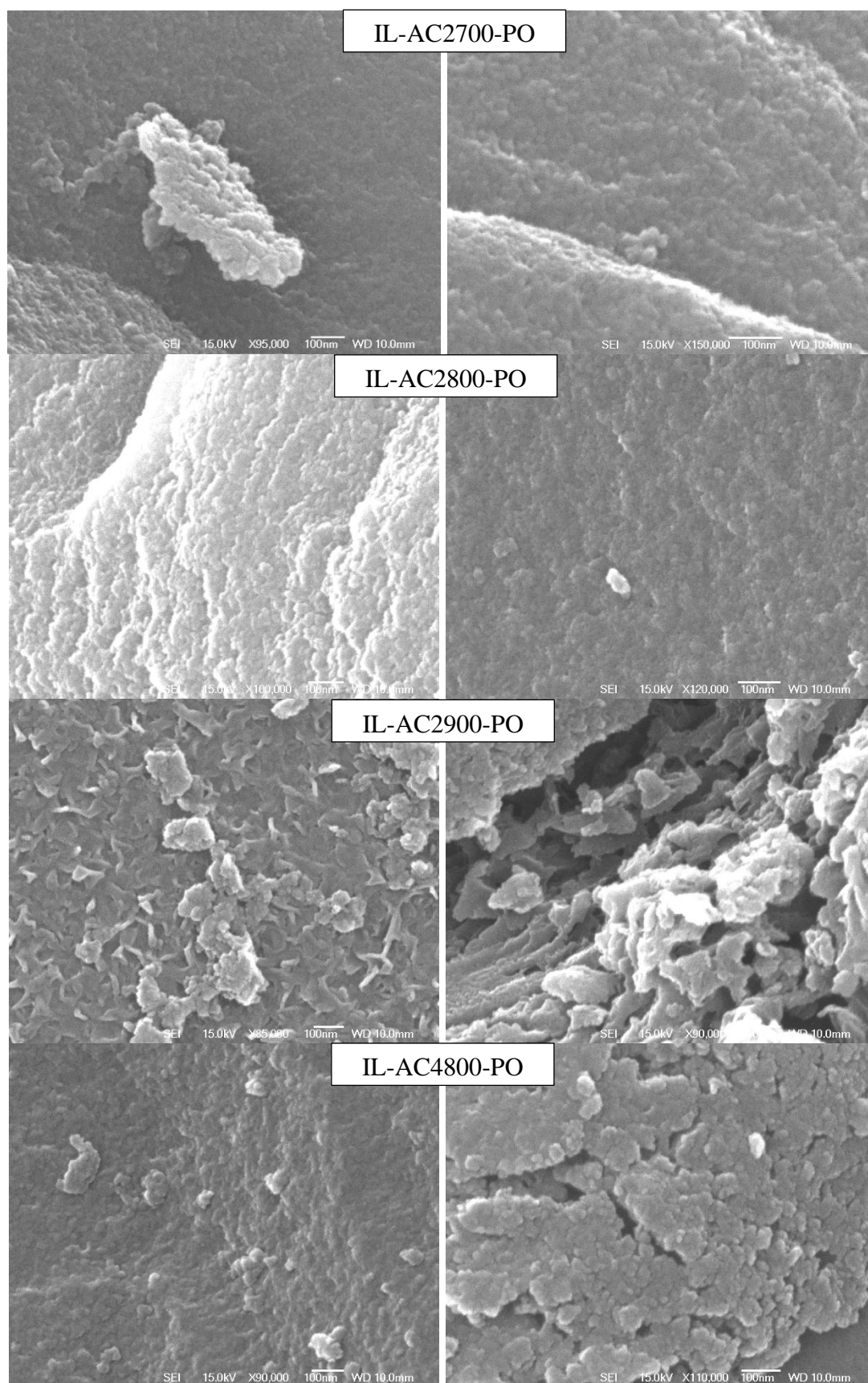


Figure 6.3. Powder XRD patterns of IL-C and IL-derived activated carbons (IL-AC_xT-PO).

Scanning electron microscopy (SEM) was employed to ascertain the role of activation temperature and/or PO/IL-C ratio in determining morphology and pore development. The SEM images in **Figure 6.4** reveal morphology characterised by the apparent presence of small pores, which is typical for activated carbons. Such a porous structure is expected when employing PO as the activating agent, as it leads to the formation of highly microporous activated carbons. Notably, the images demonstrate noticeable pore development and an increase in size of pore channels at higher activation temperatures, regardless of the amount of the activating agent used.



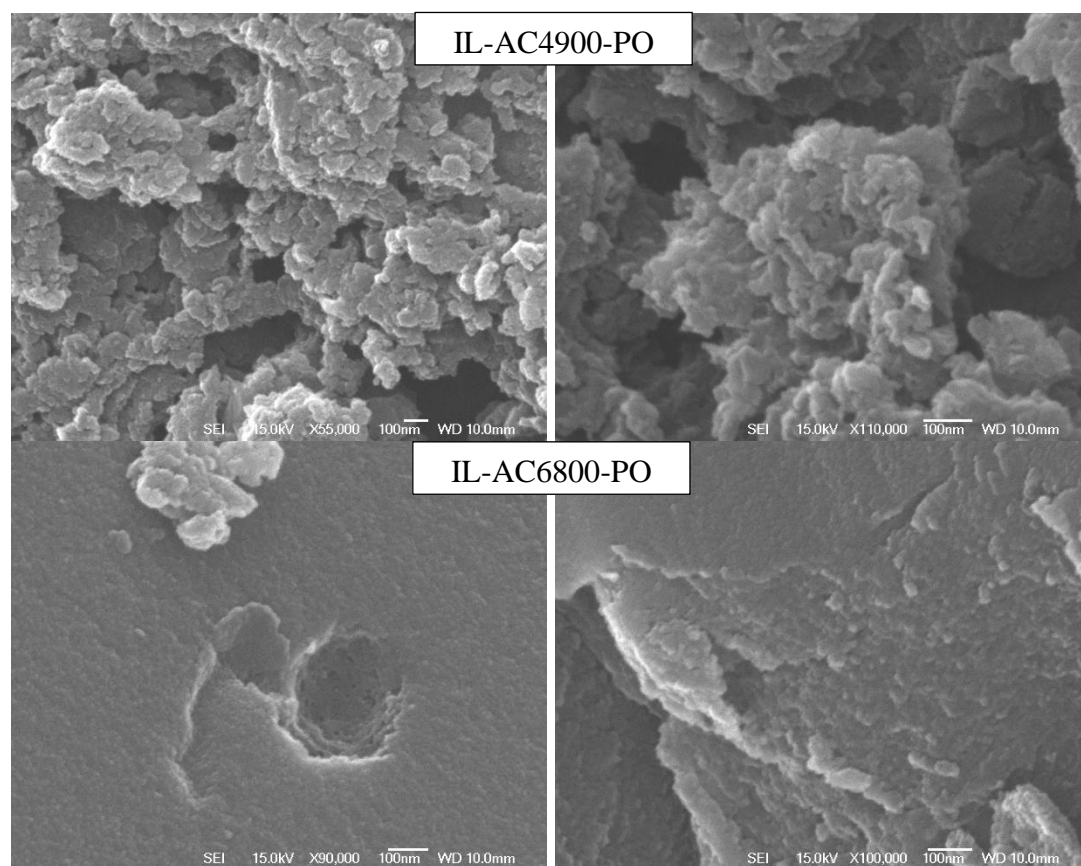


Figure 6.4. SEM images of some representative IL-ACxT-PO carbons.

6.3.2 Textural properties and porosity

The effect of activation temperature and the amount of potassium oxalate on the porosity and surface area of resulting IL-AC_xT-PO activating carbons were further analysed using nitrogen sorption isotherms. The N₂ sorption isotherms and the corresponding pore size distribution (PSD) curves are shown in **Figure 6.5**, **Figure 6.6** and **Figure 6.7**, and the textural properties are summarised in **Table 6.2**.

Effect of activation temperature. The N₂ sorption isotherms and the corresponding PSD curves of carbons activated at PO/IL-C ratio of 2 and temperatures of 700, 800 and 900 °C (IL-AC₂T-PO) are shown in **Figure 6.5**. As can be seen in **Figure 6.5A**, all carbons exhibit type I isotherms with a significant amount of N₂ adsorption accrued at a very low relative pressure ($P/P_0 > 0.1$), indicating significant levels of microporosity. The amount of N₂ adsorbed increases with activation temperature, which indicates greater pore development, as shown in **Figure 6.5B**. The isotherm of sample IL-AC₂700-PO shows a sharp adsorption knee and plateau, indicating the predominance of micropores. The sample activated at 800 °C (e. g., IL-AC₂800-PO) displays a slight enhancement and broadening in the adsorption knee, which suggests limited widening in the pore size distribution but still within the micropore region. The broadening in the adsorption “knee” becomes more pronounced for the IL-AC₂900-PO sample, which is activated at the highest temperature, indicating the presence of larger pores (microporous and small mesoporous). It is apparent that the amount of N₂ adsorbed correlates with the activation temperature, and increases at higher activation temperature.

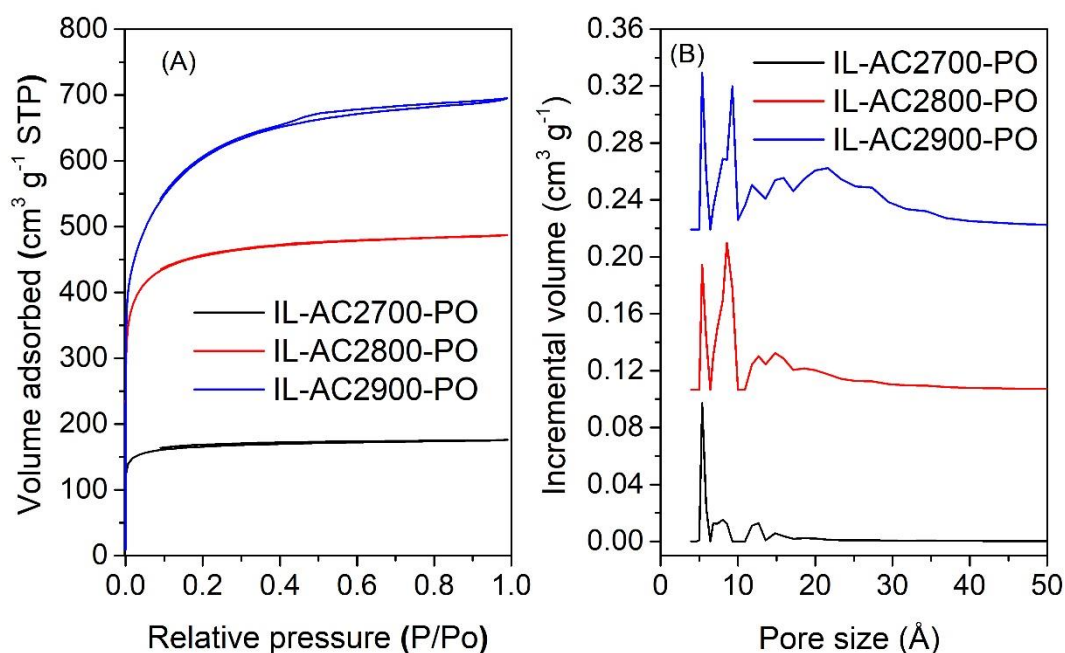


Figure 6.5. Nitrogen sorption isotherms (A) and pore size distribution curves (B) of IL-AC2T-PO carbons.

As illustrated in **Table 6.2**, the surface area and pore volume of carbons prepared at PO/IL-C ratio of 2 increase with the activation temperature. For example, IL-AC2700-PO has a surface area of $640 \text{ m}^2 \text{ g}^{-1}$ and a pore volume of $0.27 \text{ cm}^3 \text{ g}^{-1}$, which double to $1739 \text{ m}^2 \text{ g}^{-1}$ and $0.76 \text{ cm}^3 \text{ g}^{-1}$ for IL-AC2800-PO and increase further to $2202 \text{ m}^2 \text{ g}^{-1}$ and $1.08 \text{ cm}^3 \text{ g}^{-1}$ for IL-AC2900-PO. However, the micropore surface area decreases as the activation temperature increases from 800 to 900 °C, as shown in **Table 6.2**. For instance, the proportion of micropore surface area and pore volume is 81% and 74% for IL-AC2800-PO, respectively, and decreased to 48% and 43% for IL-AC2900-PO. The role of activation temperature is clearly observed in the PSD curves shown in **Figure 6.5B**. The carbons prepared at PO/IL-C ratio of 2 at 700 and 800 °C (IL-AC2700-PO and IL-AC2800-PO) primarily exhibit pores of size ca. 5 and 8 Å. However, when the activation temperature rises to 900 °C (IL-AC2900-PO) there is a widening of pore size, with a considerable proportion of 20 Å pores, as shown in **Figure 6.5B**. This increase in pore size for samples activated at higher temperature may be attributed to a greater level of activation resulting from enhanced gasification.⁹

Table 6.2. Textural properties of IL-derived IL-ACxT-PO activated carbons.

Sample	Surface area (m ² g ⁻¹)		Volume (cm ³ g ⁻¹)		Surf. area density ^c (m ² cm ⁻³)
	Total	Micro ^a (%)	Total	Micro ^b (%)	
IL-C	50	–	0.0336	–	Non-porous
IL-AC2700-PO	640	558 (87)	0.27	0.22 (82)	2370
IL-AC2800-PO	1739	1404 (81)	0.76	0.56 (74)	2288
IL-AC2900-PO	2202	1051 (48)	1.08	0.43 (40)	2039
IL-AC4700-PO	801	686 (86)	0.34	0.27 (79)	2356
IL-AC4800-PO	1396	1162 (83)	0.60	0.46 (77)	2327
IL-AC4900-PO	1669	1002 (60)	0.83	0.41 (49)	2011
IL-AC6700-PO	623	528 (85)	0.27	0.21 (78)	2307
IL-AC6800-PO	1413	1168 (83)	0.60	0.46 (77)	2355
IL-AC6900-PO	1611	1098 (68)	0.75	0.44 (59)	2148

^{a,b}Values in parenthesis are proportion of micropore surface area and micropore volume, respectively. ^cRefers to the surface area density, obtained as the ratio total surface area to the total pore volume.

The N₂ sorption isotherms and PSDs curves for IL-AC4T-PO samples activated at PO/IL-C ratio of 4 are shown in **Figure 6.6**. Overall, the IL-AC4T-PO carbons show similar trend in their N₂ sorption isotherms and PSDs curves as that observed for IL-AC2T-PO carbons. The IL-AC4T-PO carbons display N₂ isotherm type I, with significant adsorption at $P/P_0 > 0.1$, and which increases dependently on the activating temperature. The isotherm of IL-AC4700-PO has a sharp adsorption knee and plateau at $P/P_0 > 0.1$, which is gentler for IL-AC4800-PO. At the highest activation temperatures of 900 °C, the isotherm of the sample IL-AC4900-PO shows a broad adsorption knee similar to that observed in IL-AC2900-PO, suggesting to the presence of wider microporous and some level of mesoporosity.⁹ In terms of textural properties, the IL-AC4T-PO activated carbons have surface area ranging from 801 m² g⁻¹ to 1669 m² g⁻¹ and pore volume of 0.34–0.83 cm³ g⁻¹, depending on the activation temperature. Sample IL-AC4700-PO has surface area of 801 m² g⁻¹ and a pore volume of 0.34 cm³ g⁻¹, which increases to 1396 m² g⁻¹ and 0.60 cm³ g⁻¹, respectively, for IL-AC4800-PO sample. The sample activated at the highest temperature of 900 °C (IL-AC4900-PO) has surface area of 1669 m² g⁻¹ and a pore volume of 0.83 cm³ g⁻¹. However, there is a significant decrease in the proportion of micropore surface area upon increasing the activation temperature to 900 °C, dropping from 86% in IL-AC4700-PO to 60% in IL-AC4900-PO. This can be observed from the PSD curves and textural parameters of IL-AC4T-PO carbons shown in **Figure 6.6B** and **Table 6.2**. The carbons activated at 700 °C and 800 °C predominantly feature pores of size 5–8 Å, with a small proportion of 12 Å pores observed for sample IL-AC4800-PO. Conversely, the PSD of IL-AC4900-PO displays a higher proportion of pores with sizes exceeding 20 Å as shown in **Figure 6.6B**.

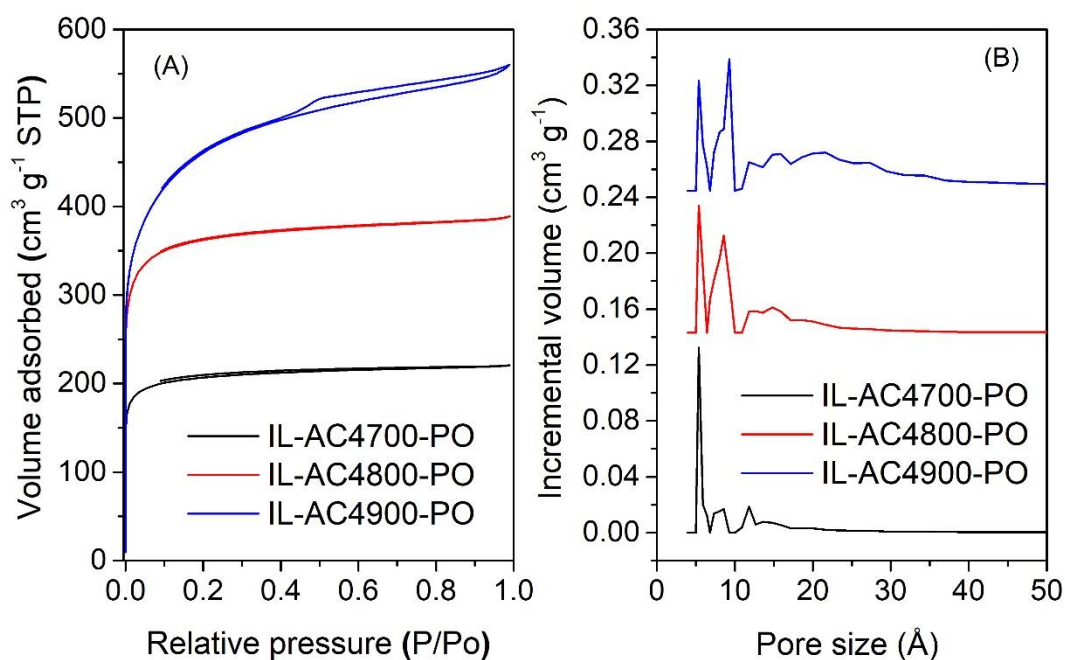


Figure 6.6. Nitrogen sorption isotherms (A) and pore size distribution curves (B) of IL-AC4T-PO carbons.

The N_2 sorption isotherms and the corresponding PSDs curves of carbons prepared at PO/IL-C ratio of 6 (IL-AC6T-PO) are shown in **Figure 6.7**. The isotherms of this set of samples display a typical type I shape and are very similar to those of IL-AC2T-PO and IL-AC4T-PO carbons in **Figure 6.5** and **Figure 6.6**, both in terms of shape and the amount of nitrogen adsorbed. It is evident that increasing the amount of PO does not seem any significant impact on the porosity, which aligns with the findings in previous studies.^{9, 12} Furthermore, the PSD curves of these carbons also demonstrate a high degree of similarity and exhibit comparable enhancements with increasing temperature, as described above. This indicates that the optimal control of porosity in these activated carbons, when using PO as an activating agent, is primarily determined by activation temperature rather than the amount of PO. This is a departure from what has been observed in **Chapter 5** when using KOH as activating agent, wherein increasing the KOH/IL-C ratio generated carbons with larger pores and greater surface area. Based on **Figure 6.7**, activation at PO/IL-C ratio of 6 results in the formation of micropores with hardly any mesopores, except for samples activated at 900 °C, aligning with what is observed for IL-AC2T-PO and IL-AC4T-PO carbons. The

presence of mesoporous in samples activated at 900 °C could be related to CO₂ and CO gases released during the high-temperature activation.^{9, 14} The surface area of IL-AC6T-PO activated carbons ranges from 623 to 1611 m² g⁻¹, and pore size of 0.27 to 0.75 m³ g⁻¹. Both surface area and pore volume increase as the activation temperature rises from 700 to 900 °C. The proportion of micropore surface area and micropore volume remain high for IL-AC6700-PO and IL-AC6800-PO carbons, and in the range of 83% and 85% for micropore surface area and 77% for micropore volume. However, at the higher activation temperature of 900 °C, there seems to be a decrease in the microporosity, with values of 68% and 59% for the proportion of micropore surface area and micropore volume, respectively.

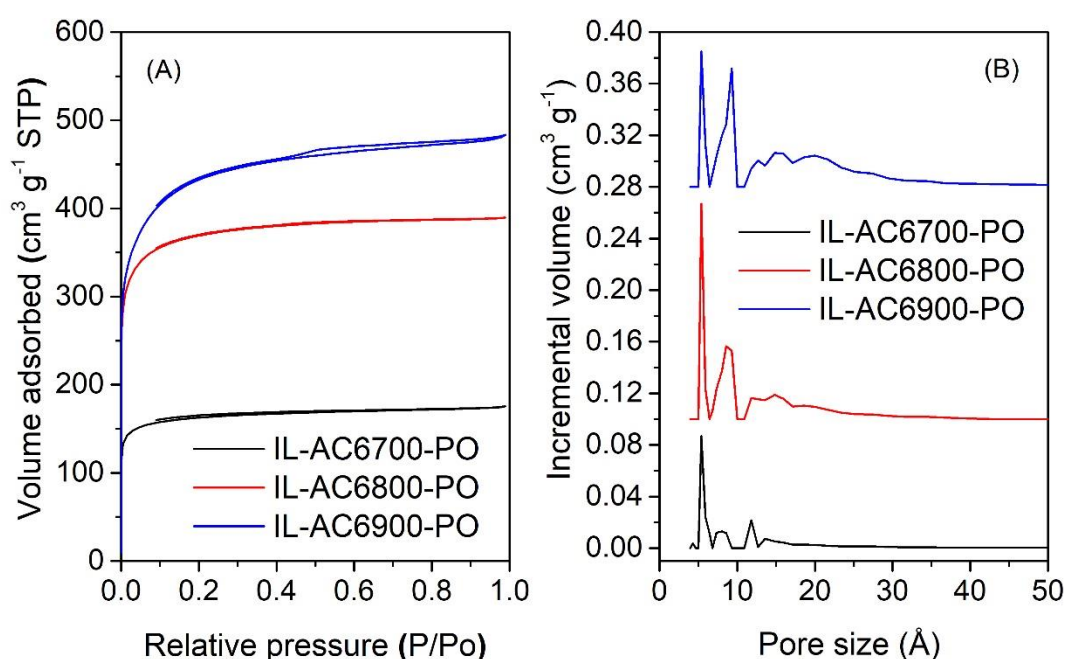


Figure 6.7. Nitrogen sorption isotherms (A) and pore size distribution curves (B) of IL-AC6T-PO carbons.

Effect of PO/IL-C ratio. The nitrogen sorption isotherms of the IL-ACxT-PO activated carbons indicate that increasing the activation temperature enhances the porosity, while changes in the amount of PO have hardly any effect on the overall porosity. For instance, IL-ACx700-PO samples show low surface area and pore volume values regardless of the amount of PO. A comparison of IL-AC2700-PO ($640 \text{ m}^2 \text{ g}^{-1}$ and $0.27 \text{ cm}^3 \text{ g}^{-1}$), IL-AC4700-PO ($801 \text{ m}^2 \text{ g}^{-1}$ and $0.34 \text{ cm}^3 \text{ g}^{-1}$), and IL-AC6700-PO ($623 \text{ m}^2 \text{ g}^{-1}$ and $0.27 \text{ cm}^3 \text{ g}^{-1}$) illustrates this trend. However, as the activation temperature increases to 800°C and 900°C , the IL-ACx800-PO and IL-ACx900-PO samples exhibit higher surface area and pore volume. The N_2 sorption isotherms and PSD curves show similarities despite increase the amount of PO, indicating that the control of porosity primarily relies on the activation temperature rather than the amount of PO. Overall, the results show that increasing the activation temperature enhances the porosity and surface area of the IL-ACxT-PO activated carbons, while the amount of potassium oxalate has a minor influence on the porosity, which is consistent with previous studies.^{9, 10, 12, 13}

6.4 Gas uptake

6.4.1 CO_2 uptake

Given the high microporosity of the IL-ACxT-PO carbons, occasioned by the use of PO in combination with a precursor with a very low O/C ratio, we explored their CO_2 uptake capacity at 25°C and pressures range of 0 – 20 bar. The CO_2 uptake isotherms are shown in **Figure 6.8**, **Figure 6.9** and **Figure 6.10**. The CO_2 uptake at various pressures (0.15, 1, and 20 bar) is summarised in **Table 6.3**. The CO_2 uptake at 1 bar, which serves as a primary focus in most studies as a performance metric for capturing CO_2 from flue gas streams in post-combustion processes, varies depending on the activation temperature. In the case of IL-AC2T-PO carbons, the CO_2 uptake at 1 bar increases from 3.2 mmol g^{-1} for IL-AC2700-PO to 4.2 mmol g^{-1} IL-AC2800-PO and then slightly decreases to 3.3 mmol g^{-1} for IL-AC2900-PO, due to widening in the pores and lower level of microporosity in the latter. Interestingly, further increases in the PO/IL-C ratio to 4 (IL-AC4T-PO) and 6 (IL-AC6T-PO) result in comparable CO_2 uptake values of ca. 3 mmol g^{-1} to 3.8 mmol g^{-1} for IL-AC4T-PO samples and between 2.9 mmol g^{-1} and 3.8 mmol g^{-1} for IL-AC6T-PO samples. The results suggest that the PO/IL-C ratio does not significantly affect the CO_2 storage capacity at 1 bar. Instead,

the activation temperature has a more pronounced influence on CO₂ uptake. For instance, when comparing IL-AC_x700-PO carbons activated at different PO/IL-C ratios but at a temperature of 700 °C, the CO₂ uptake is as follows: 3.2 mmol g⁻¹ for IL-AC2700-PO, 3.2 mmol g⁻¹ for IL-AC4700-PO, and 2.9 mmol g⁻¹ for IL-AC6700-PO. In all cases, considering the significant impact of activation temperature, it can be observed that activating at 800 °C appeared to be the optimal temperature and resulted in high CO₂ uptake at 1 bar and 25 °C of 4.2 mmol g⁻¹, 3.8 mmol g⁻¹, and 3.8 mmol g⁻¹ for IL-AC2800-PO, IL-AC-4800-PO, and IL-AC68600-PO, respectively. These results suggest that activating at 800 °C leads to optimal porosity and surface properties, resulting in enhanced CO₂ adsorption capacity. This enhanced capacity can be attributed to the optimal pore size of these samples, which outperforms all other samples in this study. Additionally, the PSD curves of these samples reveal the presence of two prominent pores systems of size 5 and 8 Å, which contribute to the significant enhancement of CO₂ uptake. This is in line with previous studies, as the uptake at 1 bar is not determined by the surface area but by the type and size of porosity, suggesting that pores smaller than 10 Å have an influence on CO₂ uptake at lower pressures.^{1, 3, 12, 13, 29-36}

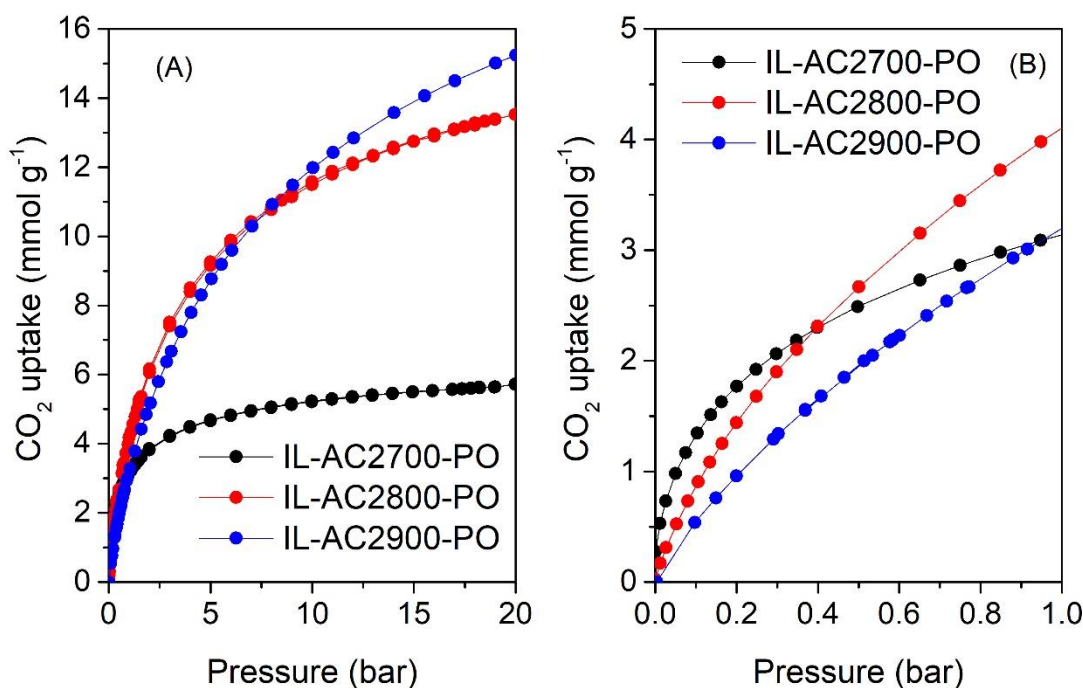


Figure 6.8. CO₂ uptake isotherms of IL-AC2T-PO carbons at 25 °C for pressure range 0–20 bar (A) and 0–1 bar (B).

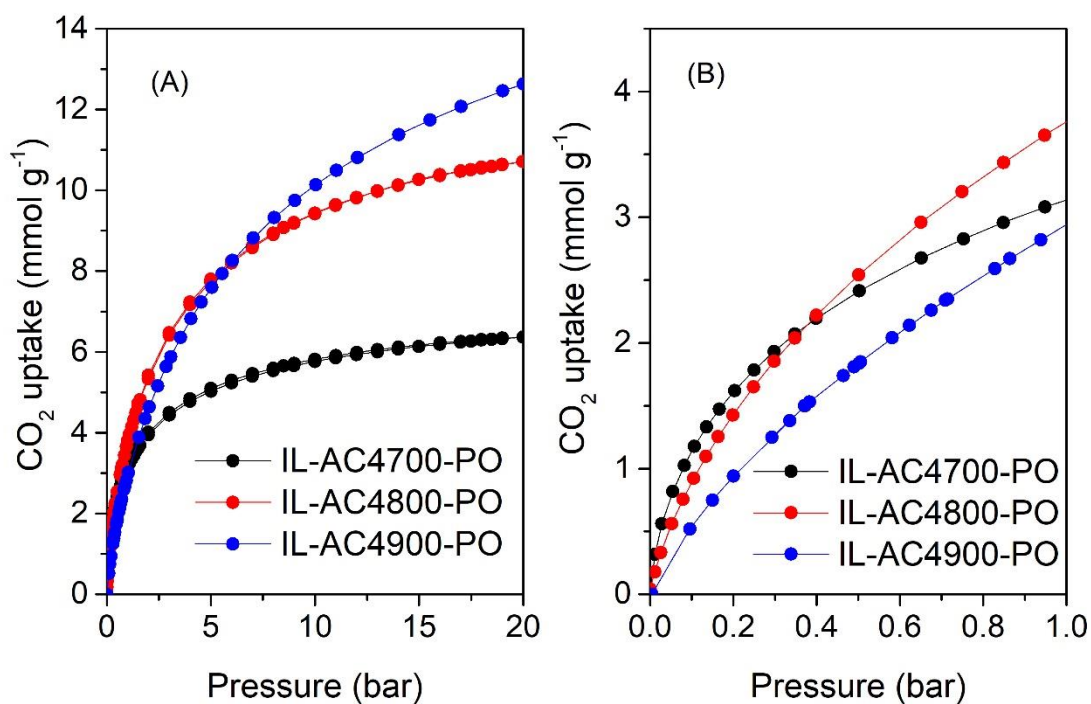


Figure 6.9. CO₂ uptake isotherms of IL-AC4T-PO carbons at 25 °C for pressure range 0–20 bar (A) and 0–1 bar (B).

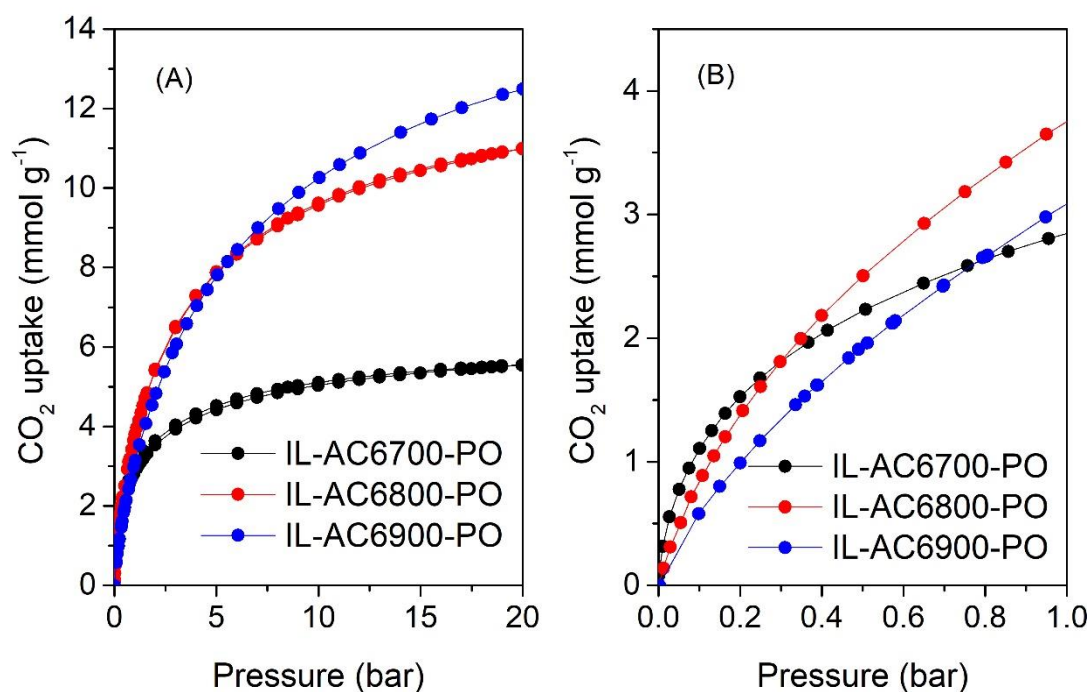


Figure 6.10. CO₂ uptake isotherms of IL-AC6T-PO carbons at 25 °C for pressure range 0–20 bar (A) and 0–1 bar (B).

Table 6.3. CO₂ uptake 25 °C and various pressures (0.15, 1 and 20 bar) of IL-ACxT-PO carbons.

sample	CO ₂ uptake (mmol g ⁻¹)		
	0.15 bar	1 bar	20 bar
IL-AC2700-PO	1.6	3.2	5.6
IL-AC2800-PO	1.2	4.2	13.5
IL-AC2900-PO	0.8	3.3	15.2
IL-AC4700-PO	1.4	3.2	6.4
IL-AC4800-PO	1.2	3.8	10.7
IL-AC4900-PO	0.8	3.0	12.6
IL-AC6700-PO	1.3	2.9	5.5
IL-AC6800-PO	1.1	3.8	11.0
IL-AC6900-PO	0.8	3.1	12.5

The CO₂ uptake at 0.15 bar is crucial as it may be used as an indicator for storage capacity from a flow gas stream from power stations, which typically contains ca. 15–20% CO₂ with the majority being N₂ (70–75%) and a small portion of water.^{37, 38} Among the present samples, IL-AC2700-PO exhibits the highest uptake of 1.6 mmol g⁻¹, followed by IL-AC4700-PO and IL-AC6700-PO with uptakes of 1.4 mmol g⁻¹ and 1.3 mmol g⁻¹, respectively. These high uptake values can be attributed to the abundance of microporosity in these carbons as shown in **Figure 6.5B**, **Figure 6.6B** and **Figure 6.7B**. Additionally, samples activated at 800 °C show high uptake as well, with IL-AC2800-PO, IL-AC4800-PO, and IL-AC6800-PO having capacity of 1.17 mmol g⁻¹, 1.18 mmol g⁻¹, and 1.13 mmol g⁻¹, respectively, which highlights the importance of small pores (5–8 Å), as illustrated in **Figure 6.5B**, **Figure 6.6B** and **Figure 6.7B**. On the other hand, the CO₂ uptake for samples activated at the highest temperature (900 °C) is lower at ~ 0.8 mmol g⁻¹, which is due to their lower levels of microporosity. Comparing the CO₂ uptake of all the samples at 0.15 bar, it can be observed that the activation temperature has a noticeable impact. To clarify, IL-ACx700-PO carbons, activated at the lowest temperature (700 °C), demonstrate the highest CO₂ uptake of between 1.3 mmol g⁻¹ and 1.6 mmol g⁻¹, which slightly decreased for higher amount of activating agent. However, as the activation

temperature increases to 800 °C, the CO₂ uptake for IL-ACx800-PO carbons decreases to the range of 1.13–1.18 mmol g⁻¹, and decreased further to ~ 0.8 mmol g⁻¹ for IL-ACx900-PO samples. Overall, the CO₂ uptake of 1.6, 1.40 and 1.3 mmol g⁻¹ at 0.15 bar and 25 °C for IL-ACx700-PO carbons is amongst the highest ever reported for any porous carbons.^{31, 32, 34, 35, 39-45}

At higher pressure (20 bar), the trend in uptake capacity is reversed, indicating a dependence on the total surface area of the activated carbons rather than the pore size. Carbons prepared at higher temperature have higher surface area, resulting in higher CO₂ uptake capacity. Thus, IL-ACx900-PO carbons have the highest uptake capacity of 15.2 mmol g⁻¹ (IL-AC2900-PO), 12.6 mmol g⁻¹ (IL-AC4900-PO), and 12.5 mmol g⁻¹ for IL-AC6900-PO. Additionally, the uptake at 20 bar is not effected by the amount of PO used. This emphasises: (i) the crucial role of activating temperature in modifying the textural properties of the activated carbons when PO is used as the activating agent, (ii) the possibility of achieving comparable properties by using a lower amount of PO, which opens up a greener synthesis process approach while maintaining a full range of porosity, and (iii) a more straightforward and environmentally friendly synthesis method, which results in activated carbons with attractive CO₂ adsorption capacity that reaches 4.2 mmol g⁻¹ at 1 bar and 1.6 mmol g⁻¹ at 0.15 bar at 25 °C.

6.4.2 CH₄ uptake

The use of milder PO in conjunction with a precursor of a very low O/C ratio generates lowly activated carbons that are predicted to have high packing density. In particular, the presence of microporosity is important in enhance the packing density, which plays a vital role in determining the volumetric methane storage capacity. Given that methane uptake generally correlates with the surface area of carbons, we determined the performance of samples with the highest surface area, namely IL-AC2800-PO, IL-AC-2900-PO, and IL-AC4900-PO. The assumption was that these samples would be suitable store for methane uptake due to their unique combination of moderate surface area, mix of microporosity with some mesoporosity, and crucially a low level of activation and thus a high packing density. The methane uptake measurements directly determined the excess uptake from which the total storage capacity was worked out by

considering the pore volume of the carbons and packing density to obtain the total gravimetric and volumetric uptake.

Figure 6.11 shows the excess and total gravimetric methane uptake isotherms at 25 °C in the pressure range of 0–100 bar, and **Table 6.4** summarises the storage capacity at 35, 65 and 100 bar. In general, the excess uptake is proportional to the surface area. The excess uptake isotherms of the carbons appear to reach saturation at pressure of 65 bar and then plateaued. This observation arises from the adsorption of supercritical fluids at high pressures, occurring when the density of the adsorbed gas is equal to the density of the bulk or free gas.⁴⁶⁻⁴⁸ This is evidenced from the excess methane uptake at 65 and 100 bar, which remains almost unchanged at ca. 8.3 mmol g⁻¹ for IL-AC2800-PO, 10.1 mmol g⁻¹ for IL-AC2900-PO, and 8.5 mmol g⁻¹ for IL-AC4900-PO. In general, the excess methane uptake is in line with the surface area of the carbons, with carbons having higher surface area exhibiting higher uptake, in the order IL-AC2800-PO < IL-AC4900-PO < IL-AC2900-PO. The total uptake at 35 bar ranges from 8.9 mmol g⁻¹ to 10.9 mmol g⁻¹, which is equivalent to 0.14 g g⁻¹ and 0.17 g g⁻¹, respectively. The uptake further increases to between 10.5 mmol g⁻¹ and 13.3 mmol g⁻¹ at 65 bar, corresponding to 0.17 g g⁻¹ and 0.21 g g⁻¹, respectively. At 100 bar, the total uptake falls within the range of 11.6 mmol g⁻¹ to 15 mmol g⁻¹, equivalent to 0.19 g g⁻¹ and 0.24 g g⁻¹, respectively.

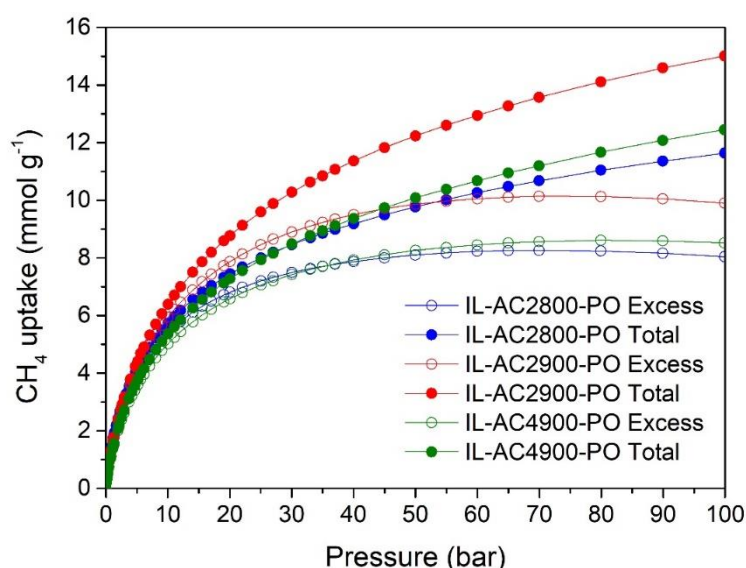


Figure 6.11. Gravimetric methane uptake comparison at 25 °C: Excess and total uptake for selected activated carbons (IL-AC2800-PO, IL-AC2900-PO and IL-AC4900-PO).

Table 6.4. Excess and total gravimetric methane uptake at 25 °C for selected activated carbons (IL-AC2800-PO, IL-AC2900-PO, and IL-AC4900-PO).

Sample	Gravimetric CH ₄ uptake (mmol g ⁻¹)					
	Excess uptake			Total uptake		
	35 bar	65 bar	100 bar	35 bar	65 bar	100 bar
IL-AC2800-PO	7.7	8.3	8.1	8.9	10.5	11.6
IL-AC2900-PO	9.2	10.1	9.9	10.9	13.3	15.0
IL-AC4900-PO	7.7	8.5	8.5	9.0	11.0	12.5

The volumetric uptake of an adsorbent is a crucial metric when considering methane uptake. Therefore, the high packing density of any adsorbent is a critical factor as a high density enables a greater amount to be confined within a given space, resulting in higher volumetric uptake. In line with this, the US Department of Energy (DOE) has established a target of 263 cm³ (STP) cm⁻³ at moderate pressure (i. e., 35–100 bar) and 25 °C for volumetric uptake capacity.⁴⁹⁻⁵² The selected activated carbons, IL-AC2800-PO, IL-AC2900-PO and IL-AC4900-PO, have high packing density of 0.98, 0.84 and 0.86 g cm⁻³, respectively. The high packing density suggests that, despite their modest surface area, the carbons may have the potential to efficiently store a significant amount of methane and show excellent performance in terms of volumetric uptake. The total volumetric methane uptake isotherms are shown in **Figure 6.12** and **Table 6.5** summarises the uptake at 35, 65 and 100 bar. Due to their high packing density, these carbons show high volumetric methane uptake at 25 °C and 35 bar, with values of 195, 204, and 173 cm³ (STP) cm⁻³ for IL-AC2800-PO, IL-AC2900-PO, and IL-AC4900-PO, respectively. The total volumetric uptake capacities of the IL-AC2900-PO at 35 bar and 25 °C of 204 cm³ (STP) cm⁻³, is amongst the best carbons or for any other porous materials reported to date but with the notable of being derived from a milder and more environmentally friendly activating agent.^{16, 26, 49-61} For instance, the best activated carbon performance to date is ascribed to activated carbons derived from date seeds (*Phoenix dactylifera*) or cloves, with storage capacities of up to 222 and 235 cm³ (STP) cm⁻³, respectively, 25 °C and 35 bar. However, it is worth noting that these activated carbons were produced utilising a corrosive activating agent (i.e., KOH).^{26, 54} The uptake of IL-AC2900-PO is also

comparable and nearly reaches the performance of the best MOF reported to date, which is monoHKUST-1 that has total volumetric uptake of $224 \text{ cm}^3 (\text{STP}) \text{ cm}^{-3}$ at 25°C and 35 bar. monoHKUST-1 is widely recognised as the benchmark material for evaluating the volumetric methane uptake of MOFs materials.⁶¹ The total volumetric methane uptake further increases to 231, 249, and $211 \text{ cm}^3 (\text{STP}) \text{ cm}^{-3}$ at 65 bar, and reaches as high as 256, 282, and $240 \text{ cm}^3 (\text{STP}) \text{ cm}^{-3}$ at 100 bar and 25°C , respectively for IL-AC2800-PO, IL-AC2900-PO, and IL-AC4900-PO. Overall, the results show that the present samples, particularly IL-AC2900-PO and IL-AC2900-PO, achieved or surpassed the DOE target for methane storage at 100 bar and 25°C , having high methane uptake capacities of 256 and $282 \text{ cm}^3 (\text{STP}) \text{ cm}^{-3}$, respectively.

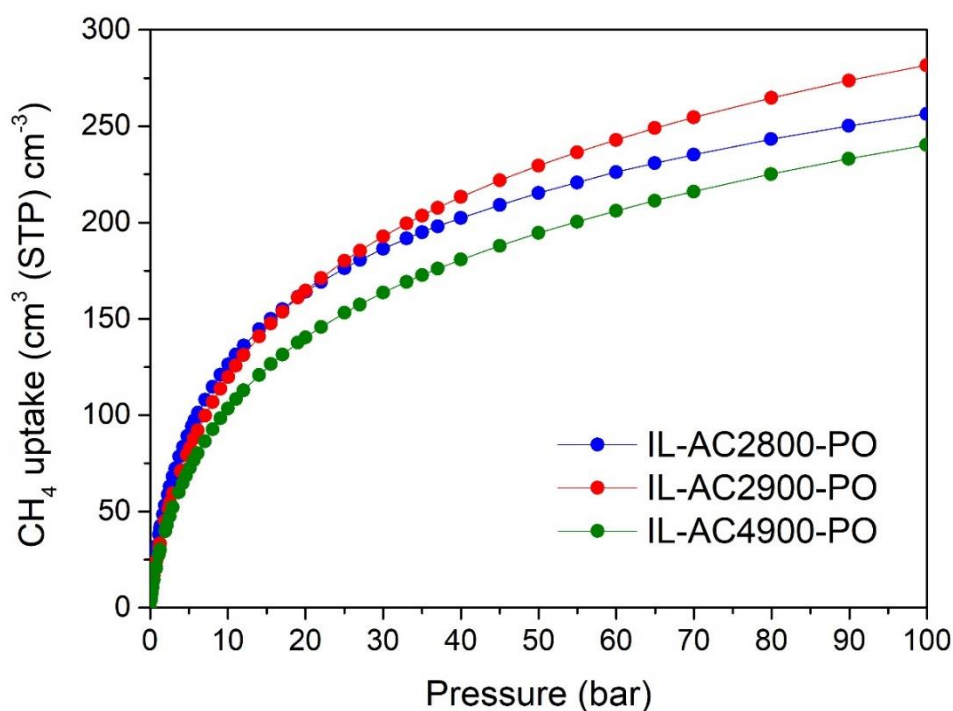


Figure 6.12. Total volumetric methane uptake at 25°C for selected activated carbons (IL-AC2800-PO, IL-AC2900-PO and IL-AC4900-PO).

Table 6.5 Total volumetric methane uptake at 25 °C and various pressures (35, 65, and 100 bar) for selected activated carbons (IL-AC2800-PO, IL-AC2900-PO, and IL-AC4900-PO).

Sample	Density (g cm ⁻³)	Total volumetric uptake (cm ³ (STP) cm ⁻³)			Working capacity ^a (cm ³ (STP) cm ⁻³)		
		35 bar	65 bar	100 bar	35 bar	65 bar	100 bar
IL-AC2800-PO	0.98	195	231	256	104	140	165
IL-AC2900-PO	0.84	204	249	282	122	167	200
IL-AC4900-PO	0.86	173	211	240	101	139	168

^aWorking capacity, defined as the difference in methane uptake between 5 bar and higher pressures (35, 65, or 100 bar).

Working capacity, defined as the difference in methane uptake between 5 bar and higher pressures (35, 65, or 100 bar), is an important measure of methane uptake performance. **Table 6.5** summarises the uptake of IL-AC2800-PO, IL-AC2900-PO, and IL-AC4900-PO, expressed in cm³ (STP) cm⁻³, revealing uptake ranging from 101 to 122 (at 35 bar), 139 to 167 (at 65 bar), and as high as 165 to 200 (at 100 bar). Notably, IL-AC2900-PO shows an impressive working capacity of 200 cm³ (STP) cm⁻³, especially considering that it is generated using a greener activating agent. Thus, the IL-AC2900-PO sample demonstrates excellent performance, with a gravimetric uptake of 0.24 g g⁻¹, a total volumetric uptake of 282 cm³ (STP) cm⁻³, and a working capacity of 200 cm³ (STP) cm⁻³ at 100 bar and 25 °C, placing it among the top-performing carbons and MOF materials.^{16, 26, 49-61} The present carbons are particularly attractive as they are environmentally friendly in terms of their production, possess high packing density, and outperform many activated carbons that utilise corrosive KOH as activator.

6.5 Conclusion

The synthesis of activated carbons from a pre-condensed imidazolium-based ionic liquid (IL), followed by activation using a milder and non-hydroxide activating agent, potassium oxalate, generates materials with characteristics suitable for energy-related applications. The activated carbons have a significant N content of up to 11 wt% and a highly microporous structure with moderate surface area of up to $2200 \text{ m}^2 \text{ g}^{-1}$, depending on the activation temperature. The activated carbons can be tailored to exhibit a highly microporous structure with porosity suitable for post-combustion CO_2 uptake. At 25°C and 0.15 and 1 bar, the carbons achieve CO_2 uptake capacity of 1.6 and 4.2 mmol g^{-1} , respectively. Furthermore, due to their high packing density of up to $0.98 \text{ cm}^3 \text{ g}^{-1}$, arising from using PO as milder activating agent, combined with a high surface area density, the carbons also demonstrate excellent methane storage capacity. At 100 bar and 25°C , the carbons achieve very attractive volumetric methane uptake of $282 \text{ cm}^3 (\text{STP}) \text{ cm}^{-3}$ along with excellent working capacity of $200 \text{ cm}^3 (\text{STP}) \text{ cm}^{-3}$ (for 100 to 5 bar pressure swing), placing them among the top-performing porous materials be they carbons and MOFs.

References

1. N. P. Wickramaratne and M. Jaroniec, *Journal of Materials Chemistry A*, 2013, **1**, 112-116.
2. B. Adeniran, E. Masika and R. Mokaya, *Journal of Materials Chemistry A*, 2014, **2**, 14696-14710.
3. N. Balahmar, A. C. Mitchell and R. Mokaya, *Advanced Energy Materials*, 2015, **5**, 1500867.
4. N. Balahmar, A. S. Al-Jumialy and R. Mokaya, *Journal of Materials Chemistry A*, 2017, **5**, 12330-12339.
5. E. A. Hirst, A. Taylor and R. Mokaya, *Journal of Materials Chemistry A*, 2018, **6**, 12393-12403.
6. N. Balahmar and R. Mokaya, *Journal of Materials Chemistry A*, 2019, **7**, 17466-17479.
7. E. Masika and R. Mokaya, *Energy & Environmental Science*, 2014, **7**, 427-434.
8. E. Masika and R. Mokaya, *Journal of Physical Chemistry C*, 2012, **116**, 25734-25740.
9. A. M. Aljumialy and R. Mokaya, *Materials Advances*, 2020, **1**, 3267-3280.
10. M. Sevilla, G. A. Ferrero and A. B. Fuertes, *Carbon*, 2017, **114**, 50-58.
11. J. Li, Q. Jiang, L. Wei, L. Zhong and X. Wang, *Journal of Materials Chemistry A*, 2020, **8**, 1469-1479.
12. A. Altwala and R. Mokaya, *Energy Advances*, 2022, **1**, 216-224.
13. A. Altwala and R. Mokaya, *RSC Advances*, 2022, **12**, 20080-20087.
14. M. Sevilla, A. S. M. Al-Jumialy, A. B. Fuertes and R. Mokaya, *ACS Applied Materials & Interfaces*, 2018, **10**, 1623-1633.
15. J. Ludwinowicz and M. Jaroniec, *Carbon*, 2015, **82**, 297-303.
16. A. Altwala and R. Mokaya, *Energy & Environmental Science*, 2020, **13**, 2967-2978.
17. M. Watanabe, M. L. Thomas, S. Zhang, K. Ueno, T. Yasuda and K. Dokko, *Chemical Reviews*, 2017, **117**, 7190-7239.
18. S. G. Zhang, K. Dokko and M. Watanabe, *Materials Horizons*, 2015, **2**, 168-197.

-
19. Z. L. Xie and D. S. Su, *European Journal of Inorganic Chemistry*, 2015, 1137-1147.
 20. J. Rouquerol, P. Llewellyn and F. Rouquerol, *Studies in Surface Science and Catalysis*, 2006, **160**, 49-56.
 21. A. Galarneau, D. Mehlhorn, F. Guenneau, B. Coasne, F. Villemot, D. Minoux, C. Aquino and J. P. Dath, *Langmuir*, 2018, **34**, 14134-14142.
 22. M. Thommes, K. Kaneko, A. V. Neimark, J. P. Olivier, F. Rodriguez-Reinoso, J. Rouquerol and K. S. W. Sing, *Pure and Applied Chemistry*, 2015, **87**, 1051-1069.
 23. J. S. Lee, X. Wang, H. Luo and S. Dai, *Advanced Materials*, 2010, **22**, 1004-1007.
 24. J. S. Lee, X. Wang, H. Luo, G. A. Baker and S. Dai, *Journal of the American Chemical Society*, 2009, **131**, 4596-4597.
 25. M. Sevilla, W. Sangchoom, N. Balahmar, A. B. Fuertes and R. Mokaya, *ACS Sustainable Chemistry & Engineering*, 2016, **4**, 4710-4716.
 26. A. Altwala and R. Mokaya, *Journal of Materials Chemistry A*, 2022, **10**, 13744-13757.
 27. L. S. Blankenship and R. Mokaya, *Materials Advances*, 2022, **3**, 1905-1930.
 28. J. C. Wang and S. Kaskel, *Journal of Materials Chemistry*, 2012, **22**, 23710-23725.
 29. W. Sangchoom and R. Mokaya, *ACS Sustainable Chemistry & Engineering*, 2015, **3**, 1658-1667.
 30. M. Sevilla and A. B. Fuertes, *Energy & Environmental Science*, 2011, **4**, 1765-1771.
 31. B. Adeniran and R. Mokaya, *Chemistry of Materials*, 2016, **28**, 994-1001.
 32. Z. Zhang, J. Zhou, W. Xing, Q. Xue, Z. Yan, S. Zhuo and S. Z. Qiao, *Physical Chemistry Chemical Physics*, 2013, **15**, 2523-2529.
 33. E. Haffner-Staton, N. Balahmar and R. Mokaya, *Journal of Materials Chemistry A*, 2016, **4**, 13324-13335.
 34. N. P. Wickramaratne and M. Jaroniec, *ACS Applied Materials & Interfaces*, 2013, **5**, 1849-1855.
 35. J. Silvestre-Albero, A. Wahby, A. Sepúlveda-Escribano, M. Martínez-Escandell, K. Kaneko and F. Rodríguez-Reinoso, *Chemical Communications*, 2011, **47**, 6840-6842.

-
36. L. S. Blankenship, N. Albeladi, T. Alkhaldi, A. Madkhali and R. Mokaya, *Energy Advances*, 2022, **1**, 1009-1020.
 37. Z. Zhang, K. Wang, J. D. Atkinson, X. Yan, X. Li, M. J. Rood and Z. Yan, *Journal of Hazardous Materials* 2012, **229**, 183-191.
 38. J. D. Figueroa, T. Fout, S. Plasynski, H. McIlvried and R. D. Srivastava, *International Journal of Greenhouse Gas Control* 2008, **2**, 9-20.
 39. A. Almasoudi and R. Mokaya, *Journal of Materials Chemistry A*, 2014, **2**, 10960-10968.
 40. X. Q. Fan, L. X. Zhang, G. B. Zhang, Z. Shu and J. L. Shi, *Carbon*, 2013, **61**, 423-430.
 41. M. Nandi, K. Okada, A. Dutta, A. Bhaumik, J. Maruyama, D. Derks and H. Uyama, *Chemical Communications*, 2012, **48**, 10283-10285.
 42. Y. D. Xia, R. Mokaya, G. S. Walker and Y. Q. Zhu, *Advanced Energy Materials*, 2011, **1**, 678-683.
 43. A. Wahby, J. M. Ramos-Fernández, M. Martínez-Escandell, A. Sepúlveda-Escribano, J. Silvestre-Albero and F. Rodríguez-Reinoso, *ChemSusChem*, 2010, **3**, 974-981.
 44. D. Lee, C. Zhang, C. Wei, B. L. Ashfeld and H. Gao, *Journal of Materials Chemistry A*, 2013, **1**, 14862-14867.
 45. G. Srinivas, J. Burrell and T. Yildirim, *Energy & Environmental Science*, 2012, **5**, 6453-6459.
 46. H. Tian, T. Li, T. Zhang and X. Xiao, *International Journal of Coal Geology*, 2016, **156**, 36-49.
 47. T. F. Rexer, M. J. Benham, A. C. Aplin and K. M. Thomas, *Energy & Fuels*, 2013, **27**, 3099-3109.
 48. I. Alali and R. Mokaya, *Journal of Materials Chemistry A*, 2023, **11**, 6952-6965.
 49. Y. He, W. Zhou, G. Qian and B. Chen, *Chemical Society Reviews*, 2014, **43**, 5657-5678.
 50. T. A. Makal, J. R. Li, W. Lu and H. C. Zhou, *Chemical Society Reviews*, 2012, **41**, 7761-7779.
 51. J. A. Mason, M. Veenstra and J. R. Long, *Chemical Science*, 2014, **5**, 32-51.
 52. B. Li, H. M. Wen, W. Zhou, J. Q. Xu and B. L. Chen, *Chem*, 2016, **1**, 557-580.

-
53. M. E. Casco, M. Martínez-Escandell, E. Gadea-Ramos, K. Kaneko, J. Silvestre-Albero and F. Rodríguez-Reinoso, *Chemistry of Materials*, 2015, **27**, 959-964.
 54. I. Alali and R. Mokaya, *Energy & Environmental Science*, 2022, **15**, 4710-4724.
 55. D. Lozano-Castello, J. Alcaniz-Monge, M. A. de la Casa-Lillo, D. Cazorla-Amoros and A. Linares-Solano, *Fuel*, 2002, **81**, 1777-1803.
 56. C. M. Simon, J. Kim, D. A. Gomez-Gualdron, J. S. Camp, Y. G. Chung, R. L. Martin, R. Mercado, M. W. Deem, D. Gunter, M. Haranczyk, D. S. Sholl, R. Q. Snurr and B. Smit, *Energy & Environmental Science*, 2015, **8**, 1190-1199.
 57. J. Abdulsalam, J. Mulopo, S. O. Bada and B. Oboirien, *ACS Omega*, 2020, **5**, 32530-32539.
 58. M. E. Casco, F. Rey, J. L. Jorda, S. Rudic, F. Fauth, M. Martinez-Escandell, F. Rodriguez-Reinoso, E. V. Ramos-Fernandez and J. Silvestre-Albero, *Chemical Science*, 2016, **7**, 3658-3666.
 59. P. N. Quirant, C. Cuadrado-Collados, A. J. Romero-Anaya, J. S. Albero and M. M. Escandell, *Industrial & Engineering Chemistry Research*, 2020, **59**, 5775-5785.
 60. M. E. Casco, M. Martinez-Escandell, K. Kaneko, J. Silvestre-Albero and F. Rodriguez-Reinoso, *Carbon*, 2015, **93**, 11-21.
 61. T. Tian, Z. Zeng, D. Vulpe, M. E. Casco, G. Divitini, P. A. Midgley, J. Silvestre-Albero, J. C. Tan, P. Z. Moghadam and D. Fairen-Jimenez, *Nature Materials*, 2018, **17**, 174-179.

Chapter 7

Summary and Future Outlook

The work in this Thesis primarily focused on the synthesis of activated carbon materials with modulated porosity that makes them suitable for use as adsorbents to enhanced CO₂ capture and storage and methane storage. The approach involved, Firstly in **Chapter 3**, building up knowledge of key parameters, namely, O/C ratio of precursors, incorporating (or presence of) heteroatoms such as N in the precursors and activation conditions, that serve as tools to modulate and customise the nature of activated carbons to meet specific requirements for CO₂ uptake and CH₄ storage. This included developing an understanding of the impact of O/C ratio of the precursors and how it can be tuned by varying the carbonisation temperature as discussed in **Chapter 3**. It was observed, for the air-carbonisation of waste Hookah Tobacco (HTb), that the carbonisation temperature is a significant factor in the preparation of carbonaceous matter with varying O/C ratios. The activation of carbonaceous matter that was carbonised at low temperatures generated activated carbons with ultra-microporosity suitable for post-combustion CO₂ capture. Furthermore, by varying the carbonisation temperature, it was possible to prepare activated carbons with a range of porosity, including high surface area samples and a mix of porosity that is suitable for enhanced CH₄ storage. Although the production of activated carbons from a biomass sources appears to provide materials that are suitable for CO₂ capture, there is a need to further increase the surface area and pore volume if they are to achieve gravimetric and volumetric methane uptake levels that align with the targets set by the US Department of Energy (DOE).

In the second approach, presented in **Chapter 4**, a route to introduce N-containing additives to biomass-derived carbonaceous matter was explored. The biomass carbonaceous matter with low O/C ratio (i.e., air-carbonised date seed, *Phoenix dactylifera*, ACDS), was deliberately chosen as it is known to be resistant to activation.

The N-rich additives used were melamine and urea, with KOH as an activating agent. The hope was that the very low O/C ratio of ACDS would work to provide activated carbons with high packing density due to its high resistance, while the addition of N would work in the opposite direction and increase the surface area. This approach resulted in flexibility in controlling the porosity of the activated carbons by varying the amount of melamine or urea added, the KOH/ACDS ratio, and the activation temperature, thus enabling enhanced CO₂ and methane uptake in the resulting materials. The outcome was the creation of ultra-high porosity carbons, with surface area nearly double that achieved by activating ACDS alone, resulting in very high methane uptake.

The approach demonstrated in **Chapter 4** provided a basis for further investigation of combining low O/C ratio and presence of N as a means of generating activated carbons that are highly suited for methane storage. **Chapter 5**, reports on the preparation of activated carbons with high micro/mesoporosity via carbonisation of an ionic liquid (1-butyl-3-methylimidazolium tricyanomethanide, [BMIm][C(CN)₃]) followed by chemical activation of the resulting carbonaceous matter with KOH. On carbonisation, the ionic liquid (IL) yields carbonaceous matter with the unusual combination of both a high N content and low O/C atomic ratio. On activation, the IL-derived carbonaceous matter (IL-C) generates activated carbons with a mix of micro and mesoporosity that have ultra-high surface area of up to ~4000 m² g⁻¹ and pore volume of up to 3.3 cm³ g⁻¹, along with comparatively high packing density. The porosity and packing density of the activated carbons is a consequence of the elemental composition of the IL-C precursor. In particular the low O/C ratio and high N content of the IL-C precursor play a role in determining the porosity. In this way, the IL-C precursor shows anomalous activation behaviour when compared to other traditional carbonaceous matter. The IL-derived activated carbons are ideal for storage of methane because of their well-balanced combination of microporosity and mesoporosity, high packing density, and large surface area. The best carbons achieve methane uptake of up to 0.53 g g⁻¹ and 289 cm³ (STP) cm⁻³ at 25 °C and 100 bar. Such uptake exceeds the storage targets for both gravimetric and volumetric uptake set by the US Department of Energy (DoE) of 0.5 g g⁻¹ and 263 cm³ (STP) cm⁻³, which would allow widespread use for vehicular transport and other purposes. In addition, the IL-derived carbons

achieve attractive deliverable methane capacity (working capacity) of up to 0.46 g g^{-1} and $248 \text{ cm}^3 \text{ (STP) cm}^{-3}$ for a pressure swing of 100 to 5 bar at 25°C .

The work reported in **Chapter 6**, further deepens understanding of the role of N as a dopant in shaping the porosity of activated carbons. Activated carbons were generated using a milder non-hydroxide agent, potassium oxalate (PO). Despite the low O/C ratio of the precursor used, namely IL-C, the PO derived activated carbons display a range of surface areas and pore volumes, suitable for post-combustion CO_2 uptake and methane storage. Depending on the activation parameters, the porosity of the activated carbons could be tailored towards a highly microporous structure suitable for post-combustion CO_2 uptake. At 25°C and pressure of 0.15 and 1 bar, the generated carbons have CO_2 uptake capacity of 1.6 and 4.2 mmol g^{-1} , respectively. Furthermore, due to their high packing density of up to $0.98 \text{ cm}^3 \text{ g}^{-1}$, occasioned by the use of the milder PO, the carbons also demonstrated excellent volumetric methane uptake of up to $282 \text{ cm}^3 \text{ (STP) cm}^{-3}$, at 25°C and 100 bar, and a working capacity of $200 \text{ cm}^3 \text{ (STP) cm}^{-3}$ for a 100 to 5 bar pressure swing.

In summary, this thesis has elaborated into the synthesis of activated carbons using various precursors and activation techniques. This has resulted in the preparation of activated carbons characterised by ultra-high surface area and pore volume. The primary focus has been on enhancing CO_2 uptake and methane storage. This work has helped to address the challenges associated with achieving a delicate balance between gravimetric and volumetric methane uptake and also opens doors to other applications. One promising application for future investigation involves the application of these activated carbons in hydrogen storage.